DISSERTATION

submitted to the
Combined Faculties for the Natural Sciences and for Mathematics
of the Ruperto-Carola University of Heidelberg, Germany
for the degree of Doctor of Natural Sciences

Put forward by
Dipl.-Phys. Christoph Deil
born in Bayreuth, Germany

Oral examination: December 16th, 2011

HESS & Fermi Surveys of the Galactic Gamma-ray Source Population

Referees:
Prof. Dr. Werner Hofmann
Prof. Dr. Stefan Funk

Abstract

The High Energy Stereoscopic System (HESS) is an array of four imaging atmospheric Cherenkov telecopes, located in Namibia, observing the gamma-ray sky at energies > 100 GeV since 2004. For the first time HESS has surveyed the Galactic plane (approximately in the range GLON = -110 to +70 deg, GLAT = -3 to 3 deg) and detected a number of sources, each one a cosmic particle accelerator emitting gamma rays produced in interactions of the cosmic rays with ambient matter and radiation fields. In this thesis the full HESS Galactic plane survey dataset was used to derive significance and flux maps as well as a catalog of 62 sources containing their position, extension and spectrum. Several new methods for an improved and semi-automatic detection and analysis of all sources were developed. The Fermi Large Area Telescope (LAT) is a space-based gamma-ray telescope, continuously performing an all-sky survey above 100 MeV since June 2008. Based on two years of data in the energy range 100 MeV to 100 GeV the LAT collaboration has published a catalog of 1873 sources, 244 of which, mostly of Galactic origin, are located inside the HESS survey region. In this work all-sky significance and flux maps and catalogs of 74 Fermi sources above 10 GeV and 42 sources above 100 GeV are derived and a preliminary comparison with the HESS data is presented. This work can serve as the basis for future detailed studies of the Galactic gamma-ray source population.

Kurzfassung

Das High Energy Stereoscopic System (HESS) ist ein Array von vier atmosphärischen Cherenkov-Teleskopen in Namibia, das seit 2004 den Himmel im Bereich hochenergetischer Gammastrahlung (> 100 GeV) beobachtet. In einem erstmaligen Survey der Galaktischen Ebene (circa im Bereich GLON = -110 bis +70 deg, GLAT = -3 bis +3 deg) wurde eine Reihe neuer Gamma-Strahlungs-Quellen entdeckt. Diese Objekte sind kosmische Teilchenbeschleuniger, in denen Gamma-Strahlung durch die Wechselwirking von kosmischer Strahlung mit umgebenden Materie- und Strahlungsfeldern entsteht. In dieser Arbeit wurde der gesamte HESS-Datensatz f§r die galaktische Ebene benutzt um Signifikanz- und Flußkarten sowie einen Katalog von 62 Quellen zu erstellen, der ihre Position, Ausdehnung und Spektrum angibt. Neue Methoden f§r eine verbesserte und halb-automatische Erkennung und Analyse aller Quellen wurden entwickelt. Das Fermi Large Area Telescope (LAT) ist ein Satellit, der seit Juni 2008 das Universum kontinuierlich im Bereich von Gammastrahlung oberhalb von 100 MeV observiert. Basierend auf den Daten der ersten 2 Jahre im Bereich von 100 MeV bis 100 GeV hat die LAT-Kollaboration einen 1873 Quellen umfassenden Katalog verŽffentlicht, wovon 244 Quellen, vorwiegend galaktischen Ursprungs, im Bereich des HESS-Surveys liegen. In dieser Arbeit wurden Signifikanzkarten und Kataloge von 74 Fermi-Quellen über 10 GeV und 42 Quellen über 100 GeV erstellt und ein vorläufiger Vergleich mit den HESS-Daten wirt präsentiert. Die in dieser Arbeit erstellten Daten können als Grundlage für zukünftige detaillierte Analysen der galaktischen Gamma-Quellen-Population dienen.

Contents

List of Figures

List of Tables

1. Introduction

The introduction will give a short summary of the past, present and future of Galactic gamma-ray astronomy as well as on surveys of the Milky Way in general. Most of the issues mentioned here will be discussed in more detail in the following chapters.

1.1. Gamma-ray Astronomy

1.1.1. TeV astronomy

In 1989 the first teraelectronvolt (TeV) gamma-ray source—the Crab pulsar wind nebula (PWN)—was discovered by the Whipple imaging atmospheric Cherenkov telescope in Arizona (Weekes et al., 1989). This discovery was followed by a handful of active Galactic nuclei in the 1990s, the first being Markarian 421 (Punch et al., 1992) and Markarian 501 (Quinn et al., 1996).

Progress on Galactic sources was slow, and a number of false discovery claims was made, e.g. the reported detections of the pulsar PSR 1706-44 (Kifune et al., 1995) and the supernova remnant (SNR) SN 1006 (Tanimori et al., 1998) by CANGAROO in Australia were later shown to be incorrect by the more sensitive HESS Cherenkov telescopes (by placing upper limits an order of magnitude below the flux reported by CANGAROO) (Aharonian et al., 2005a,b) and eventually recanted (Yoshikoshi et al., 2009).

In hindsight it is possible to list the first real detections of Galactic TeV sources in chronological order (although all detections except the Crab were at very low statistical significance and reported source morphology and spectra were often not correct): (1) Crab PWN by Whipple (Weekes et al., 1989). (2) Vela X PWN by CANGAROO (Yoshikoshi et al., 1997). (3) RX J1713.7-3946 SNR by CANGAROO (Muraishi et al., 2000). (4) Cassiopeia A SNR by HEGRA on the Canary island of La Palma (Aharonian et al., 2001). (5) TeV J2032+4130 by HEGRA (Aharonian et al., 2002). This is an *unidentified dark* source, i.e. one without good counterpart candidate, even today. (6) Galactic center by CANGAROO (Tsuchiya et al., 2004). This is an *unidentified confused* source, two good counterpart candidates have been identified, the supermassive black hole in the center of the Milky Way and the PWN candidate G359.95-0.04. (7) Vela Junior SNR by CANGAROO (Katagiri et al., 2005).

So in 2004, when the High Energy Stereoscopic System (HESS)[1] telescopes

[1] www.mpi-hd.mpg.de/hfm/HESS

were built, seven Galactic sources were known (3 SNR, 2 PWN, 2 UNID). HESS had clear advantages over previous instruments:

- About an order of magnitude better sensitivity than previous instruments. The Crab could be detected in a minute and a 1% Crab source in 25 hours of observation.
- Good angular resolution and a 5 degree field of view, making it possible to survey the Galactic plane, where before only pointed observations at one source at a time where possible that was suspected to possibly emit gamma rays on theoretical grounds.
- Located in Namibia, with a clear view at the inner Galaxy, whereas the other instruments had been in the northern hemisphere.

The *HESS Galactic plane survey* quickly discovered 14 new Galactic gamma-ray sources in the inner Galaxy (Galactic longitude ± 30 deg and latitude ± 3 deg) (Aharonian et al., 2006a). This survey has been ongoing ever since, and the resulting image (as of 2007) is shown in Figure 1.1, bottom. A catalog (all-sky) of TeV sources (as of 2009) is shown in Figure 1.1, top. Figure 1.10 shows the exponential increase in source count in X- and gamma-ray astronomy with time.

Currently three major Cherenkov telescope arrays are in operation: HESS with four 100 m^2 telescopes in Namibia, MAGIC[2] with two 230 m^2 telescopes on the Canary island of La Palma and VERITAS[3] with four 100 m^2 telescopes in Arizona. They all have similar performance: ~ 1 % Crab sensitivity in 25 hours, energy threshold ~ 100 GeV, field of view ~ 4 deg and ~ 1000 h observation time per year.

Currently the HESS collaboration is building a fifth, much larger (600 m^2) HESS 2 telescope in the center of the existing array, which will lower the energy threshold to ~ 50 GeV and improve the overall sensitivity (Deil et al., 2008a; Becherini et al., 2008a).

The next-generation Cherenkov telescope array (CTA)[4] is currently in the design phase. It will contain ~ 100 telescopes (a mix of small, medium and large) and achieve a factor two better angular resolution (~ 0.05 deg, lower energy threshold (~ 30 GeV) and an order of magnitude better sensitivity (0.1 % Crab in 25 h) than the current instruments (CTA Consortium, 2010). It is expected that it will detect hundreds of sources, as e.g. illustrated in the simulated view of the Galactic plane shown in Figure 1.2.

The TeV results described so far were obtained with imaging atmospheric Cherenkov telescopes (IACTs) that reconstruct the energy and direction of the primary gamma by imaging the (tertiary) Cherenkov light emitted in ~ 10 km

[2] wwwmagic.mppmu.mpg.de
[3] veritas.sao.arizona.edu
[4] www.cta-observatory.org

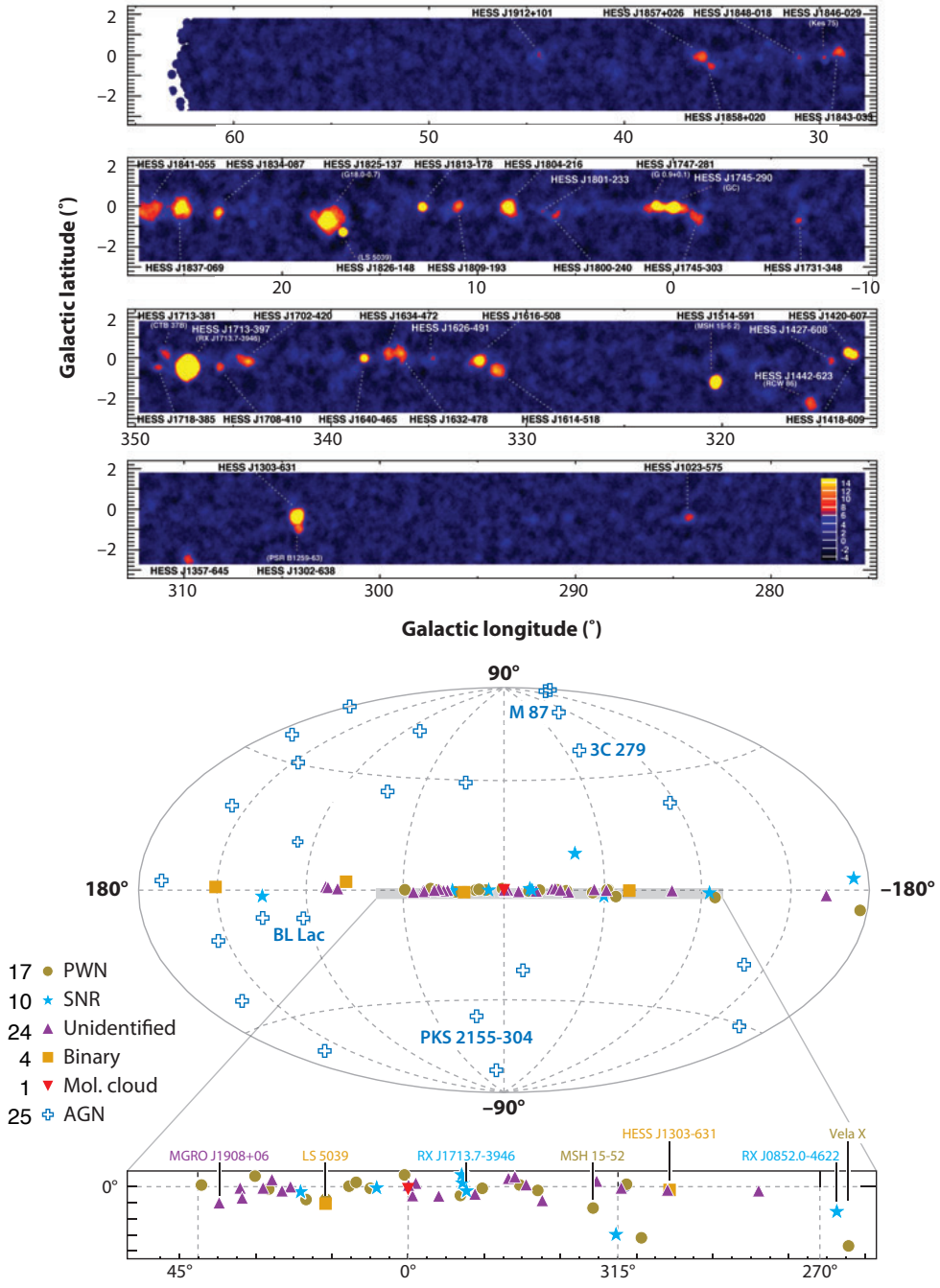

Figure 1.1.. *Top:* HESS Galactic plane survey of TeV sources (longitude range -90 to +60 deg, energy band $\sim$ 0.3 to 30 TeV, angular resolution ~ 0.1 deg, units are statistical significance). *Bottom:* Positions of TeV gamma-ray sources in Galactic coordinates. The number of sources per class is given in the legend. Figures taken from Hinton and Hofmann (2009).

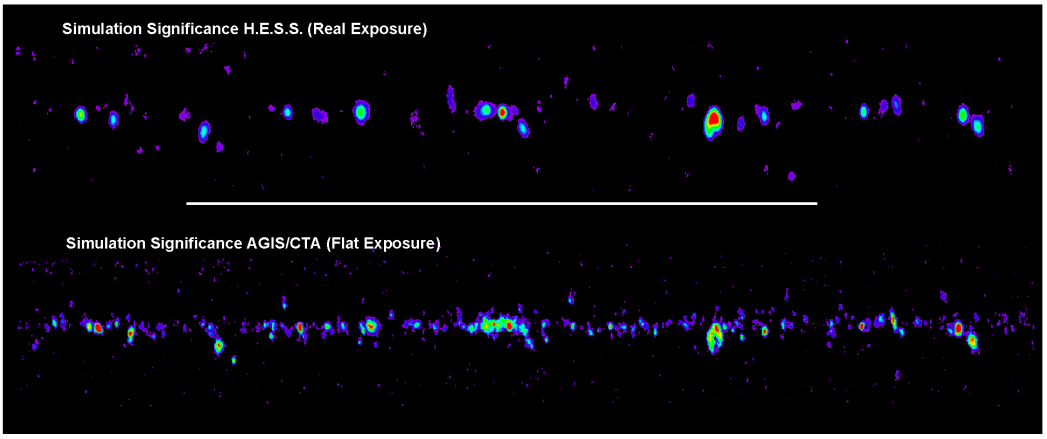

Figure 1.2.. Simulated significance images of the inner Galaxy ($l < \pm 20, b < \pm 3$ deg) observed with HESS (top) and the next-generation CTA (bottom) with sensitivity improved by an order of magnitude and angular resolution by a factor of two. Figure taken from Funk et al. (2008).

height by the particles in the (secondary) air shower that forms when the gamma-ray interacts with the Earth atmosphere. For higher-energy gamma rays the secondary air shower particles reach the ground and their distribution and arrival times can be used to reconstruct the energy and direction of the primary gamma ray. The MILAGRO[5] water Cherenkov detector operated from 2001 to 2008 at an altitude of 2500 m in New Mexico and surveyed the whole northern hemisphere (see Atkins et al. (2004) and Abdo et al. (2007) for details on the Galactic plane) with an energy threshold of ~ 5 TeV, sensitivity of 20 % Crab and angular resolution of 1 deg (these numbers are somewhat zenith-angle dependent).

They have detected one AGN (Mkr 421), four Galactic sources (significance $> 6\sigma$) and four source candidates (significance $> 5\sigma$). As shown in Figure 1.3 they did however—due to their location in the northern hemisphere—not observe the inner Galaxy, but only longitudes > 30 deg and < -140 deg. The detected sources are the Crab, MGRO J2019+37 for which the Dragonfly PWN has been suggested as a counterpart, as well as two unidentified sources MGRO J2031+41 and MGRO J1908+06. Later HESS J1908+063 was discovered in spatial and spectral compatibility with the Milagro source (Aharonian et al., 2009a). As expected the spectrum is hard (spectral index 2.1) without indication for a cutoff.

Recently MILAGRO has published a search for emission at 34 positions of identified or suspected Galactic sources reported by *Fermi* (Abdo et al., 2009a) (explained in more detail below) and found 14 detections above 3σ, with a prob-

[5] www.lanl.gov/milagro

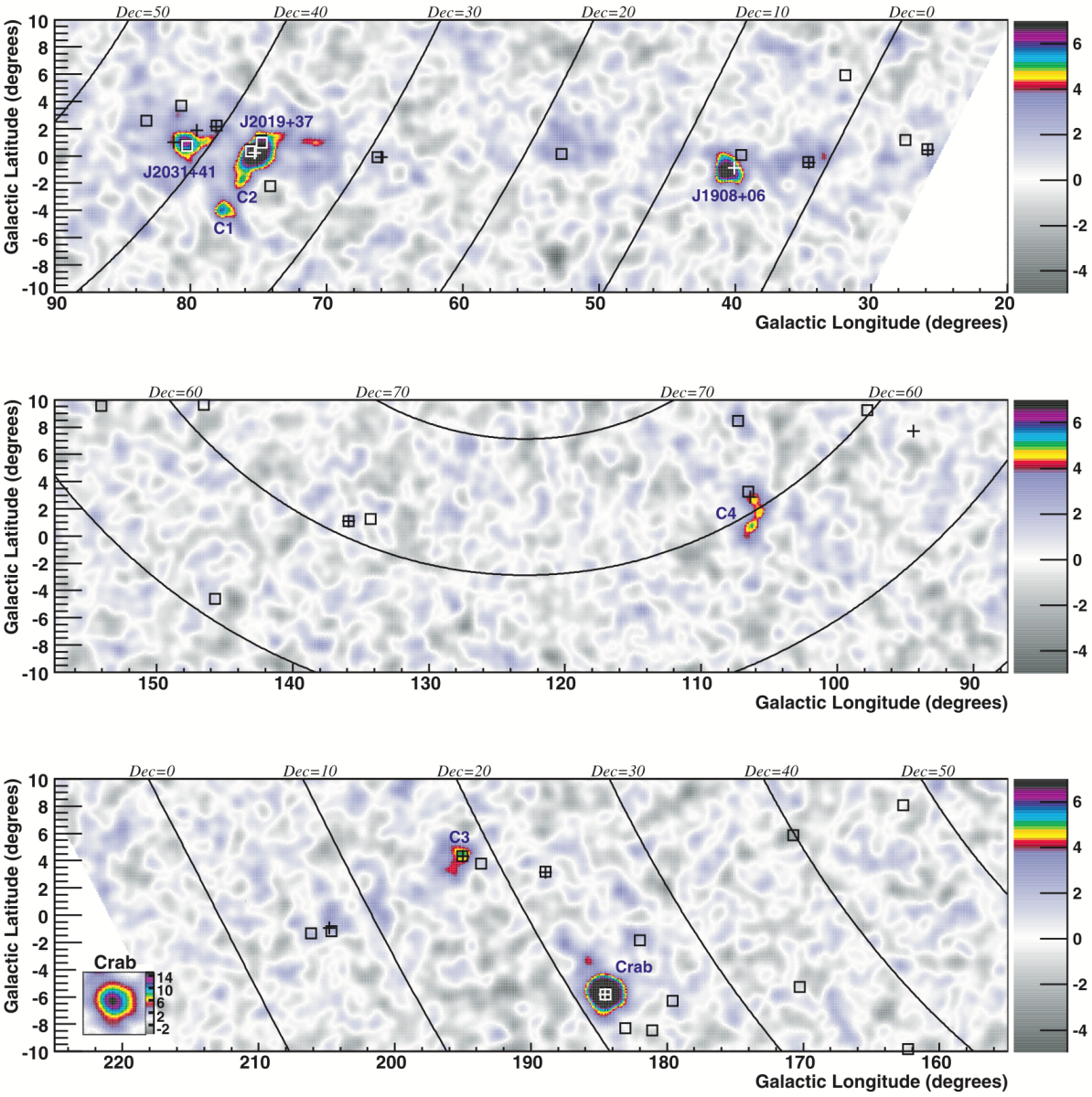

Figure 1.3.. MILAGRO Galactic plane survey of multi-TeV sources (longitude range +30 to +220, energy band ~ 10 to 100 TeV, angular resolution 1.1 deg, units are statistical significance with a very sharp transition at 4). Four sources and four hotspots (denoted C1 to C4) are labeled, boxes denote EGRET 3EG GeV sources. Figure taken from Abdo et al. (2007).

ability of only 4% that one of those detections is false.

The example of MGRO J1908+06 shows that water Cherenkov detectors are complementary to Air Cherenkov telescopes (ACTs) for gamma-ray surveys. ACTs have good point-source sensitivity (now 1% Crab, next-generation 0.1% Crab for 25 hours of pointed observation), but surveying the Galactic plane takes many years even if half of the observing time is spent on this effort. Also it is not possible to survey the whole sky with good sensitivity, e.g. the HESS Galactic plane survey ($\Delta l = 200$ deg and $\Delta b = 6$ deg) only covers 3% of the sky. One important point to note is that the sensitivity of ACTs for sources that are larger than the PSF (~ 0.1 deg) degrades linearly with source size (Hinton and Hofmann, 2009), and the detection of sources of sizes comparable to the FOV or larger is not possible. For water Cherenkov detectors the sensitivity for sources below their PSF (~ 1 deg) is constant and they can detect e.g. multi-degree sources or diffuse emission, such as e.g. the result by MILAGRO on the Galactic plane and Cygnus region (Abdo et al., 2008).

The High Altitude Water Cherenkov Experiment (HAWK)[6] will be the MILAGRO successor and will be build at a 4100 m altitude site in Mexico (Sandoval et al., 2009; On Behalf Of The Milagro et al., 2010). The detection of 14 Galactic sources by MILAGRO (out of 34 candidates pre-defined by Fermi) shows that HAWC with about an order of magnitude better sensitivity will detect many source by itself and provide an extension of the spectrum (or detection of a cut-off) out to 100 TeV for all the sources in the HESS and CTA Galactic plane surveys.

Recent reviews of TeV astronomy are Hinton and Hofmann (2009); Aharonian et al. (2008); Weekes (2008). TeVCat[7] is a continuously updated list of TeV sources, which currently (May 2011, Version 3.3) contains 123 sources.

1.1.2. GeV astronomy

The air Cherenkov technique described above requires a minimum number of Cherenkov photons (~ 100, see Hinton and Hofmann (2009)) in the shower image for a successful reconstruction of the gamma-ray direction and distinction from the orders of magnitude from more common cosmic-ray induced air showers. This results in an energy threshold below which gamma-ray sources cannot be detected, which depending on the zenith angle of the observation and the cuts applied typically lies in the range 200 GeV to 700 TeV for current-generation instruments like HESS.

Pair production telescopes aboard satellites on the other hand directly measure the tracks of the electron and positron produced inside the detector. The Energetic Gamma Ray Experiment Telescope (EGRET) on the Compton Gamma Ray Observatory (CGRO) observed the whole sky in the 30 MeV to 20 GeV band

[6] `hawc.umd.edu`

[7] `tevcat.uchicago.edu`

from 1991 to 1995 and published a catalog of 271 sources (Hartman et al., 1999). In June 2008 the Large Area Telescope (LAT, Atwood et al. (2009); Rando and for the Fermi LAT Collaboration (2009)) on the Fermi Gamma-ray Space Telescope[8] was launched and since then has surveyed the entire sky at energies of 20 MeV to more than 300 GeV.

A Bright Source List (BSL, a.k.a. 0FGL) of 205 high-significance sources was published based on three months of data (Abdo et al., 2009b), followed by the First Fermi LAT Source Catalog (1FGL) of 1451 sources based on 11 months of data and the Second Fermi LAT Source Catalog (2FGL) of 1873 sources bases on 24 months of data in the energy range 100 MeV to 100 GeV. As can be seen in Figure 1.4, the major extragalactic source population are AGN. The First LAT AGN Catalog (1LAC) gives details on 671 sources from the 1FGL at high latitudes ($|b| > 10$ deg) that are statistically very likely to be associated to known AGN (Abdo and for the Fermi-LAT Collaboration, 2010). The most populous class of identified Galactic sources are pulsars (83 in the 2FGL). For all gamma-ray pulsars an exponential cutoff with E_{cut} $1 - -10$ GeV was measured, which makes it understandable why pulsars have not been detected by ACTs—except for the Crab pulsar, which was detected by MAGIC above 25 GeV using special-build hardware to achieve this low-energy threshold (Aliu et al., 2008).

Besides pulsars, which can be unambiguously identified via the pulses seen in their folded lightcurve, the majority of the Galactic sources is unidentified. The reason is their small latitude distribution, in the Galactic plane there are 164 sources within $|b| < 1$ deg, 119 of which within $|l| < 60$ deg. This means that the average distance between sources is ~ 1 deg, and thus their signals overlap given the LAT angular resolution of ~ 3 deg at 100 MeV. This is the reason why most Galactic sources are flagged in the 2FGL by appending a 'c' to their name, as "a warning that the existence of the source or its measured properties (location, flux, spectrum) may not be reliable." (Abdo et al., 2010a).

1.2. The Galactic Gamma-ray Source Population.

Before we discuss the properties of the Galactic gamma-ray sources, let us briefly review the structure of the Galaxy. As illustrated in 1.5 the Milky Way is a spiral galaxy and the Sun is located in the disk at a distance of ~ 8 kpc from the Galactic center (Majaess, 2010). Figure 1.6 top left shows the resulting distribution of stars on the sky. There are several components, a bulge and halo that are roughly spherical as well as a thin and thick disk. Figure 1.6 bottom left shows that the gas is confined to the thin disk. Star formation only happens in giant molecular clouds within spiral arms in that disk.

Massive stars end their life quickly (within a few million years) in core-collapse supernovae, an event in which the stellar core collapses into a neutron star or black hole while the outer hulls are ejected. Typically the ejecta have

[8] `fermi.gsfc.nasa.gov`

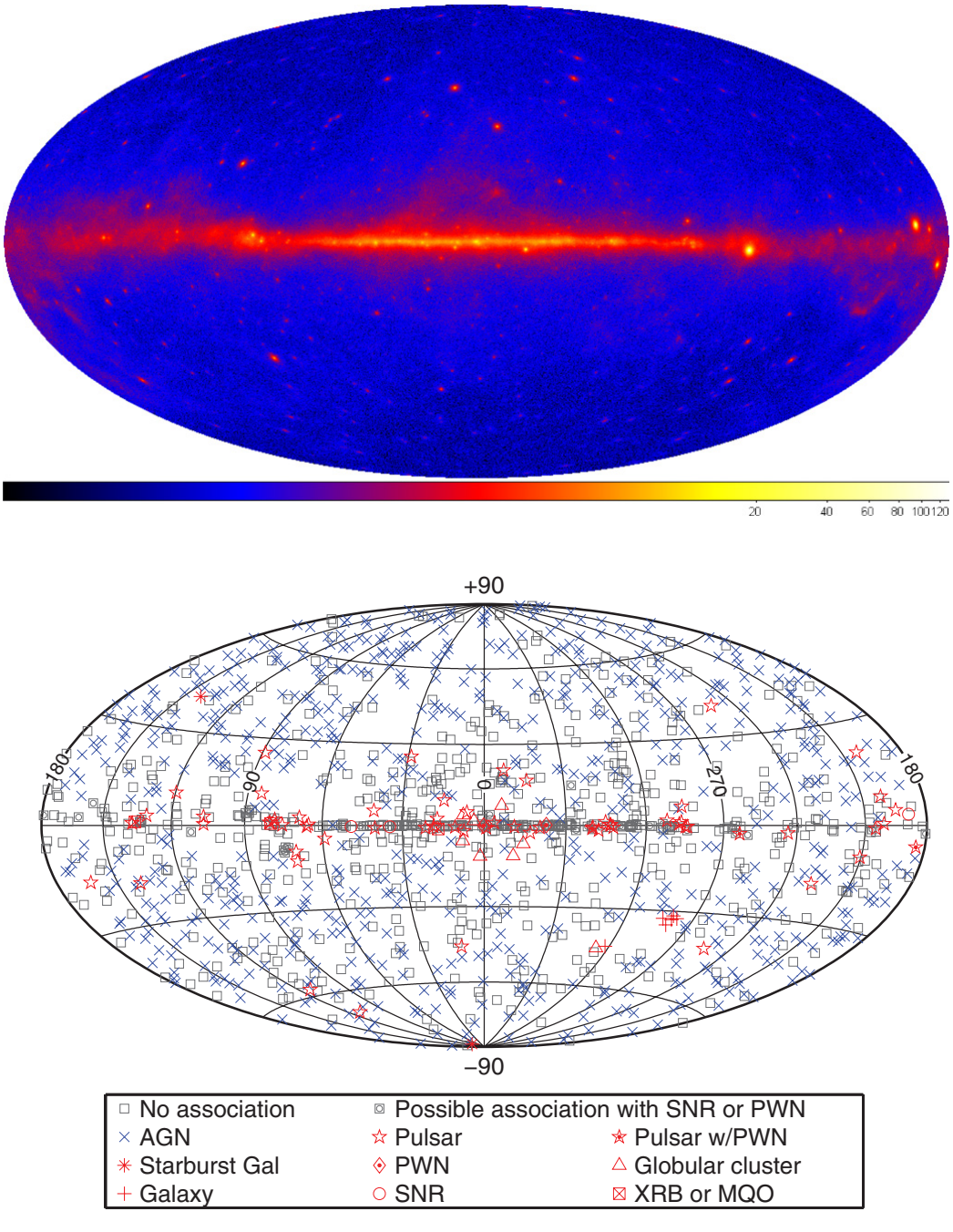

Figure 1.4.. Fermi LAT all-sky survey of GeV sources. *Top:* Gamma-ray intensity in the 300 MeV to 100 TeV band in $m^{-2}\ s^{-1}\ sr^{-1}$. The angular resolution is ~ 3 deg. *Bottom:* Second Fermi LAT Source Catalog (2FGL) containing 1873 sources. Figures taken from Abdo et al. (2010a).

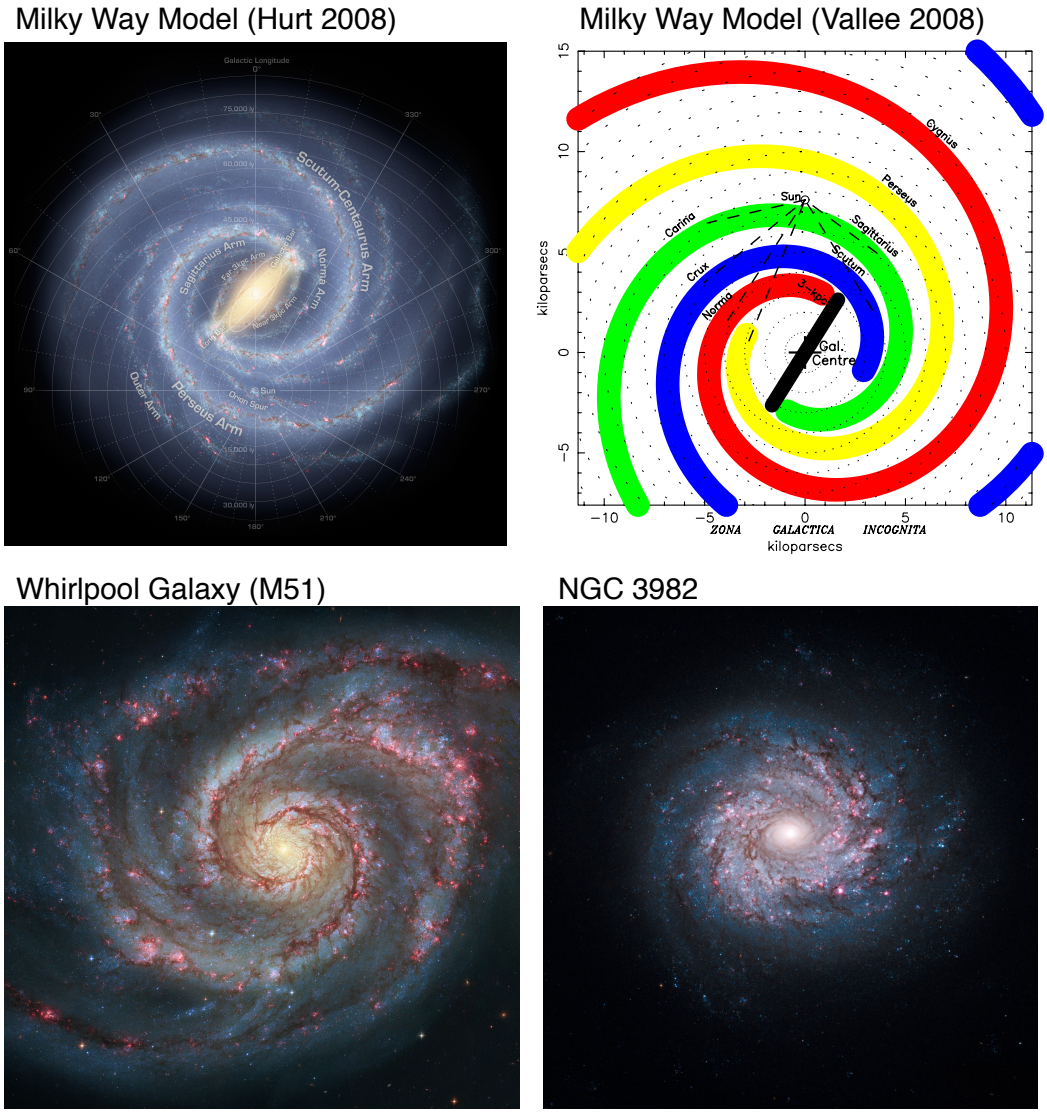

Figure 1.5.. *Left:* Annotated roadmap to the Milky Way by Robert Hurt `ssc2008-10b@http://www.spitzer.caltech.edu/images`. *Right:* A more recent model of the spiral arm structure of the Milky Way according to Vallée (2008). Note that the schematic on the right is rotated 180 deg the artist drawing on the left, and that the names as well of the starting points of some of the spiral arms differ. Most authors agree (see Vallée (2008) and references therein) that the Milky Way has four major spiral arms and that the sun is located in the "Orion Spur" (a.k.a. Local Spur / Arm), a minor spiral arm located outside the Carina-Sagittarius and inside the Perseus arms.

a kinetic energy of 10^{51} erg and because they move at supersonic velocities of a few 1000 km s^{-1} a *shock front* forms where they collide with the interstellar medium. A process called *diffusive shock acceleration* is thought to accelerate a fraction of the particles in the vicinity of the shock from thermal to relativistic energies. These *cosmic rays* then emit broadband non-thermal radiation when interacting with ambient target gas, magnetic and photon fields, with luminosity proportional to the product of the cosmic ray and target density. Every gamma-ray source either is a *cosmic accelerator* itself or a passive cloud that has been flooded by cosmic rays from a past nearby accelerator.

The interstellar medium is filled with random magnetic fields of strength $\sim 3\mu$G (Sun et al., 2008), causing the cosmic rays to perform a random walk with deflections on the scale of the gyroradius

$$R_G = 1pc \left(\frac{E}{10^{15}eV}\right) \left(\frac{B}{1\mu G}\right)^{-1}. \tag{1.1}$$

Even at PeV energies the gyroradius $R_G \sim 0.4$ pc is much smaller than the scale height of the Galactic disc (even the thin disk is ~ 100 pc (Kong and Zhu, 2008), but the magnetic field is thought to extend to several kpc (Strong et al., 2007)), so diffusion will govern the escape of cosmic rays from the Milky way.

The entire Milky Way is filled with cosmic rays of energy density $u_{CR} \sim 1$ eV cm^{-3} and the question arises if supernova remnants (SNRs) are energetic and frequent enough to be the major source. Using a simple leaky-box model of the Galaxy with volume $V = 200$ kpc^3 one finds an average cosmic ray escape time of $t_{esc} \sim 10^7$ yr (Strong et al., 2007; Rosswog and Bruggen, 2007). By balancing the rate of energy inflow $R_{in} = \eta E_{SN}/t_{SN}$ and outflow $R_{out} = u_{CR}V/t_{esc}$ in the box we can solve for the required fraction η of kinetic energy available in the ejecta converted into cosmic rays so that SNRs can compensate for the loss via escape,

$$\eta = 10\% \left(\frac{u_{CR}}{1eVcm^{-3}}\right) \left(\frac{V}{200kpc^3}\right) \left(\frac{E_{SN}}{10^{51}erg}\right) \left(\frac{t_{SN}}{100yr}\right) \left(\frac{t_{esc}}{10^7yr}\right). \tag{1.2}$$

Although other source classes might contribute some fraction of the Galactic cosmic rays, SNRs are thought to be the bulk supplier of hadronic cosmic rays (Hillas, 2005) for the following reasons:

- They are frequent and energetic enough.
- A theoretically well-understood acceleration mechanism exists (diffusive shock acceleration).
- X-ray and gamma-ray observations have proven the existence of PeV cosmic rays in the shock fronts of several SNRs (although the proof that the emission is hadronic as opposed to leptonic has not been achieved).

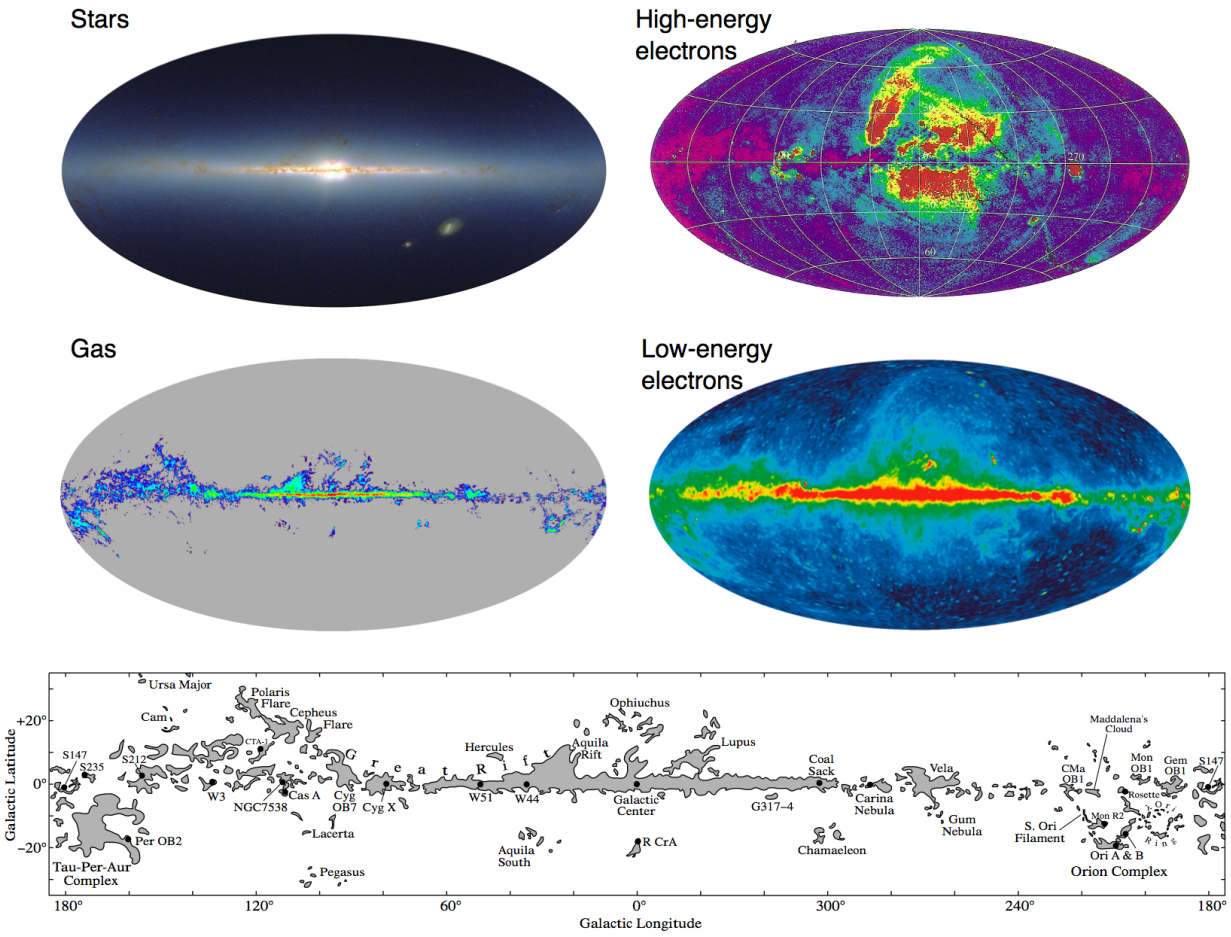

Figure 1.6.. Multiwavelength Milky Way. Figure taken from `skymaps.info`.

- The only other obvious cosmic accelerator, pulsars and their nebulae (see below), occur only about half as often (because type Ia SNe don't produce neutron stars) and typically only have an energy of 10^{49} erg, i.e. 1% of the SNR energy, so from Equation 1.2 we must conclude that they are not energetic enough. Also they are thought to mainly transfer energy to electrons, not hadrons.

The diffuse emission from the Milky Way seen in Figure 1.4 is the result of the interaction of this see of cosmic rays with the gas distributed in the Milky way disk as seen in Figure 1.6.

Figure 1.7 shows an example system where a core-collapse supernova left a visible pulsar, PWN and SNR behind. The Crab supernova is another example that has no SNR shell. And Cas has no PWN.

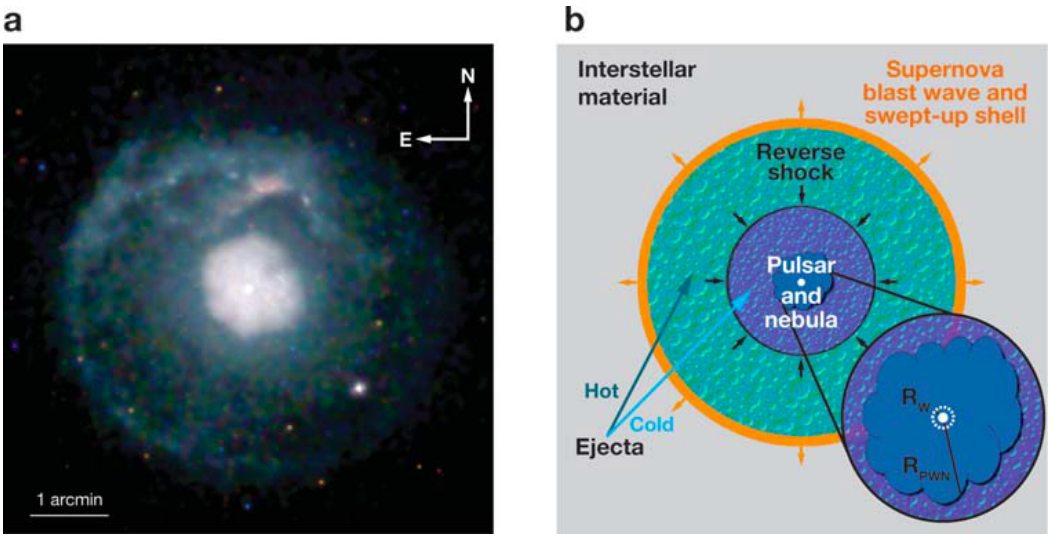

Figure 1.7.. Illustration of the pulsar-PWN-SNR complex. (a) An X-ray image of the composite SNR G21.5-0.9, with the young pulsar J1833-1034 at the center (white dot), surrounded by the PWN (1.5 arcmin), surrounded by the SNR (5 arcmin). (b) A schematic diagram of a composite SNR showing the swept-up interstellar medium shell, hot and cold ejecta separated by the reverse shock, and the central pulsar and its nebula. The expanded PWN view shows the wind termination shock. Figure taken from Gaensler and Slane (2006).

All three—pulsar, SNR and PWN—are the result of a supernova explosion. There are two types of supernovae (SNe): a white dwarf can accrete too much mass from a companion star and explode (type Ia) or the core of a massive star can implode into a neutron star or black hole while the outer hulls explode (core-collapse SN). White dwarfs are old stars that are not necessarily confi

Pulsars, supernova remnants and pulsar wind nebulae have been firmly identified as classes of Galactic gamma-ray sources.

- **Pulsars** are the most numerous class below 1 GeV, but because their spectrum cuts off at a few GeV they are not a TeV source class. Note that in addition to the 56 1FGL sources identified as pulsars there must be many unidentified low-significance sources that are pulsars as well, but the signal wasn't strong enough to detect the pulsation. Only 10% (6 out of 56) of identified pulsars have significance < 10, but 66% (952 out of 1451) sources do.

- **Supernova remnants** have been detected at GeV (Knödlseder and for the Fermi/LAT Collaboration, 2010; Abdo et al., 2009c; Abdo and for the Fermi LAT Collaboration, 2010; Abdo, 2010; The Fermi-LAT Collaboration: A. A. Abdo, 2010; The Fermi-LAT Collaboration, 2010; Abdo and Fermi LAT Collaboration, 2011) and TeV energies (see Figure 1.8).

- **Pulsar wind nebulae** are the most numerous source class at TeV energies for HESS and MILAGRO (see Figure 1.9), and a few have been detected by Fermi (The Fermi LAT Collaboration and Timing Consortium, 2010; Slane et al., 2010; Abdo et al., 2010b).

1.3. Astrophysics

Gamma-ray emission occurs when cosmic rays (relativistic charged particles such as nuclei and electrons) interact with matter or radiation fields. The production rate depends on the product of the densities of cosmic rays and target and the interaction cross section of the emission process.

Cosmic rays are produced in cosmic accelerators, e.g. supernova remnants or pulsar wind nebulae, which for a limited time period ($\sim 10^2 - 10^5$ years) develop powerful shock fronts where a process called *diffusive shock acceleration (DSA)* takes place.

The accelerator or nearby clouds become gamma-ray *sources* until at some point either the cosmic rays loose their energy or dissipate via diffusion or convection. In addition to these sources the Milky Way is flooded with a certain cosmic ray density that generates the so called *diffuse Galactic emission*. The Galactic cosmic rays diffuse for $\sim 10^7$ years in interstellar magnetic fields until they finally leave the Milky way.

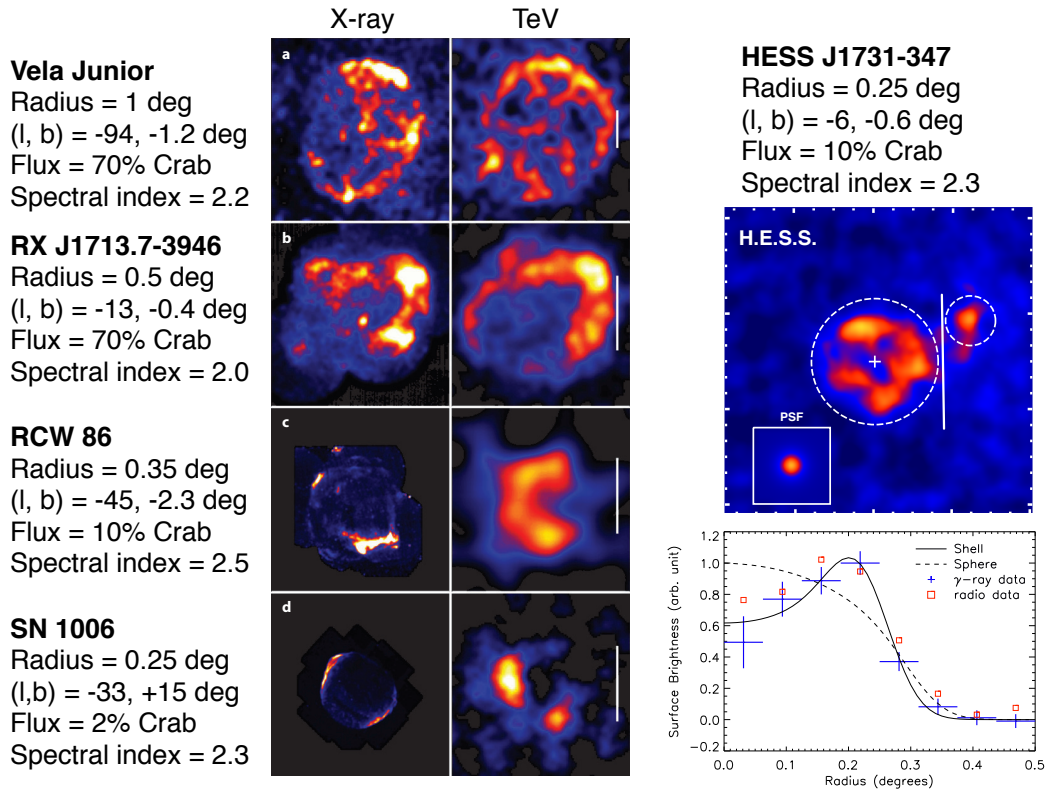

Figure 1.8.. The 4.5 currently resolved TeV shell-type SNRs (the shell-type morphology in RCW 86 is not significant). Nonthermal X-ray synchrotron emission has been detected from all of them, which in all cases matches the TeV morphology well (after taking the different angular resolution of the images into account). The quoted flux was computed by comparing the integral flux above 1 TeV to the Crab (100% Crab $= 2.1 \cdot 10^{-11}$ cm^{-2}s^{-1} (Meyer et al., 2010)). The four images on the left have been taken from Hinton and Hofmann (2009) and the spectral information from Hinton and Hofmann (2009,?); Aharonian et al. (2009b,b,b). *Right:* In HESS J1731-347 (HESS Collaboration and Abramowski, 2011) the shell-type morphology could recently be identified. The common method used to establish shell-type morphology is to fit the radial profile (shown in the lower right) with a shell and a center-filled model (such as sphere or Gauss) and test if the shell-type model is significantly more likely.

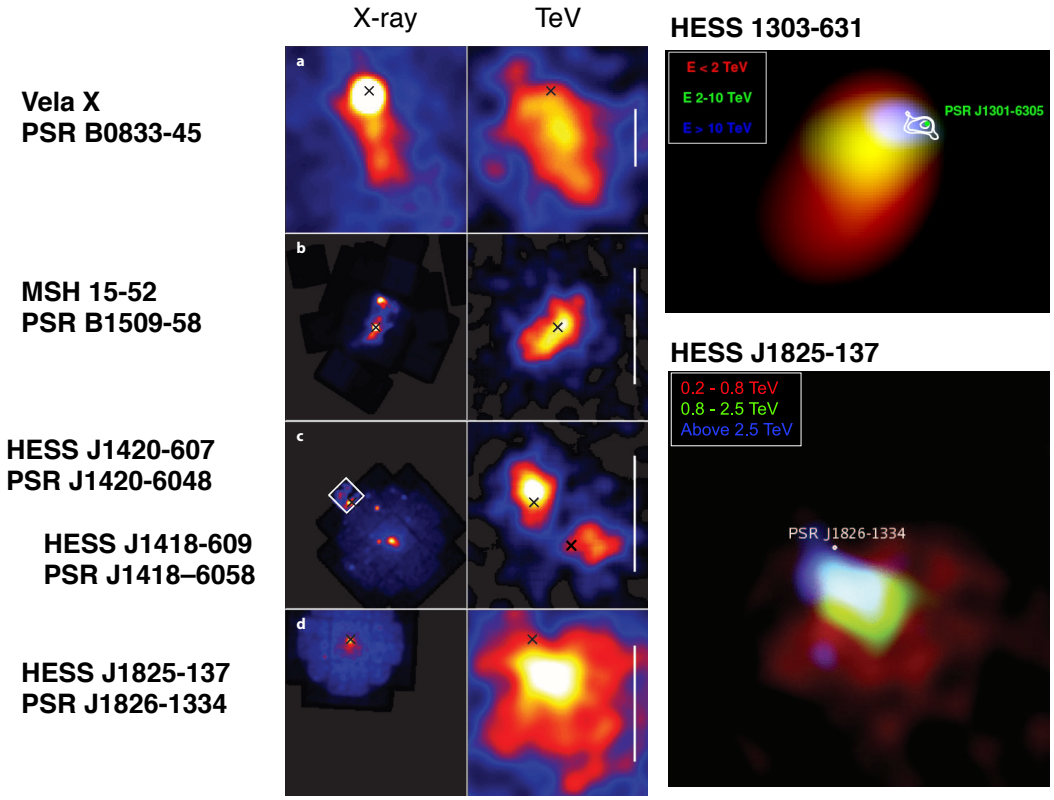

Figure 1.9.. Pulsar wind nebulae detected by HESS at TeV energies. Vela X (Aharonian et al., 2006b) and MSH 15-52 (Aharonian et al., 2005c) have been identified via matching X-ray synchrotron PWNe, shown on the left. In the case of HESS J1825-137 (Aharonian et al., 2006c) the TeV nebula is much more extended than the X-ray nebula. However, as shown in the color image on the right, the TeV nebula becomes smaller at higher energies and the emission centroid shifts towards the pulsar PSR J1826-1334. Since the X-ray synchrotron emitting electrons have even higher energies than the TeV IC emitting electrons and the nebulae in both bands extend to the south, it is assumed that both the X-ray and gamma-ray source are the PWN generated by the pulsar. Recently significant energy-dependent morphology was found in a second TeV source, HESS 1303-631 (Aharonian et al., 2005d; de Naurois, 2011), again with the high-energy emission region smaller and closer to PSR J1301-6305. The two sources HESS J1420-607 and HESS J1418-609 in the Kookaburra complex (Aharonian et al., 2006d) are very good candidate PWNe. They have corresponding young and energetic pulsars and synchrotron X-ray nebulae, and no other viable counterpart (such as a SNR or molecular cloud) was found. Figures on the left taken from Hinton and Hofmann (2009). The color image of HESS J1303-631 is from `www.mpi-hd.mpg.de/hfm/HESS/pages/home/som/2011/01`, the one of HESS J1825-137 from The H. E. S. S Collaboration: S. Funk et al. (2007).

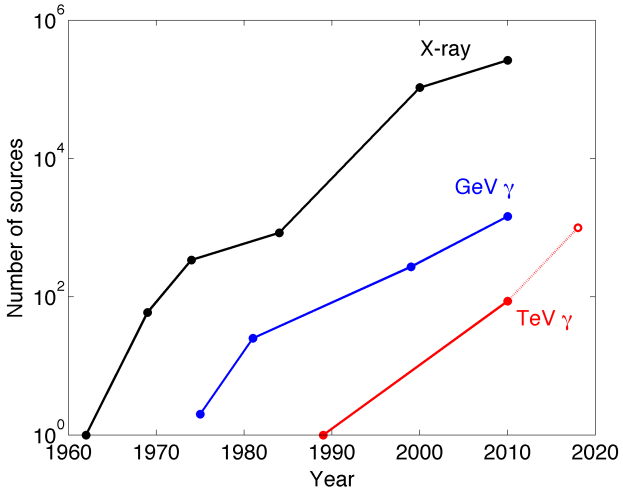

Figure 1.10. "Kifune" plot showing the exponential increase in source count with time. The latest count in the GeV curve is for the 1451 sources in the 1FGL catalog. For TeV the latest count is 86 based on TeVCat Version 3.1, and an expectation for CTA of 1000 sources is shown. Figure taken from Vandenbroucke and for the Fermi LAT collaboration (2010).

In this Section a brief review of the characteristics of the acceleration, emission and energy loss mechanisms that are important to understand gamma-ray astronomy is given, see Hinton and Hofmann (2009) and Reynolds (2008) and references therein for further details and derivations of the formulae.

1.3.1. Particle Acceleration

Introduction

Already in 1934 Baade and Zwicky hypothesized that "cosmic rays are produced in the super-nova process" (Baade and Zwicky, 1934):

In the 1970s a number of authors (e.g. Bell (1978); Blandford and Eichler (1987); Krymskii (1977)) suggested that a mechanism called *diffusive shock acceleration (DSA)* (a.k.a. first or Fermi acceleration) occuring in the shock fronts of supernova remnants might be able to efficiently produce cosmic rays. The basic idea is that particles gain energy every time they cross the shock front and that they do so many times because they are deflected by random magnetic fields in the shock region.

The first observational evidence to support that hypothesis came in 1995 with the detection of nonthermal X-rays from SN 1006 with the ASCA satellite. As we will discuss in detail later, assuming the emission mechanism is synchrotron radiation by electrons in a magnetic field of $\sim$10 μG, the observed 10 keV X-rays are produced by 100 TeV electrons.

In the last decade, gamma-ray emission up to more than $\sim$ 10 TeV has been observed from several types of sources (e.g. SNRs, PWNe, AGN) and even up to 100 TeV in the case of RX J1713.7-3946 (Aharonian et al., 2007). Because of energy conservation in any interaction process, this requires the presence of

charged cosmic rays of at least that energy.

Figures 1.11 and 1.12 show high-resolution images of the synchrotron radiation from two of the most famous cosmic accelerators, the supernova remnant SN 1006 and the Crab pulsar wind nebula, which is the result of a supernova in the year 1054.

The basic picture of the acceleration process in the cosmic accelerators is as follows:

Shell-type SNRs have a *blast wave shock* that is moving outwards at a non-relativistic velocity of a few $U \sim 1000$ km/s, i.e. 1% of the speed of light. Unshocked gas is outside and shocked gas is inside. For computations on shock acceleration it is customary to consider planar shocks and do the computations in the so called *shock frame* in which the shock is standing still. In the case of SNRs in the shock frame the material is streaming into the shock from outside (called upstream) at velocity u and streaming away from the shock into the SNR (called downstream) at velocity $u/4$. This means that in the SNR rest frame the downstream material is moving outwards at a velocity $3u/4$. To summarize: supernova remnant blast wave shocks accelerate both electrons and nuclei originating from the thermal plasma via *diffusive shock acceleration* (Reynolds, 2008).

Pulsars are compact stars (radius $\sim$ 10 km, mass $\sim$ 1 M_{sun}) with a very high dipole magnetic field ($\sim 10^{12}$ Gauss at the surface) that are rotating fast (millisecond to second periods). If they were in empty space they would loose energy via dipole radiation, i.e. as electromagnetic waves at their rotation frequency. In reality they have charge-filled magnetospheres surrounding the pulsar in which particle acceleration occurs via electric fields. The net result is a wind of electromagnetic energy and particles that in almost all theoretical models is Poynting flux dominated near the pulsar. Observations of the Crab nebula however require that the wind further out is particle dominated, so the nature of the wind has to change in between using some unknown mechanism (Gaensler and Slane, 2006). The details of the charge flows and acceleration processes in the pulsar magnetosphere are not known. Also it is unclear if the pulsar wind consists only of electrons/positrons created via pair production above the polar caps, or if it also contains nuclei that were ripped out of the neutron star. The pulsar wind has not been directly observed, although it has to e.g. produce inverse Compton emission at some level. To summarize: pulsars accelerate electrons originating from pair cascades in the magnetosphere (and possibly also electrons/nuclei ripped out of the pulsar) using *electric fields*.

Pulsar wind nebulae have a *standing wind termination shock* that occurs when the pulsar wind collides with the pulsar wind nebula. The pulsar wind is an outflow of relativistic particles moving almost at the speed of light $u = c$ with a Lorentz factor of $\gamma \sim 10^6$ (corresponding to GeV electron energies)

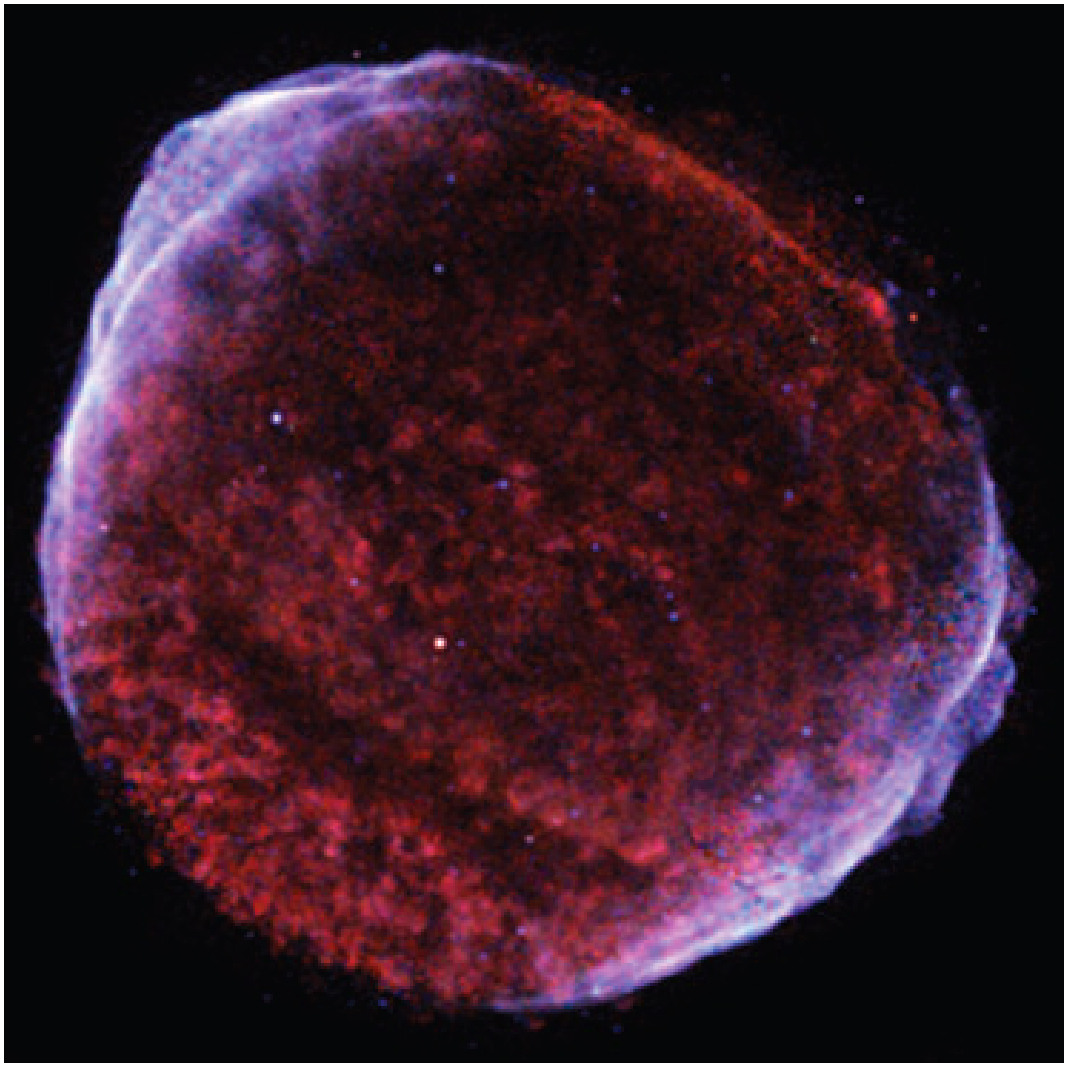

Figure 1.11.. X-ray image of the supernova remnant SN 1006 taken by the Chandra telescope. Red 0.5-0.9 keV, cyan 0.9-1.3 keV, blue 1.3-3 keV. Soft X-rays (red) are thermal emission, hard X-rays (blue) are synchrotron emission from cosmic rays. SN 1006 is somewhat special in that although the remnant evolution is approximately spherical, particle acceleration takes only place in the north-east and south-west regions. The reason is thought to be due to magnetic field obliquity-dependent acceleration rates, although it is unknown if the ambient magnetic field is oriented in the NE-SW or NW-SE direction (Reynolds, 2008). Figure taken from Reynolds (2008).

Figure 1.12.. Image of the synchrotron emission from electrons in the Crab pulsar wind nebula. Radio observed with the VLA (red), visible light with HST (green) and X-rays with Chandra (blue). The Crab pulsar is the bright blue point source at the center, surrounded by a dark region which is thought to be the unshocked pulsar wind, terminating in a standing shock front beyond which lies the nebula. A torus / jet structure is visible in the X-ray emission. Moving further out electrons loose energy due to adiabatic and radiative losses, resulting in the optical and radio emission to be located further away. Note that no visible shell-type supernova remnant has formed yet (contrary to G21.5-0.9 shown in Figure 1.7), although clearly the Crab nebula is pressing against it from the inside. Figure taken from Hester (2008).

in the case of the Crab. The nebula consists of shocked wind particles and magnetic field accumulated from the wind over the lifetime of the pulsar. Both the location of the inner and outer edge of the nebula is the result of a pressure balance against the pulsar wind on the inside and the supernova remnant ejecta on the outside. Both the wind and the nebula consist of relativistic particles. The difference is that the wind is a cold flow (all particles moving away from the pulsar) but the nebula is a hot plasma (particles move in random directions). Acceleration (up to energies of 100 TeV in the case of the Crab nebula) takes place at the termination shock via diffusive shock acceleration, which in this case is called *relativistic shock acceleration*. For SNRs, especially young ones where acceleration still takes place, the shock front is often clearly visible in synchrotron radiation. For PWNe the Crab is the only object where an underluminous wind region between the pulsar and the nebula could be resolved, in all other cases only the pulsar is visible immediately followed by the nebula, which represents the downstream region of the shock. To summarize: pulsar wind nebulae termination shocks accelerate relativistic particles from the pulsar wind via *relativistic shock acceleration*.

Diffusive Shock Acceleration

In this section it will be shown that diffusive shock acceleration results in power-law particle spectra with differential flux $dN/dE \sim E^{-\alpha}$ where $\alpha = 2$. Not all results are derived from first principles, for the basics about shocks and acceleration consult Longair (1994) or Rosswog and Bruggen (2007), a recent review is Reynolds (2008).

The *Rankine-Hugoniot* shock jump conditions are relations for velocity, density, pressure and temperature up- and downstream of a shock derived from mass, energy and momentum conservation. For a *strong shock*—defined as one in which the shock velocity u is much larger than the speed of sound in the upstream medium—and an ideal gas with adiabatic index $5/3$ one finds a compression ratio of $r = 4$. This means that the densities ρ and velocities v of the gas up- and downstream of the shock will be given by

$$\frac{\rho_d}{\rho_u} = \frac{v_u}{v_d} = r = 4$$

.

Now think of a supernova remnant blast wave with speed u and the three relevant frames:

Shock frame: Gas is flowing in with speed u and out with speed $\frac{1}{4}u$.

Unhocked frame: The shock is approaching with speed u and the shocked gas with speed $\frac{3}{4}u$.

Shocked frame: The shock is receding with speed $\frac{1}{4}u$ and the unshocked gas is approaching with speed $\frac{3}{4}u$.

The critical point is that a particle will gain energy (on average) both when crossing into the up- and downstream region, because in both cases the particles in the region it is crossing into will come toward and (on average) a head-on collision takes place.

Qualitatively one can think of a full cycle as consisting of the following four steps:

1. The particle is in the unshocked (upstream) region and on average at rest within that medium. Because the shock is coming towards it, it eventually crosses into the shocked (downstream) region, collides head-on and gains energy.

2. It then scatters collissionlessly on random magnetic fields, and starts performing a random walk (diffusion) without loosing or gaining energy.

3. Even though now the shock is receding with speed $\frac{1}{4}u$, the particle has much higher velocity c and thus a high probability P of recrossing the shock into the upstream region. When it does, it collides head-on and gains energy.

4. Finally it again isotropizes its direction with respect tothe upstream medium.

The only difference between up- and downstream is that cosmic rays upstream don't leave the acceleration process, but particles downstream sometimes are advected by the downstream flow and simply accumulate inside the SNR without being accelerated further.

One can show (Rosswog and Bruggen, 2007)) that the mean energy gain per full cycle (i.e. crossing the shock twice) for a relativistic particle is

$$\frac{\Delta E}{E} = \frac{4}{3}\frac{u}{c} \tag{1.3}$$

and that the probability of remaining in the acceleration region is

$$P = 1 - \frac{u}{c}. \tag{1.4}$$

Because this gain is first-order in shock velocity this process of diffusive shock acceleration is also called *first-order Fermi acceleration*. Enrico Fermi already in 1949 proposed a mechanism known today as *second-order Fermi acceleration* (Fermi, 1949), in which particles are accelerated by magnetized clouds, moving in random directions through the interstellar medium at speed u. However in that case tail-on collisions would be almost equally as likely as head-on collisions and one can show that in that case the mean gain in energy per cycle is

$$\frac{\Delta E}{E} = \frac{8}{3}\left(\frac{u}{c}\right)^2,$$

i.e. only second-order in cloud velocity and because $\frac{u}{c} \ll 1$ too inefficient to work in practice.

According to Equation (1.3) a particle with initial energy E_0 will gain a factor

$$\beta = 1 + \frac{u}{c} \tag{1.5}$$

and thus after j cycles will have energy $E = E_0\beta^j$. Starting with N_0 particles of energy E_0, after j cycles there will be $N = N_0\beta^j$ particles, and combining these two facts we find

$$\frac{N}{N_0} = \left(\frac{E}{E_0}\right)^{\frac{\log P}{\log \beta}} \tag{1.6}$$

or in differential form

$$\frac{dN}{dE} \sim E^{-\alpha} \text{ with } \alpha = 1 - \frac{\log P}{\log \beta} \sim 2 \text{ for } \frac{u}{c} \ll 1 \tag{1.7}$$

The scenario we've been discussing so far is overly simplistic. In reality acceleration can be so efficient that a significant fraction (10% and more) of the total energy goes into cosmic rays, so that the shock can no longer be considered adiabatic (Ellison et al., 2007) and even the Sedov-Taylor evolution of the SNR can be modified (Castro et al., 2011). Also the cosmic rays diffuse in the up-stream region and generate a so called shock precursor (Berezhko and Ellison, 1999), slowing the up-stream fluid down before it reaches the sub-shock (see Figure 1.13). Another important effect that has actually been measured in several SNRs is that the cosmic rays can amplify the magnetic field by a factor of 100 and more (Bell, 1978), increasing the acceleration rate and making efficient cosmic ray production possible in the first place (see Equation (1.8)).

Maximum Energy There are several factors that limit the *maximum energy* obtained, i.e. in practice the power-law will cut off at some energy E_{max}:

Finite age: The acceleration rate is determined by the rate of shock crossings, which in turn is determined by the diffusion coefficient. For Bohm diffusion, maximum proton energies for an SNR of age t with shock velocity u and magnetic field B are (Hinton and Hofmann, 2009)

$$E_{max} = 1TeV \left(\frac{u}{1000kms^{-1}}\right)\left(\frac{t}{1000yr}\right)\left(\frac{B}{1\mu G}\right). \tag{1.8}$$

Escape: A very general condition—known as the *Hillas condition*—for the maximum energy of an accelerator is given by the fact that the particle gyroradius cannot be larger than the acceleration region:

$$E_{max} = 1000TeVZ\beta\left(\frac{L}{1pc}\right)\left(\frac{B}{1\mu G}\right) \tag{1.9}$$

For SNRs in the Sedov phase this condition turns out to be very similar to Equation (1.8) (Hillas, 2005).

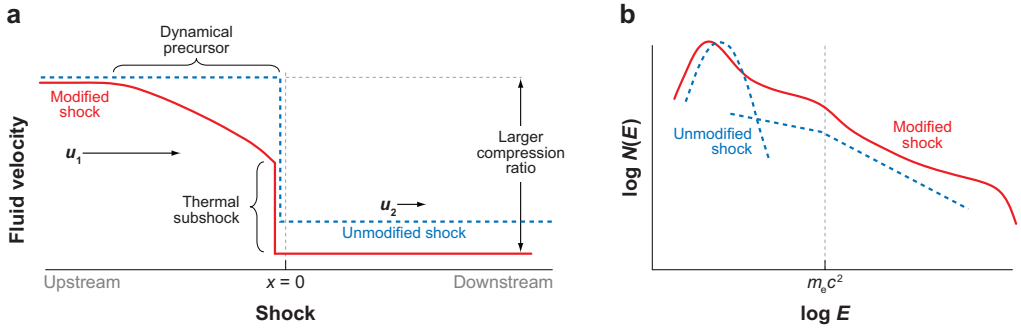

Figure 1.13.. Schematic shock profile (a) and corresponding particle energy distribution (b). The blue curves show the unmodified shock profile with a compression ratio of 4 on the left and a thermal and power-law cosmic ray particle energy distribution. Figure taken from Reynolds (2008).

Energy losses: By interacting with the magnetic field, radiation field or matter cosmic rays loose energy by emitting synchrotron, inverse Compton and Bremsstrahlung radiation. In practice nuclei accelerated in SNRs do not loose energy, but electrons are limited by synchrotron losses to a maximum energy of (Zirakashvili and Aharonian, 2007)

$$E_{max} = 100 \text{ TeV } \left(\frac{u}{1000 kms^{-1}}\right)\left(\frac{B}{1\mu G}\right)^{-\frac{1}{2}} \tag{1.10}$$

1.3.2. Radiation Processes

As we discussed in the last Section, cosmic accelerators will generate a population of relativistic nuclei and/or electrons.

- Nuclei interact with nuclei of the ambient gas, creating neutral pions, which decay into gamma rays.
- Electrons interact with magnetic fields and produce synchrotron radiation from the radio to X-ray, in the case of the Crab nebula even up to 300 MeV gamma-rays.
- Electrons produce gamma-rays via the inverse Compton (IC) process, by up-scattering photons from the cosmic microwave background (CMB), infrared, optical or X-ray photon fields.

As an example Figure 1.14 shows the gamma-ray spectral energy distribution (SED) of the SNR RX J1713.7-3946 together with hadronic and leptonic models. In general hadronic models show a broad bump with a cutoff on the right

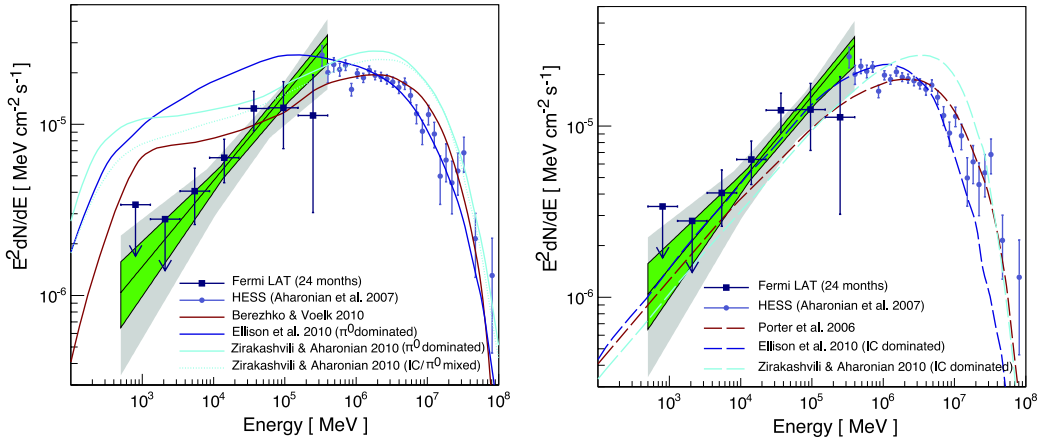

Figure 1.14.. Energy spectrum of RX J1713.7-3946 in gamma rays. Both panels show the same data—Fermi and HESS measurements in the 500 MeV to 100 TeV range. All models shown pre-date the Fermi measurement and were tuned to match the HESS points. One can see that all predominantly hadronic models (left) are incompatible with the Fermi points whereas most leptonic models (right) describe the data well. Figure taken from Abdo and Fermi LAT Collaboration (2011).

due to the cutoff in the cosmic ray spectrum (sometimes resulting in a pile-up on the right side of the bump), and a cutoff on the left due to a cutoff in the interaction cross section. Leptonic models in the simplest case are power-laws with a cutoff at the high-energy end as shown here, but they can also exhibit breaks or even more complicated shapes (see e.g. the Crab SED in Figure 1.15) that can look similar to the hadronic models shown in Figure 1.14. As far as I know RX J1713.7-3946 is the only SNR where it was possible to clearly identify the dominating gamma-ray emission component as leptonic (Abdo and Fermi LAT Collaboration, 2011).

Electrons

The following review on synchrotron and inverse Compton emission from electrons follows Hinton and Hofmann (2009), Hoppe (2008) and Nedbal (2008). For derivations of the results consult Blumenthal and Gould (1970).

Synchrotron radiation An electron with energy E_e in a magnetic field of strength B emits most of its *synchrotron radiation* at energy

$$E_{Sy} = 0.087\text{eV} \left(\frac{B}{1\mu\text{G}}\right) \left(\frac{E_e}{1TeV}\right)^2 \tag{1.11}$$

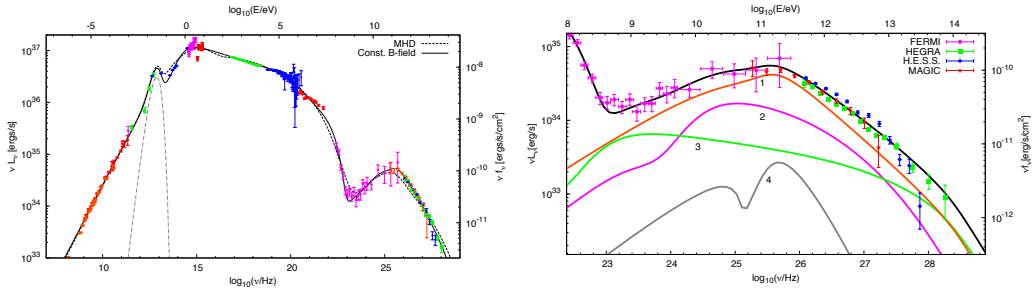

Figure 1.15.. Crab nebula spectral energy distribution. The left plot shows the full range from radio (μeV) to gamma-rays (40 TeV) with the bright and broad synchrotron peak and the faint inverse Compton peak together with two models. The right plot is a zoom-in on the inverse Compton peak, showing the total IN flux with the constant B-field model in black, as well as the components from different photon seed field: (1) synchrotron, (2) thermal dust, (3) CMB and (4) line emission from filaments. Figure taken from Meyer et al. (2010).

The synchtrotron cooling time[9] is

$$\tau_{Sy} = 1.3 \cdot 10^7 \mathrm{yr} \left(\frac{B}{1\mu G}\right)^{-2} \left(\frac{E}{1TeV}\right)^{-1} \tag{1.12}$$

IC radiation There are two regimes, the *Thomson limit*

$$b = \frac{4E_e E_T}{m^2c^4} \sim 15 \left(\frac{E_e}{1TeV}\right)\left(\frac{E_T}{1eV}\right) \ll 1 \ (E_T \text{ is the target photon energy}), \tag{1.13}$$

where the electron will loose small fractions of its energy in individual scatterings and the *Klein-Nishina regime* $b \gtrsim 1$ where it will loose a sizeable fraction of its energy in one collision.

In the Thomson limit, an electron of energy E_e scattering off target photons emits most of its IC radiation at

$$E_{IC} \sim 5GeV \left(\frac{E_T}{1meV}\right)\left(\frac{E_e}{1TeV}\right)^2, \tag{1.14}$$

where

$$E_T \sim 2.8kT \sim 10^{-4}eV \left(\frac{T}{1K}\right) \tag{1.15}$$

[9]The *cooling time* of any process causing (in our case electron) energy loss is defined as $\tau = E_e/(dE_e/dt)$.

is the average target photon energy in a black-body radiation field of temperature T.

The IC cooling time is given by

$$\tau_{IC} = 3.1 \cdot 10^5 yr f_{KN}^{-1} \left(\frac{U_{rad}}{1eVcm^{-3}} \right)^{-1} \left(\frac{E_e}{1TeV} \right)^{-1}, \tag{1.16}$$

where the Klein-Nishina suppression factor can be approximated as (Moderski et al., 2005)

$$f_{KN} \sim (1+b)^{-1.5} \sim \left(1 + 40 \left(\frac{E_e}{1TeV} \right) \left(\frac{kT}{1eV} \right) \right)^{-1.5} \text{ for } b < 10^4 \tag{1.17}$$

Synchrotron – IC Relations The results for synchrotron radiation and inverse Compton radiation in the Thomson regime are very similar.

IC photons of energy E_{IC} and synchrotron photons of energy E_{Sy} were generated by electrons of energy E_e if (see Equations (1.11) and (1.14))

$$E_{IC} \sim 0.38TeV \left(\frac{E_{Sy}}{1keV} \right) \left(\frac{B}{1\mu G} \right)^{-1}, \tag{1.18}$$

and the ratio of the luminosities (i.e. $E^2 dN/dE$, e.g. in erg/s) at those corresponding energies is given by the ratio of energy densities of the radiation and magnetic field,

$$\frac{L_{IC}(E_{IC})}{L_{Sy}(E_{Sy})} = \frac{U_{rad}}{U_B}, \text{ where } U_B = \frac{B^2}{8\pi} \sim 0.024eVcm^{-3} \left(\frac{B}{1\mu G} \right). \tag{1.19}$$

For example, an electron with energy 11 TeV will produce 1 TeV IC photons on the cosmic microwave background (temperature $T \sim 2.7$ K, energy density of $U_{CMB} \sim 0.25$ eV cm^{-3}). For a 100 μG magnetic field the synchrotron emission will be 10 times stronger than the IC emission and yield 1 keV photons, cooling the electron within 100 years. For a 1 μG field the synchrotron emission will be at 10 eV and the IC emission will be 10 times stronger, limiting the electron lifetime to 10^5 years.

SEDs for power-law electron populations For a region filled homogeneously with electrons, magnetic field and blackbody radiation—a so called *one-zone model*—the synchrotron and IC spectra are simply reflections of the electron spectrum. Power-law distribution of electrons with spectral index α_e will emit

a power-law synchrotron and IC spectra with spectral index[10]

$$\Gamma = \frac{\alpha_e + 1}{2}. \tag{1.20}$$

For the case of continuous injection of electrons with spectral index α_e, cooling will result in a broken power-law with a spectral steepening by $\alpha_{e,cooled} = \alpha_e + 1$. The break energy can be found by setting the cooling timescale equal to the age of the system, using Equation (1.12) for synchrotron-dominated cooling and Equation (1.16) for IC-dominated cooling.

In some cases Equation (1.19) allows a measurement of the average magnetic field in the source region, assuming that the IC target fields are known and that within the emission region the radiation fields and magnetic field can be approximated by their average values. For example, Meyer et al. (2010) find $B \sim 125\mu$G for the Crab nebula.

Nuclei

The inelastic collisions of cosmic ray nuclei with gas nuclei results (amongst other particles) in the production of π^0- and η-mesons, which quickly decay into gamma-rays. The largest fraction of nuclei—both in the gas and in the cosmic rays—are protons, so we concentrate on this case here. On average 17% of the proton energy is converted into gamma rays, 75% through the π^0 channel and 25% through the η channel. The following discussion is based on Kelner et al. (2006).

The proton-proton interaction *cross-section* in the GeV-TeV energy range can be approximated as

$$\sigma_{pp} \sim (34.3 + 1.88L + 0.25L^2) \left[1 - \left(\frac{E_{th}}{E_p}\right)^4\right] \text{ mb}, \tag{1.21}$$

where $L = \ln\left(\frac{E_p}{1\,\text{TeV}}\right)$ and $E_{th} = m_p + 2m_\pi + m_\pi^2/2m_p = 1.22$ GeV is the energy threshold for π^0 production. For proton energies above a few GeV the energy-dependence of the cross-section $\sigma_{pp} \sim 35$ mb is very weak and the cooling time in a gas of density n is given by

$$\tau_{pp} \sim 3 \cdot 10^7 \text{ yr } \left(\frac{n}{1cm^3}\right). \tag{1.22}$$

[10] In the deep Klein-Nishina regime the IC spectrum shows a steepening by $\Delta\Gamma = (\alpha_e + 1)/2$, so at the very high energy end the shapes of the synchrotron and IC component in the SED can differ. Note that in many sources the main radiation field is thought to be the CMB, where the Klein-Nishina regime starts at electron energies of 300 TeV and IC energies of 30 TeV, so in practice this break has never been observed because either the electron population in the source has a cutoff or because the source is too faint to be detected at energies > 30 TeV by current detectors.

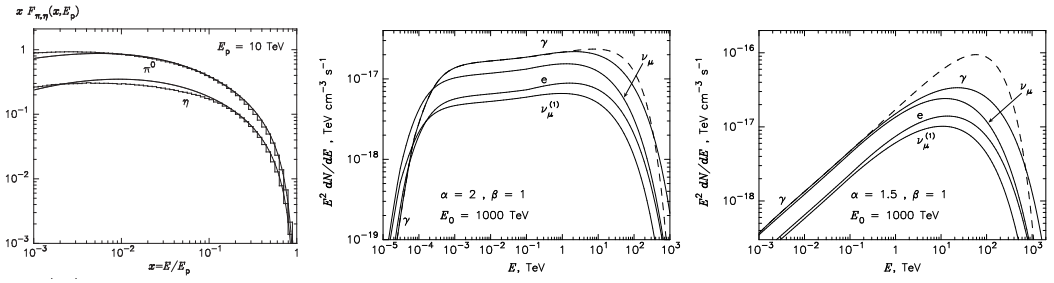

Figure 1.16.. Energy spectra from p-p interactions. *Left:* π- and η-mesons for a proton of energy $E_p = 10$ TeV (histogram shows numerical simulation, lines analytical representations). *Middle/right:* Gamma-ray and leptons for an exponential cutoff power-law proton spectrum $J_p(E_p) \propto E_p^{-\alpha} \exp\left[-\left(\frac{E_p}{E_0}\right)^\beta\right]$ with cutoff energy $E_0 = 1000$ TeV, $\beta = 1$ and spectral index $\alpha = 2/1.5$ (middle/right). The gamma-ray spectrum roughly has the same shape as the proton spectrum, with $\alpha_\gamma = \alpha_p$, $E_{0,\gamma} = E_{0,p}/16 = 60$ TeV and $\beta_\gamma = 0.5$, i.e. with an earlier and softer cutoff. Figure taken from Kelner et al. (2006).

Given a proton spectrum $J_p(E_p)$ and target density n, the gamma-ray production rate is given by

$$Q_\gamma(E_\gamma) = c\,n \int_{E_\gamma}^{\infty} \sigma_{pp}(E_p) J_p(E_p) F_\gamma\left(\frac{E_\gamma}{E_p}, E_p\right) \frac{dE_p}{E_p}, \tag{1.23}$$

where F_γ, the so called gamma-ray *emmissivity*, can be parameterized by an analytical formula that is good to a few % above 100 GeV (Kelner et al., 2006).

Using this formula the resulting gamma-ray spectrum can be computed for any assumed proton spectrum using numerical integration. The left plot in Figure 1.16 illustrates that the resulting gamma-ray spectra for a single proton energy are very broad, contrary to leptonic emission, where the synchrotron and IC spectra for a single electron energy peak around a single photon energy (see Equations (1.11) and (1.14)).

Nevertheless it turns out that for a power-law proton spectrum with exponential cutoff—as expected from acceleration theory (see Section 1.3.1)—the resulting gamma-ray spectrum is also (not in detail, but roughly) a power-law with a soft exponential cutoff (see Figure 1.16).

2. HESS Data Analysis

The HESS[1] telescopes in Namibia, shown in Figure 2.1, have been observing the very-high energy (VHE, above ca. 100 GeV) gamma-ray sky since 2003. This chapter describes how they collect data and how that data is processed to make images and spectra of astronomical gamma-ray sources.

The methods described here are then applied in Chapter 3 to the sources in the HESS Galactic plane survey region, so if you are interested in results, skip ahead to the description of the resulting maps in Section 3.2, catalog in Section 3.3 or spectra in Section 2.8.

HESS is an array of four air Cherenkov telescopes (ACTs) that detect gamma-rays using an indirect method from the ground. This complicated process consists of the imaging of (tertiary) Cherenkov light from (secondary) charged particles in an air shower created by a (primary) gamma ray in the Earth's atmosphere and is described in Sections 2.1, 2.2 and 2.3.

Section 2.4 explains how the air shower images are used to reconstruct the energy and direction of the primary particle that produced the shower. Actually only a small fraction of the events recorded by ACTs were induced by gammas, for the majority the primary particle was a charged cosmic ray (protons, electrons and nuclei). Section 2.4 describes how it is possible to reduce this unwanted background by 2 to 3 orders of magnitude via gamma-hadron separation cuts on parameters computed from the shower images, while keeping $\sim 80\%$ of the gammas. The resulting post-cut HESS instrument performace (effective areas, point spread function, ...) as determined mainly from air shower and detector simulations is described in Section 2.4.

Higher-level analysis techniques for background estimation, maps and spetra will be described in Chapter 3.

2.1. Air Showers

The Milky Way contains cosmic accelerators that produce very high-energy charged particles and gammas. The gammas travel on straigt lines and thus arrive at Earth non-isotropically, pointing back to the sources. The charged cosmic rays are deflected in interstellar magnetic fields and arrive (at TeV energies) almost isotropically.

As a result the Earth's atmosphere is constantly hit by gammas and by cosmic rays, with a chemical composition of about 90% protons, 8% alpha particles, 1%

[1] http://www.mpi-hd.mpg.de/HESS/

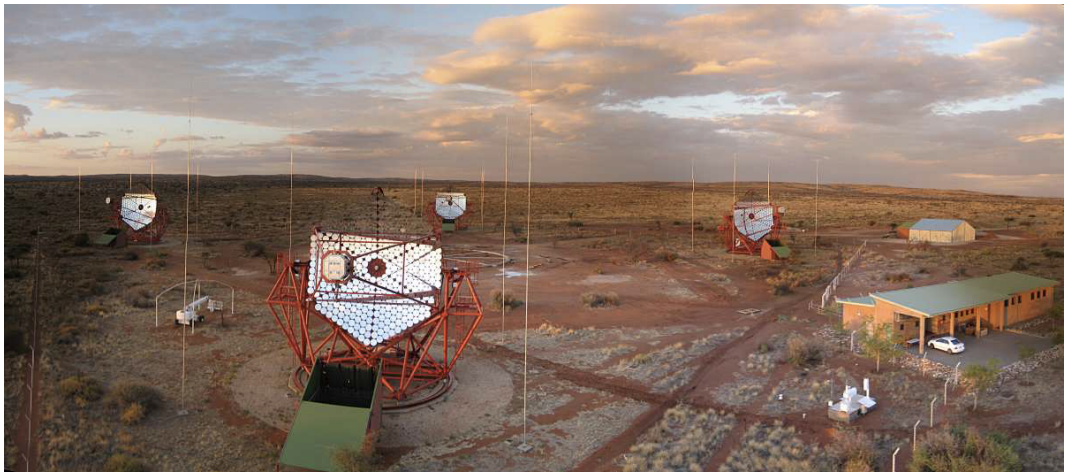

Figure 2.1.. The HESS Cherenkov telescope array. The control building and weather station can be seen on the right. Image taken from Nedbal (2008).

heavier nuclei and 1% electrons. Each individual primary particle generates a cascade of secondary particles called an *air shower* when colliding with particles in the air (see Figure 2.2). The charged particles in the air shower travel at speeds greater than the speed of light in air and emit Cherenkov light, making the shower detectable from the ground.

Leptonic showers

For primary photons, electrons and positrons a *leptonic* air shower will occur. Photons create electron-positron pairs in the Coulomb field of an air nucleus. Electrons and positrons get deflected in the Coulomb field of an air nucleus and emit a Bremsstrahlung photon. As the leptonic shower develops, more and more particles of lower and lower energy are present. When the mean particle energy drops below ~ 80 MeV, ionization losses of air molecules dominate over the production of new particles and the air shower starts to die out. Observationally air showers produced by electrons or positrons are almost indistinguishable from photon-induced air showers.

Hadronic showers

For primary hadrons, i.e. atomic nuclei, a *hadronic* air shower occurs. The cosmic ray nucleus inelastically scatters on air nuclei in strong force interactions and produces mesons (pions, kaons), nucleons and hyperons. The mesons decay into gammas and leptons, which results in leptonic sub-showers within the hadronic shower, containing about one third of the total primary energy.

In some cases most of the energy is channeled into a π^0 particle in one of

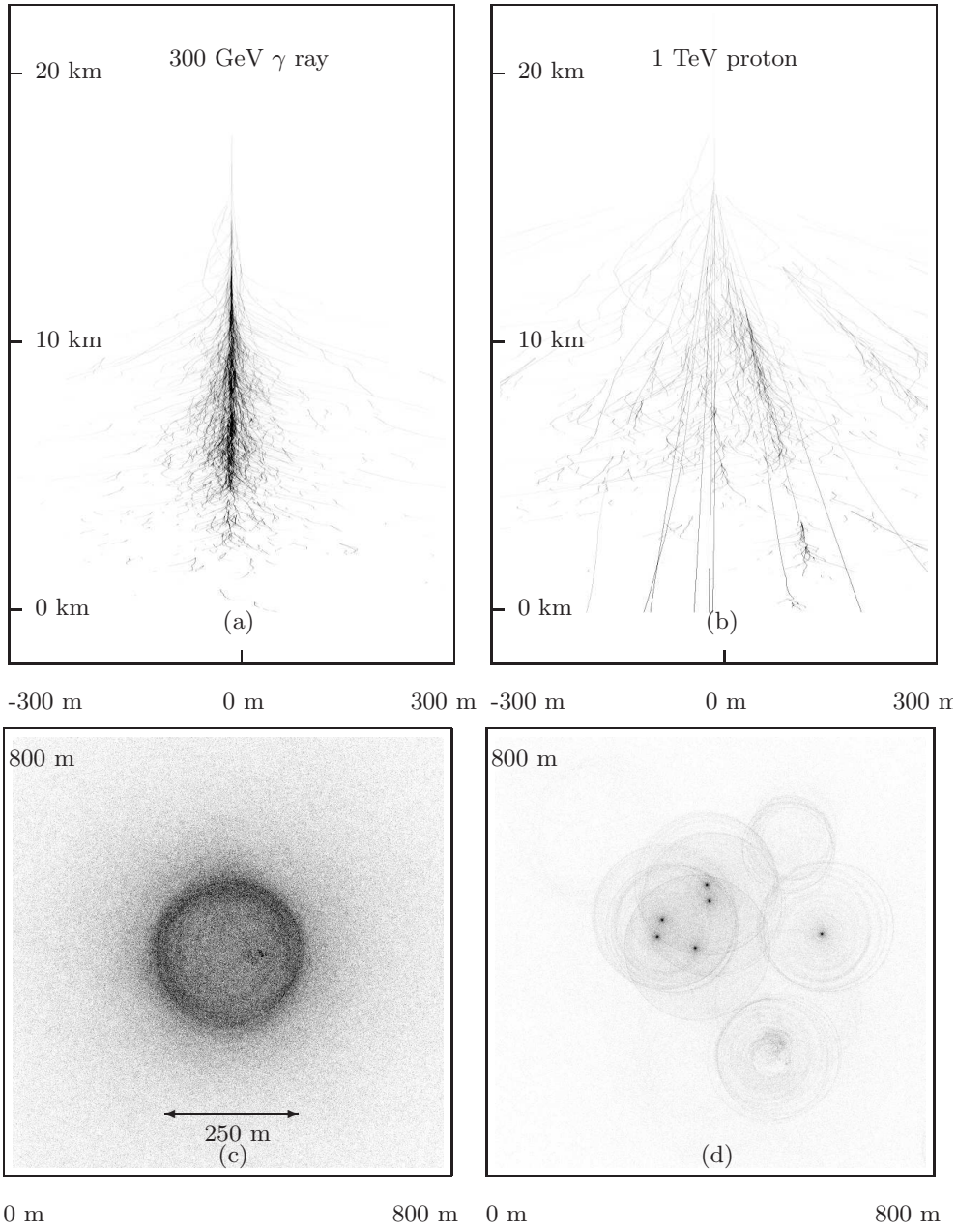

Figure 2.2.. Air shower and Cherenkov emission for a 300 GeV gamma ray (left) and 1 TeV proton (right). The top figures are side views of the particle tracks in the atmosphere. The bottom images show the resulting distribution of Cherenkov light on the ground. Simulation by Konrad Bernlöhr, figure taken from Ohm (2010).

the first interactions, resulting in a mostly leptonic shower even if the primary particle was a hadron. However in most cases hadronic showers differ significantly from leptonic showers in that they are broader, more irregular, penetrate deeper into the atmosphere and produce only one third of the Cherenkov light for a given primary particle energy.

Cherenkov light

Most of the particles in the air showers will have speeds $\beta = v/c$ larger than the light velocity in air and thus emit Cherenkov ratiation. The threshold Lorentz factor γ_{min} depends on the refrective index as $\gamma_{min} = (1 - n^{-2})^{-0.5}$. The refractive index of air at 10 km height is about 1.0003, which results in a Cherenkov threshold for electrons of ~ 20 MeV and for protons of ~ 40 GeV.

The opening angle θ of the Cherenkov cone is given by $\cos(\theta) = \frac{1}{n\beta}$, for particles with velocity $\beta = v/c \sim 1$ about 1 deg, corresponding to a circle of radius ~ 100 m when the Cherenkov light reaches the ground.

Figure 2.2 bottom shows the resulting Cherenkov light distribution on the ground generated by all the particles in showers initiated by a 300 GeV gamma-ray and a 1 TeV proton. Note that leptonic showers have a well-defined light pool of diameter ~ 250 m that contains most of the Cherenkov light, the distribution for hadronic showers is much more irregular.

The light yield of a 1 TeV electron from zenith is about 100 Cherenkov photons per m^2 on the ground, with a spectrum peaking in the near ultraviolet (most of the emission below 300 nm is absorbed by Ozon) but extending well into the optical spectrum.

The shower takes $\sim 30\mu$s to develop along its ~ 10 km length and the Cherenkov light takes another $\sim 30\mu$s to reach the ground. Nevertheless because the shower develops in a thin shower front, at a given position on the ground almost all Cherenkov light (and particles if there are any survivors) arrives within ~ 10 ns.

2.2. Imaging Atmospheric Cherenkov Technique

Imaging atmospheric Cherenkov telescopes (IACT) have emerged as the best detectors for pointed TeV gamma-ray observations (Hinton and Hofmann, 2009). A description of the history and status of the field was given in Section 1.1.1, here we will explain how it works.

IACTs such as HESS use large optical reflectors to focus the Cherenkov light into a focal plane, where a high-speed Cherenkov camera is located (see Figure 2.3). Different points in the camera correspond to different directions on the sky, and because leptonic air showers are roughly 3D-ellipsoids in the atmosphere the resulting light distribution in the air shower image is roughly a 2D ellipse (see Figures 2.3, 2.4, 2.6).

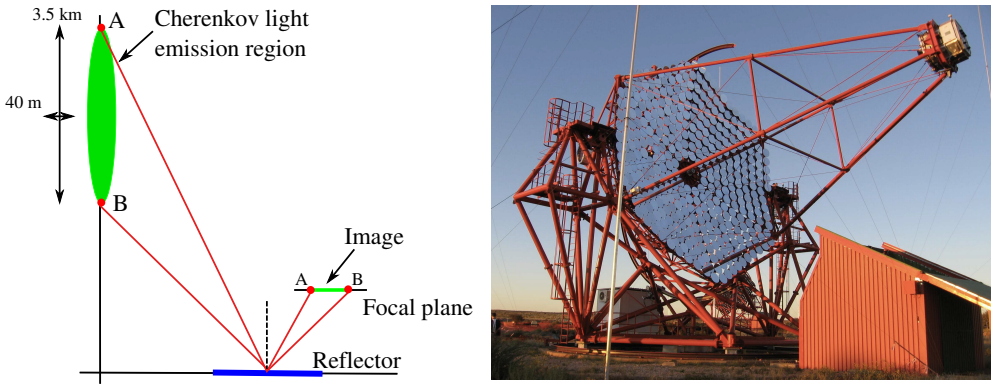

Figure 2.3.. Air showers are imaged with a reflecting telescope into a Cherenkov camera. *Left:* Principle (from Hoppe (2008)) *Right:* Practice: a HESS telescope.

The basic goal is to reconstruct for each event the direction, energy and type (lepton or hadron). As it turns out, all of these tasks can be done much more reliably if the air shower was imaged from multiple directions, as illustrated in Figure 2.4. All current high-sensitivity IACT experiments (HESS, VERITAS, MAGIC) have arrays of (4, 4, 2) telescopes and a central trigger to only record the events seen by at least two telescopes Hinton and Hofmann (2009).

The basic performance parameters of current-generation IACT arrays are:

Effective Area $\sim 10^5$ **m**^{2} roughly given by the Cherenkov light pool on the ground.

Energy Threshold ~ 100 **GeV** roughly given by the Cherenkov photon density (~ 10 m^{-2}) and reflector area (~ 100 m^2).

2.3. HESS Telescope System

HESS is an array of four IACTs, located in the Khomas highland of Namibia at an altitude of 1800 m above sea level, which started operations in 2003. An image of the array is shown in Figure 2.1 and a closeup of one of the telescopes in Figure 2.3.

The HESS telescopes have been described in many of the early HESS PhD theses, such as Bolz (2004); Gillessen (2004); Berge (2006); Funk (2005). Here we will only briefly list its main characteristics:

Array: The four telescopes are located at the corners of a square with side length 120 m.

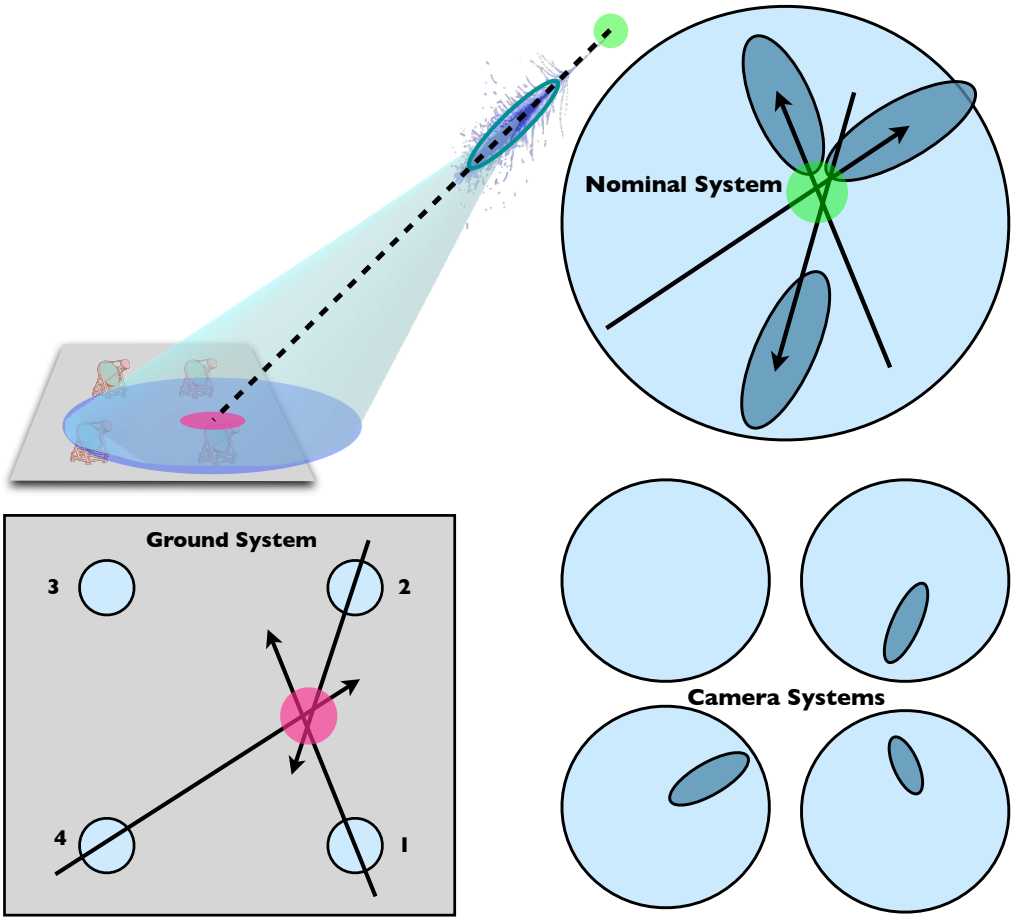

Figure 2.4.. Air shower reconstruction coordinate systems. The direction on the sky is shown in green and the core position on the ground in pink. Figure by Karl Kosack, private communication.

Structure: Each telescope has a reflector of diameter 13 m and focal length of 15 m. An altitude-azimuth-mount is used, with wheels on a rail for azimuth movement and horizontal bearings located on towers of each side of the dish for altitude movement. The Cherenkov camera is held in the focal plane by a quadrupod.

Optical system: The segmented reflector consists of 382 round segments of 60 cm diameter that give a total reflecting area of 107 m^2. The reflectivity at 330 nm is about 80 %.

Camera: Each camera consists of 960 photomultiplier tubes (PMTs) with the layout shown in Figure 2.6 covering a field of view of 5 deg. The PMTs have a quantum efficiency of $\sim 25\%$ and have a hexagonal light funnel of diameter 0.16 deg in front, reducing the light-insensitive area to less than 5%. The signal is sampled at 1 ns resolution and stored in an analog ring buffer for the past 128 ns. When taking an image the camera integrates over a 16 ns time window, the dynamic range is 1 to 1600 photo-electrons (pe).

Camera trigger: Each camera is segmented into 64 overlapping sectors of 8×8 pixels. A camera triggers when a signal of at least 5 units of photoelectrons (pe) was measured in at least 3 pixels within one sector within 1.5 ns.

Central trigger: The central trigger unit receives the camera triggers and if at least two camera triggers arrive within 50 ns, a central trigger command is issued to read out the participating cameras. This number of available shower images is called the *event multiplicity*.

Each camera triggers at a rate of about 400 Hz, the sytem trigger rate (for 2, 3 and 4-multiplicity events) is about 200 Hz, resulting in each camera being read out at a rate of about 150 Hz.

2.4. Event Reconstruction

The HESS data after calibration (see Aharonian et al. (2004)) consists of two or more images per shower in units of photoelectrons (pe) (see Figure 2.6 for a simulated example).

The first step is to "clean" the image, i.e. to only keep pixels with intensity 10 pe that have a neighbor of at least 5 pe or vice versa. This gets rid of the large parts of the image that only contain fluctuations from the night sky background (NSB) and helps make the next step fast and stable. Images that are too faint or too close to the edge of the camera are discarded (preselection).

The second step is to parametrize the remaining shower image as a 2D elongated Gaussian light distribution by computing the second moments of the im-

age, resulting in six ellipse parameters per image (a.k.a. Hillas parameters): position (x, y), length, width, orientation angle and total intensity.

Direction Reconstruction

These ellipses in the camera coordinate systems are illustrated in Figure 2.4 on the lower right. Using coordinate transformations it is possible to transform each ellipse from its own *camera system* into a common *ground system* (literally the position on the ground in meters) as well as the so called *nominal system* (a tangential spherical projection centered on the array pointing position, with coordinates in deg corresponding to positions in the sky).

By intersecting the major axes of the ellipses in the ground system, the *impact or core position* is determined, which is the position the gamma ray which hit the Earth would have had it not showered in the atmosphere. The gamma ray direction is reconstructed by intersecting the major axes of the ellipses in the nominal system. For showers seen by N telescopes there will be $N(N-1)/2$ reconstructed directions and several weighting methods exist to find an average (Hofmann et al., 1999). The achieved angular resolution scales as $1/\sqrt{(N)}$.

Lookups

The next step is to reconstruct the energy, which is the first step in the analysis chain that is no longer possible using the data and calibration information alone. The measured total intensity in p.e. of the cleaned image (a.k.a image "size") depends on the Cherenkov light yield of electromagnetic air showers and on the HESS detector response, e.g. primary mirror area and reflectivity, Winston cone efficiency, PMT entrance window transmissivity, PMT photocathode quantum efficiency.

Detailed simulations exist for the whole process (Bernlöhr, 2008). CORSIKA[2] (Heck et al., 1998)) is used to simulate the air shower and Cherenkov light yield, then (in absense of atmospheric monitoring) average atmospheric transmissivities for the HESS site are assumed (Bernlohr, 2000) and finally the response by the HESS optical and electronic system is modelled in great detail.

During analysis the result of these simulations is accessed via so called lookups, described in more detail in Section 2.4.

Energy Reconstruction

In the case of the energy lookup, the mean E_{MC} and rms energy for a given optical configuration, azimuth, zenith, offset, telescope ID, total image amplitude (size) and impact distance is looked up for each event and telescope (see Table 2.1). This energy estimate is then further corrected for the difference in

[2] `http://www-ik.fzk.de/corsika/`

lookup file (.root)	histogram	parameters	x-axis	y-axis	z-axis
ScaleInfo	avg_length	opt,azm,zen,off	$\ln(\mathrm{size}/p.e.)$	d/m	$\langle L\rangle/\mathrm{mrad}$
	avg_width	opt,azm,zen,off	$\ln(\mathrm{size}/p.e.)$	d/m	$\langle W\rangle/\mathrm{mrad}$
	sigma_length	opt,azm,zen,off	$\ln(\mathrm{size}/p.e.)$	d/m	σ_L/mrad
	sigma_width	opt,azm,zen,off	$\ln(\mathrm{size}/p.e.)$	d/m	σ_W/mrad
EnergyInfo	MeanTrueEnergy	opt,azm,zen,off,tel	$\ln(\mathrm{size}/p.e.)$	d/m	E/TeV
	SigmaTrueEnergy	opt,azm,zen,off,tel	$\ln(\mathrm{size}/p.e.)$	d/m	$\sigma(E)/\mathrm{TeV}$
EffectiveAreas	EffArea_TrueEnergy	opt,telp,azm,zen,off	$E_{\mathrm{true}}/\mathrm{TeV}$	$A_{\mathrm{eff}}/\mathrm{m}^2$	
	EffArea_RecoEnergy	opt,telp,azm,zen,off	$E_{\mathrm{reco}}/\mathrm{TeV}$	$A_{\mathrm{eff}}/\mathrm{m}^2$	
	EnergyBias	opt,telp,azm,zen,off	$\log_{10}(E/\mathrm{TeV})$	$(E_{\mathrm{reco}}-E_{\mathrm{true}})/E_{\mathrm{true}}$	
PSF	ThetaSq	opt,telp,azm,zen,off	$\log_{10}(E/\mathrm{TeV})$	θ^2/deg^2	p.d.f. value
EnergyReconstruction	EnergyReconstructionPDF	opt,telp,azm,zen,off	$\log_{10}(E/\mathrm{TeV})$	$(E_{\mathrm{reco}}-E_{\mathrm{true}})/E_{\mathrm{true}}$	p.d.f. value
RadialAcceptance	RadialLookup	zen	$(\Delta\Psi)^2/\mathrm{deg}^2$	acc/a.u.	

Table 2.1.. Lookups. Table taken from `hddst/scripts/lookups/lookups.pdf` in the HESS software.

OptConf	Phase	Start	Muon Efficiency				Comment
			CT1	CT2	CT3	CT4	
100	1	2000-01-01	0.1075	0.1075	0.1075	0.0992	Brand new
101	1b	2004-05-26	0.0724	0.0724	0.0724	0.0724	Degrading
102	1c	2007-07-03	0.0635	0.0574	0.0633	0.0635	Degrading
103	1c1	2010-04-27	0.0634	0.0574	0.0883	0.0634	CT3 recoated
104	1c2	2010-10-17	0.0635	0.0755	0.0813	0.0634	CT2 recoated

Table 2.2.. HESS optical configurations

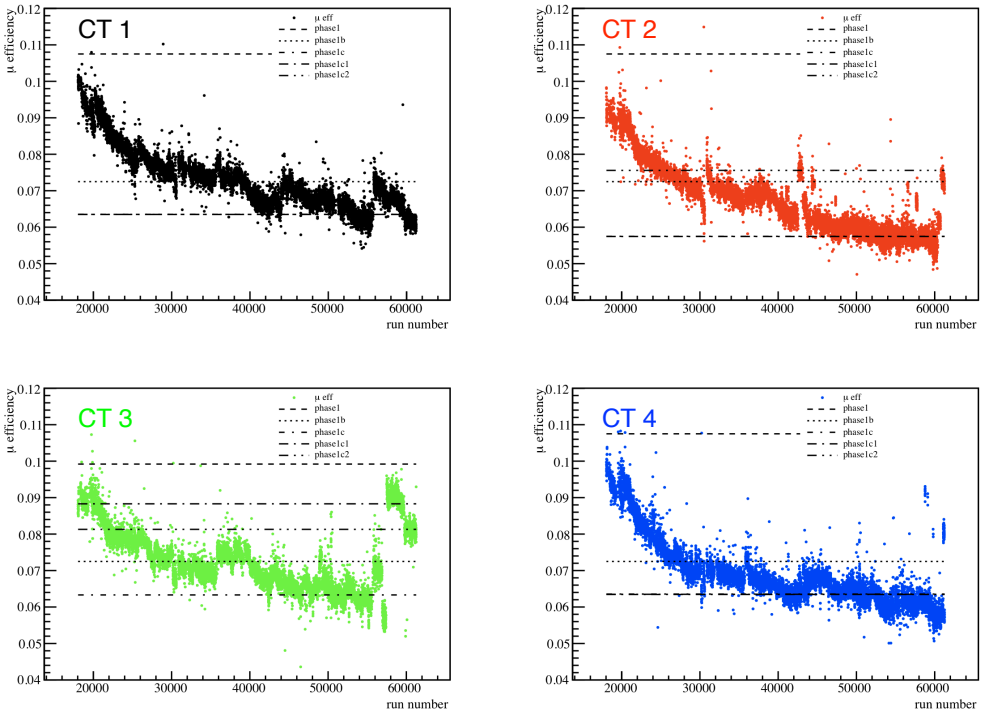

Figure 2.5.. HESS optical efficiency. The circles show measured efficiency for each run, the horizontal lines show the values assumed in the MC simulations for each phase (see Table 2.2).

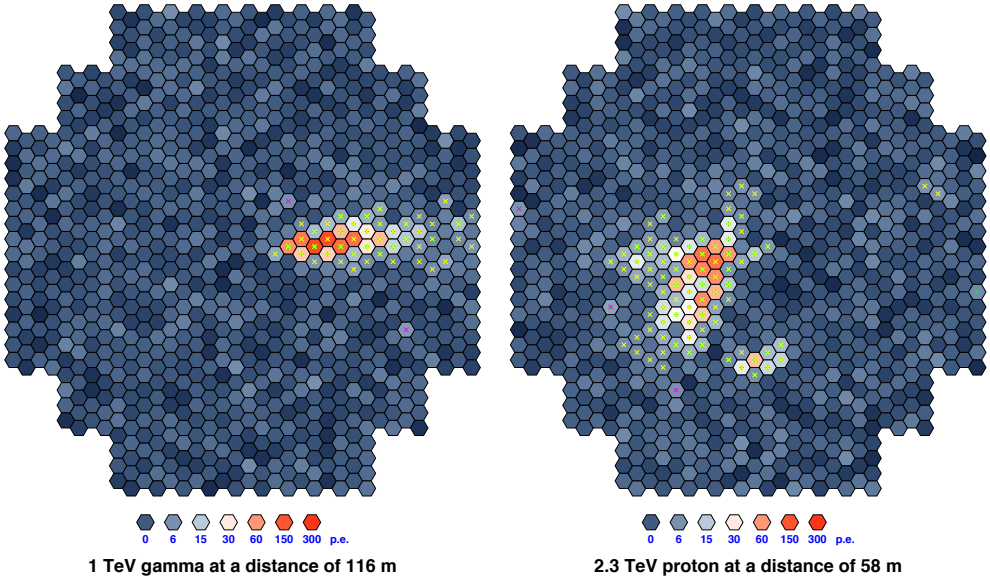

Figure 2.6.. Simulated HESS Cherenkov camera shower images. The proton image on the right is wider and more irregular than the gamma image on the left. Pixels with an intensity of more than 5 or 10 photoelectrons (p.e.) are marked with a yellow or green cross. Simulation by Konrad Bernlöhr, figure taken from Ohm (2010).

optical efficiency (measured from muons) between MC and the current run,

$$E = \frac{\epsilon_{run}}{\epsilon_{MC}} E_{MC}. \tag{2.1}$$

Then a weighted mean energy is computed from these energy estimates of each telescope. The resulting energy resolution is $\sim 15\%$.

The reconstruction method described here (Hillas parameters) is only one of three methods used in the the HESS collaboration. More advanced methods fit the shower images model light distributions. The Model 3D method (Lemoine-Goumard et al., 2006; Naumann-Godó et al., 2009) used a 3D ellipsoid as a model for the shower and computed the resulting expected model images, the Model++ method (de Naurois and Rolland, 2009) used semi-analytic models incorporating a lot of shower physics. Both Model 3D and Model++ are more sensitive than Hillas, mainly concerning the gamma-hadron separation described in the next section.

Gamma-hadron Separation

Most of the air showers observed by HESS are not from gammas but from charged cosmic rays. As illustrated in Figure 2.6 hadronic showers are much wider and irregular than leptonic showers. To discriminate between the two types of events two parameters, the mean reduced scale width (MRSW) and mean reduced scale length (MRSL). As can be seen in Figure 2.7 for simulated data, the distributions for gammas are approximately Gaussian with peak at zero with width one, whereas the proton distributions are offset to the right. By applying the cuts on these parametes as defined in Table 2.3 about 95% of the background can be removed while keeping approximately 80% of the gammas. Two sets of standard analysis cuts have been defined with standard cuts optimized for the detection of sources with 10% Crab flux and spectral index 2.6 and hard cuts for 1% Crab flux sources with spectral index 2. The Theta square cut given in Table 2.3 was optimized for point source detection for the spectral analysis of extended sources, larger theta cuts are used for spectral analysis. The main difference between standard and hard cuts is in the size cut (80 vs. 200 p.e.) resulting in a lower energy threshold for standard cuts but better background suppression for hard cuts.

Recently, Ohm et al. (2009) have developed an improved Gamma-hadron separation technique where, in addition to the MRSW and MRSL, four additional parameters are used (see Figure2.8). Also, instead of doing simple box cuts on these six parameters they are combined into one 'gammaness' parameter Zeta computed using the boosted decision tree (BDT) method (see Figure 2.8). The BDT is trained using Montecarlo gammas and real background data in energy and zenith angle bands. The decision to keep or reject an event is done by applying a cut on the Zeta computed for each event, where Zeta is chosen for each energy zenith angle band such that 84 / 89% of gammas are kept for `std_zeta` / `hard_zeta` cuts (see Table 2.3.)

2.5. Statistics

Before we discuss the methods used to make maps and spectra in the next two sections, let us briefly describe the common statistical methods used, which concern the detection and measurement of an excess signal in Poisson data in the presence of background.

The measurement is illustrated in Figure 2.9. A counting detector looks at a suspected source for some time t_{on} and finds N_{on} events, then looks at a *background region*—known to contain no source but the same background rate as the *source region*—for a time t_{off} and finds N_{off} events. It actually doesn't matter if the ts are times in seconds or areas on the sky Ω in deg^2 or background

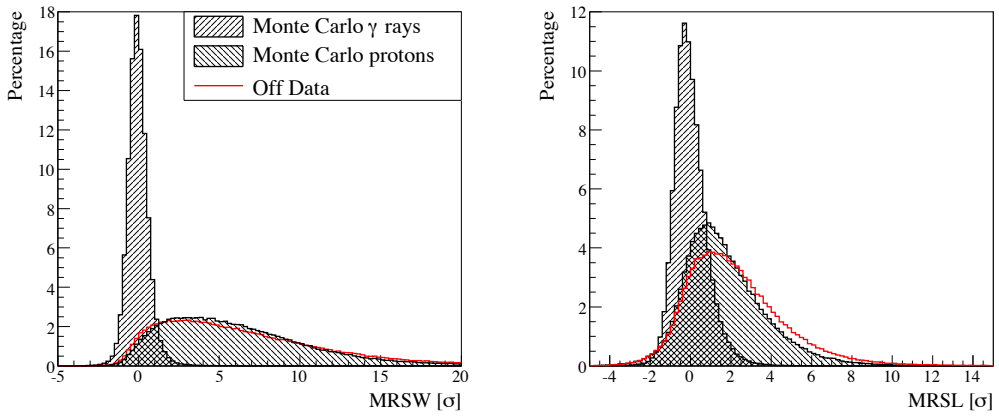

Figure 2.7.. Gamma-hadron shower shape separation parameters. The distributions shown here are for simulations at 20 deg zenith angle and for real off data at 15 to 25 deg, after applying the size cut of the standard configuration as given in Table 2.3. Figure taken from Ohm (2010).

Configuration	Size Min pe	Theta Max deg	MRSW Max	MRSL Max	$\epsilon_\gamma(\zeta)$ Min
std	80	0.12	0.9	2	—
std_zeta	60	0.12	—	—	0.84
hard	200	0.10	0.7	2	—
hard_zeta	160	0.10	—	—	0.89

Table 2.3.. HESS event cuts. The Hillas cuts (std, hard) have been defined in Aharonian et al. (2006e), the TMVA cuts (std_zeta, hard_zeta) in Ohm et al. (2009) with one minor modification: currently $\epsilon_{\gamma(\zeta),max} = 0.89$ is used instead of 0.83 as given in the paper. The std cuts have been optimized for the detection of sources with 10% of the integrated Crab flux above 200 GeV and spectral index 2.6, the hard cuts for 1% Crab flux and index 2.0. A minimum cut of -2 is applied both for std and hard on MRSW and MRSL.

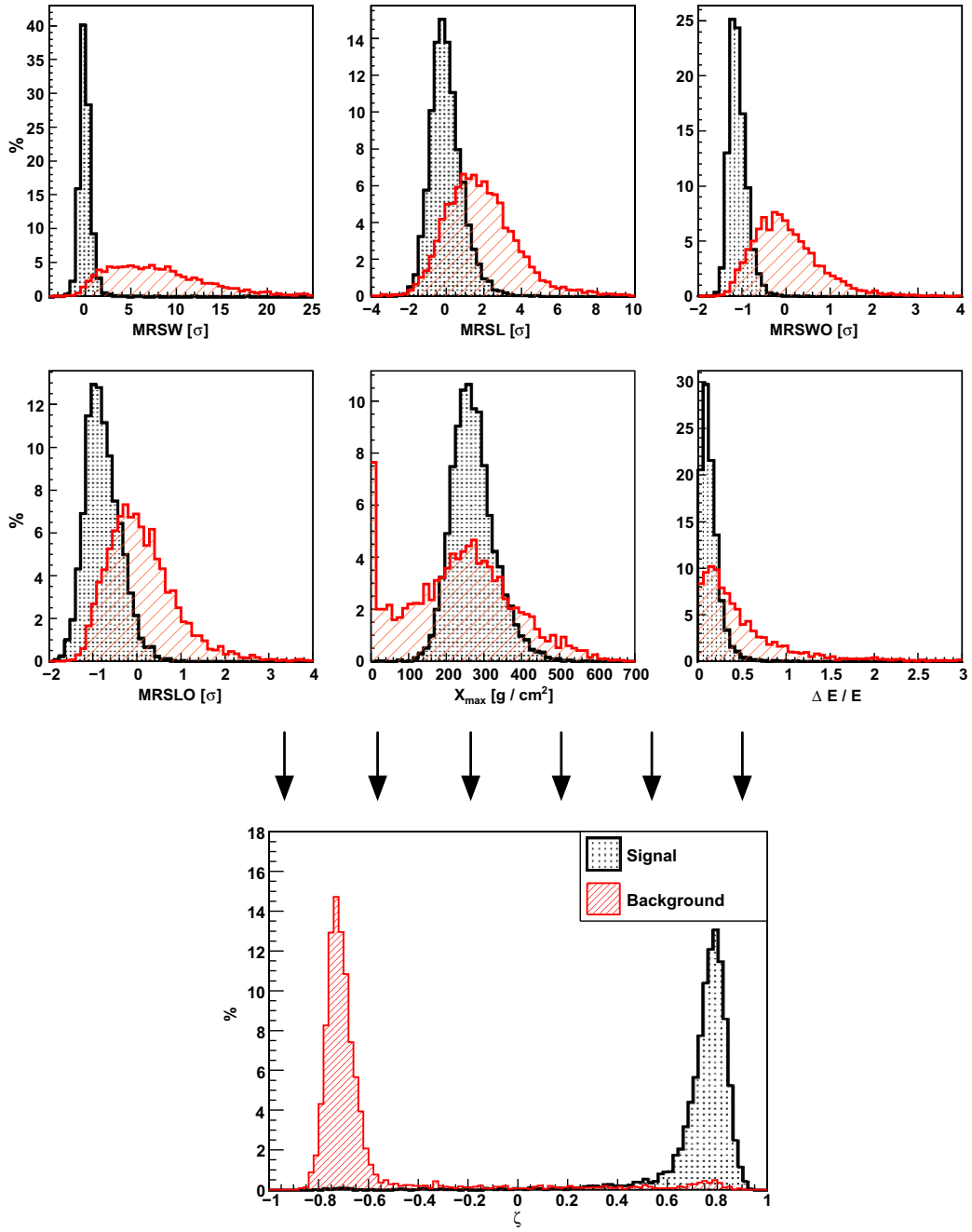

Figure 2.8.. TMVA gamma-hadron separation parameters. The distributions shown here are for energies of 0.5 to 1 TeV and zenith angles 15 to 20 deg. Simulated gammas in black and cosmic rays from off data in red. Figure adapted from Ohm et al. (2009).

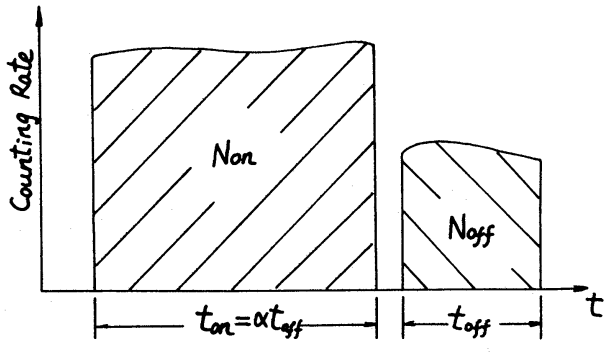

Figure 2.9.. A typical observation in gamma-ray astronomy. Figure taken from Li and Ma (1983).

effective areas A in cm^2, all that matters is that there is a ratio

$$\alpha = \frac{t_{on}}{t_{off}} \tag{2.2}$$

describing the relative exposure of the on and off region for background.

Excess and Significance

The number of background events in the on-region can be estimated as

$$N_B = \alpha N_{off} \tag{2.3}$$

and thus the number of excess signal events as

$$N_S = N_{on} - \alpha N_{off} = N_{on} - N_B. \tag{2.4}$$

Given that N_{on} and N_{off} are Poisson-distributed, their variance is equal to their value, and the error of the excess can be estimated as

$$\Delta N_S = \sqrt{N_{on} + \alpha N_{off}} = \sqrt{N_{on} + N_B} = \sqrt{N_S + 2N_B} \tag{2.5}$$

and the significance as

$$S = \frac{N_S}{\Delta N_S} = \frac{N_S}{\sqrt{N_S + 2N_B}} = \frac{N_{on} - \alpha N_{off}}{\sqrt{N_{on} + \alpha N_{off}}} \tag{2.6}$$

Li and Ma (1983) have shown that Equations (2.5) and (2.6) are incorrect for $\alpha \neq 1$. Assuming some true mean expected number of signal events n_S and

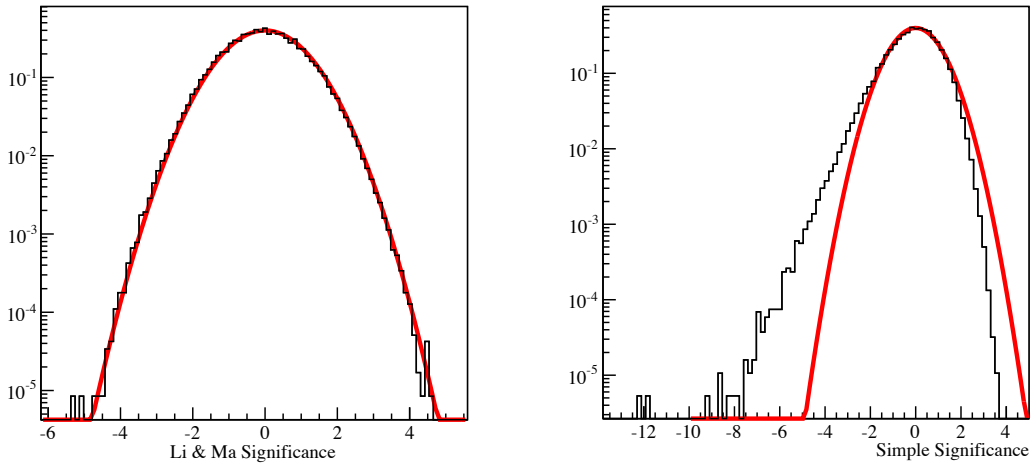

Figure 2.10.. Significance distribution for 10^6 random draws using $n_S = 0, n_B = 140, \alpha = 0.1$ computed using the Li&Ma formula (2.10) (left) and the simple formula (2.6) (right).

mean expected number of background events n_B in the on region[3] and drawing random Poisson variables according to

$$P(N_{on}; n_S + n_B) = \frac{(n_S + n_B)^{N_{on}} e^{-(n_S+n_B)}}{N_{on}}, \tag{2.7}$$

$$P(N_{off}; n_B/\alpha) = \frac{(n_B/\alpha)^{N_{off}} e^{-(n_B/\alpha)}}{N_{off}}, \tag{2.8}$$

one can see that the significance and

$$\chi = \frac{N_S - n_S}{\Delta N_S} \tag{2.9}$$

distributions don't follow a standard normal distribution (see Figure 2.10 right).

Using the likelihood ratio method and a different estimate for N_B Li&Ma derived the following improved formula to compute a significance,

$$S = \sqrt{2}\left\{ N_{on} \log\left[\frac{1+\alpha}{\alpha}\left(\frac{N_{on}}{N_{on}+N_{off}}\right)\right] + N_{off}\log\left[(1+\alpha)\left(\frac{N_{off}}{N_{on}+N_{off}}\right)\right]\right\}^{1/2} \tag{2.10}$$

and it is also possible (although as far as I know only numerically by finding the points where $\Delta L = 0.5$) to compute asymmetric errors on the excess such

[3]Note that here one has the choice to introduce the number of background events in the on or off region as a parameter, so the formulas given here might differ from other texts if they chose the opposite convention.

that the significance and chi distribution does follow the standard normal distribution for any α (see Figure 2.10 left).

In the limit $\alpha \to 0$, for a given N_B, we have $N_{off} = N_B/\alpha \to \infty$ and for the error $\Delta N_B = \alpha\sqrt{N_{off}}$ we find $\Delta N_B/N_B = 1/\sqrt{N_{off}}$, i.e. the background level will be known without error. For known background level n_B, the Li & Ma formula can be simplified as

$$S = \sqrt{2}\left[N_{on}\log\left(\frac{N_{on}}{n_B}\right) - N_{on} + n_B\right]^{1/2} \tag{2.11}$$

Upper and lower limits on the number of source events n_S, taking into account the physical constraint $n_S \geq 0$, are computed using the Rolke et al. (2005) profile likelihood method is used, which properly takes into account the N_{off} fluctuations. Unfortunately no analytical formula exists, the limits have to be computed numerically (root finding where $-2\Delta\log(L(n_S)) = 1$).

Excess sensitivity is computed using the normal excess formula (2.4), but instead of taking the measured N_{on}, a value N_{on} is computed that would correspond to a given significance S (5 is commonly used), i.e. Equation 2.10 is solved for N_{on} given the background N_{off} and α. Note the difference between upper limit and sensitivity: the upper limit does depend on N_{on} and if a source is present, will never fall below the excess, whereas sensitivity is independent from N_{on} and the fact if a source is present in the on region or not, it is only determined by the background level.

Further discussions on the estimation of errors, limits, significances and sensitivities can be found in Cousins (1995); Narsky (2000); Schwanke (2004); Rolke et al. (2005) and Kashyap et al. (2010).

HESS data is often 'background-dominated', i.e. $N_S \ll N_B$, in which case we find simplified formulae for the excess error, significance and sensitivity:

$$\Delta N_S = \sqrt{2N_B}, S = \frac{N_S}{\sqrt{2N_B}}, N_S = S\sqrt{2N_B}. \tag{2.12}$$

Typically both the signal and background counts will be the result of the observation of a signal $N_S = tA_SF_S$ and background $N_B = tA_BF_B$ flux (in units $\mathrm{cm}^{-2}\ \mathrm{s}^{-1}$), and the real quantity of interest is the signal flux. Substituting into (2.12), we find

$$\Delta F_S = \frac{1}{\sqrt{t}}\frac{A_BF_B}{A_S}, S = \sqrt{t}\frac{A_SF_S}{\sqrt{2A_BF_B}}, F_S = \frac{1}{\sqrt{t}}\frac{S\sqrt{2A_BF_B}}{A_S}, \tag{2.13}$$

i.e. significance increases as square root time, and flux error as well as sensitivity decrease as square root time. That is on average, of course, each individual realisation will fluctuate around this mean behaviour.

One more point worth pointing out is that sensitivity is a flux, a 'low sensitivity' observation is actually a good one, whereas some people use this term incorrectly to mean 'low exposure', which is the opposite. In this thesis I will use the terms 'good sensitivity' and 'bad sensitivity' to be unambiguous.

Likelihood

Now consider a number of M on/off measurements, each with its own expected number of signal n_S and background n_B events predicted by a signal and background model with a few parameters x. We want to make a fit the model to the data by maximizing the product likelihood of the individual measurements, so the question boils down to how to compute the likelihood of one on/off measurement.

1. If there is a model for the signal and the background, N_{on} and N_{off} can simply be considered as two measurents and the likelihood is given by the product of the Poisson probabilities (see Equations (2.7) and (2.8) as well as Figure 2.11)

$$L(N_{on}, N_{off}; n_S, n_B, \alpha) = P(N_{on}; n_S + n_B)P(N_{off}; n_B/\alpha). \tag{2.14}$$

2. If no background model is available, then Equation (2.14) cannot be used, because n_B is unknown. One possibility is to choose n_B such that $\log L$ is maximized, i.e. choose the most likely background level.[4] Setting the first derivative $\frac{\partial \log(L)}{\partial n_B}$ to zero results in a quadratic equation in n_B with solution (illustrated by the white line in Figure 2.11)

$$\begin{aligned} n_B &= \frac{C + \Delta}{\alpha + 1} \\ C &= \alpha(N_{on} + N_{off}) - (1 + \alpha)n_S \\ \Delta^2 &= C^2 + 4\alpha(\alpha + 1)N_{off}n_S. \end{aligned} \tag{2.15}$$

   So just to be perfectly clear, the likelihood used is given by formula 2.14 with n_B set to the value in formula 2.11.

3. As mentioned already in the last section, in the limit $\alpha \to 0$ the background level will be known as $n_B = \alpha N_{off}$. In this case there is only the on-measurement with Poisson statistical error and the likelihood function becomes

$$L(N_{on}, N_{off}; n_S, \alpha) = P(N_{on}; n_S + \alpha N_{off}) \tag{2.16}$$

Currently—in absense of a good background model—option number 2 is used to fit the spectra and option number 3 to fit the morphology of HESS sources.

Note that it is not obvious that option number 2 will work, because effectively a new free fit parameter n_B per bin is introduced, which is then fixed to its maximum likelihood value. The main concern is that this likelihood might not have correct normalization for the 1, 2, 3 sigma error computation via steps of 1, 4, 9 in $-2\log(L)$, although in principle there could also be a bias in the estimated parameters. Extensive simulations of spectra have shown that option number 2 does yield excellent results, though.

[4] The following formulae were taken from the French `MathUtils::OnOffFitter` class and implemented in the Heidelberg `flux` module.

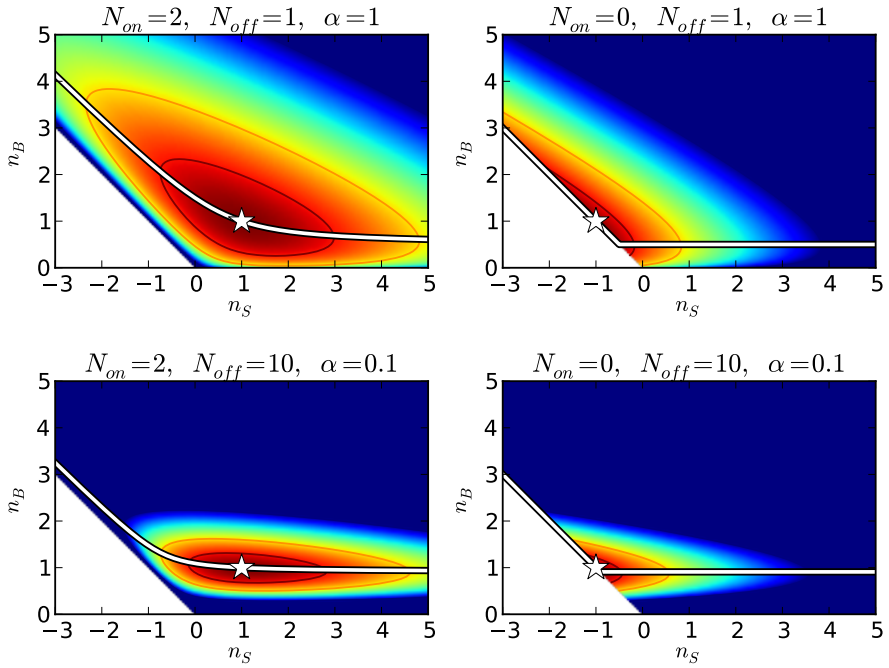

Figure 2.11.. On-off likelihood function from Equation 2.14 (note that it can only be computed for $n_B > 0$ and $n_S + n_B > 0$). Color shows $-2\log(L)$ with contours at 1, 4, 9 to indicate 1, 2 and 3 standard deviation errors. The white star shows the maximum likelihood solution if both n_S and n_B are free, the white line shows the maximum likelihood solution for n_B for a given n_S, for which an analytical formula exists. The background $N_B = \alpha N_{off}$ is 1 in all cases, the excess $N_S = N_{on} - N_B$ is 1 on the left and -1 in on the right. The top panels show an example with poorly determined background level ($\alpha = 1$), in the bottom panel the background level is well-measured ($\alpha = 0.1$).

2.6. Maps

The goal of HESS data analysis is to measure the morphological and spectral properties of sources. In principle it would be best to fit models for the morphology and spectrum of the source simultaneously to the data (binned in position-energy cubes or unbinned), however this is currently not implemented in the software. Instead, the position and energy information of the events is used separately to produce maps (described in this section) and spectra (described in the next section).

Maps can be produced for any set of cuts. Typically maps are produced using either std or hard cuts (or their TMVA equivalents) and possibly by applying an additional energy cut. This can either be a fixed energy cut (e.g. 1 TeV) or each run can be cut at its safe energy (described in Section 2.8).

The basic strategy of the HESS software is to process the data one run at a time to only store basic *summable* information like counts and exposure, but not derived (non-summable) information like significance. This also has the advantage that runs can be processed in paralled and then runwise-results quickly summed at the end.

In the HESS software there are six basic maps, which are illustrated as the top six maps of Figure 2.12. The on map is simply the count map and contains signal and background events. The exposure map is computed as

$$\text{Exposure} = \int\int A(E, \mu, zen, az, \psi) E^{-\Gamma} dE dt, \tag{2.17}$$

where A is the effective area as a function of energy E, muon efficiency μ, zenith, azimuth and offset angle ψ. Note that exposure is equal to the number of expected counts for an assumed power-law source with spectral index Γ (typically chosen in the range 2 to 3 to match the actual spectral index of Galactic sources in the map) and differential flux at 1 TeV of 1 cm^{-2} s^{-1} TeV^{-1}. The exposure is defined in such a way that the flux can simply be computed as

$$\text{Flux} = \text{Excess}/\text{Exposure}. \tag{2.18}$$

Note that the images shown in Figure 2.12 are the sum of over 100 runs, for an individual run the exposure map would be almost radially symmetric with respect to the observation position.

The arcs visible in the exposure image (and even better visible so in the on-exposure and background images) of Figure 2.12 are the result of the HESS wobble observation pattern, where most of the data on a given target is taken by shifting the observation position by 0.5 or 0.7 deg north, south, east and west (in Equatorial coordinates, these images are in Galactic coordinates) of the target center. Also because the HESS effective area and background rejection efficiency at high offsets is not well known, a maximum offset cut is applied (at 2 deg in this example), i.e. all the runwise maps are set to zero beyond this cut.

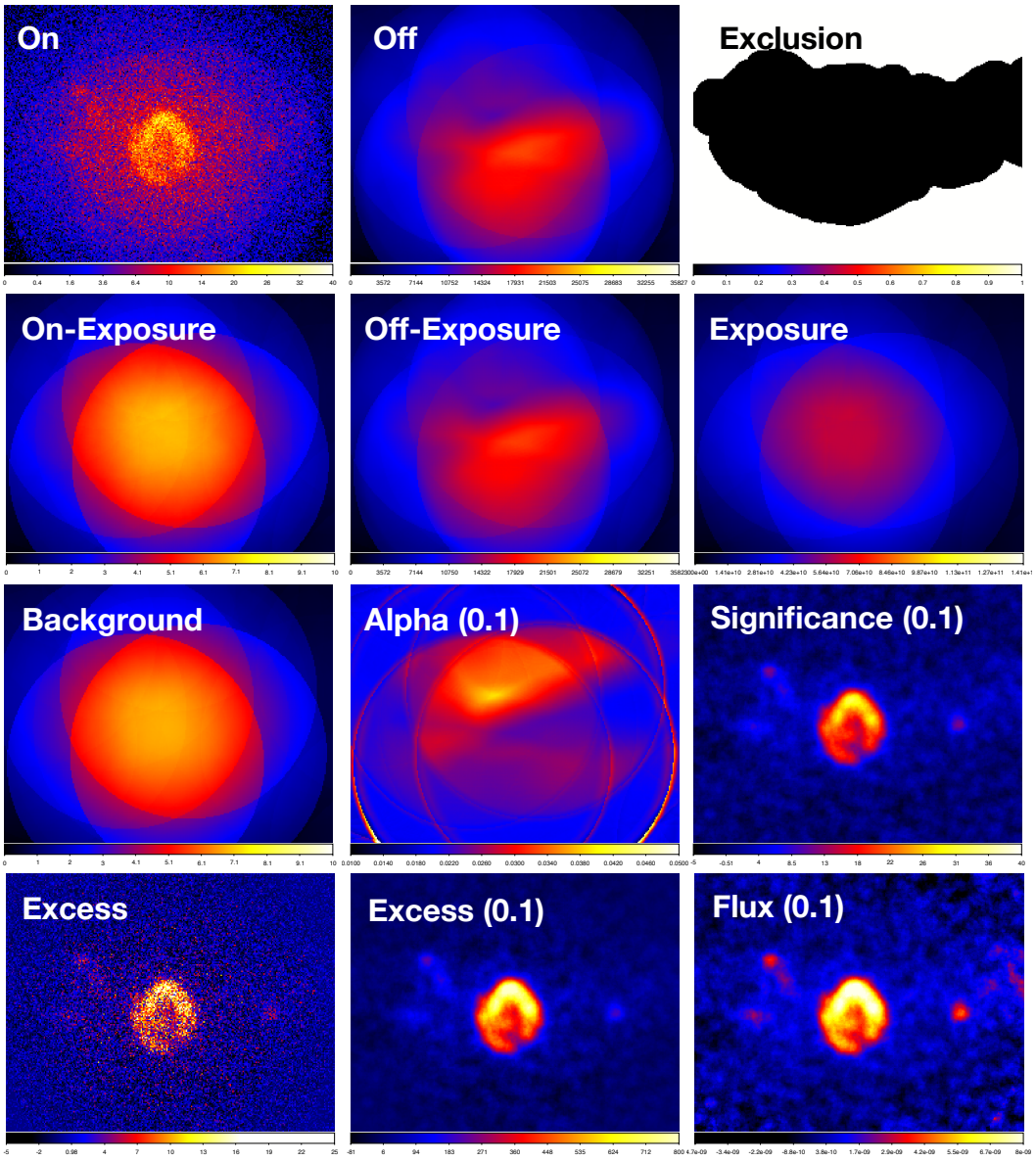

Figure 2.12.. Illustration of the HESS maps (hard cuts) using the region around the supernova remnant RX J1713.7-3946 (Galactic coordinates). See main text for explanations. For correlated maps the correlation radius (0.1 deg) is noted. The off and off-exposure maps are ring-correlated, but not tophat-correlated by 0.1 deg. RX J1713.7-3946 is 1 deg in diameter.

The other four basic maps deal with background modelling. As can be seen in the count map, besides RX J1713.7-3946 and the other weaker sources, there is a high background, roughly equal in shape to the exposure map, but not quite. The reason the shapes are not equal is that e.g. at high offset angles, it becomes more difficult to distinguish gammas from hadrons.

For HESS, the hadronic background is treated very differently in the analysis than gammas. For gammas effective areas lookups $A(E, \mu, zen, az, \psi)$ are computed using Monte-Carlo simulations. Background lookups $B(E, zen, \psi)$ differ in that only energy, zenith and offset are considered as parameters and that the absolute level is considered unknown (i.e. B doesn't have a meaningful unit like rate or flux) and has to be estimated from each run individually.

For a given run a so called 'acceptance curve' is constructed that represents the offset-dependence of the background for the given zenith angle and energy band (see Figure 2.13, top left for examples). Using this curve, the on-exposure image (see Figure 2.12) is then constructed by rotating the curve around the observation position and normalizing the resulting image such that the sum of pixel values outside exclusion regions matches the sum of the on map outside exclusion regions.

The on-exposure map is somewhat of a misnomer, it really is the estimated background map (in this case with approx. 7 background counts per 0.02 x 0.02 deg pixel at the position of RX J1713.7-3946) using the so called 'Field of view (FOV) background method' Berge et al. (2007). Its name was chosen because it uses the whole FOV (apart from excluded regions suspected to contain gamma-ray sources) to adjust the background level normalization.

With the FOV background method the estimated background is radially symmetric, so if the real background is not, errors will be made. The most common deviation from radial symmetry are linear gradients across the FOV, e.g. because background rates are higher at lower zenith angles and the zenith angle changes by a few degrees across the FOV.

One method to remove linear gradients is the ring-background method (illustrated in Figure 2.13). It fills two additional maps, the off map is a ring-correlated (exclusion x on) map, and the off-exposure map is a ring-correlated (exclusion x on-exposure) map. In this case a ring with inner radius 0.5 and outer radius 0.87 was used, which results in an off-count of $\sim 20,000$ in the center. To use the ring-background maps, alpha = on-exposure / off-exposure, background = alpha x off and excess = on - background is used, as described in Section 2.5.

Sometimes inside very large exclusion regions, most of the ring is contained inside the exclusion region. In order to obtain a good measurement of the background nonetheless, for those regions the outer ring radius is expanded adaptively, which is illustrated in Figure 2.14. In this case the 'ConstantInnerRadius' method was chosen with a maximum outer ring radius of 1.7 deg. The effect of this outer ring radius expansion can be seen in the 0.1 deg correlated alpha map in Figure 2.12. In this case the default ring had 50 times the area

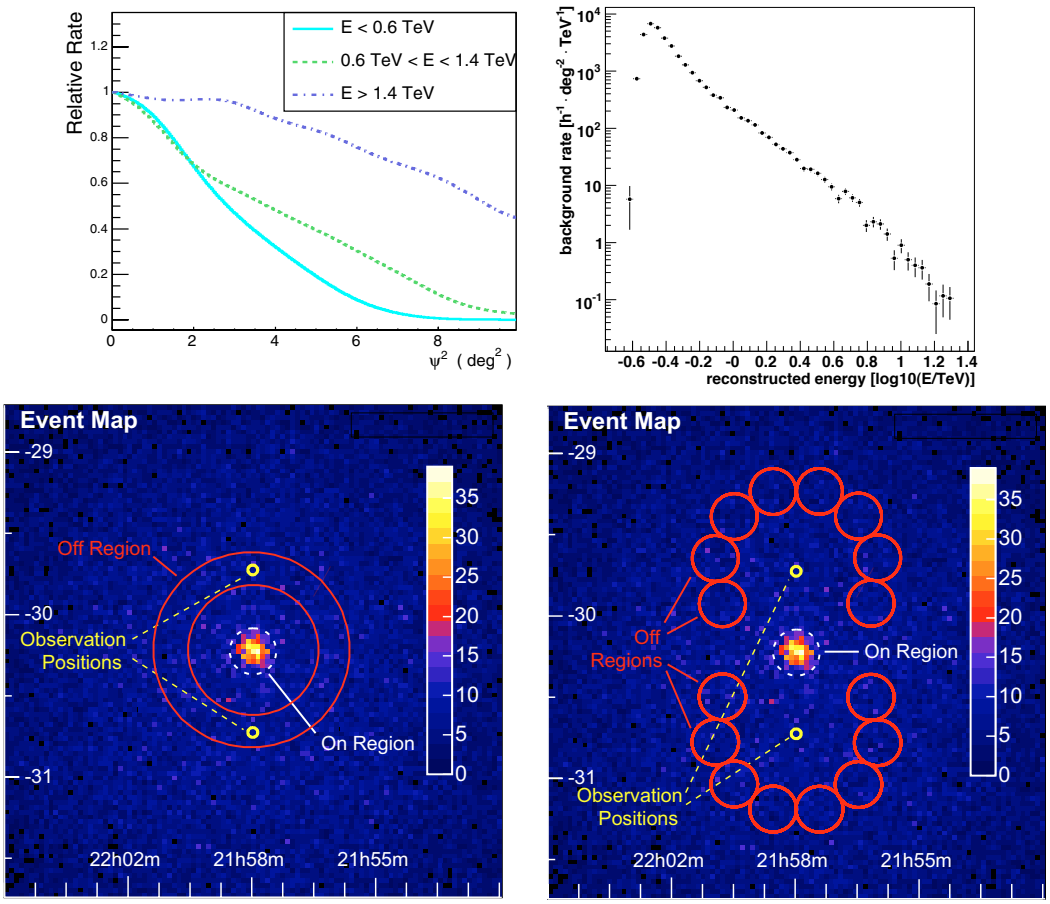

Figure 2.13.. *Top left:* HESS background rate as a function of offset for different energy bands (Berge et al., 2007). *Top right:* Background rate after std cuts for a zenith angle of 30 deg and an offset of 0.5 deg (Glück, 2011). *Bottom left:* Ring background estimation method. *Bottom right:* Reflected background estimation method. See main text for explanations. Background method illustrations from Berge et al. (2007).

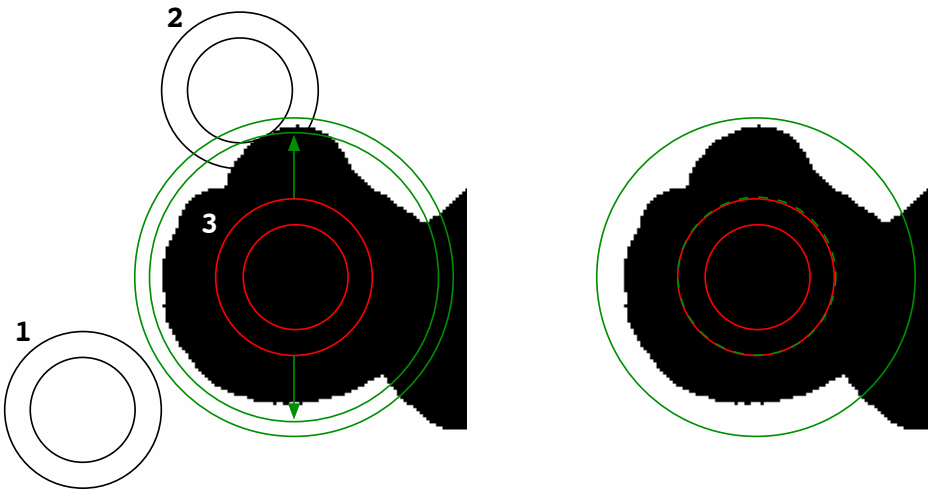

Figure 2.14.. Illustration of adaptive ring background method. In cases 1 and 2 no adaptive ring expansion is necessary. In case 3 the standard ring falls entirely in an exclusion region and is expanded using the `ConstantArea` method on the left and the `ConstantInnerRadius` method on the right. Figure by Henning Gast, private communication.

of the 0.1 deg correlation circle, so outside the exclusion regions, alpha = 0.02. The fact that on the right side of the image, even inside the exclusion region, alpha = 0.02 is due to the ring adaptively expanding to cover more non-excluded area above and below the exclusion region. In the center of the image, alpha increases to 0.04 in some parts, because even with the outer ring radius expanded to 1.7 deg, an alpha of 0.02 cannot be achieved. Note that alpha is not simply circle area over ring area, but sum(on-exposure, circle) / off-exposure, where off-exposure = sum(exclusion x on-exposure, ring).

Finally, Figure 2.12 also shows an uncorrelated excess map as well as correlated excess, significance and flux maps.

2.7. Morphology Fits

The morphology fits are done using a Poisson likelihood statistic

$$\text{on} = \text{Poisson}(\text{background} + \text{PSF}(\text{exposure} \times \text{sources})), \tag{2.19}$$

which is Equation 2.16 with n_S = PSF(exposure $\times$ sources). As sources we choose a collection of symmetric 2D Gaussians,

$$S = A \exp\left[-\frac{(x-x_0)^2 + (y-y_0)^2}{2\sigma^2}\right], \tag{2.20}$$

with amplitude A, width σ and position (x_0, y_0) as free parameters.

The fits are done in CIAO Sherpa 4.3 Refsdal et al. (2009); Refsdal et al. (2011) using the Levenberg-Marquardt optimier and the CASH statistic. The PSF is modelled analytically as a triple 2D Gaussian (see Figure 2.15). Using the HESS software, the expected θ^2 distribution (θ is the offset from the source position) is computed, including errors, by first looking up the event distribution in ($\log(E)$, θ^2) for each run (see Table 2.1) and then weighting it with the expected counts assuming a spectral index of 2.

To avoid binning errors, the θ^2 distribution was fit with a triple-Gaussian analytical model,

$$PSF(\theta^2) = S\left[\exp\left(-\frac{\theta^2}{2\sigma_1^2}\right) + A_2 \exp\left(-\frac{\theta^2}{2\sigma_2^2}\right) + A_3 \exp\left(-\frac{\theta^2}{2\sigma_3^2}\right)\right] \tag{2.21}$$

Figure 3.12 shows an example where a number of nearby sources have been fit simultaneously. The middle panel shows the model image in units of statistical significance, i.e.

$$\text{model} = \text{PSF}(\text{exposure} \times \text{sources}) \tag{2.22}$$

has been computed and then Formula 2.11 was used with n_B = background and $N_{on} = n_B$ + model. Also the residual significance after putting the model in the background was computed to assess if the region has been modelled adequately, i.e. again Formula 2.11 as used, this time with n_B = background + model and N_{on} = On, i.e. the count map.

2.8. Spectra

Aperture Photometry

The HESS software uses aperture photometry to derive spectra, i.e. for each source an aperture (a 2D region on the sky) is chosen, such that most of the emission from the source (even after PSF-convolution) is contained in that region. Although the HESS software can handle arbitrary aperture shapes, usually circles are chosen, except for a few very bright sources where a non-circular morphology is evident.

In this thesis we will model sources as 2D Gaussians, and although the HESS PSF is actually rather a triple-Gaussian than a Gaussian, for all but the smallest sources, the PSF-convolved intensity distribution is again approximately

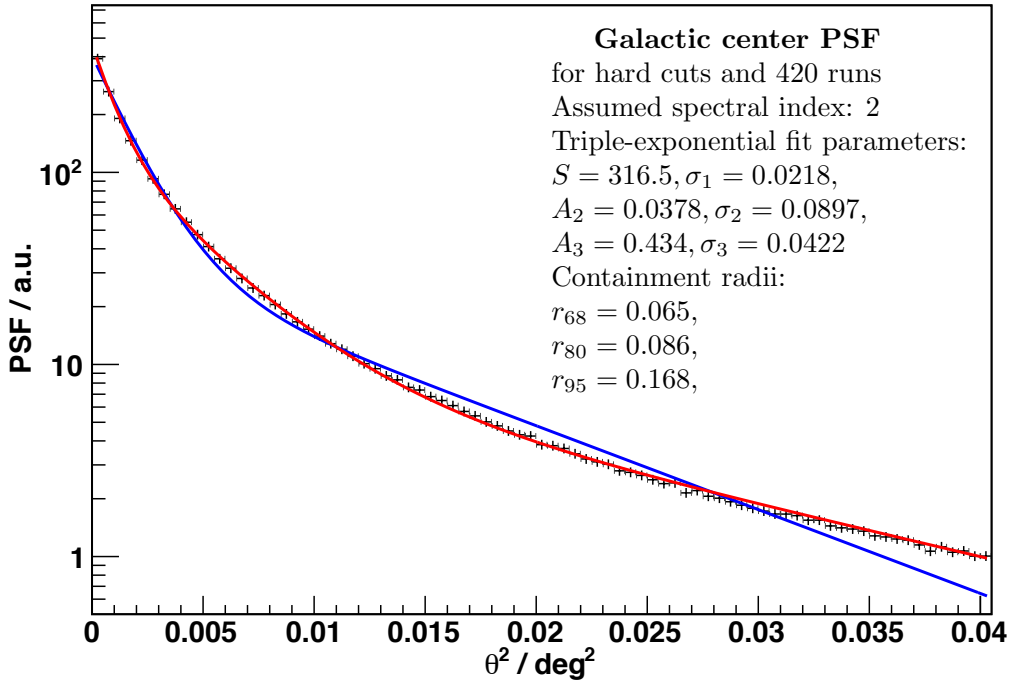

Figure 2.15.. HESS PSF computed for the Galactic center position and assuming a power-law source with spectral index 2 for hard cuts. The triple-Gaussian parameters are given as well as a few selected containment radii (in deg). The black points represent the expected θ^2 photon distribution, the blue and red line the double- and triple-exponential approximation.

θ/σ	Excess	Background	$\frac{\text{Excess}}{\text{Background}}$	Significance	Sensitivity
1.59	71.5	100	100	100	100
1.00	39.3	40	138	87	115
2.00	86.5	159	76	96	104
3.00	98.9	358	39	73	137
1.51	68.0	91	105	100	100
1.79	80.0	128	87	99	101
2.15	90.0	183	69	93	108
3.03	99.0	367	38	72	138

Table 2.4.. Possible choices for the theta cut (in units of Gaussian width σ) for a 2D Gaussian intensity distribution. The resulting containment fraction, background, excess / background, significance and sensitivity (all in %) are listed. See Figure 2.16.

Gaussian, with width

$$\sigma = \sqrt{\sigma^2_{source} + \sigma^2_{PSF}}, \tag{2.23}$$

where the PSF width is approximately $\sigma_{PSF} = 0.06$ deg. Before we describe further how HESS reconstructs spectra, let's first look at how containment fraction, excess / background, significance and sensitivity depend on the chosen aperture radius for a 2D Gaussian intensity distribution of width σ. This is illustrated in Figure 2.16 and Table 2.4, which show that an optimal theta cut (i.e. highest significance) would contain 70% of the emission. Because actually there is no reason to believe that source intensity distributions actually are exactly Gaussian, we have chosen to use a 90% containment angle instead. As shown in the table and figure, the resulting losss in sensitivity is only 8% relative to the optimal theta cut. The advantage is that results are more robust, i.e. depend less on the exact shape of the source morphology.

Computing counts and exposure

The basic principle to make spectra is the same as for maps. For each run counts and exposure are filled in bins—this time bins in energy instead of position—and then summed for all runs.

The background estimation method used is different though. Remember how for maps a background lookup $B(E, zen, off)$ was used to compute acceptance curves for integral energy bands. This lookup was filled from all available 'off runs', i.e. runs that have no or only one point-like source in the FOV (half of the HESS data are AGN observations with exactly one point source in the FOV, which can be cut out for filling the background lookup). The energy-dependence

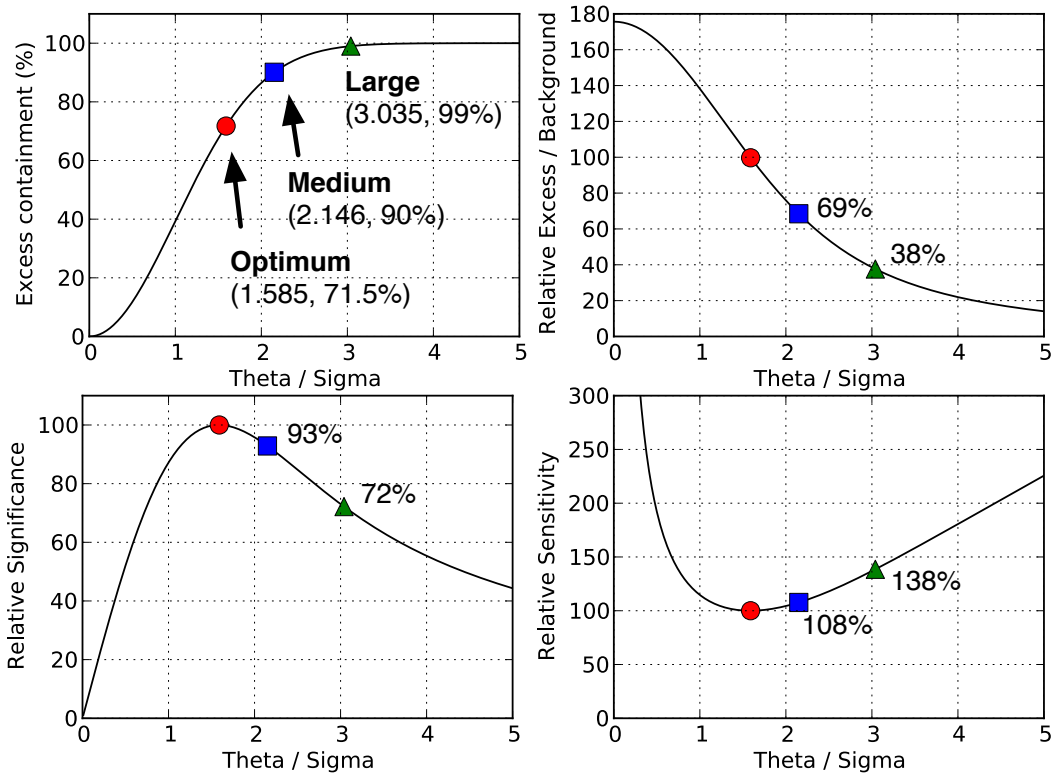

Figure 2.16.. Dependence of containment, excess / background, significance and sensitivity on theta cut (in units of Gaussian width σ) for a 2D Gaussian intensity distribution. Three possible choices are highlighted, further numbers can be found in Table 2.4.

of this background lookup is cosidered to be too unstable to be useful for spectral analysis[5].

Instead the reflected background method is used (illustrated in Figure 2.13), where the background is estimated from off regions, which are obtained by rotating the on region around the observaiton position. This has the advantage that the off regions are at exactly the same offsets as the on region, which is important considering the energy-dependence of the acceptance curves shown in Figure 2.13. Note that e.g. the ring background method samples from smaller and larger offsets than the on-region and for position close to the ψ-cut at 2 deg completely samples from positions at smaller offsets than the on retion.

A binning of 24 bins per decade in log energy is used, which is below the HESS energy, so effectively no information is lost and the likelihood analysis on these fine bins gives results which should match an unbinned analysis (which is currently not implemented in the HESS software, though). The quantities that are filled are on, off, on-exposure, off-exposure and gamma-exposure, where on is the number of counts in the on region, off the number of counts in all off regions, on-exposure = 1 and off-exposure = number of off regions. So in the case of the reflected background method, the computation of the hadron exposures is trivial. The gamma-exposure is filled using Equation 2.17, the same equation that was used for maps.

Fitting and Flux Points

The final spectral result that is published are fitted model parameters and flux points (see Figure 2.17 for an example).

First the model is fit. There are many models implemented in the HESS software, but in this thesis, we only consider the power law

$$F(E) = F_0 \left(\frac{E}{E_0} \right)^{-\Gamma} \tag{2.24}$$

and the exponential cutoff power law

$$F(E) = F_0 \left(\frac{E}{E_0} \right)^{-\Gamma} \exp\left(-\lambda E\right) \tag{2.25}$$

$$\tag{2.26}$$

with cutoff energy $E_{cut} = 1/\lambda$. The reason we chose λ and not E_{cut} as fit parameter is that the latter is unstable, jumping from $-\infty$ to $+\infty$ as the spectrum bends up or down. Also the resulting probability distributions for E_{cut} are highly asymmetric, so it is difficult to quote an error on that parameter.

[5] I suspect that it could be possible to make spectra using background energy spectra from lookups, at least I have not seen an attempt that has failed.

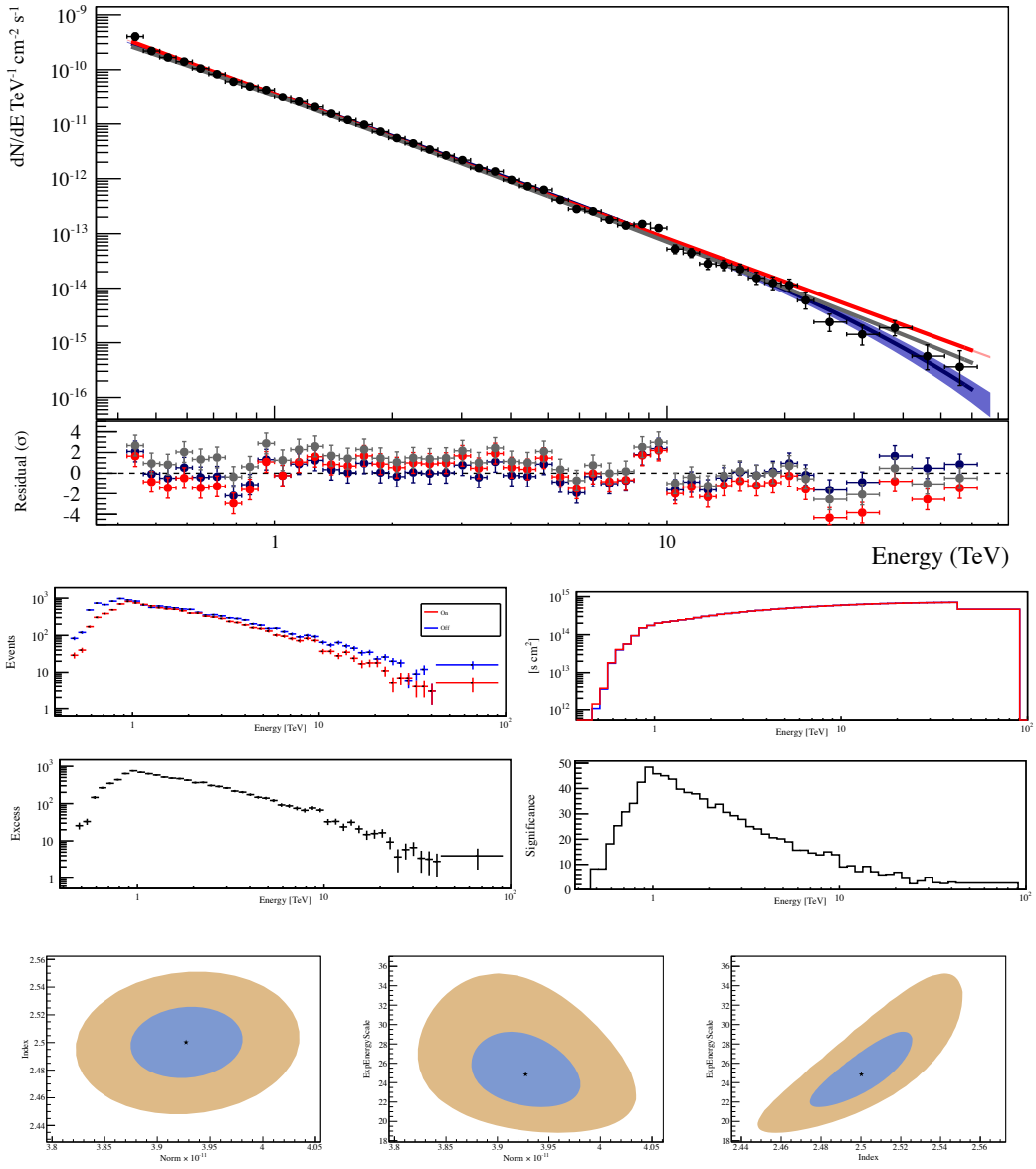

Figure 2.17.. HESS Crab spectrum. The top panel shows flux points as well as the power-law fit in red, exponential cutoff power-law fit in blue and reference Meyer spectrum Meyer et al. (2010) in grey. Residuals of the flux points wrt. each model are shown in units of standard deviations. Below are some of the diagnostic plots we use to assess if the spectrum was computed and fitted correctly.

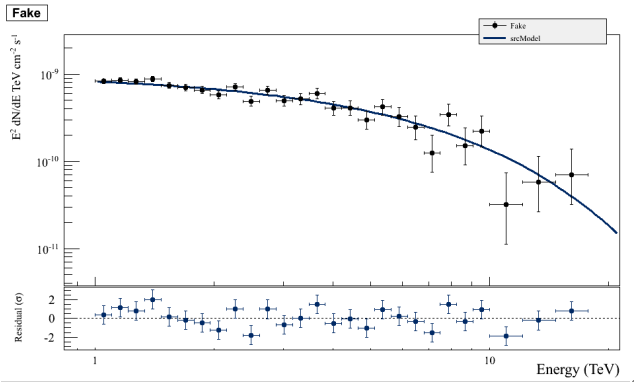

Figure 2.18.. Example of a simulated exponential cutoff spectrum with best-fit solution and computed flux points.

The on-off likelihood Formula 2.14 is used, i.e. option number 2 from Section 2.5 using the MINUIT optimizer James and Roos (1975), which is integrated into the ROOT[6] data analysis framework on which the HESS software is built. Minimization of $-2\log(L)$ is done using MIGRAD, symmetric errors are computed using HESSE via a numerical estimate of the matrix of second derivatives at the minimum and using MINOS using profile likelihood. Likelihood contours for each pair of parameters are computed to visually check that the fit was successful (see Figure 2.17).

For the computation of flux points, as a first step the spectrum was rebinned to achieve at least a Li& Ma significance of 2 per bin. This was done by merging fine bins (i.e. summing counts and expected counts) left to right until no further significant bin was found. Note that this method inherently has problems at the high-energy end, a possible alternative that was investigated is to rebin by at least 5 or 10 on counts. That reduces that bias for flux points at the high-energy end, but has the problem that flux points can become negative, which is hard to explain as a reasonable effect to some people.

Flux point errors are computed using the profile likelihood method.

A 'SpectrumFaker' was implemented to check that for all commonly occuring sets of parameters (e.g. spectral index 1.5 to 4, flux 1 to 100% Crab, cutoff energy 1 to 1000 TeV) the true parameters could be recovered by without significant bias[7] and with correct error coverage. One such simulated spectrum is shown in Figure 2.18.

Finally tests on real data were performed, shown in Figure 2.19. Note how the minimum significance adaptive binning works nicely for all of these cases

[6] `http://root.cern.ch/`

[7] Well, for very high-statistics simulated spectra there was a significant bias, but always well below the systematic errors we typically quote of 20% on flux and 0.2 on spectral index. These biases could be the results of binning errors or a result of the likelihood function used.

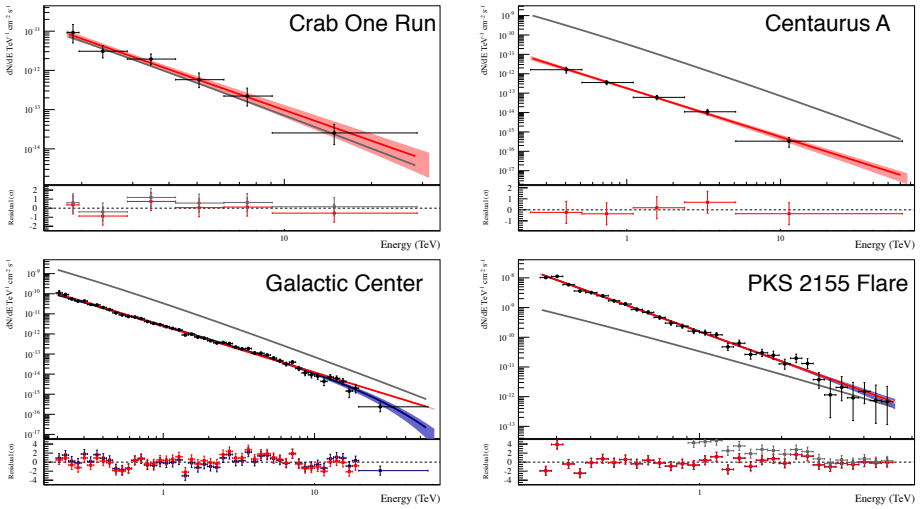

Figure 2.19.. Examples of HESS spectra reconstructed using the new flux module. The one run Crab spectrum is an example of a high signal / background, but low-statistics observation. The Galactic center is an example of a 10% Crab source, Centaurus A an example of a 1% Crab source, the PKS 2155-304 flare spectrum a unique example of a 1000% Crab source. In each case the published spectrum could be reproduced. The Crab Meyer et al. (2010) spectrum is shown as a grey line in each case as a reference. Flux points were adaptively rebinned to 2 sigma per point.

(some rather extreme).

The big advantage of the new flux module (the implementation of which was a significant part of this thesis) is that spectra come out correctly without requiring manual fiddling with energy fit range and binning. This was a requirement for the automatic spectral analysis of all sources in the HESS Galactic plane survey described in Chapter 3. The likelihood fit always uses the full energy range (lowest to highest energy event) and works on fine bins. Flux points are computed after fitting taking the best-fit model into account. Previously first flux points were computed using a problematic weighting method and then a chi^2 fit was performed on these flux points (see e.g.Hoppe (2008) Method A in Section 3.4).

3. The HESS Survey at TeV Energies

As explained in the introduction (1.2), the Galactic TeV emission is the sum of *diffuse emission* from a sea of cosmic rays filling the Milky Way and of *emission from sources*. A source is defined as a cosmic ray accelerator, i.e. is localized both in space and time. The ultimate goal of the HESS survey is to measure this diffuse and source emission and infer the characteristics of individual astrophysical objects and source populations as well as the spatial distribution and spectrum of the diffuse emission.

In this chapter an attempt is presented to construct a catalog of Galactic TeV sources from the HESS Galactic plane survey (HGPS) in a systematic way. This was done once rather at the beginning of the HESS survey Aharonian et al. (2006a) for the region $\pm$ 30 in Galactic longitude, and using 230 h of observation, 17 sources were discovered. Since then all further source discoveries or re-analyses were published in individual papers. In the meantime the HESS survey has expanded to cover the longitude range -110 to 70 deg and 2300 h of observations, resulting in a better sensitivity and the HGPS catalog presented in Section 3.3 and listed in Appendix B contains 62 sources. Such a systematic characterization of the sources is a prerequisite to a possible measurement of the diffuse emission in the future, as the spatial distribution of sources and expected diffuse emission is similar.

As will be shown in this chapter, in practice what can actually be inferred from the HESS survey data is limited by a number of issues, which I would like to briefly mention here before expanding on them in the following sections. I will use the region around the supernova remnant RX J1713.7-3946 shown in Figure 3.1) for illustration.

- First of all the definition of source and diffuse emission is vague. Even though the acceleration site itself is well localized for SNRs and PWNe, the cosmic rays diffuse and or are advected away and can eventually fill an extended halo around the actual source, eventually merging completely into the sea of cosmic rays. It is possible that the emission extending a few degrees to the left and right of RX J1713.7-3946 is the result of cosmic rays diffusing out from the SNR. While this claim has not been made by the HESS collaboration to date, this mechanism was suggested as the one responsible for the Galactic center ridge emission (Aharonian et al., 2006f), with extends about a degree to the left and right of the Galactic center point source HESS J1745-290.

- Another possibility is that the extended emission around RX J1713.7-3946

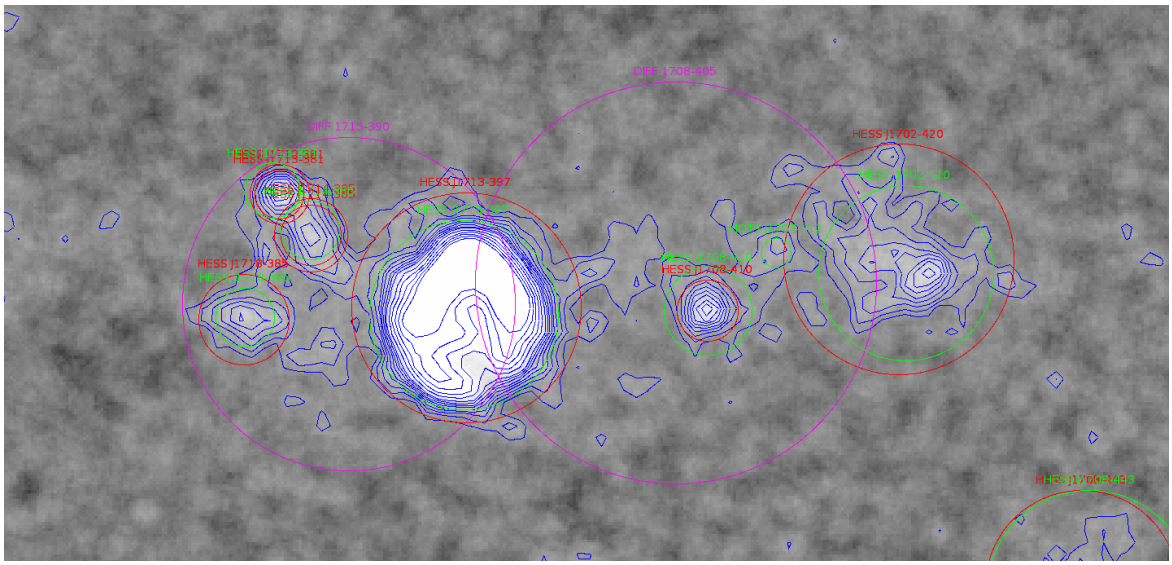

Figure 3.1.. RX J1713.7-3946 (HESS J1713-397) and Westerlund 1 (HESS J1646-458) region in the HESS Galactic plane survey (HGPS). The grayscale shows significance on 0.1 deg correlation scale, with contours at 2 to 20, with spacing 1 below and 2 above 10. HGPS catalog sources are shown in red, a compilation of previous work on the region by the HESS collaboration is represented by the green sources.

and HESS J1745-290 is instead the result of a collection of unrelated cosmic accelerators in those regions, which is possible given the high density of sources in the plane and the relatively poor sensitivity (detection limit at a few % of the flux of the brightest sources present) and angular resolution of ~ 0.1 deg of HESS.

- Another problem is that most Galactic TeV sources are extended and of unknown morphology. This means that there is no 'right way' to make a catalog, but the number of sources and their extensions one finds is heavily influenced by the arbitrary choice of one or a few allowed morphology models. E.g. consider the two sources HESS J1713-381 and HESS J1714-385, likely corresponding to the CTB 37 B / G348.7+0.3 and CTB 37 A / G348.5+0.1 SNRs. One could try to model these sources as points, disks, Gaussians, shells or even use the radio or X-ray emission as a template for the HESS emission. For isolated sources it is easily possible to fit a handful of different models and discuss their relative likelihoods. For crowded regions of overlapping sources the number of possible combinations quickly becomes excessive as more complicated models are allowed. Even only allowing for elongated Gaussians there are many cases where it is possible to model the emission as either one very elongated Gaussian or as two more or less round Gaussians, with 'the better choice' depending on the exact criteria and thresholds used or even on the small difference in energy band between hard and standard cuts.
  HESS J1702-420 (possibly the PWN of PSR J1702-4128) is an example of a source with an extended halo component and a much smaller core emission region inside. Although it is from a statistical point much preferred to model the emission as two sources, there is no reason to believe that there are two cosmic accelerators or even acceleration regions. Core / halo structures are observed even much more clearly for the bright PWNe HESS J1825-137 and HESS J1303-631.

- Finally one has to note that there there are limitations arising from the HESS observation strategy and analysis techniques. Flux is measured as excess over a quite high background, which is modelled for each observation individually. The net result is that diffuse emission on scales larger than the FOV (2 deg radius) is simply attributed to this background and cannot be measured using the standard techniques. For degree-scale extended emission it is unclear what fraction is substracted, so possibly the extended emission we see in the RX J1713.7-3946 region is actually brighter than shown in Figure 3.1.
  Another limitation is that currently it is only possible to measure spectra using aperture photometry. In many cases it is not possible to choose an aperture which according to the fitted morphological model would cover

say 90% of the emission, e.g. because there are other bright nearby sources or because that aperture would be so large that background estimation for the spectrum becomes impossible. So one is required to choose smaller apertures, knowing that they only contain part of the flux from the source. Correcting for the fraction outside the aperture is problematic also e.g. for core / halo sources like HESS J1702-420.

The catalog presented in this thesis is a first attempt, which can serve as the basis for starting discussions on how to construct the HESS Galactic plane survey catalog that is eventually going to be published. Note that the catalog in any case only represents one possible choice to roughly describe the emission. The other important product that will also be released are the survey maps, described in Section 3.2 and shown in appendix A.

3.1. Data Set

In this section we describe the characteristics of the HESS Galactic plane survey dataset used in this thesis. As described in the last chapter, HESS takes pointed observations with a field of view (FOV) of approximately 2 deg radius and a duration of about 28 minutes. Each run is calibrated and analyzed individually, and only at the very end are the run-wise exposures and counts and background estimates summed to obtain a survey map.

Observation Strategy

The full HESS dataset available at this time contains 12,130 good-quality runs covering the time period January 2004 to August 2011 (First run 18136, last run 66335)[1]. The GPS survey maps described later cover the range GLON = -113 to +75 and GLAT = -4 to 4 and contain 5,301 of the runs. This is illustrated in Figure 3.2, which shows the observation position of each run as a colored circle, with color representing the mean zenith angle of the run[2]. It can be seen that the survey data consists of systematic scan observations at a grid of longitudes and latitudes, as well as individual target observations. These targeted observations are typically carried out using a so-called wobble pattern, where the observation positions are shifted with respect to the known or suspected target location by offsets in Right Ascension (RA) and Declination (DEC) by typically 0.5 or 0.7 deg, in the case of large sources sometimes more. The reason for wobbling is that the only reliable method to derive a spectrum is the

[1] Runs are not always numbered consecutively and there are many calibration runs in addition to the observation runs we are considering here).

[2] The zenith angle varies during a run as the telescopes track a fixed observing position on the sky and the earth rotates. Typically observations take place at culmination, so actually zenith angle variations are not very large.

reflected background method, which requires that the region used to measure the spectrum not contain the pointing position.

In the 7.6 years of HESS observations considered here, 5175 hours of good-quality data was collected, 44% of which was spent on the HESS Galactic plane survey region. Figure 3.3 shows the latitude distribution of the livetime for the GPS region, split by scan and source observations.[3]

Here is a brief history of how the scan observations progressed over the years starting in the inner Galaxy, going outwards (see top panel of Figure 3.2):

2004 GLON = -30 to +30, at GLAT = -1, 0 and +1

2005 GLON = -30 to -62, at GLAT = -0.7 and +0.7

2006 GLON = -62 to -70, at GLAT = -1.8, -0.8 and +0.2, as well as GLON = +30 to +60, at GLAT = -0.7 and +0.7, in the range GLON = +40 to +50 instead at GLAT = -1 and +0.4

2007 GLON = -75 to -93, at GLAT = -1.8, -0.8 and +0.2

2008 GLON = +60 to +70, at GLAT = -0.7 and +0.7, as well as GLON = -97 to -110, at GLAT = -1.5, -0.5 and 0.5

2009 GLON = -5 to +5, at GLAT = -3.5 and +3.5, as well as GLON = +38 to +48, at GLAT = -3.5 and +3.0.

After that, in 2010 and 2011, time was mostly devoted to filling up exposure gaps in the already observed regions. Also a larger fraction of the observing time was devoted to individual targets, which is natural given the fact that it takes much more time to detect a faint source (sensitivity $\propto$ (observation time)$^{-1/2}$) and the deeper the survey becomes, the fainter the sources are on average.

The high-latitude extensions of the survey in 2009 were unsuccessful in the sense that they did not result in the detection of a new source, but they might prove valuable in the future both to constrain a possible high-latitude source population and to understand possibly systematic problems in the HESS background estimation methods resulting from the bright starlight in the Galactic plane and the need to exclude most of the Galactic plane for background estimation because of the high source density.

Non-uniform energy threshold

Another interesting point to note about the GPS data set, illustrated in Figure 3.2, is that the smallest possible observation zenith angle varies from 0 deg in the inner Galaxy to 45 deg at GLON = 60 deg and 40 deg at -60 deg. Small

[3] Runs within 0.0005 deg of GLAT = $0, \pm 0.1, \pm 0.2, \pm 0.3, \ldots$ were classified as scan observations, which probably means that 5 to 10% of the runs classified as scan runs here were actually targeted at a particular source.

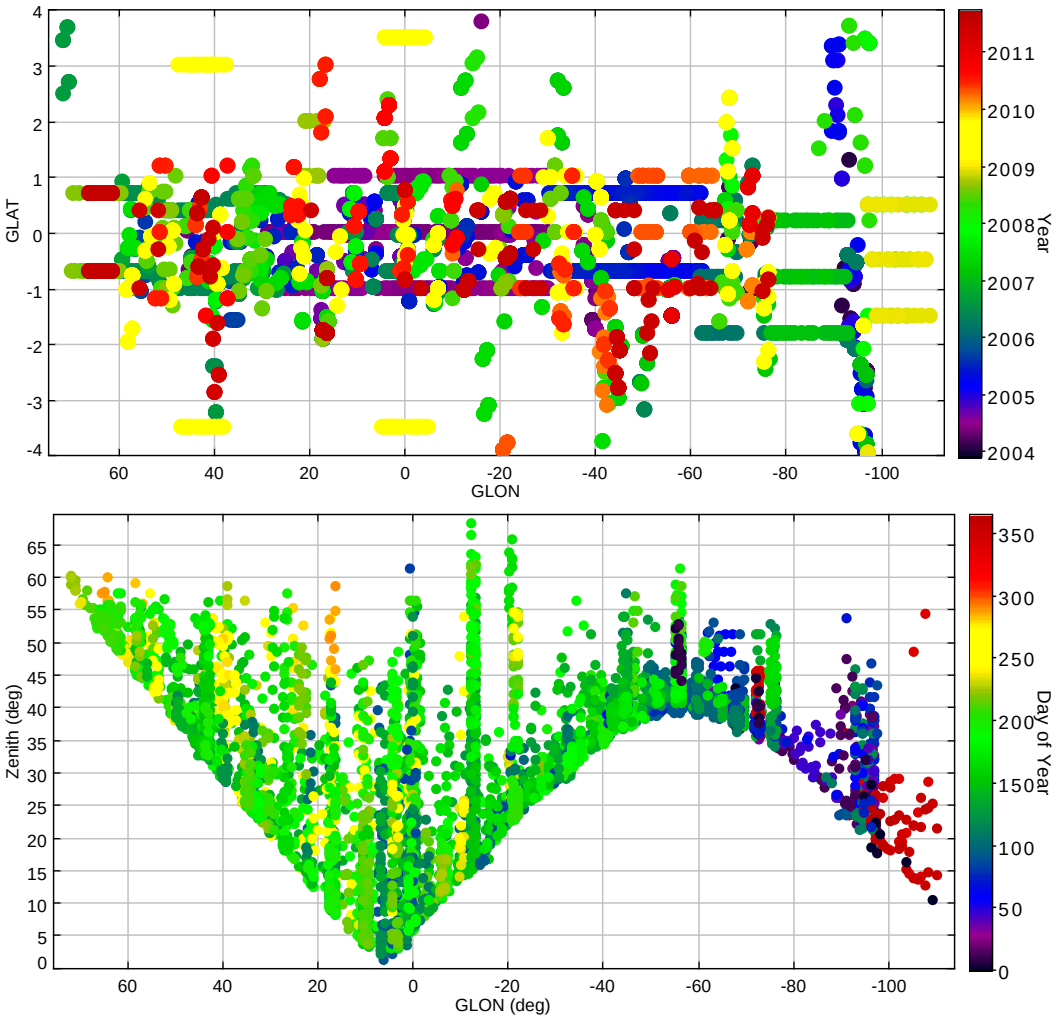

Figure 3.2.. HESS GPS observation runs (most with a duration of 28 minutes). The top panel shows the observation center in Galactic coordinates, with color representing the year the data was taken. The scan observations are clearly visible as lines of pointings at fixed latitudes. The bottom panel shows the zenith angle for each observation as a function of longitude. The sharp minimum line corresponds to the minimum zenith angle with which the given position on the Galactic plane can be observed from the HESS site. This minimum zenith angle is only available at a given time of the year, which is shown by the color scale. See main text for further explanations.

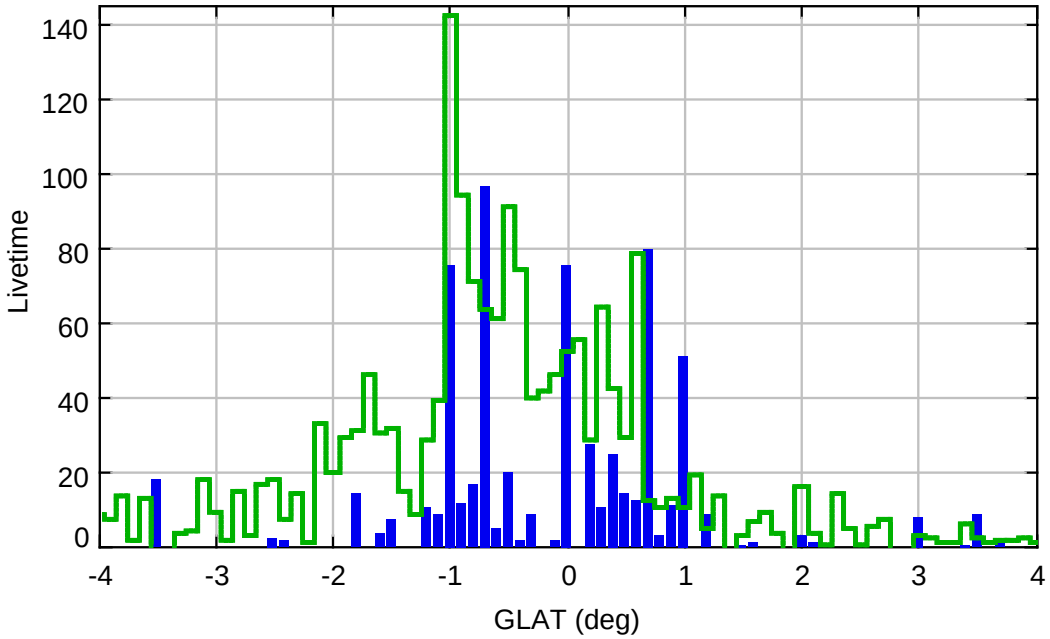

Figure 3.3.. HESS observation position GLAT distribution. Runs have been binned by 0.1 deg (with the center of the middle bin at GLAT = 0) and weighted by run livetime. Scan observations are shown in blue, individual source observations in green. As could already be seen in the top panel of Figure 3.2, most of the scan observations took place at $GLAT = 0, \pm 0.7, \pm 1.0$. Note that the distribution is not centered on zero, but most of the observations were centered on negative latitudes to match the gas distribution and thus expected source population of the Milky Way.

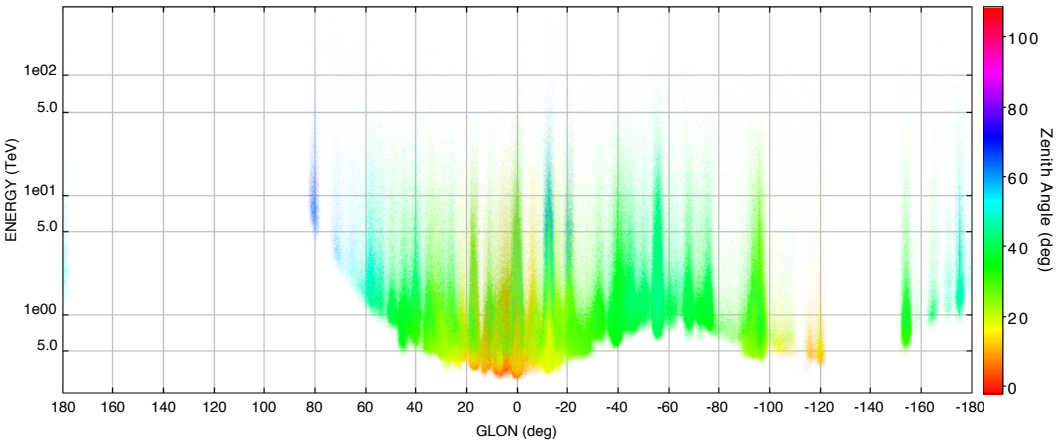

Figure 3.4.. HESS event energy distribution after hard cuts as a function of Galactic longitude for all HESS data with GLAT = -10 to 10 deg. Note how the energy threshold matches the zenith angle distribution shown in the bottom panel of Figure 3.3, as described in the main text. Note that only a very small fraction of these events are actually gammas. It can be seen that high-zenith-angle observations were used to extend the spectrum of RX J1713.7-3946 to 100 TeV Aharonian et al. (2007).

zenith-angle observations are in general preferable, as they provide a lower energy threshold and better sensitivity. For a few sources, like e.g. the Galactic center source HESS J1745-290 and the SNR RX J1713.7-3946 at GLON = -12 deg, intentionally high-zenith-angle observations were performed to extend the spectrum to very high energies, as the effective area at high energies increases with zenith angle.

The net result is that the HESS survey maps (and spectra of individual sources) have an energy threshold that varies from approximately 0.2 / 0.4 TeV for std / hard cuts in the inner Galaxy to 0.7 / 1.1 TeV at GLON = 60 deg (see Figure 3.4). At high longitudes the HESS survey effectively runs into a sensitivity barrier, where even with a lot of investment in terms of observation time good sensitivity (expept possibly for extremely hard sources) cannot be achieved. This precludes e.g. HESS observations of the Cygnus region at GLON = 65 to 85, where several sources as well as diffuse emission have been reported by Fermi and Milagro Abdo et al. (2008). In 2007 VERITAS has started a survey of that region and has started to discover sources (Weinstein and for the VERITAS Collaboration, 2009).

On the other side, the worst zenith angle occurs around -60 deg, where the two prominent HESS sources HESS J1303-631 (a PWN with energy-dependent morphology) and HESS J1302-638 (an binary system containing PSR B1259-63 with variable TeV emission) are located. Nevertheless HESS has decided

to survey that region from the inner Galaxy outwards, because although the outer Galaxy could be observed at higher sensitivity for a given investment in observation time, also the expected density of sources there is lower. In addition one has to note that the good zenith angles beyond -60 deg (e.g. containing the Vela region at GLON = -95 deg) occur in winter, where due to the rainy season in Namibia much less observation time is available than in summer (see color scale in the bottom panel of Figure 3.2)

Data Quality

Data quality is an important issue, because e.g. compared to the Fermi (see Chapter 4) the HESS data is much more inhomogeneous. The main issues are unstable hardware and atmospheric conditions. Some quality selection criteria are applied per telescope, some for the array as a whole. A number of parameters characterizing the detector and atmosphere stability are chosen and cuts are made to select good / bad quality data. The result of data quality selection is a bitpattern for each run, representing a pass / fail for each telescope. In this thesis only runs with at least 3 good-quality telescopes are considered. In some cases the fourth telescope didn't participate in data taking in the first place (e.g. because some component was broken or mirrors were being recoated), in other cases one telescope didn't pass one of the telescope-wise data quality cuts (e.g. the number of broken pixels was too high). The number of good-quality two-telescope runs is very small (a few %) and their performance is much worse than 3- or 4-telescope runs, adding them would bring more problems than exposure.

Here is a list of the most important cuts (there are additional cuts that are only needed in addition to the ones listed here in a few special cases):

- The run duration has to be at least 10 minutes.
  Typically runs last 28 minutes as scheduled, but sometimes the shift crew noticed a problem such as an incorrectly configured array withing the first few minutes and aborted the run. 99% of the runs longer than 10 minutes actually have a duration of 28 ± 1 minute.

- The tracking, as recorded by position encoder on the telescope axis, must match the nominal pointing position within 1 arcminute. In addition the RMS of the tracking position must be less than 10 arcseconds. This ensures that the pointing position was stable within 10 arcseconds, but allows for a constant, known offset for the whole run, which can be corrected for in data analysis.

- The number of broken pixels in each camera (there are 960 pixels per camera) must be smaller than 120. The term 'broken pixel' is simply used to mean inactive, it could actually be broken e.g. because of faulty electronics, or it could have been turned off because based on the pointing

position it was determined that it contained a bright star and could not have measured Cherenkov light.

- The participation fraction of each telescope to system triggers must be at least 32.5% or 40%, depending on the zenith angle.

- The system trigger rate must be stable, i.e. the rate at the end of the run must be within 30% of the rate at the beginning of the run, and the RMS must be smaller than 10%. This cut removes runs where clouds pass the line of sight of the telescopes.

- The sytem trigger rate must be larger than 80% of the expected trigger rate. This cut removes runs where the atmosphere contained significant amounts of dust or water vapour and was much less transparent than usual.

One has to note that the system trigger rate cuts are absolutely essential, because HESS is not monitoring the atmospheric transparency (there are experimental attempts using LIDARs or an optical telescope). Since the reconstructed event energy is approximately proportional to the number of detected photoelectrons, a hazy atmosphere would mean an underestimation of the energy of each event. Given that gamma-ray spectra are power laws, this corresponds to a shift of the whole spectrum to lower energies, equivalent with an underestimation in flux level. Unless there is a cutoff in the spectrum, in which case the shift to lower energy is not equivalent to a shift to lower fluxes.

The system trigger rate evolution in time for the HESS array is shown in Figure 3.5. It is basically the result of the stable cosmic ray background flux, modified by the zenith angle (changing air mass and distance to the shower), atmospheric transparency and optical efficiency of the telescope mirror and camera. The zenith angle is known and the optical efficiency can be measured with atmospheric muons Bolz (2004), and from those two quantities the expected trigger rate is computed for each run. One finds a distribution of actual over expected rate centered on 100% with width of about 10%, with a tail of runs with low trigger rate. The width of 10% is mainly the result of variations in the atmosphere, and to a smaller extent errors in the measurement of the optical efficiency and represents a lower limit on the systematic error on flux measurements that can be achieved with HESS.

Note that in the analysis we do correct for the rate variation in the background estimation (by adjusting the background level to the observed number of events outside exclusion regions for each run), but we do not correct for the rate variations in the gamma-ray exposure, although that would in principle be possible (after correcting for the different spectral indices of the background and gamma rays). Instead a hard cut at 80% measured over expected rate is applied, leaving some bias (up to 20%) flux underestimation for a few % of the runs.

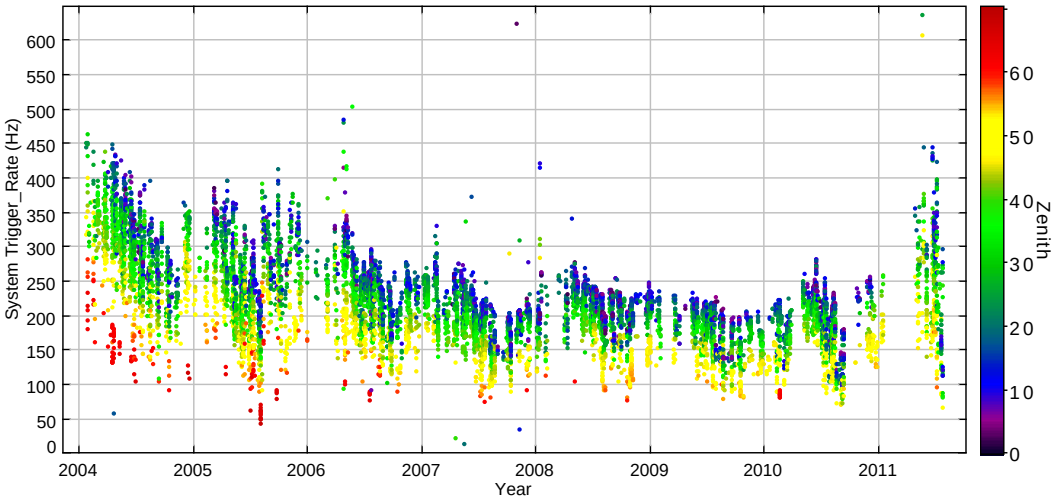

Figure 3.5.. HESS trigger rate evolution over time (4-tel runs only). The expected trigger rate decrease with increasing zenith angle as well as with decreasing optical efficiency due to mirror degradation over the years is clearly visible. The large gap in early 2011 corresponds to a particularly long rainy season at the HESS site, more pronounced than in previous years. The increase in trigger rate in 2011 is the result of several telescopes having recoated mirrors.

3.2. Maps

As described in the last section, the HESS survey is the result of 5,301 individual observations with FOV radius 2 deg collected over a period of 7.6 years with a detector of varying energy threshold, effective area, PSF etc. In this section we describe how to combine these runs into survey maps that can be used to assess the significance and morphology (and to a certain extent the flux) of every source without having to go back to the individual run data.

Individual Run Processing and Combination into Survey Maps

Runwise maps are centered on the closest position in an 0.1 deg grid in GLAT / GLON, which makes it possible to combine them later on without having to resample pixel content into a survey map. The second fact that makes this possible is that the HESS software uses maps (called 'SkyHist') that are in a special Cartesian (CAR) projection Calabretta and Greisen (2002), where the reference point for the pixel to world transformation is put at GLAT = 0, even if the map is located at higher latitudes. This has the effect that map and pixel boundaries exactly correspond to lines of constant GLON / GLAT. So to combine runwise maps into a survey map, first an empty (all values zero) survey map is constructed (currently for the range GLON = -113 to +75 and GLAT = -4 to 4) and then each run-wise map is added to it taking the integer pixel offset into account.

For speed about 70 computer cores are used in parallel, a number limited by two factors. One limitation is the speed with which the event lists can be read from disk. One run of HESS data contains approximately 360,000 events (215 Hz average trigger rate times 28 minutes run duration) and uses approximately 200 MB of disk space. One run takes about 5 minutes to process (the most CPU-intensive part is the gamma-exposure computation), which means that data is read at a rate of 'only' (70 x 200 MB) / (5 x 60 sec) = 50 MB / sec, without causing a problem for our cluster Lustre file system. The second bottleneck is the HESS MySQL database, which is queried multiple times per run in an inefficient manner to determine the muon efficiency coefficients of that run or the closest one where this information is available. Both of these bottlenecks could be removed, the muon coefficients could be stored in the DST file and the DST size can be reduced to 1% by applying std / hard cuts (leaving only 640 / 2680 gamma-ray like events per run on average) once to produce MiniDSTs.

The ~ 5000 runs are processed in bunches of 25 runs per HAP job, resulting in 200 output files containing 25 small run-wise maps. The merging into one survey map is actually done in two steps, by first making a full (mostly empty) survey map containing the 25 runs for each HAP output file, and then finally summing these 200 survey maps into one survey map. Finally for this survey map correlated excess, flux, upper limit, significance etc. maps are computed and converted to FITS format, which is used for all further analysis.

In total it takes about five hours to produce one HESS survey map, a full set of maps (std / hard cuts and 0.1 / 0.22 / 0.4 deg correlation radii) takes a day. In the beginning many survey maps were produced to study the different background estimation methods and ways to make exclusion regions, now that we have found good parameters we produce survey maps less often and these computation requirements are less of an issue.

A binning of 0.02 deg is used, which is well below the PSF resolution and effectively only a negligible amount of information is lost wrt. an unbinned analysis. The maximum event offset used (typically called the 'psi cut') is 2 deg to limit systematic uncertainties in the background estimation and effective area known to be present at large offsets The runwise maps have a half-width of 2.5 deg to fully contain the psi cut. The adaptive ring background method with the constant inner radius option, a stepsize of 0.02 deg and a maximum radius of 1.7 deg is used, otherwise the ring parameters are for the three correlation radii are given in Figure 3.7.

Exclusion Regions and Adaptive Ring Background

Traditionally exclusion regions were a list of circles, maintained by hand and with new ones added from time to time where someone thought a source was. The radius of these exclusion circles was chosen for each source somewhat arbitrarily, probably such that the circle covered some contour level on a survey significance map.

For the survey with its high density of sources along the Galactic plane, and automatic method to generate an exclusion mask has been implemented, i.e. a binary image with zero representing excluded pixels (so that one can simply multiply a given image with the exclusion mask to apply the exclusion region). The use of these exclusion masks has also been implemented into the HESS analysis software as the 'BooleanMap' class, which is a subclass of the 'Region' class. Exclusion masks are used both for maps and for spectral analysis.

The algorithm used to produce exclusion masks is:

1. Produce six survey significance maps using std and hard cuts and correlation radii 0.1, 0.22 and 0.4 deg.

2. Threshold and dilate all significance maps.

3. Combine (at least some of) the resulting masks by multiplying them.

4. Iterate steps 1 to 3 a few times until the resulting exclusion mask is stable, i.e. no longer changes from one iteration to the next.

Actually we have produced three exclusion masks—called small, standard and large—using the parameters given in Table 3.1 and shown in Figure A.5. If the exclusion region is chosen too small, significance and fluxes of sources

Name	Threshold	Dilation	Cuts	Scales	Area
Small	5	0.1	std, hard	0.1, 0.22	79
Medium	5	0.3	std, hard	0.1, 0.22	134
Large	5	0.3	std, hard	0.1, 0.22, 0.4	175

Table 3.1.. Exclusion regions used for the HESS survey region. For comparison, the area of the 'tratitional' exclusion regions used before have a total area of 66 deg. See Figure A.5.

will be underestimated because the off regions will contain gamma-ray emission. If the exclusion region is chosen too large, no background estimate and thus no significance and flux measurement will be possible at all for the biggest sources like Vela Jnr, HESS J1825-137 or Westerlund 1. A compromise has to be made. The reason to combine different cuts and correlation radii is that one actually needs to exclude hard- and soft-spectrum sources as well as small and big sources.

Dilation is a standard image processing technique to grow masks, where any pixel within the dilation radius of a pixel excluded after thresholding is also excluded[4]. The idea is that many HESS sources are center-filled, i.e. brightest in the center, with the surface brightness gradually decreasing outwards. This means that for any chosen threshold larger than zero, there will be some emission outside the thresholded mask and dilating is a way to also exclude that emission.

One question is which exclusion regions to use for the first iteration and when to stop the iteration. It turns out that even starting with no exclusion regions at all, after three interations one finds masks that are close to the final ones. Further iterations tend to grow existing regions by a few %, we never did more than four iterations (due to the cost of making survey maps), but believe that A) our masks are almost independent of the exclusion regions used for the first iteration and B) are only a few % different (smaller in most regions) from the stable solution one would reach after many more iterations.

I want to note that there is no particular reason why thresholding and dilating significance maps using the parameters from Table 3.1 should yield optimal results. We also discussed thresholding other maps, like e.g. excess or excess / background or excess / sqrt(background) and other thresholds and ways to dilate. E.g. one could dilate by a radius proportional to the correlation radius used to make the significance map or by a radius proportional to the size of the current segment (or even size of a fitted source model).

For a measurement of the diffuse emission with HESS, exclusion regions certainly have to be studied in more detail, however for all but the largest sources we believe that the regions we currently have are big enough. One argument is

[4] http://en.wikipedia.org/wiki/Dilation_(morphology)

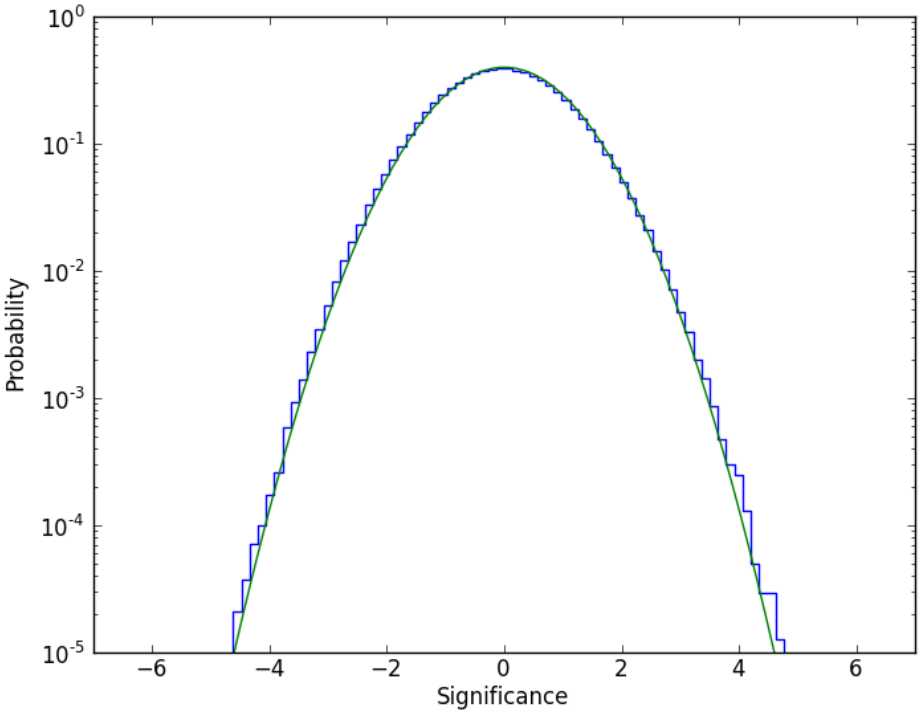

Figure 3.6.. HESS Galactic plane survey excluded significance distribution (hard cuts, 0.1 deg correlation radius). The minimum is -4.7, the maximum +4.8. Clearly no significant sources are present outside the exclusion regions.

that the excluded significance distribution, shown in Figure 3.6 looks clean, another argument is that the difference in excess between the small and standard exclusion regions for sources is only 10% (see Figure 3.8).

Overall the new automatic exclusion regions and the adaptive ring background method lead to a a big improvement over previous survey maps, which always had holes at the locations of the biggest sources and in general showed stripes of on average negative significance and excess below and above the Galactic plane, because emission in the plane hadn't been excluded and thus the background below and above the plane overestimated with the ring method.

Sensitivity and Survey Region

The HESS survey is very inhomogeneous, because the livetime, mean zenith angle and mean offset vary strongly. As a result, also the exposure, background, sensitivity and PSF vary. In this section and the next one, I want to give an impression of how strong these variations are and also give some summary

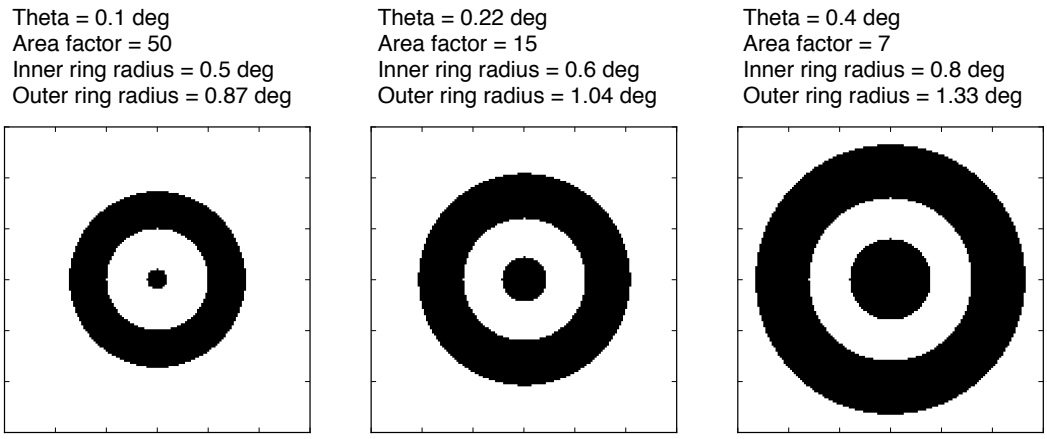

Figure 3.7.. Illustration of the three correlation circles and rings used for the survey maps. Ideally one wants a thick ring, so that background fluctuations will be negligible (area factor > 10) and ring width > 2 x theta such that the correlation length in the significance map and thus the number of trial factors is not limited by the background estimation. This can easily be achieved for the small scales, but for 0.4 the ring would have to be very large, leading to systematic errors, so a compromise was chosen.

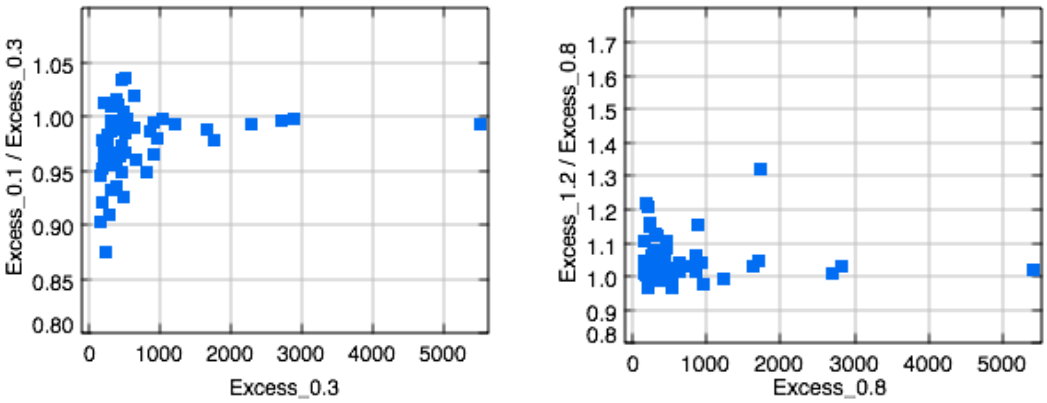

Figure 3.8.. HESS systematic errors on the excess (hard cuts, 0.22 deg correlation) of all sources in the GPS with significance > 5. *Left:* Reducing the exclusion region dilation scale from 0.3 to 0.1 deg can lead to some contamination of the off region by sources and thus an excess underestimate of up to 10%. *Right:* The excess measured using inner ring radius of 0.8 to 1.2 degree differs by up to 20%. The outlier at 30% difference is HESS J1825-137.

statistics for the whole survey like excess and background levels for std and hard cuts.

First of all we need to define the survey region is. Currently the survey maps we produce cover the region GLON = -113 to +75 and GLAT = -4 to 4, but there is quite some area at the edge where we actually haven't surveyed the Galaxy at all, so quoting that would be misleading. A better possibility is to define a mask that exactly describes the region we have surveyed according to some criterion. A simple choice would be to define the survey region as those pixels with a non-zero exposure. That would mean however that at the upper and lower edge there are some regions covered by only one run at large offset and very few detected counts for the 0.1 deg correlation. Actually since we only use the Li& Ma formula for at least 5 on counts, for those very low-exposure regions we can't even to compute a significance or the sensitivity we reach. In addition at the left edge, around GLON = 70, we have quite a few runs, but all at very high zenith angle, and thus very bad point source sensitivity of 10 to 100% Crab.

The method chosen here was to define the survey region as the pixels with point-source sensitivity 10% Crab or better. More precisely, a power-law spectrum with index 2.5 was assumed in the computation of the sensitivity map (described below) and the threshold was chosen at 2.26×10^{-12} cm^{-2} s^{-1} above 1 TeV (using all events after hard cuts, also the ones below 1 TeV). Because actual measured background is used to compute sensitivity the sensitivity map has statistical fluctuations and a hard threshold results in ragged edges with both isolated small segments outside the main region below 10% Crab and isolated small segments inside the main region above 10% Crab. To get a well-defined smooth contour, an opening operation[5] was applied with a radius of 0.5 deg, which is a standard image processing technique to remove noisy edges from masks.

This has the desired effect of removing the single-run exposure regions on the top and bottom of the map as well as the low-sensitivity region (with quite high exposure, but also high background) an the left side.

3.3. Catalog

The catalog was produced in two steps:

1. Morphology fit
2. Spectral analysis

The morphology fit was performed as described Section 2.7. The GPS was split up in 31 ROIs containing 1 to 9 sources in such a way that there were clear

[5] Opening is a dilation followed by an erosion. See `http://en.wikipedia.org/wiki/Opening_(morphology)`

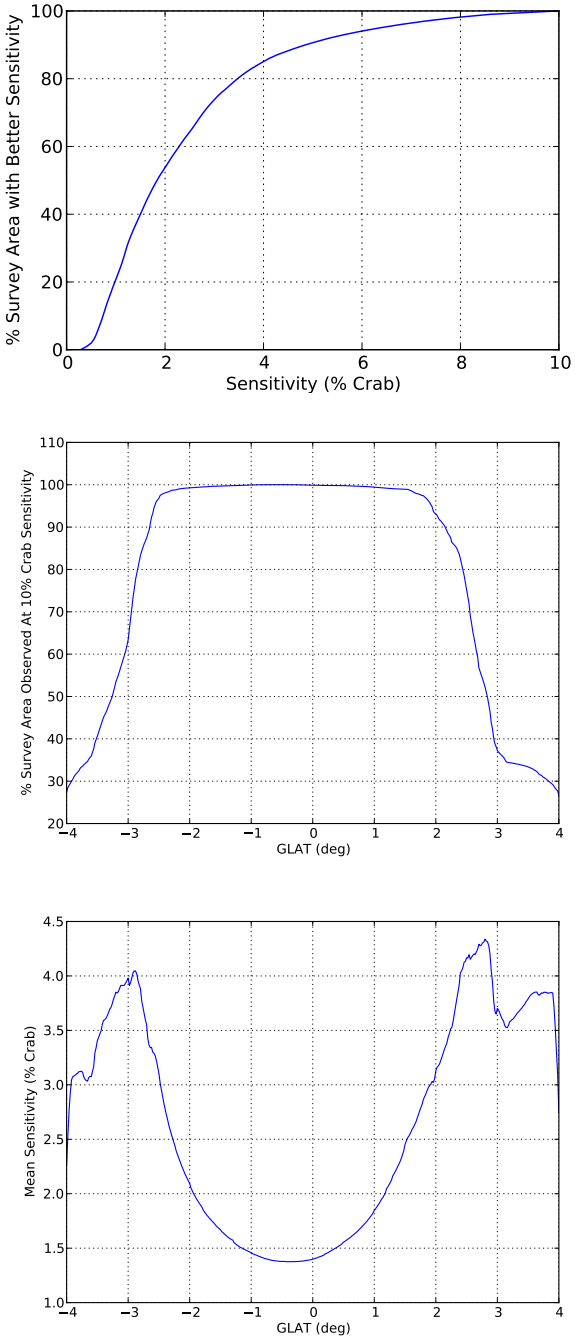

Figure 3.9.. HESS sensitivity latitude profiles. The top panel shows that the sensitivity varies by about an order of magnitude across the survey region. The bottom panel shows that the sensitivity rapidly decreases outside b = -2.5 .. 2, because most observations took place at latitudes b = -1.5 .. 1 (see Figure 3.3) and the FOV has a radius on 'only' 2 deg.

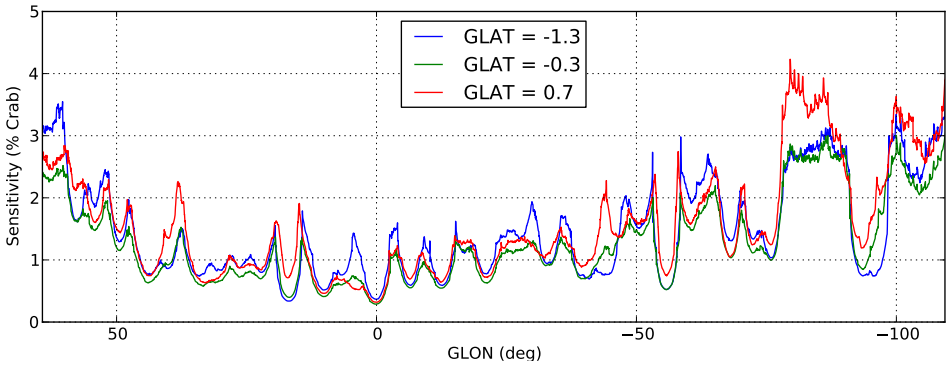

Figure 3.10.. HESS sensitivity longitude profiles. As could already be seen in Figure 3.9, top, the sensitivity varies by about an order of magnitude (0.3 to 3% Crab).

Pre → Post				Post → Pre			
S_{pre}	P_{pre}	P_{post}	S_{post}	S_{post}	P_{post}	P_{pre}	S_{pre}
5.0	2.9e-07	0.54	-0.1	0.0	0.5	2.6e-07	5.0
5.5	1.9e-08	0.05	1.6	1.0	0.16	6.4e-08	5.3
6.0	9.9e-10	0.0027	2.8	2.0	0.023	8.5e-09	5.6
6.5	4.0e-11	0.00011	3.7	3.0	0.0013	5.0e-10	6.1
7.0	1.3e-12	3.5e-06	4.5	4.0	3.2e-05	1.2e-11	6.7
7.5	3.2e-14	8.6e-08	5.2	5.0	2.9e-07	1.1e-13	7.3
8.0	6.2e-16	1.7e-09	5.9	6.0	9.9e-10	3.3e-16	8.1

Table 3.2.. Conversion table pre $\longleftrightarrow$ post significances and probabilities for the HESS survey with currently $2.7 \cdot 10^6$ trials.

gaps of zero emission between the ROIs. So effectively the resulting catalog would be that same if all sources were fit simultaneously.

The morphology fitting is not completely automatic. This turned out to not be possible because for the fits to converge reasonable starting values for position, amplitude and size for each source had to be set.

For each ROI a number of solutions (in some cases 10 different attempts) were made to model the emission and then one 'best' solution was chosen in each case. Typically sources were added one by one, until the global TS no longer increased by 36. The criteria for picking the 'best' solution are not well-defined yet, but roughly are as follows:

1. The global TS must be 36 higher than the highst-TS solution with one source less.

2. Each source must have a TS of 36 (this was always fulfilled)

3. Sources inside other sources were not allowed, i.e. core and halo components were not modelled as two sources, even if highly significant as e.g. for HESS J1825-137 or HESS J1303-631.

4. Six 'diffuse' sources were added to model very strong, very extended emission in some ROIs. This was necessary in order to get converget fits on the smaller sources at all.

5. If two sources were so close to each other that their contour on the model significance map did not show a dip, they were not modelled as two sources, even if the TS increase would have been > 36.

Figure 3.11 shows one of the 31 regions of interest (ROIs) defined to fit the morphology and establish the significance of the sources in the HESS survey. Note that this is a special case, because one bright source known to not have Gaussian morphology, RX J1713.7-3946, was cut out in order to get better estimates on its neighbouring sources.

Also HESS J1708-443, being well-separated from this group of sources, was cut out and fit separately in its own ROI. The reason for doing this is that with seven sources and four free parameters for each (GLON, GLAT, Sigma, Amplitude), the fit has already 28 free parameters and is already quite slow (about a minute to estimate all parameters and errors for well-chosen starting values).

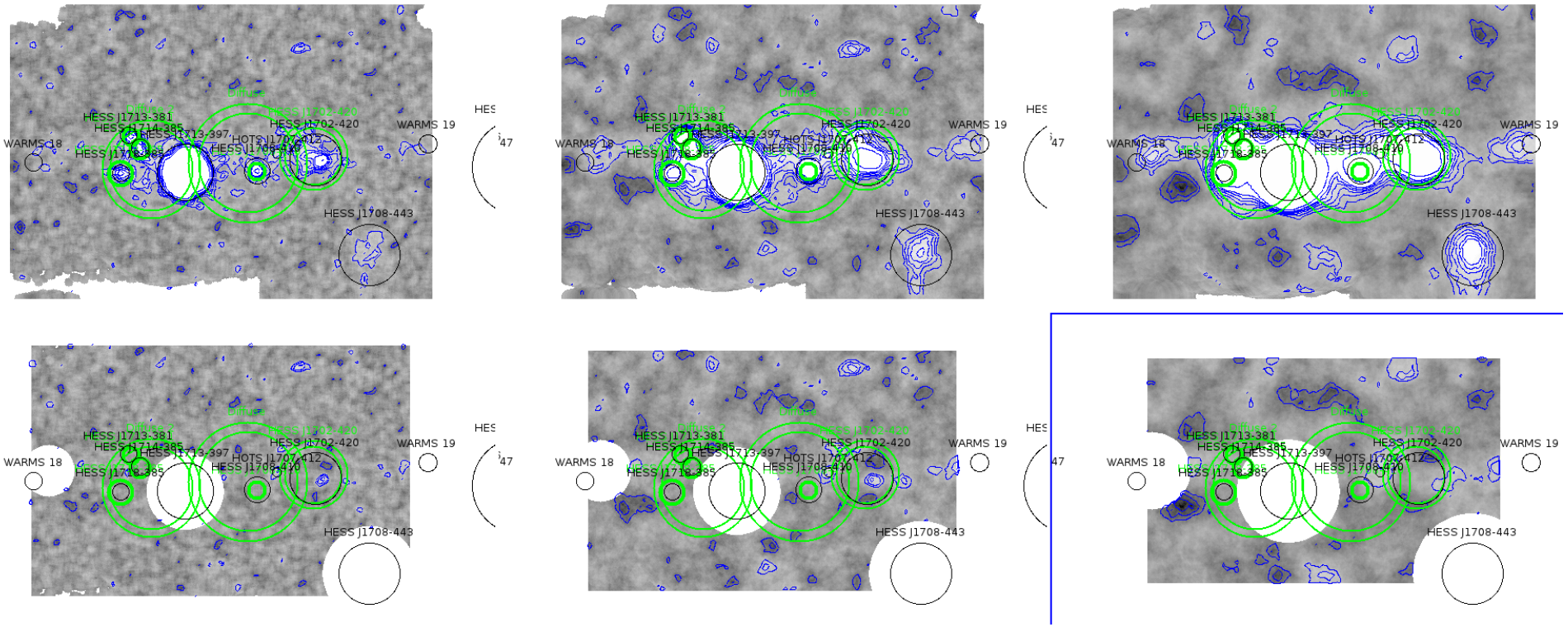

Figure 3.11.. Example of an ROI in which the solution chosen for the catalog contains five sources and two diffuse components (green). Previously defined sources and hotspots are shown in black. The top panel shows the regular HESS hard cuts significance map for 0.1, 0.22 and 0.4 deg correlation radius, the bottom panel shows the residual significance map after putting the fitted sources in the background. Color scale is sqrt from -5 to 8, contour levels are -5,-4,-3,-2, 2, 3, 4, 5, 6, 7, 10.

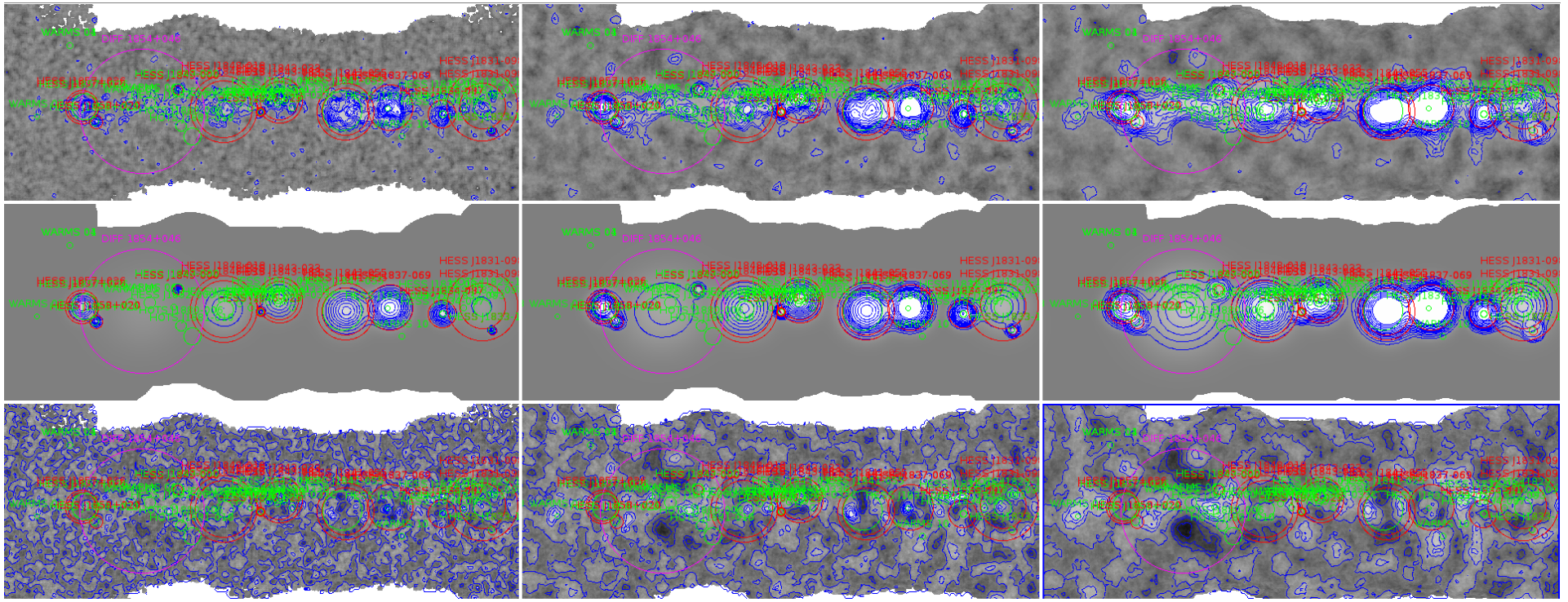

Figure 3.12.. Second HESS morphology fitting example. Top: significance, middle: model, bottom: residuals. Left to right 0.1, 0.22, 0.4 deg correlation radius.

For the spectral analysis the best-fit position as well as the 90% containment radius was chosen, except in the following cases:

1. No thetas larger than 1 deg were allowed. For such large theta cuts it would not have been possible to find off regions for the reflected background method.

2. No thetas smaller than 0.15 deg were allowed. For such small thetas there would have been a bias on the reconstructed flux and index because of the energy-dependence of the PSF.

3. In about 10 other cases radii were restricted below the 90% containment radius in order not to overlap with other nearby sources.

After defining the positions and aperture radii, the spectral analysis and fitting was completely automatic as described in Chapter 2.

The main parameter distributions of the catalog sources are summarized in a number of histograms and scatter plots.

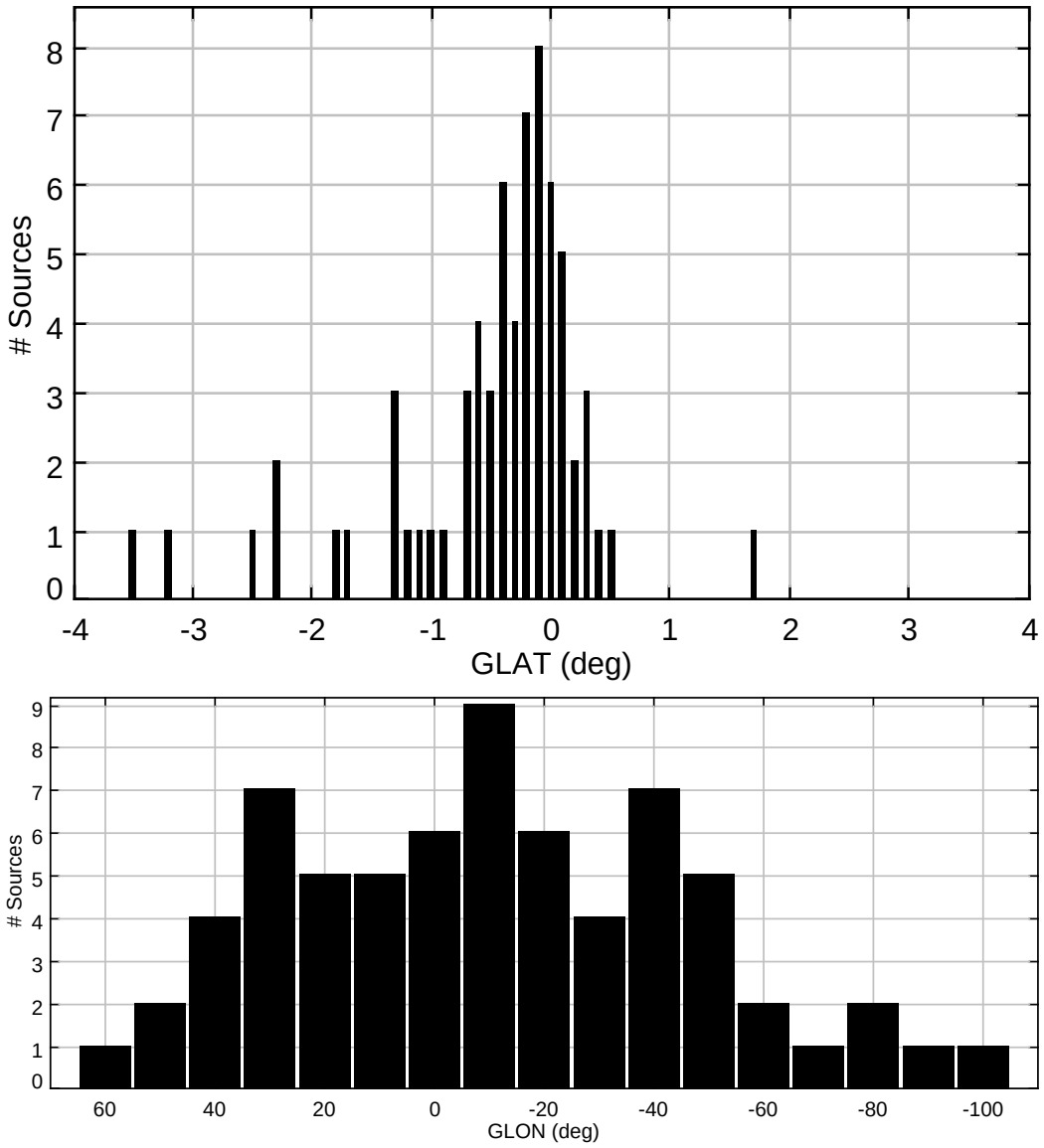

Figure 3.13.. Latitude and longitude distribution of the sources in the HGPS.

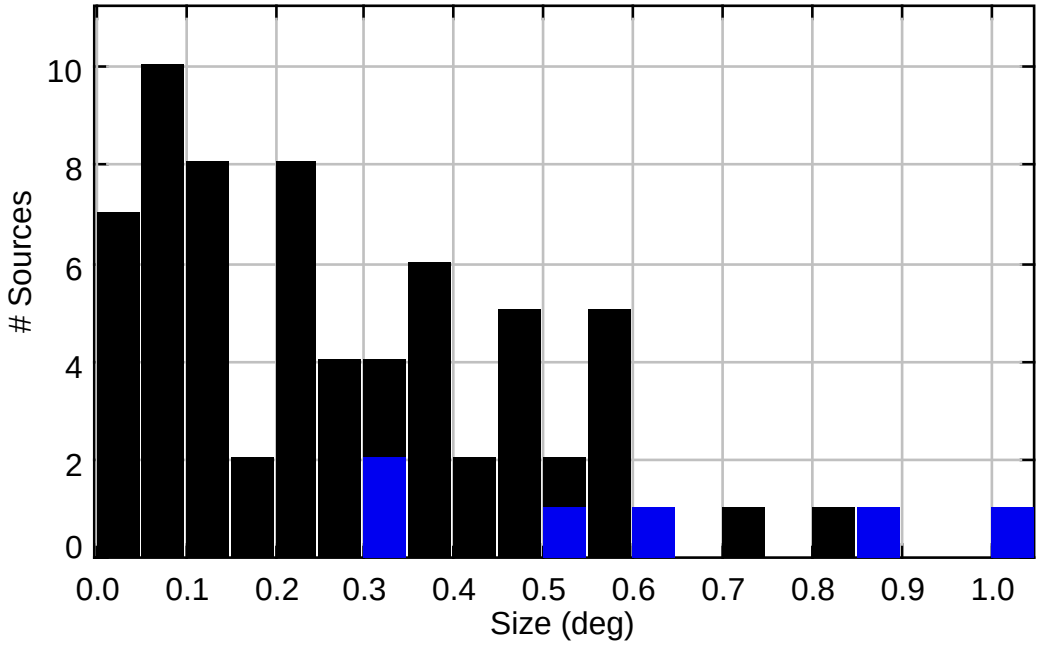

Figure 3.14.. Size distribution (Gaussian width) of the sources in the HGPS. The six diffuse sources are shown in blue.

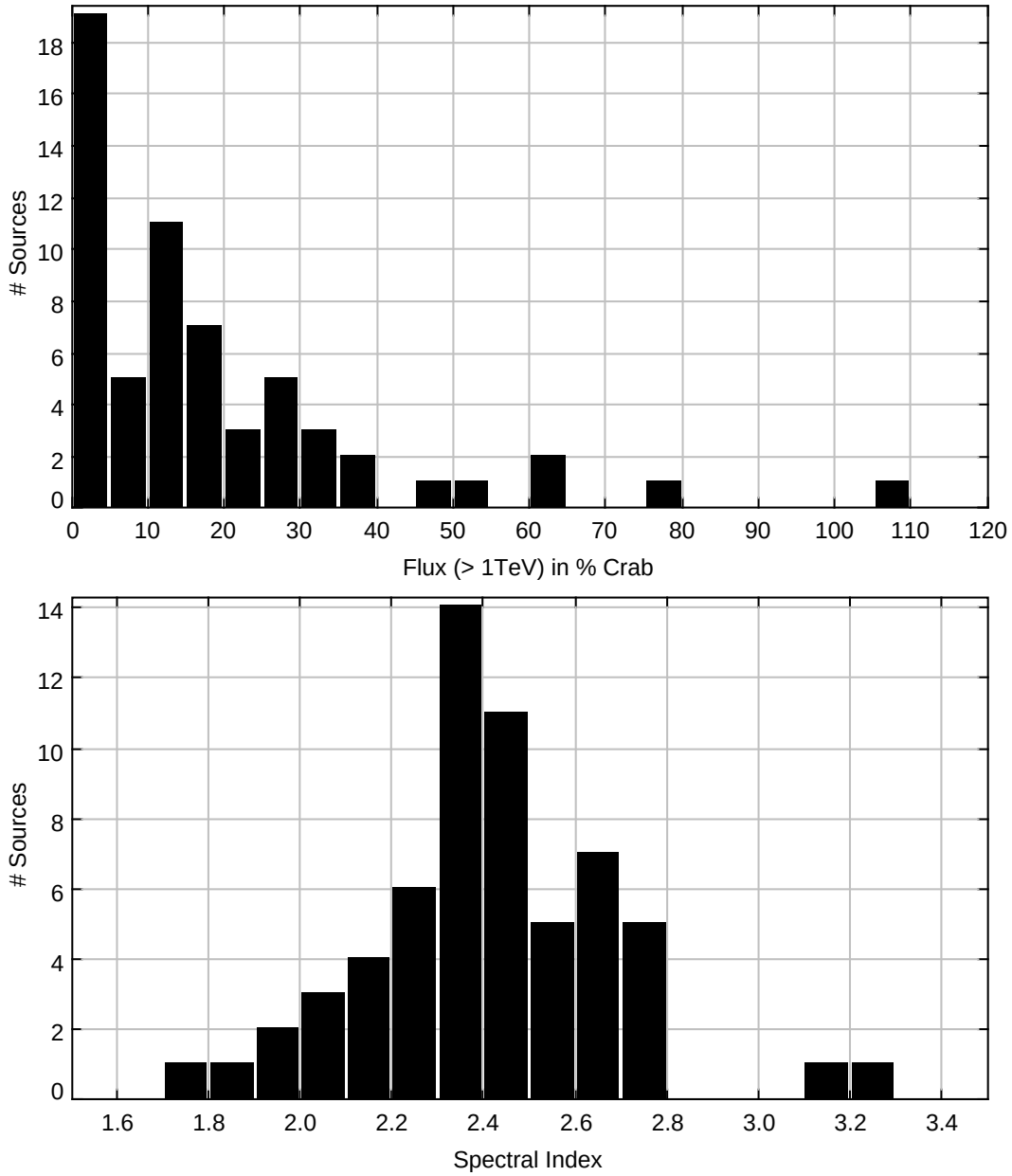

Figure 3.15.. Flux (integral, above 1 TeV) and spectral index distribution of the sources in the HGPS as derived from the power-law fit.

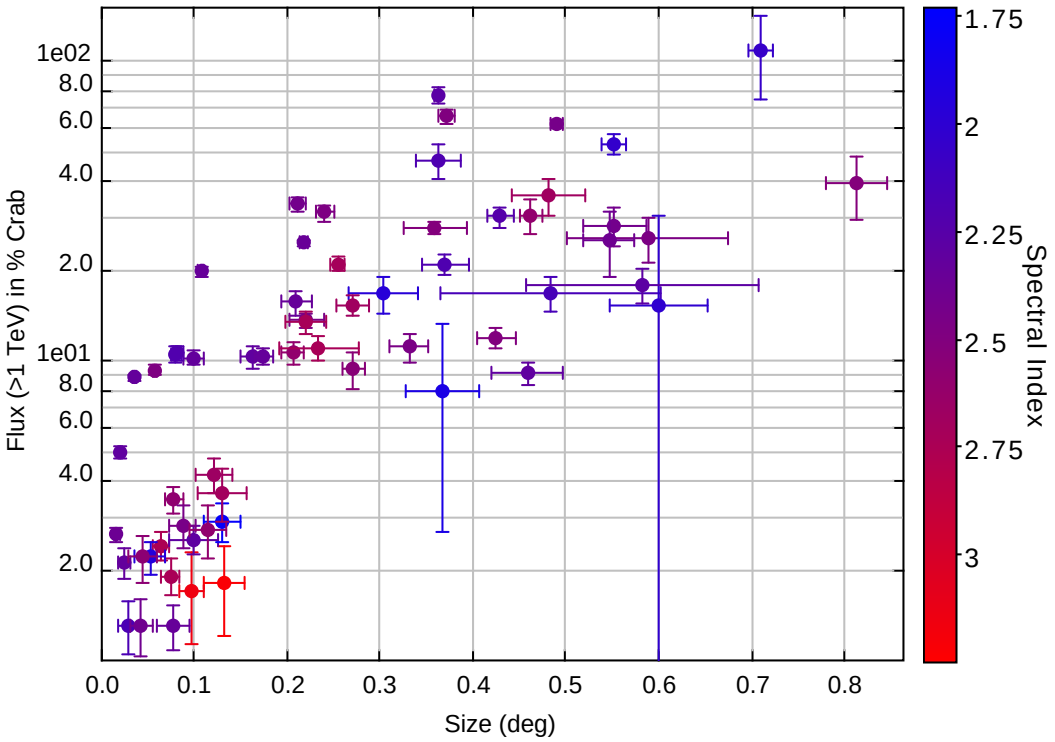

Figure 3.16.. Size – flux scatter plot for the sources in the HGPS, with spectral index shown in color. The size-dependent sensitivity of the survey is clearly visible; the detection threshold is higher at higher flux for larger sources. The fact that there are no sources in the upper left corner is not a selection effect, a source located there would have been detected.

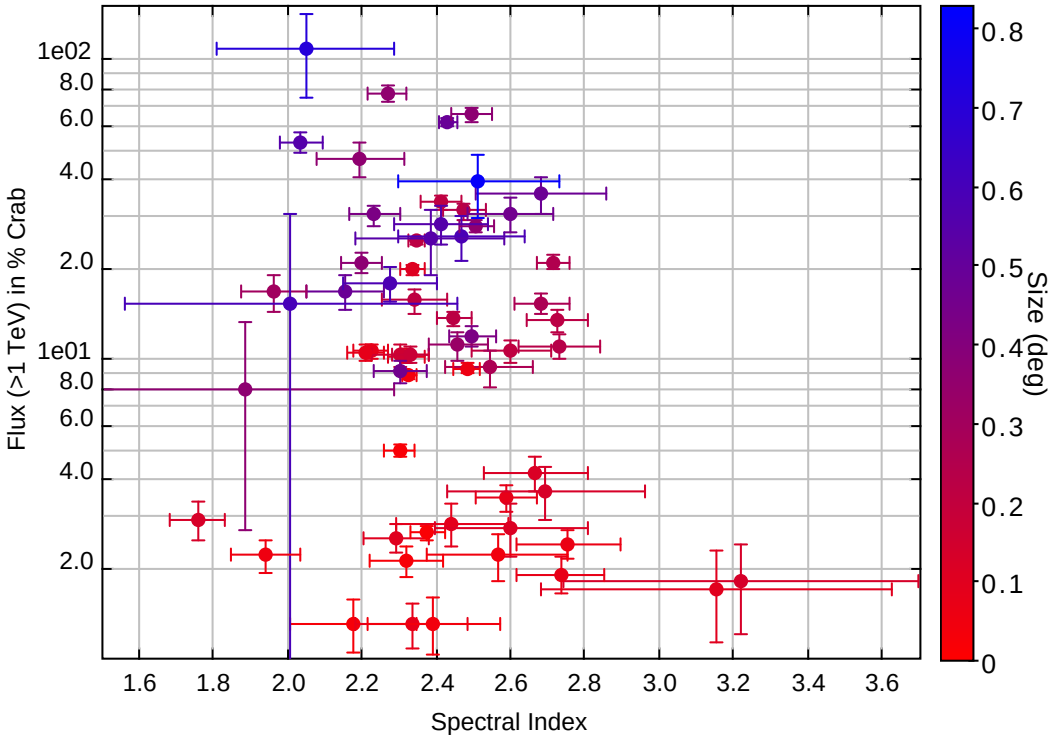

Figure 3.17.. Spectral index – flux scatter plot for the sources in the HGPS, with size (Gaussian width) shown in color. No correlation is apparent.

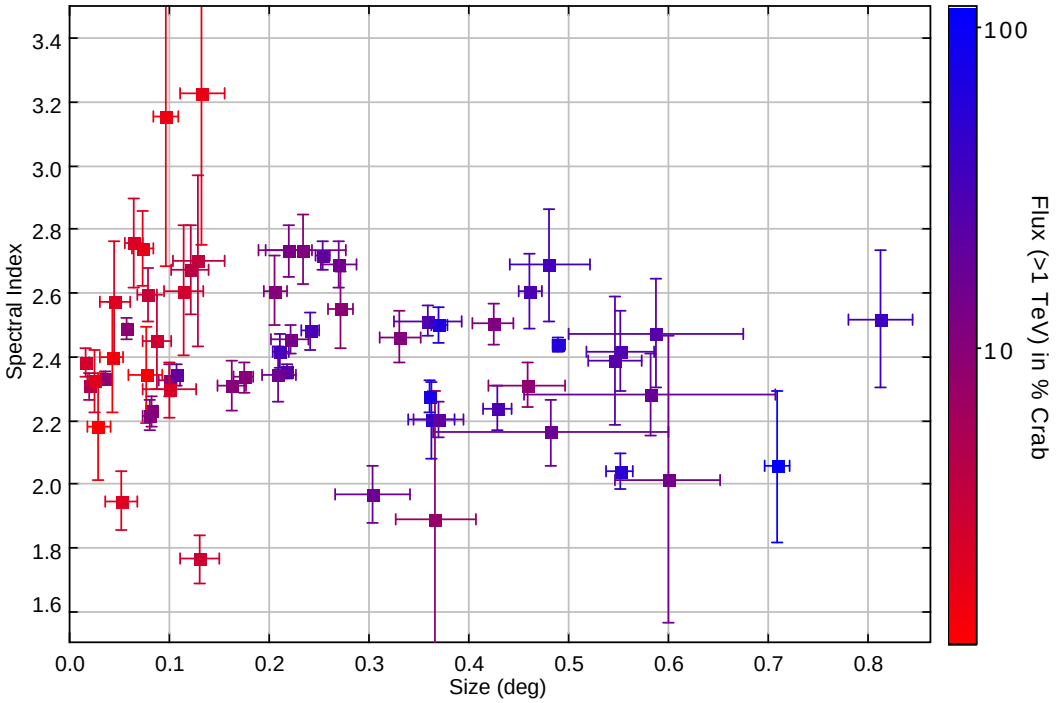

Figure 3.18.. Size (Gaussian width) – spectral index scatter plot for the sources in the HGPS, with flux shown in color. No correlation is apparent.

4. The Fermi Survey at GeV Energies

The Fermi Gamma-ray Space Telescope[1] was launched on June 11, 2008. It's primary instrument is the Large Area Telescope (LAT) (Atwood et al., 2009), an imaging, wide field-of-view gamma-ray detector[2], covering the energy range from about 20 MeV to more than 300 GeV.

A second instrument, the GLAST[3] Burst Monitor (GBM), complements the LAT in the observation of transient sources in the energy range 8 keV to 40 MeV. In this thesis only LAT observations are discussed and in some places the term 'Fermi' is used, even though 'Fermi/LAT' would be more precise.

Following an on-orbit calibration phase (Abdo et al., 2009d), Fermi started to operate in survey mode on August 4, 2008 (Abdo et al., 2009b) and has done so most of the time since. For the first year the data was private to the Fermi LAT collaboration, but since then is public, within less than a day of observation, via the Fermi Science Support Center (FSSC)[4]. The mission design lifetime is 5 years, with a goal of 10 years.

The LAT collaboration has published a bright source list (BSL) (Abdo et al., 2009b) with 205 sources based on three months of data, a first source catalog (1FGL) (Abdo et al., 2010a) with 1451 sources based on eleven months of data and a second source catalog (2FGL) with 1873 sources based on 24 months of data (The Fermi-LAT Collaboration, 2011). In this work we will use the 2FGL catalog, as it features improved statistics, diffuse background modelling and instrument response modelling compared to previous work. Both the 1FGL and 2FGL catalog used data from the energy range 100 MeV to 100 GeV, with detections mainly determined by $\sim$ GeV photons, as illustrated in Fig. 18 of Abdo et al. (2010a).

Catalogs of sources above 100 GeV were published by Neronov et al. At high Galactic latitudes ($|b| > 10$ deg), 74 sources were detected using data up to April 2010 Neronov et al. (2010). At low Galactic latitudes ($|b| < 10$ deg), 19 sources were detected using data up to September 2010 (Neronov and Semikoz, 2010).

Similarly to Neronov et al., the main idea of the analysis presented in this chapter is to only use data above 10 GeV, i.e. to focus on the high-energy subset of the Fermi data. The reason for this restriction is that the angular resolution of Fermi at 10 GeV is ~ 0.2 deg, similar to the HESS angular resolution,

[1] `http://fermi.gsfc.nasa.gov/`

[2] field of view is defined as $= \int A_{eff}(\theta, \phi) d\Omega / A_{eff}(0, 0)$, which for the LAT is 2.4 sr at 1 GeV.

[3] Gamma-ray Large Area Space Telescope (GLAST) was the pre-launch name of the Fermi satellite.

[4] `http://fermi.gsfc.nasa.gov/ssc/`

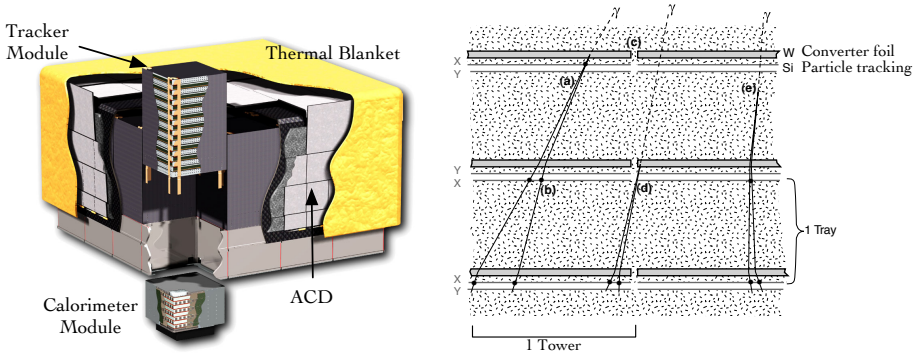

Figure 4.1.. *Left:* Schematic diagram of the Fermi LAT. The telescope's dimensions are 1.8 m $\times$ 1.8 m $\times$ 0.72 m. The power required and the mass are 650 W and 2789 kg, respectively. *Right:* Schematic diagram of part of the tracker showing layers of Wolfram conversion foils followed by silicon strip detectors (only two modules and three planes are shown). Both figures adapted from Atwood et al. (2009).

whereas it is ~ 5 deg at 100 MeV (see Figure 4.4). The typical distance of 2FGL sources in the inner part of the Galactic plane is ~ 1 deg. In the 1FGL and 2FGL catalogs most sources in the *Galactic ridge*—roughly defined as the region $|l| < 60$ deg and $|b| < 1$ deg—have been flagged by an appended 'c' to their name, as "a warning that the existence of the source or its measured properties (location, flux, spectrum) may not be reliable." Indeed the high-energy view of the Galactic ridge presented here will be very different from the 2FGL catalog—lower statistics, but higher resolution.

This chapter is structured as follows. The Fermi/LAT detector and instrument response to gamma rays are described in Section 4.1 and 4.2. Characteristics of the data set used here are presented in Section 4.3, the analysis method (unbinned likelihood fitting) and software in Section 4.4. The fluxes observed by Fermi are the sum of contributions by sources as well as diffuse Galactic and isotropic components, which are modelled as described in Section 4.5. The analysis results—low-resolution all-sky maps as well as high-resolution maps of the Galactic plane in several energy bands as well as a catalog of sources above 10 and above 100 GeV—are presented in Sections 4.6 and 4.7.

4.1. The Fermi Large Area Telescope

Detector

The Fermi Large Area Telescope (LAT) is a pair-conversion telescope. It consists of three major parts (see Figure 4.1):

Tracker: Gamma-rays enter from the top and interact within a converter foil to produce an electron-positron pair. Both particles continue roughly in the direction of the incoming gamma ray because the gamma-ray energy is much larger than the electron and positron rest mass. This pair is tracked with silicon-strip detectors, allowing a reconstruction of the original gamma-ray direction.

Calorimeter: The electron-positron pair is stopped in the calorimeter at the bottom. The measurement of the deposited energy allows a reconstruction of the original gamma-ray energy. Above a few GeV the shower is no longer fully contained and the energy resolution decreases (see Figure 4.4 right).

Anticoincidence Detector (ACD): For every gamma ray, $10^2 - 10^5$ cosmic rays enter the LAT and produce a very large background of tracker and calorimeter hits. Most of this background can be rejected by a veto from the ACD, which surrounds the LAT.

The following sections describe the three major parts of the LAT in some detail. For a much more detailed description and as a reference to the facts quoted here, consult Atwood et al. (2009) as well as Abdo et al. (2009d) and Rando and for the Fermi LAT Collaboration (2009).

Tracker

As shown in Figure 4.1, the tracker consists of 16 modules (a.k.a. towers), each consisting of 18 XY silicon-strip tracking detector (SSD) planes. Each XY plane has strips running in X direction and strips running in Y direction allowing the localization of charged particles passing through.

The first 12 planes have tungsten converter plates with thickness of 0.035 radiation length in front of the SSDs, the next 4 planes with thickness 0.18 and the last two planes have no converters.

Most gamma rays convert in one of the tungsten plates, only some convert e.g. in the telescope structure or the silicon strips. The initial electron and positron directions are reconstructed from the tracks recorded by the SSD planes following the conversion point. At low energy, the angular resolution is limited by angular deflections of the electron and positron by secondary scatterings within the first converter plane. At high energy the width of the silicon strips is the limiting factor.

The thickness of the converter planes (thin in the front, thick in the back) is a compromise between good angular resolution and large effective area. In the LAT about half of the high-energy photons convert in the front, the other half converts in the back. Effectively, the thick converter planes in the back make sure very few high-energy photons pass through the tracker without interacting, resulting in an increase in effective area by a factor of two, with the

drawback that the direction reconstruction for the back-converting events is worse by a factor of two compared to front-converting events.

Calorimeter

Below each of the 16 tracker modules sits a calorimeter module, consisting of 96 CsI(Tl) crystals that are optically isolated from each other. Each crystal is read out by two photodiodes at each end measuring the scintillation light induced by charged particles.

The crystals are arranged in 8 planes of 12 crystals alternating in XY to provide an image of the shower development profile for cosmic ray background rejection. The total vertical depth of the calorimeter is 8.6 radiation lengths, enough for to provide a calorimetric energy measurement for GeV photons.

Anticoincidence Detector

The ACD is composed of 89 plastic scintillator tiles, with a very high detection efficiency of $> 99.97\%$ for singly-charged particles entering the FoV of the LAT. This allows the on-board veto of most cosmic-ray events (factor $\sim 10^3$), resulting in managable data rates sent to Earth.

One major design improvement of the LAT compared to previous gamma-ray satellites like EGRET (Kanbach et al., 1988; Thompson et al., 1993; Esposito et al., 1999) is that the ACD is segmented. For the monolithic EGRET ACD, a problem called the *backsplash effect* lead to a reduction of the effective area by a factor > 2 at 10 GeV and above. Backsplash occurs when a high-energy photon creates an electromagnetic shower in the calorimeter and some of the shower particles travel back and pass the ACD, sometimes causing false vetoes. This effect is greatly suppressed in the LAT because only ACD segments near the incident gamma are allowed to veto, rejecting less than 20% of the otherwise accepted photons.

Observing Mode

The Fermi telescope resides in a low-earth circular orbit at an altitude of ~ 565 km, a period of ~ 95 min and an inclination angle of 28.5 deg wrt. the Earth's equator. In survey mode, which is used most of the time, the LAT's primary pointing direction is towards zenith, i.e. away from earth. A uniform exposure (up to 25%) over the whole sky is achieved by 'rocking' the telescope 35 deg north and south w.r.t. the orbital plane in alternating orbits[5]. The result is that the LAT with its very large FoV (2.4 sr = 20% of the sky) observes every point in the sky at least for 30 minutes every 3 hours.

Figure 4.2 shows the average raw LAT tracker trigger rates as a function of terrestrial coordinates. The increase in trigger rate due to an increase in cosmic

[5]The rocking angle was increased in May 2009 to 39 deg for operational reasons.

ray background flux over the South Atlantic Anomaly (SAA) is clearly visible. The LAT does not take data during the 13% of the time it spends inside the SAA as defined by the polygon in Figure 4.2. The SAA is the main cause of the exposure nonuniformity in the Fermi data, as shown in Figure 4.12.

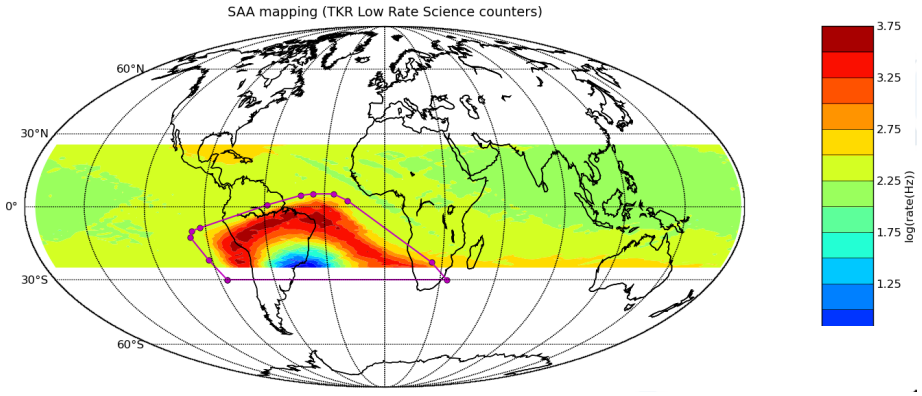

Figure 4.2.. Raw tracker trigger rate by cosmic rays as a function of orbit position. The South Atlantic Anomaly (SAA) region where the LAT does not take data is outlined with a polygon. Figure taken from `http://web.phys.ntnu.no/~mika/baldini.pdf`.

Trigger and Data Aquisition System

The LAT data aquisition system (DAQ) collects the data from all subsystems and implements a hardware multi-level event trigger. The task of this trigger is to reduce the instrument deadtime associated with reading out the detector subsystems. Mostly thanks to the ACD, a reduction from MHz to kHz is possible, resulting in a readout dead time of $\sim 9\%$.

Besides this readout dead time, about 13% of observing time is lost during the passage of the satellite through the South Atlantic Anomaly. The total live time efficiency is 74%, i.e. less than 5% of potential observation time is lost to calibration runs, operational issues or data loss during transmission.

The DAQ also processes events at a rate of ~ 2 kHz and runs filter algorithms to reduce the rate of downlinked events by an order of magnitude to ~ 400 Hz, corresponding to a data rate of ~ 1.2 Mbps. Note that still most of these events were induced by cosmic rays, the gamma-ray detection rate of the LAT is only ~ 1 Hz[6].

[6]A gamma-ray rate of 1 Hz is obtained for `P6_V3_SOURCE` cuts, for other cuts the rate differs by a factor of a few because of the change in effective energy threshold. Cuts are further discussed in Section 4.2.

Event Reconstruction and Classification

Every event that is sent to the ground is analyzed in detail with the goal to classify if it was induced by a photon or cosmic ray and to reconstruct its energy and direction. This is done by comparing the 'hits' recorded by all the tracker, calorimeter and ACD channels to expectations for gamma rays and cosmic rays (Atwood et al., 2009).

These expectations for observable signals (e.g. pulse heights, hit positions, time delays) are obtained through detailed simulations of the interaction processes of photons and charged particles in the detector. Also pre-flight measurements from test beams at CERN and GSI with known particle directions and energies as well as post-launch observations of bright sources of gammas and cosmic rays were used for calibration and optimization of reconstruction and classification methods (Abdo et al., 2009d).

Data Products

The result of the data aquisition and reconstruction described in the previous section is an *event list* containing $\sim$ 200 parameter values characterizing the event, called the 'merit n-tuple'. Most of the events are not astrophysical photons and most of the parameters are not needed for gamma-ray data analysis. A *photon file* is provided that contains only 22 event parameters and only events that pass `TRANSIENT` cuts (see Section 4.3), i.e. which have event class 1 or higher. The photon file also contains a list of *good time intervals (GTIs)* that represent the time intervals during which the photons were detected and that are used for exposure computation (explained later).

The second file required for analysis besides the photon file is the *spacecraft file*. For each 30 sec time interval it contains 27 parameters that determine the spacecraft position and orientation during that time interval.

Both the photon and spacecraft file are available in FITS format Pence et al. (2010) from the Fermi Science Support Center (FSSC) data server[7]. The user enters a position and radius, as well as a start and stop time and a minimum and maximum energy in a web form, then the data server generates the files within seconds to minutes and the user can download it via http. For all-sky analyses weekly photon and spacecraft files are available.

4.2. Instrument Response Functions

As described above the process of detecting gamma rays with the Fermi LAT is quite complicated. However for the analysis of gamma-ray data the details don't matter and the detector can be modeled via simple *instrument response*

[7] `http://fermi.gsfc.nasa.gov/cgi-bin/ssc/LAT/LATDataQuery.cgi`

functions (IRFs) that describes the efficiency (after event selection cuts) of detecting a given photon of true energy E arriving from position p, as well as the resolution of the energy and position reconstruction:

$$R(E_r, p_r|E, p) = A(E, p) \times P(p_r|E, p) \times D(E_r|E, p). \tag{4.1}$$

The total instrument response R is the product of three components:

Effective area A (cm^2): the physical detector area times the efficiency to trigger and pass all cuts (Figure 4.3).

Point spread function (PSF) P: the probability density to reconstruct at position p_r for true position p (Figure 4.4, left).

Energy resolution D: the probability density to reconstruct at energy E_r for true energy E (Figure 4.4, right).

The IRF version used here (`P6_V3`, Pass 6, version 3) models the energy and inclination angle dependence, but not e.g. the known mild effective area dependencies on azimuth angle and cosmic ray background rate. Because the LAT energy resolution is quite small ($\sim$10%) and has a small effect on analysis results, it is actually not implemented in the likelihood fitting tool `gtlike` (see Section 4.4).

Both the effective area and the PSF are the result of simulations and comparison to real data. Pre-flight `P6_V1` IRF models were quickly adapted to `P6_V3` after on-orbit calibrations Abdo et al. (2009d). The effective area is stored and can be looked up as a function of energy and inclination angle, whereas for the PSF an analytical model is used and the model parameters are stored and can be looked up, also as a function of energy and inclination angle (although the dependence on inclination angle is negligible).

For the results presented here the `P6_V3_DATACLEAN` IRFs were used. Initially the LAT collaboration made three sets of cuts (a.k.a. event classes) available called (1) `TRANSIENT`, (2) `SOURCE` and (3) `DIFFUSE` that were supposed to have background rates of 2, 0.4 and 0.1 Hz and be optimal for the detection of transient sources, point source and extended sources / diffuse emission (Atwood et al., 2009). In orbit it was realized that background rates were higher than expected and a fourth event class (4) `DATACLEAN` was defined (The Fermi-LAT collaboration, 2010).

Now the recommended event class for point-source analysis as well as bright extended source analysis up to 20 GeV is (3) `DIFFUSE`, and (4) `DATACLEAN` for the analysis of extended sources at high energies and diffuse emission in general[8].

For this work `DATACLEAN` was chosen over `DIFFUSE` because as can be seen in Figure 4.3 at high energies the effective area (and thus the number of detected

[8] `http://fermi.gsfc.nasa.gov/ssc/data/analysis/documentation/Cicerone/Cicerone_Data_Exploration/Data_preparation.html`

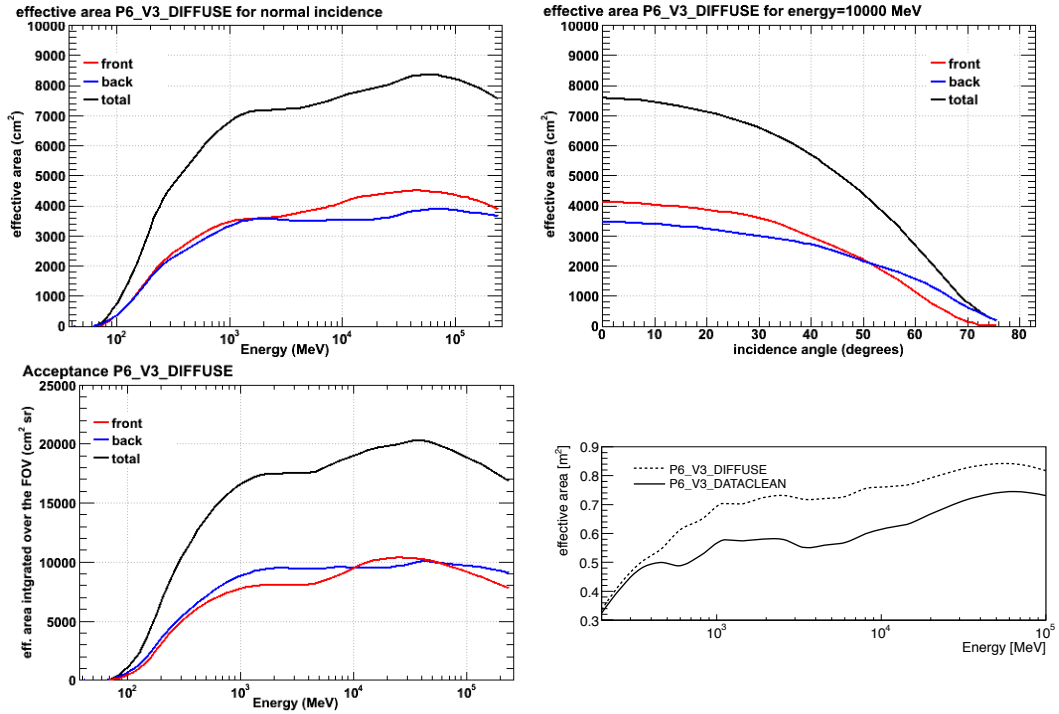

Figure 4.3.. Fermi LAT effective area as a function of energy (top left) and incidence angle (top right) as well as integrated over the field of view (bottom left) for `P6_V3_DIFFUSE`. Figures taken from `http://www-glast.slac.stanford.edu/software/IS/glast_lat_performance.htm`. The bottom right plot shows that the effective area for `P6_V3_DATACLEAN` cuts (used in this thesis) is reduced by about 20% wrt. the `P6_V3_DIFFUSE` cuts. Figure taken from The Fermi-LAT collaboration (2010).

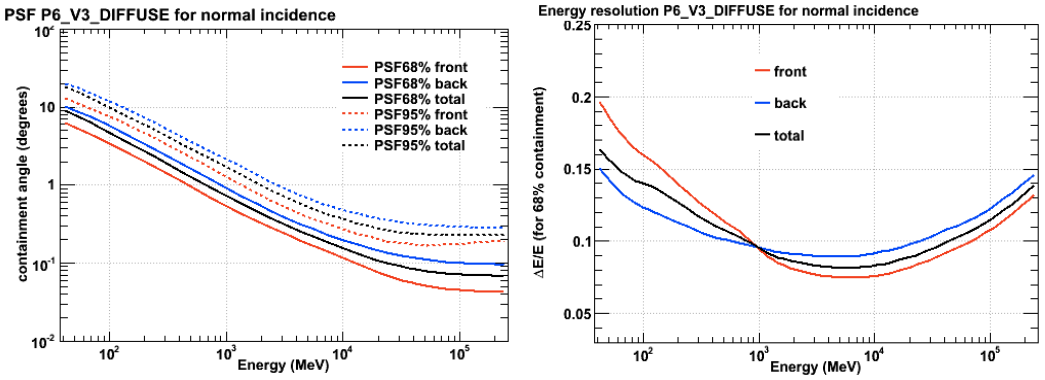

Figure 4.4.. Fermi LAT angular (left) and energy (right) resolution as a function of energy. The curves shown here are for normal incidence and `P6_V3_DIFFUSE`, but are very similar for all inclination angles and `P6_V3_DATACLEAN` as well. Figures taken from `http://www-glast.slac.stanford.edu/software/IS/glast_lat_performance.htm`.

photons from a source) is only 10% less (peak 0.74 m^2 compared to 0.84 m^2), but the isotropic background is reduced by a factor of 6 at 100 GeV (see Figure 4.5).

Figure 4.6 shows the Fermi LAT 1-year sensitivity, which has two regimes, clearly visible in the integral version on the left.

- At low energies the limiting factor is the background. For a 5-sigma detection is $N_S = 5 \cdot \sqrt{N_B}$, i.e. that the number of source photons N_S within the PSF area must be five times as large as the RMS variations in the background level.

- At high energies the limiting factor is the exposure, which in turn is limited mainly by the size of the detector. Fermi has an effective area $A \sim 8000$ cm^2, livetime efficiency 80% and FOV 20% of the sky, so the exposure of any given source in a year is

$$AT = 4 \cdot 10^{10} cm^2 s. \tag{4.2}$$

  The (energy-independent) integral flux sensitivity $F \sim 2 \cdot 10^{-10}$ cm^{-2} s^{-1} shown in Figure 4.6 corresponds to $N = FAT = 8$ photons.

A likelihood-based derivation of the sensitivity and comparison to the actual sensitivity limit seen in the 1FGL catalog is given in Appendix A of Abdo et al. (2010a).

For further information on Fermi IRFs / cuts / caveats see the documentation on the web.[9]

[9] `http://fermi.gsfc.nasa.gov/ssc/data/analysis/documentation/Cicerone/`

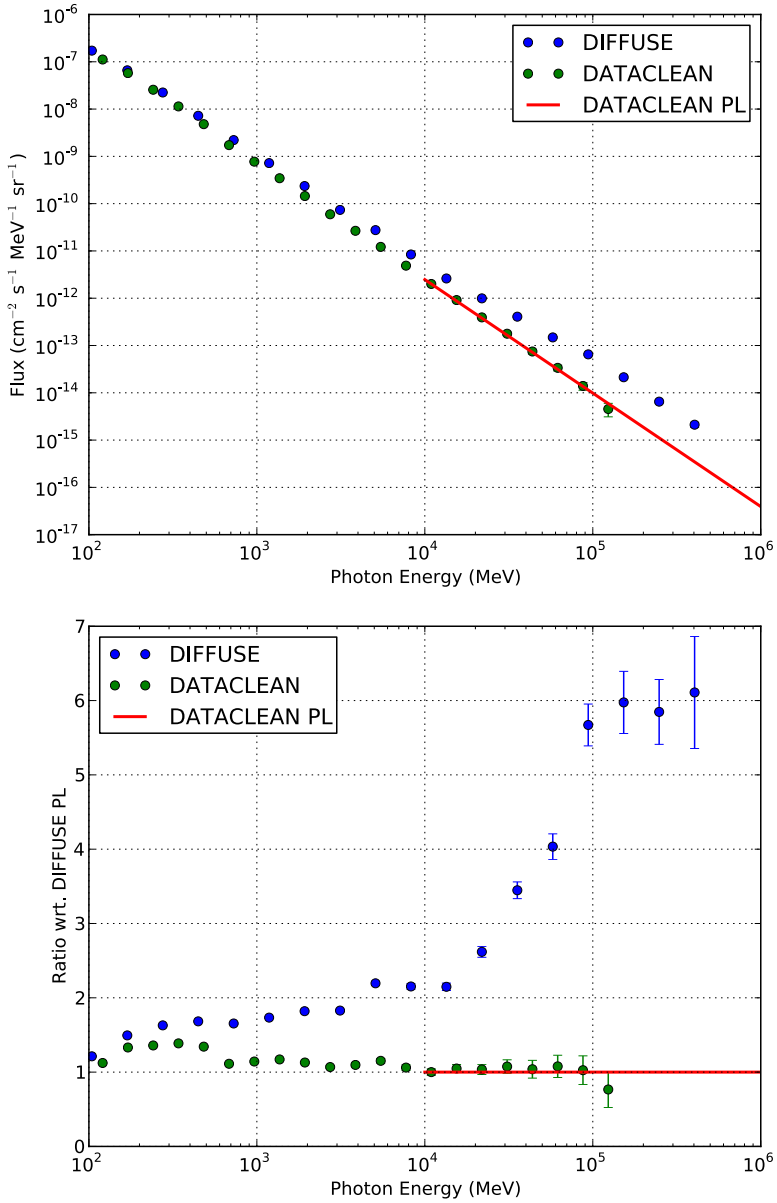

Figure 4.5.. Fermi LAT isotropic background for `P6_V3`. The `DIFFUSE` and `DATACLEAN` points were derived by the LAT collaboration from the data, the `DATACLEAN PL` power law was used to extend the `DATACLEAN` background model up to 1 TeV. See Section 4.5 for a detailed discussion.

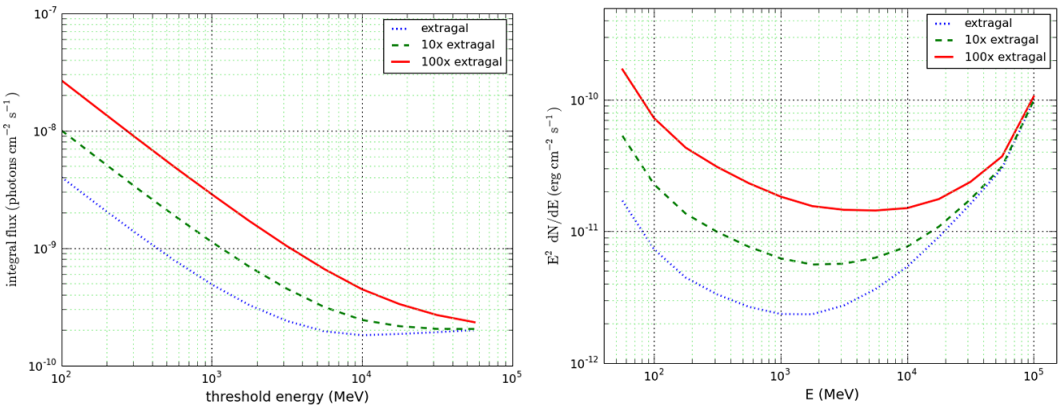

Figure 4.6.. Fermi LAT point-source 1-year sensitivity for an integral flux above a threshold energy (left) and for a differential flux in an energy band spanning a quarter decade around a given energy (right). The sensitivity is computed as the flux that will within one year (on average, disregarding statistical signal and background fluctuations) result in a $TS = 25$ detection assuming a livetime efficiency of 80% and isotropic `extragal` power-law background of $F(> 100MeV) = 1.5 \cdot 10^{-5}$ cm^{-2} s^{-1} sr^{-1} with spectral index 2.1 and `P6_V3_DIFFUSE` cuts. The 100 `extragal` level roughly corresponds to the diffuse Galactic background level in the Galactic center. Figures taken from `http://www-glast.slac.stanford.edu/software/IS/glast_lat_performance.htm`

4.3. Data Set and Pre-Processing

The data analysis steps described in this and the following sections follows standard prescriptions from the "Cicerone", analysis threads and tool reference manuals[10].

The analysis presented in this chapter uses 134 weeks of data, from August 2008 to February 2011 (see Table 4.1 for details) using the weekly photon files `lat_photon_weekly_w009_p116_v001.fits` to `lat_photon_weekly_w142_p116_v001.fi` were downloaded from the web.[11] At the time of writing no documented procedure exists to combine the weekly spacecraft files. Instead the current standard procedure is to download one spacecraft file for all data [12] using the dummy coordinates `RA, DEC = 0, 0` (not used in the production of the spacecraft file) and full time interval `TMIN, TMAX = START, END` and deselecting 'photon data'. These resulting spacecraft file `L110224154428E0D2F37E73_SC00.fits` contains the telescope pointing and livetime history for all 134 weeks.

The data was preprocessed as illustrated in Figure 4.7 by applying the following steps (the Fermi science tools are described in more detail in Section 4.4):

`gtselect` was run to combine the weekly all-sky FITS files into one FITS file containing the whole data. Three cuts were applied, `ENERGY > 100 MeV`, `EVENT_CLASS == 4 (DATACLEAN)` and `ZENITH_ANGLE > 105 deg`, resulting in a reduction of data volume from 44 GB to 2 GB. Because mostly events above 10 GeV were used, a second photon file (11 MB) was produced with the additional cut `ENERGY > 10 GeV`. Note that the primary purpose of `gtselect` is not to merge event list files, but to apply energy, region of interest (ROI) and other cuts, which is done by running `gtselect` a second time. The usage of ROIs in analysis and the second `gtselect` pass is described in detail Section 4.4.3. The basic idea of ROIs is to only consider a small part of the sky around the position of interest, ignoring all the far away sources and photons that don't influence the measurement at the current position of interest.

`gtmktime` was run to update the GTIs (second extension in the photon file) according to the information in the spacecraft file and to apply the following GTI filter: `(DATA_QUAL == 1 && LAT_CONFIG == 1 && ABS(ROCK_ANGLE) < 52)`. No ROI cut was applied (`roicut = no`).

Cicerone_LAT_IRFs/
http://www-glast.slac.stanford.edu/software/IS/glast_lat_performance.htm
http://fermi.gsfc.nasa.gov/ssc/data/analysis/LAT_caveats.html

[10] http://fermi.gsfc.nasa.gov/ssc/data/analysis/documentation/

[11] http://fermi.gsfc.nasa.gov/FTP/fermi/data/lat/weekly/

[12] http://fermi.gsfc.nasa.gov/cgi-bin/ssc/LAT/LATDataQuery.cgi

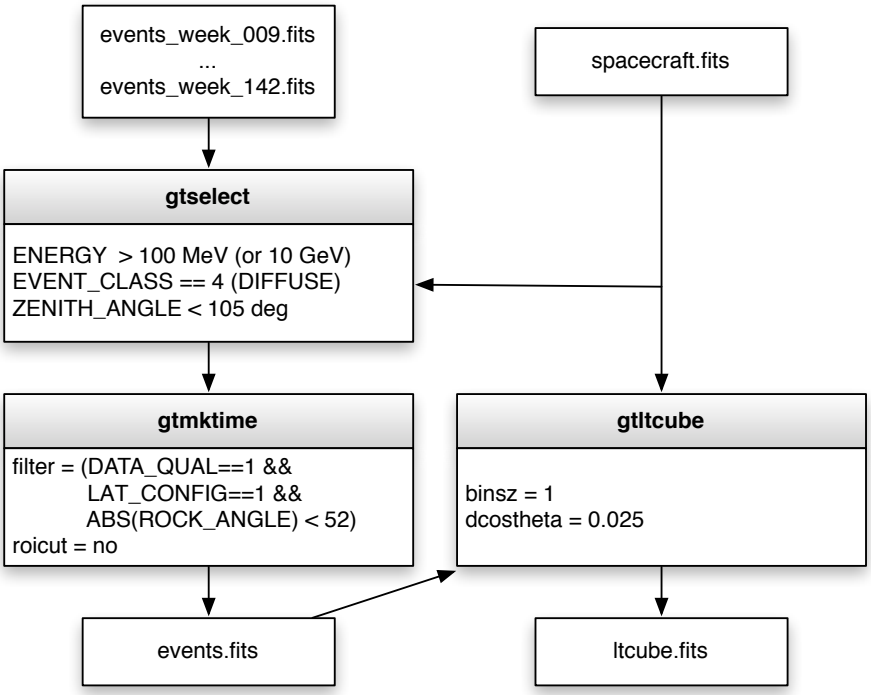

Figure 4.7.. Fermi data pre-processing steps.

Parameter	Value	Description
DATE-OBS	2008-08-04	start date
DATE-END	2011-02-23	end date
TSTART	239557417	start mission time
TSTOP	320197276	end mission time
ONTIME	66.15 Ms	sum of GTI lengths
TELAPSE	80.64 Ms	TSTOP - TSTART
GTIs	14658	Number of GTIs

Table 4.1.. Fermi data set time period. 133 weeks with 82% up time.

`gtltcube` was run to compute the livetime cube using the option `zmax = 105`, corresponding to the cut applied on the events when running `gtselect`. The spatial HEALPIX binning was set to 1 deg, the offset binning to `dcostheta = 0.025`.

This reduction of the data volume by a factor $4 \cdot 10^3$ was important, because in the production of the all-sky TS maps the photon data had to be processed for ~ 2500 ROIs and four energy bands, i.e. read from disk $\sim 10,000$ times. The computation of the livetime cube takes several hours, comparable in CPU time to the second computationally intensive task in the analysis tool chain, the TS map computation (see Figure 4.13). As described in the manual[13] (Option 2, rocking angle cut + zmax option in `gtltcube`, used by LAT team for 1FGL, 2FGL and diffuse analysis), it is possible to use the same livetime cube for different ROIs and energy bands. The key is to apply the rocking angle cut with `gtmktime` as a substitute for the more commonly applied ROI cut, to exclude time periods when the earth blocks the LAT FOV and earth albedo photons enter the LAT.

Table 4.1 summarizes the time period for the data set. The energy bands used in the following sections, as well as the total number of events after the selections described above are shown in Table 4.2.

Figure 4.8 shows the distribution of some important event parameters. A few points worth noting:

- The shape of the energy distribution is given by the product of the LAT effective area (shown in Figure 4.3 and the power-law energy spectra mainly of the Galactic diffuse emission, but also from the isotropic diffuse emission and sources.

- The latitude distribution is shown in $\sin(GLAT)$ bins, because that way each bin corresponds to the same area on the sky and an isotropic distri-

[13] `http://fermi.gsfc.nasa.gov/ssc/data/analysis/documentation/Cicerone/Cicerone_Likelihood/Exposure.html`

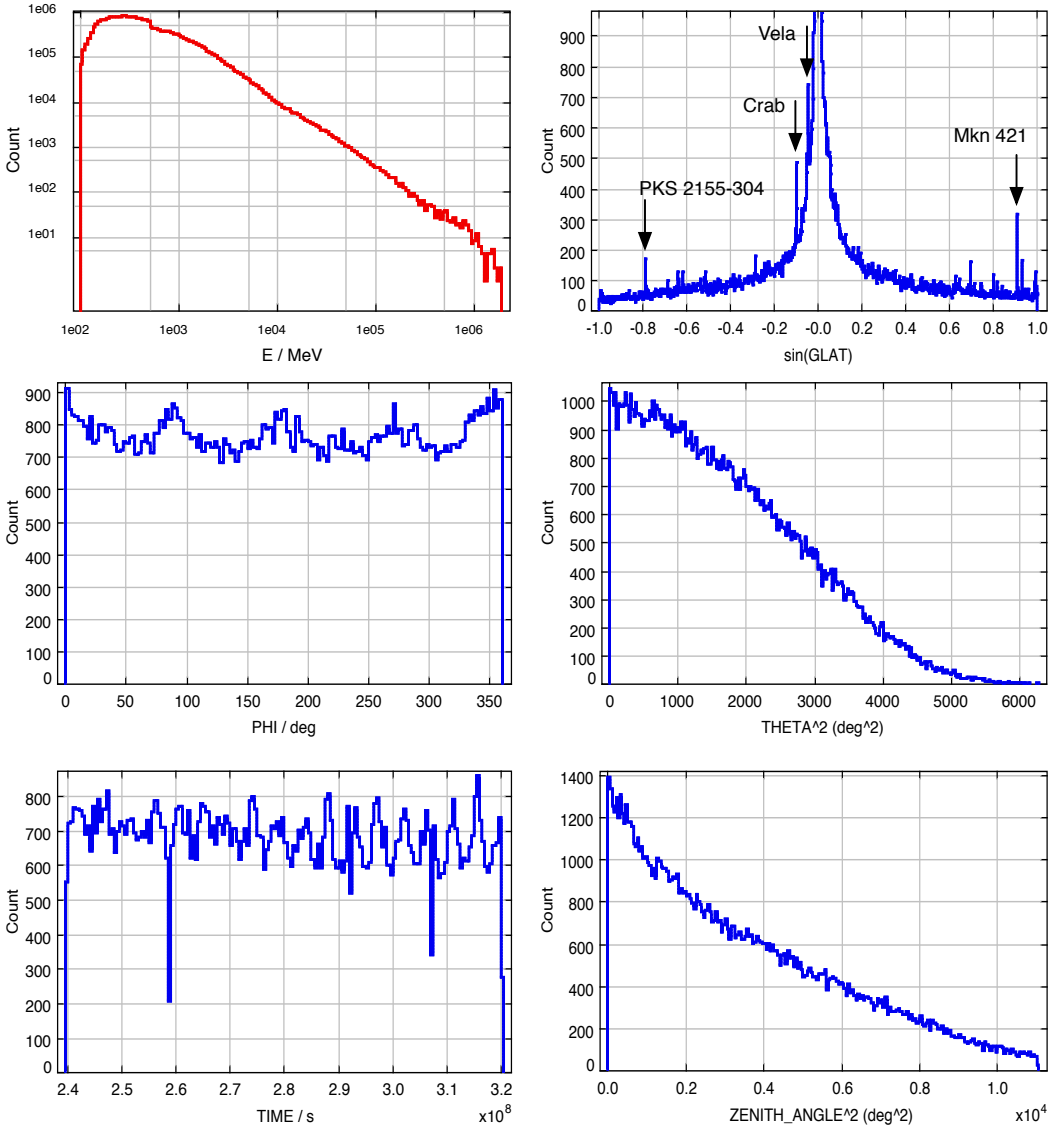

Figure 4.8.. Fermi event parameter distributions. The y axis always shows number of events per bin and the x axis shows Energy (E), Galactic latitude (B), incidence azimuth angle (PHI), incidence offset angle squared (THETA^2), arrival time (TIME) and earth zenith angle squared (ZENITH_ANGLE^2). The energy distribution shows all events above 100 MeV, the other distributions only show events above 10 GeV.

E_{min} GeV	E_{max} GeV	Events	Fraction %	Exposure 10^{10} cm^2 s	Color	Resolution deg
0.1	1	20.146.076	84.8	4.8		5
1	10	3.502.276	14.7	6.5		0.7
10	30	86.139	0.36	8.0	R	0.2
30	100	20.172	0.085	8.2	G	0.1
100	1000	3.505	0.015	5.9	B	0.07

Table 4.2.. Energy bands used in this work and total number of events they contain. In total there are 23.758.223 events above 100 MeV and 109871 events above 10 GeV. Above 1 TeV there are 45 events (with the highest-energy event at 1.8 TeV), which are not included in the last energy band. RGB maps are made using the colors indicated here. The exposure was computed as the mean over the whole sky at the log bin center (see Section 4.4.2 and Figure 4.12). The angular resolution given here is the 68% containment radius at the lower energy edge of the band, as shown in Figure 4.4, which is a good approximation because due to the power-law nature of the spectra most events are at low energies in any band.

bution on the sphere would appear flat. The distribution is the sum of the Galactic diffuse, isotropic and point source contributions.

- The PHI and TIME distributions are constant within $\sim 10\%$.

  The PHI distribution shows four peaks at 0, 90, 180 and 270 deg, corresponding to the sides of the cube detector, i.e. the effective area in the corners is reduced by 10%.

  The TIME distribution shows a 55 day modulation, which is a known period of Fermi observations. The rate modulation is the result of the precession of the Fermi orbit in combination with the SAA passage and the fact that the southern Sky is brighter because it contains the inner region of the Milky Way with it's bright diffuse emission.

- The THETA^2 distribution reflects the effective area incidence angle dependence shown in Figure 4.3. The ZENITH_ANGLE^2 dependence is the result of the rocking pattern of the detector and the effective area incidence angle dependence.

4.4. Analysis Methods and Software

The Fermi Science Tools v9r18p6[14] together with self-written python scripts were used to create maps of the GeV emission above 10 GeV in several energy

[14] http://fermi.gsfc.nasa.gov/ssc/data/analysis/software/

bands defined in Table 4.2.

Before the tools and parameters are described in detail, we explain some basics of likelihood analysis.

4.4.1. Likelihood Analysis

The likelihood analysis of EGRET gamma-ray data is described in Mattox et al. (1996). The Fermi collaboration has not published a paper yet detailing how the likelihood function was implemented in their tools, the formulae given in this section were taken from presentations available on the web.[15]

The inputs to the likelihood function are:

1. A *source model* $S(E, p, t; x)$ giving the surface brightness S (units cm^{-2} s^{-1} sr^{-1} MeV^{-1}) at each energy E, position p and time t. We will only consider steady sources and drop the time dependence from the formulae. For any number of pointlike and extended sources in addition to isotropic and Galactic diffuse background, the source model can be written as

$$S(E, p; x) = \sum_i S_i(E; x_i)\delta(p - p_i) + \sum_l S_l(E, p; x_l) + S_{gal}(E, p; x_{gal}) + S_{iso}(E; x_{iso}), \tag{4.3}$$

   where S_i are pointlike source, S_l are extended sources, S_{gal} is the Galactic diffuse emission and S_{iso} is the isotropic diffuse emission.

2. The *data*, given by the reconstructed energy E_r and reconstructed position p_r (which is really a two-component vector $p_r = (l_r, b_r)$) for the unbinned likelihood function or by the number of events in bin j with bin size dE_r (MeV) and dp_r (sr). The goal of the likelihood analysis is to fit the model parameters x such as the source position, flux or spectral index.

3. The *exposure*, given by the pointing history of the detector (spacecraft file), good time intervals (GTIs in photon file) and instrument response functions as given in Equation (4.1).

The binned likelihood function is given by the product of the Poisson likelihoods in each GLON-GLAT-ENERGY bin j,

$$L = \prod_j \frac{\theta_j^{n_j} e^{-\theta_j}}{n_j!}, \tag{4.4}$$

where n_j / θ_j is the observed / predicted number of events in bin j with

$$\theta_j = \int_j dE_r dp_r \int_{SR} dE dp R(E_r, p_r; E, p) S(E, p; x). \tag{4.5}$$

[15] http://silicondetector.org/download/attachments/28521/likelihood.pdf
http://www.isdc.unige.ch/sf2010/fermiSession/fermi_AT.pdf

In practice actually all computations are done using the log likelihood for numerical precision and speed, given by

$$\log(L) = \sum_j (n_j \log(\theta_j) - \theta_j) - \cancel{\log(n_j!)} = \sum_j (n_j \log(\theta_j)) - N_{pred}, \tag{4.6}$$

where the $n_j!$ term has been dropped because not the absolute value of L, only changes in L as a function of model parameters x are of interest. $N_{pred} = \sum_j \theta_j$ is the total number of expected counts in the region of interest (ROI).

The region of interest (ROI) and source region (SR) are illustrated in Figure 4.9. The ROI must be chosen[16] such that it contains all emission from the source under investivation (for point sources e.g. the 95% containment radius of the PSF), as well as enough region around that source such that it is possible to measure the parameters x of any sources with significant overlap with the source of interest as well as the isotropic and diffuse background levels. Because at the edge of the ROI there will be photons contributed by sources and diffuse emission from outside the ROI, a second larger SR is chosen that extends further out to include that emission. In practice the ROI and SR are chosen as circles centered on the source or position of interest.

The unbinned likelihood function can be obtained from Equation (4.6) in the limit of small bins, where each bin either contains $n_j = 0$ or $n_j = 1$ events. Defining the IRF-convolved model as

$$M(E_r, p_r, t; x) = \int_{SR} dEdpR(E_r, p_r; E, p, t) S(E, p; x), \tag{4.7}$$

the likelihood function can be written as

$$\log(L) = \sum_j \log(M(E_r, p_r, t; x)) - N_{pred}, \tag{4.8}$$

with N_{pred} again the total number of predected events in the ROI,

$$N_{pred} = \int_{ROI} dEdpdtM(E_r, p_r, t; x). \tag{4.9}$$

Computing the likelihood function is cost intensive[17] and the question arises whether binned or unbinned analysis should be used. Generally the computation per bin or per photon is about equally cost intensive, so unbinned is faster when $N_{photon} < N_{bins}$. The bins must be chosen to match the PSF size, so typically there will be $N_{bins} = (r_{ROI}/r_{PSF})^2$ bins, which for Fermi data above 10 GeV means $N_{bins} = (0.1deg/10deg)^2 = 10^4$ bins. As can be seen in Figure 4.10, most ROIs contain < 500, in the Galactic plane there are up to 5000 events per ROI. In higher energy bands N_{obs} is much smaller still, which is the reason

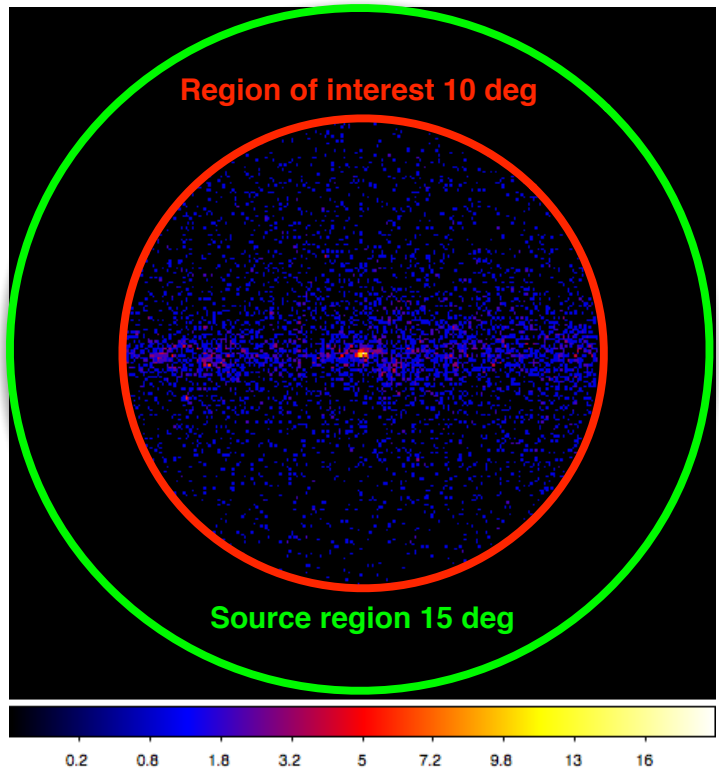

Figure 4.9.. Illustration of the region of interest (ROI) and source region (SR) used in likelihood analysis. This example shows the Galactic center count map above 10 GeV.

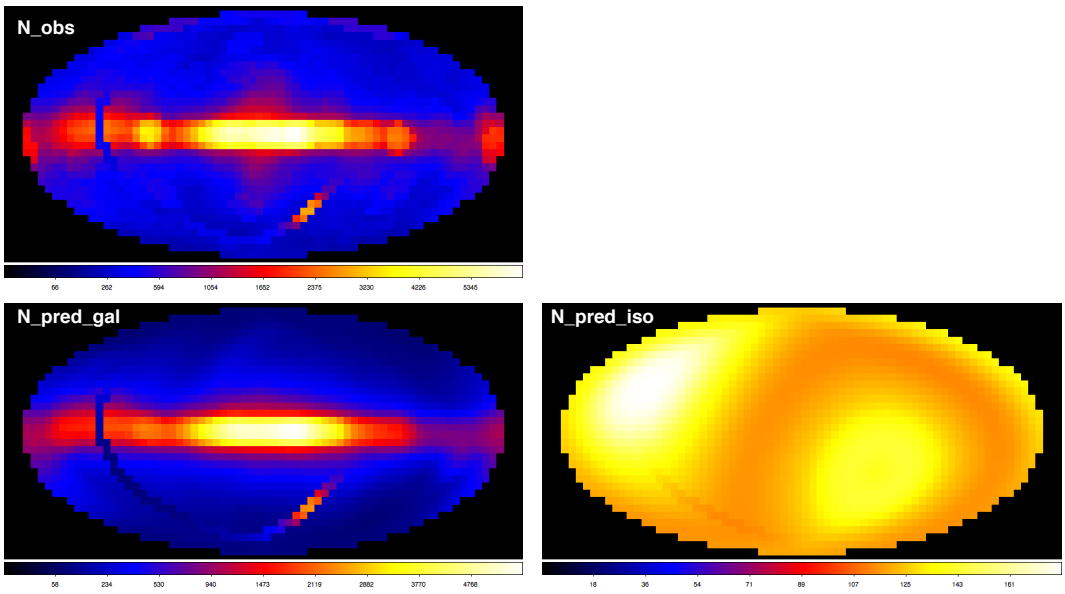

Figure 4.10.. Fermi observed and predicted numbers of events per ROI above 10 GeV. Bright source like the Crab and Vela pulsars as well as the Cygnus region are visible in the N_{obs} image. The curve in the lower and left part of the images is the result of a bug in the analysis script for ROIs containing the $RA = 0$ line.

unbinned likelihood analysis was chosen in this thesis. To save time, the unbinned likelihood computation is actually split up in three parts (`gtdiffrsp`, `gtexpmap` and `gtlike`), as described in Section 4.4.3.

In principle source models can be arbitrary functions of position and energy $S(E, p; x)$, e.g. a PWN model could have energy-dependent morphology, in which case all parameters x have to be fit simultaneously. In practice the Fermi science tools contain two tools (`gtlike` and `gtfindsrc`) to fit models of the form

$$S(E, p; x) = S_E(E; x_E)\delta(p - p_i), \tag{4.10}$$

where `gtlike` can fit the spectral source parameters x_E given an assumed source position and `gtfindsrc` can fit the position given an assumed source spectrum.

The significance of a source is quantified using the *Test Statistic (TS)*

$$TS = 2\log\left(\frac{L_1}{L_0}\right) = 2(\log(L_1) - \log(L_0)), \tag{4.11}$$

where L_0 is the likelihood of the *null hypothesis*—the data is the result of model $S_0(x_0)$—and L_1 is the likelihood of the *alternate hypothesis*—the data is the result of another model $S_1(x_1)$. For the TS maps presented in Section 4.6, we used

$$S_0 = S_{iso} + S_{gal} \tag{4.12}$$

$$S_1 = S_0 + S_{test}, \tag{4.13}$$

i.e. the null hypothesis is that there is only isotropic and diffuse emission and the alternate hypothesis is that there is an additional power-law *test source* at the position in the TS map.

Wilk's theorem states that under certain conditions TS will follow a χ^2 distribution with number of degrees of freedom equal to the extra number of free parameters in the alternate hypothesis. Some of the requirements of Wilk's theorem (Mattox et al., 1996; Protassov et al., 2002) are not met in our case: the number of source photons is not infinite, but very small, and the flux normalization factor has zero as a hard limit. Indeed simulations seem to indicate[18] that even for high-statistics sources the TS distribution is only approximately chi^2.

Nevertheless it is very common to assume that TS very roughly follows a $\chi^2/2$ distribution, i.e. that

$$S = \sqrt{TS} \tag{4.14}$$

[16] See guidelines for choosing ROI and SR radii at `http://fermi.gsfc.nasa.gov/ssc/data/analysis/documentation/Cicerone/Cicerone_Likelihood/Choose_Data.html`

[17] We mean CPU cycle intensive, but in the end computing a TS map costs CPU cycles, the CPU consumes power and power costs money.

[18] `http://silicondetector.org/download/attachments/28521/likelihood.pdf`

Map	Projection	Center (deg, deg)	nxpix	nypix	binsz deg	bin_area 10^{-7} sr
GPS	Cartesian (CAR)	(-20, 0)	10,001	401	0.02	1.22
All-sky	Aitoff (AIT)	(0, 0)	7,200	3,600	0.05	7.62

Table 4.3.. Fermi map geometries. Note that the AIT projection is an equal-area projection, so is the CAR projection within the small latitude range used here. Therefore it is possible to convert between flux and surface brightness by simply multiplying / dividing by the bin area.

has a normal distribution of width 1 for positive S with half of the time $S = 0$, whenever a "negative excess" occurs. Really all we will assume is that high values of S indicate a source, without making a statement about the probability that a given measurement is a background up fluctuation. Such a statement would require extensive simulations, which could be done with `gtobssim`, another Fermi tool.

4.4.2. Binned Analysis

Usually the Fermi toolchain `gtselect` → `gtmktime` → `gtltcube` → `gtbin` → `gtexpcube` → `gtsrcmaps` → `gtlike` is used to fit source parameters as described in the last section. However in this thesis the goal was to make *uncorrelated count, exposure and flux cubes*, for which only the tools `gtbin`, `gtexpcube`, `gtsrcmaps` and `gtmodel` are required, as shown in the workflow in Figure 4.11. Note that all files (counts, exposure, flux, background, significance, excess and source_flux) are not 2D images, but 3D `ENERGY-GLON-GLAT` cubes with the energy binning defined in Table 4.2 and the spatial binning defined in Table 4.3.

The processing steps are:

`gtbin` is used to bin the events into the `ENERGY-GLON-GLAT` cube. The resulting count maps are shown in Figure A.1 for the whole sky and in Figure A.3 for the Galactic plane.

`gtexpcube` is used to compute the exposure (cm^2 s) of each bin at the log bin center in energy. Figure 4.12 shows that the exposure varies across the sky by $\sim \pm 20\%$ (see Figure caption for details) and Table 4.2 and Figure 4.3 that it varies in energy above 1 GeV by $\sim 30\%$ with a peak at ~ 50 GeV.

`gtsrcmaps` & `gtmodel` can, in principle[19], be used to compute an expected counts cube for the background (isotropic and Galactic diffuse emission),

[19] `gtsrcmaps` is generally not suited for survey work. E.g. it is not possible to make an all-sky survey map in Aitoff (AIT) projection as e.g. the one shown in Figure A.1, because it contains

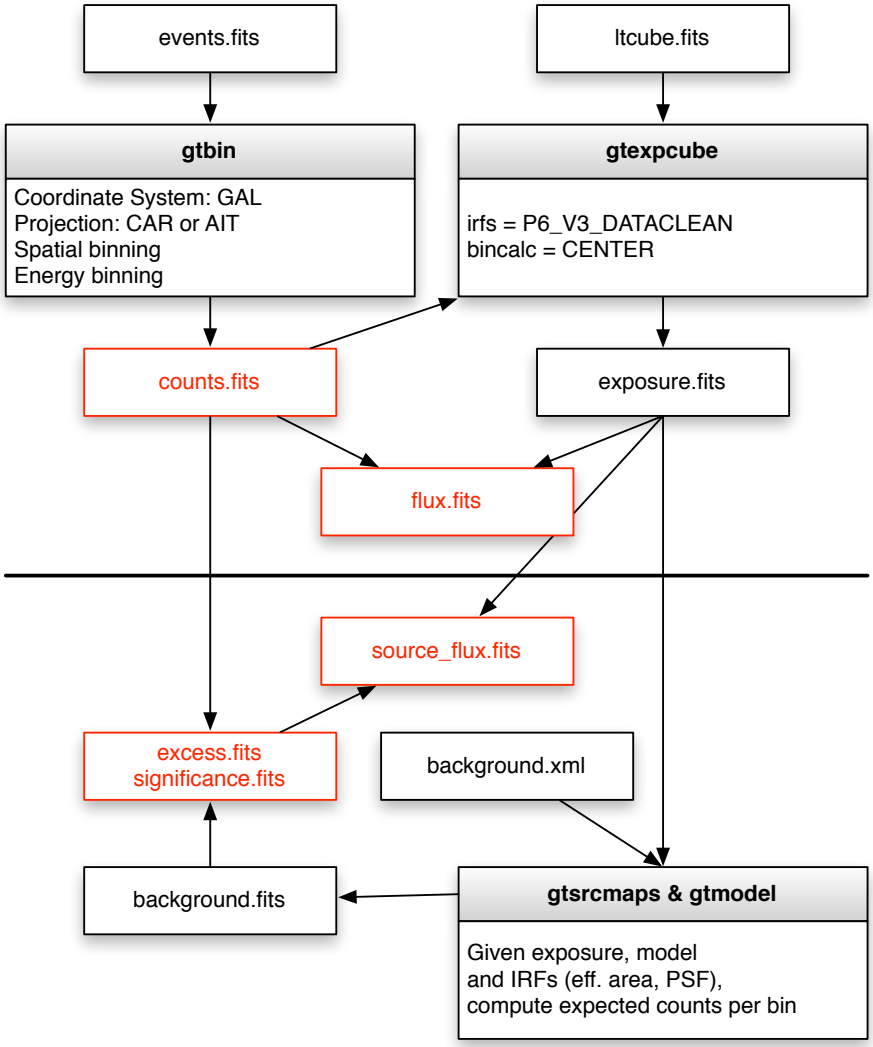

Figure 4.11.. Fermi binned analysis steps. Note that the `events.fits` and `ltcube.fits` files are the result of the preprocessing steps described in Section 4.3.

given the IRFs and exposure.

By computing flux = counts / exposure an uncorrelated flux map can be obtained, errors and limits can be computed as described in Gehrels (1986) and Kraft et al. (1991). However this count and flux measurement is the sum of the desired source flux and the unwanted background. To separate the contributions, the background has to be substracted, resulting in an excess measurement. The source flux can simply be computed as excess / exposure.

Upper and lower errors and limits on the excess and flux can be computed using the methods described in Section 2.5 for the special case of $\alpha = 0$.

Also it is possible to integrate over arbitrary source regions to make aperture-photometry spectra or to make a correlated excess / significance / flux map by tophat-convolving with some correlation radius The same advantages / disadvantages of using such counting methods versus likelihood fitting methods have been discussed in Section 2.5 and equally apply here.

4.4.3. Unbinned Analysis

The main goal of the unbinned likelihood analysis was to make survey significance (i.e. $\sqrt{TS}$) maps to check for known HESS sources if they are GeV-bright and also to identify new promising targets. In the beginning the `gttsmap` tool was used to make significance maps, but eventually was replaced by a self-written python script for the following reasons:

- Computing TS maps is slow, so to make a survey TS map the map has to be split in many small segments which are processed in parallel and put together at the end. Because `gttsmap` doesn't allow complete control over the binning it is not possible to make the small maps such that they perfectly fit together, requiring a reprojecting onto the survey map. While

pixels in the edges that do not correspond to positions on the sky, which makes `gtsrcmaps` crash. Next I tried making an all-sky map in Cartesian (CAR) projection, which contained mirrored double-images of the Galactic diffuse component. Finally following a suggestion from the Fermi helpdesk[20] I tried Mercator (MER) projection, which did not show the double-image problem, but for my map in Galactic coordinates had holes at the Ecliptic poles (i.e. at declination $DEC = \pm 90$ deg). Also `gtbin` v9r18p6 segfaults e.g. for `emin=100 emax=1000 enumbins=2` for the GPS map, but not for some other energy ranges. In summary I did not manage to produce the excess, significance and source_flux maps described in Figure 4.11 for the maps and energy bands described in Tables 4.3 and 4.2, although it does work for small maps (say 30×30 deg). Making survey maps by stitching together small maps is not trivial because unbinned maps count maps cannot be resampled without introducing artifacts and making small maps with edges that perfectly fit together is not possible because with ther Fermi science tools one does not have full control e.g. of the `CRPIX` and `CRVAL` parameter that control the map center. Hopefully these issues will be resolved in future versions of the Fermi science tools so that unbinned survey maps and HESS-style analysis becomes possible. E.g. making Li&Ma significance maps for extended sources by tophat-correlating is about 10^5 times faster than making TS maps, and makes more sense to find new sources, for which one can then still run a full likelihood fit.

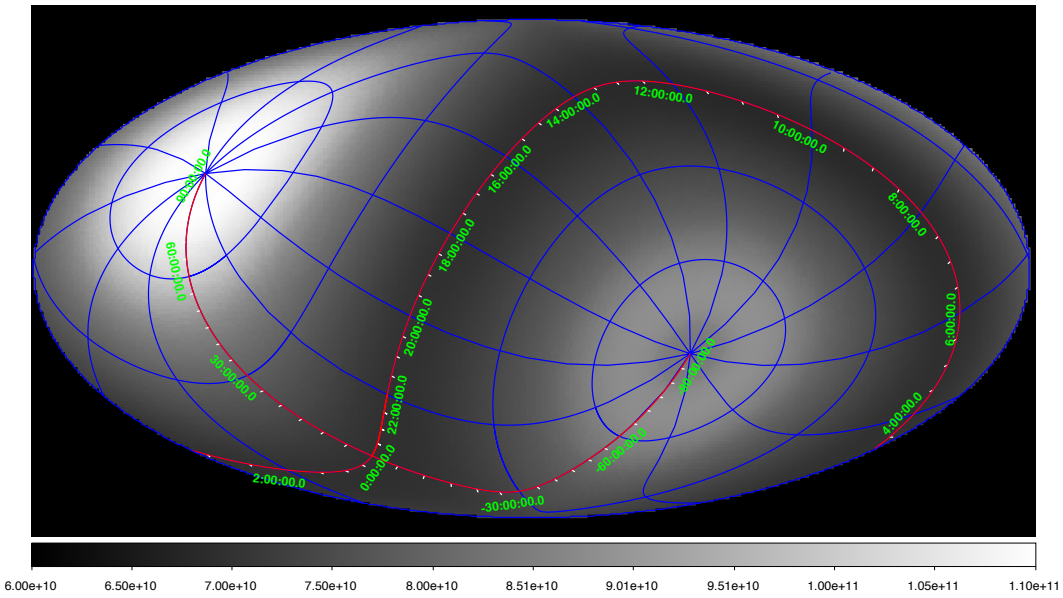

Figure 4.12.. Fermi all-sky exposure image at 100 GeV in Galactic coordinates an Aitoff projection. The graticules show equatorial coordinates, i.e. lines of constant right ascension and declination. The min / mean / max exposure is $(6.8/7.9/11) \cdot 10^{10}$ cm^2 s, i.e. varies by -14 and +40%. The pattern shown here doesn't change significantly at other energies. The exposure within the GPS region varies by 25%, being lowest at $l = +30$ deg ($7.0 \cdot 10^{10}$ cm^2 s) and highest at $l = -60$ deg ($8.7 \cdot 10^{10}$ cm^2 s)

this is possible using the python Kapteyn package[21] or command-line tools like SWARP[22] or MONTAGE[23], it is an unnecessary complication.

- `gttsmap` doesn't give control over the the source model and e.g. fix the spectral index to get a more robust flux estimate at high energies where there are not enough photons to measure the spectral index. Also one has little control over the fit process, e.g. I could not get the Galactic diffuse model norm to converge in some ROIs.
- The most important limitation though is that `gttsmap` only outputs a TS map, and not the corresponding flux and spectral index map, even though these best-fit model parameters have to be computed anyways to compute TS.

The unbinned analysis workflow is illustrated in Figure 4.13. The following Fermi tools were used:

`gtselect` was used to select events within an energy band (E_{min}, E_{max}) and ROI (radius 10 deg, illustrated in Figure 4.9).

`gtdiffrsp` is used to compute the diffuse response,

$$r_j = \int dp S_{diffuse}(E_r, p) R(p_{r,j}; E_{r,j}, p), \tag{4.15}$$

which is proportional to the probability density that photon j came from the diffuse source $S_{diffuse}(E, p)$. This quantity is pre-computed for each photon before running `gtlike`. The diffuse response for the standard isotropic S_{iso} and Galactic S_{gal} diffuse models is already included in the photon file, but because we used a custom isotropic diffuse model instead (see Section 4.5), for this component we had run `gtdiffrsp`. Note that the diffuse response has to be computed for extended sources (S_l term in Equation (4.3)) as well, only pointlike sources (S_i term in Equation (4.3)) don't require the PSF convolution of the source model, because the convolved pointlike model simply is given by the PSF shape.

`gtexpmap` computes

$$\epsilon(E, p) = \int_{ROI} dE_r dp_r dt R(E_r, p_r, t; E, p), \tag{4.16}$$

i.e. the source-independent part of

$$N_{pred} = \int_{SR} dE dp S(E, p) \epsilon(E, p). \tag{4.17}$$

[21] `http://www.astro.rug.nl/software/kapteyn/`
[22] `http://www.astromatic.net/software/swarp`
[23] `http://montage.ipac.caltech.edu/`

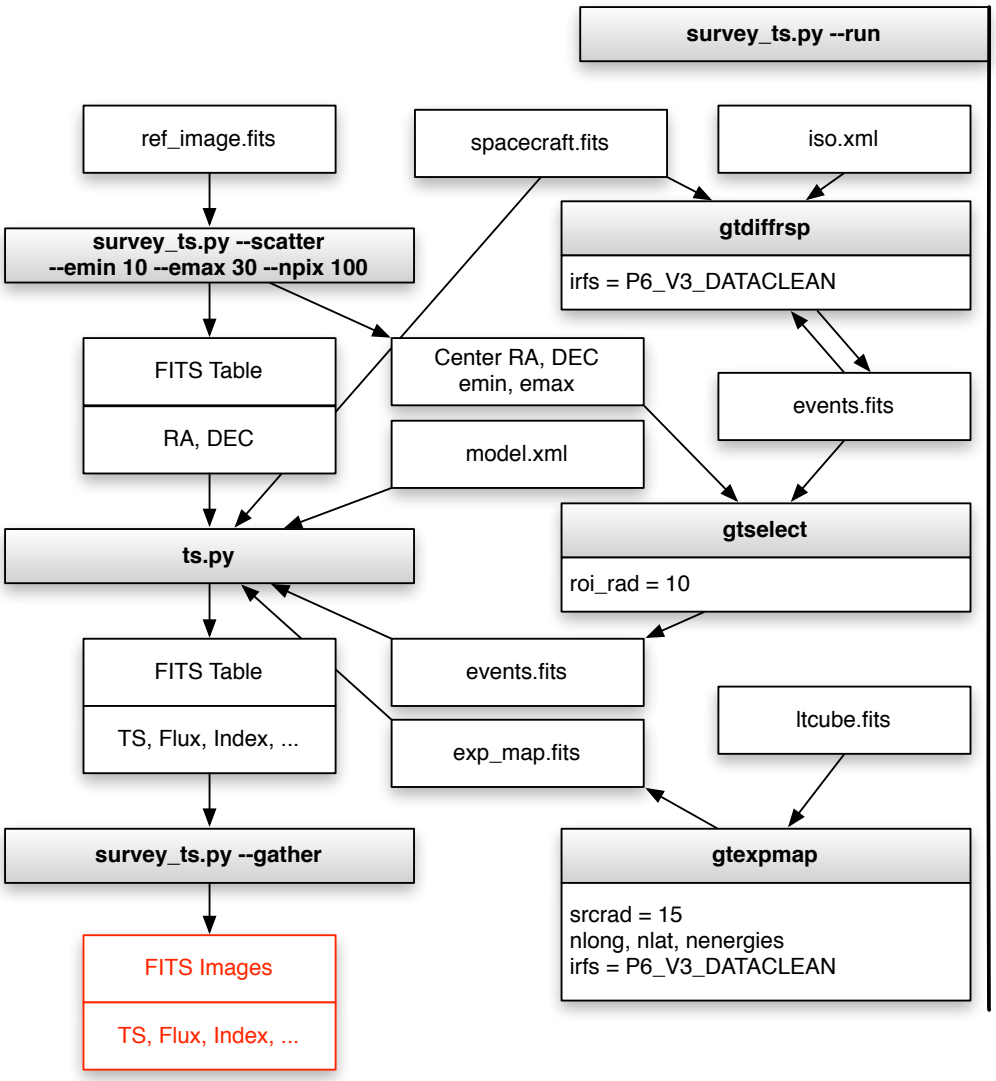

Figure 4.13.. Fermi unbinned analysis steps. Note that the `events.fits` and `ltcube.fits` files are the result of the preprocessing steps described in Section 4.3.

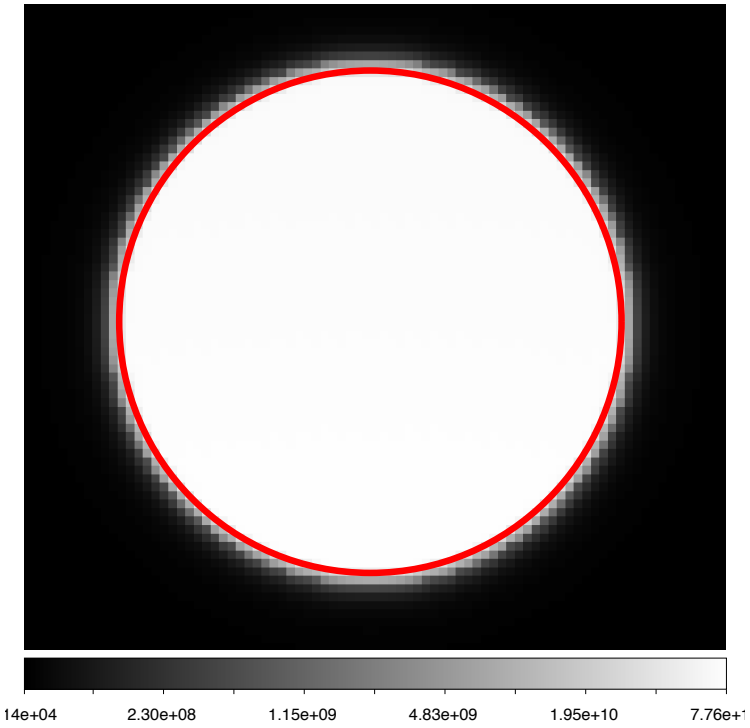

Figure 4.14.. Fermi exposure map for one ROI as used in unbinned analysis. Note that the exposure extends outside the ROI (10 deg, red circle) by one PSF width. Inside the ROI the exposure has a linear gradient with 10% change top to bottom (not visible because the scale has been chosen to make the small exposure outside the ROI visible).

The exposure map (see Figure 4.14) contains the total exposure in cm^2 s, but multiplying this exposure ϵ with a source model S at this position describes the number of expected counts that will fall in the ROI and thus contribute to N_{pred}, not the expected number of counts at the given position itself. This is different from the exposure cube computed by `gtexpcube`, where the interpretation is simpler. Inside the ROI, more than a PSF width away from the edge, the exposure map and exposure cube values agree.

Really the details of which parts of the likelihood function `gtdiffrsp` and `gtexpmap` pre-compute are not that important. The two important scripts in Figure 4.13 are

ts.py that computes the null likelihood L_0 for the ROI and then for a grid of positions computes the source $L_1, F_0, \Gamma, \Delta F_0, \Delta\Gamma, cov(F_0, \Gamma), N_{pred}$ and from

this TS using Equation (4.11). This is done by making the same computations `gtlike` does, but through the UnbinnedAnalysis python interface.

survey_ts.py takes any referece image as input, splits it into small quadratic pieces that are easily contained within ROIs of 10 deg, submits batch jobs to a computing cluster to run `ts.py` in parallel using many CPUs, and when all jobs have finished, gathers the pieces into survey TS, flux, etc. maps. Really the whole pipeline operates on lists of positions using FITS tables instead of images, so it would e.g. also easily be possible to work with HEALPIX[24].

The resulting maps can be seen e.g. in Figures 4.15 and A.4, which will be described in more detail in Section 4.6.

4.5. Diffuse Background

The diffuse background is modelled as the sum of two components, Galactic and isotropic, described in the following sections.

4.5.1. Galactic

As mentioned in Chapter 1, the Galaxy is filled with comic rays (nuclei and electrons), that produce a diffuse background of gamma rays when they interact with gas (π^0 emission for nuclei, Bremsstrahlung emission for electrons) or radiation fields (IC emission from electrons). The flux level at Earth for a given position on the sky is given by the line of sight integral over (cosmic ray density $\times$ target density $\times$ interaction cross section).

Figures A.1 and A.3 show this diffuse emission in the Fermi count maps. The Fermi LAT collaboration has released a model (`gll_iem_v02.fit`) that is the result of a combination of detailed modelling (GALPROP[25], as well as observations from the radio to the gamma-ray range. Figure 4.16 shows images of that model at 12 and 100 GeV and Figure 4.17 shows spectra at a few selected locations.

The Fermi LAT collaboration diffuse model is described in more detail on the web.[27]

As can be seen in Figure 4.18, the Galactic diffuse model is far from perfect and is—together with source confusion—the largest problem for source analysis in the Galactic plane. One problem is that the latitude scale height is only ~ 1 deg, and the `gll_iem_v02.fit` gamma-ray model as well as the gas maps it is based on only have a pixel resolution of 0.5 deg Dame et al. (2001). Another problem is that the diffuse Galactic gamma-ray emission observed by Fermi

[24] `http://healpix.jpl.nasa.gov/`
[25] `http://galprop.stanford.edu`
[27] `http://fermi.gsfc.nasa.gov/ssc/data/access/lat/BackgroundModels.html`

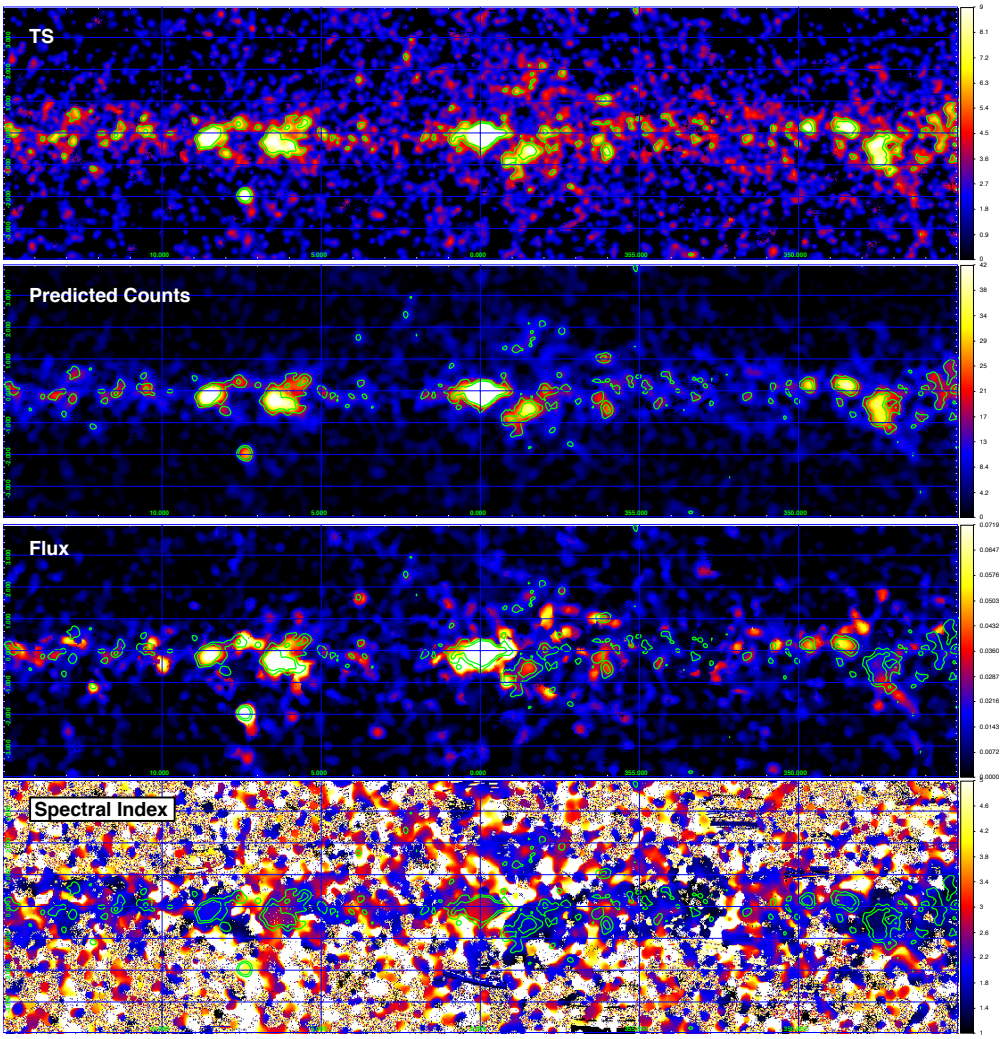

Figure 4.15.. Fermi maps resulting from the unbinned likelihood analysis in the 10 to 1000 GeV energy band in the region $l = \pm 15, l = \pm 4$ deg. The contours are identical in all four images and correspond to significance 5 and 7. Note that significance, predicted counts and flux look very similar (no tricks were played to make it appear so, all images are shown in a linear color scale covering 99% of the min / max range). The main difference is that significance shows structure on smaller scales and is higher in low-background regions, because $S \sim F/\sqrt{B}$. On the other hand the spectral index map gives a completely new view on the data, with soft spectrum sources in yellow and hard spectrum sources in blue.

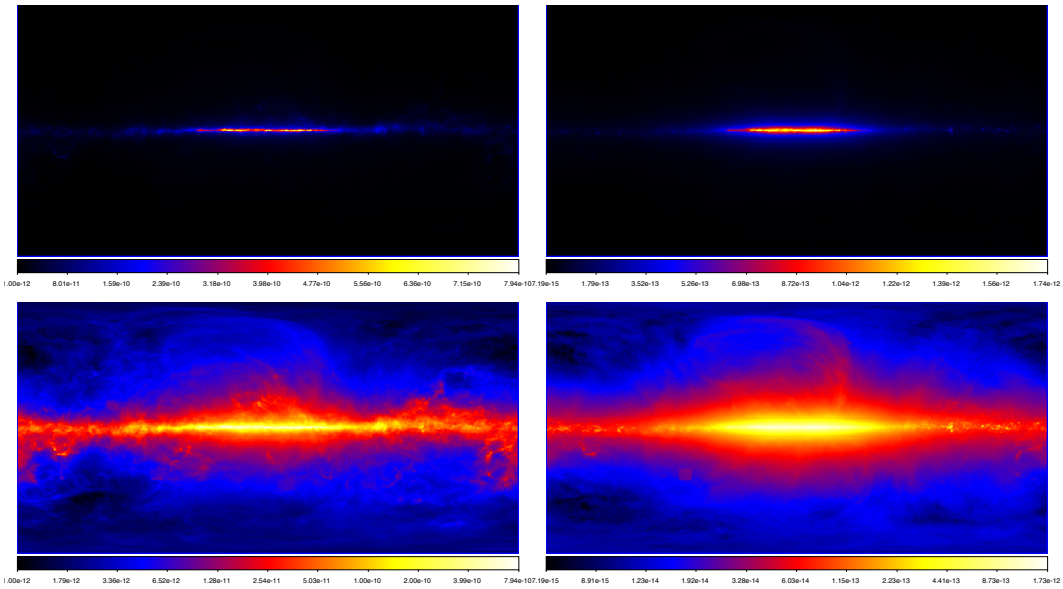

Figure 4.16.. Fermi Galactic diffuse background model at 12 GeV (left) and 100 GeV (right). These energies correspond to planes #21 and #30 in the FITS cube `gll_iem_v02.fit`. The same data is shown twice for each energy, once in a linear color scale (top) and once in a log color scale (bottom). It is useful to compare this image the spectra shown in Figure 4.17 and to the distribution of gas and electrons in the Milky way as inferred from radio observations and shown in Figure 1.6. Note that this image is flipped left to right with respect to the astronomical convention and all other images in this thesis, i.e. here the longitude increases to the right!

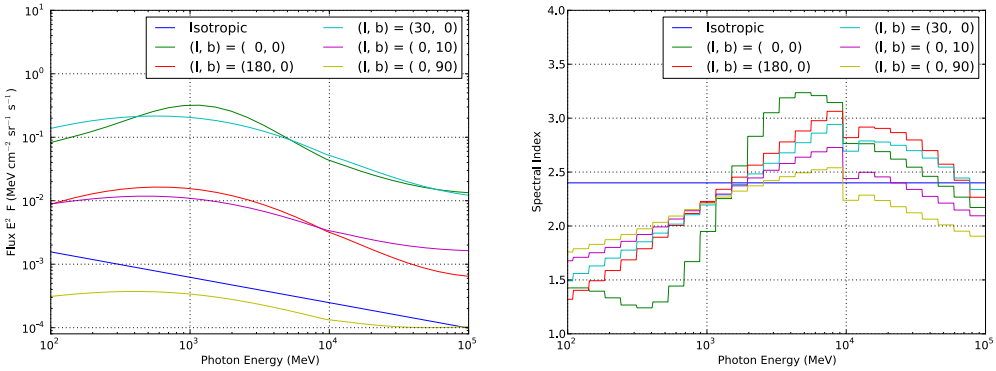

Figure 4.17.. Fermi Galactic and isotropic diffuse background spectra. The isotropic component is a power law with spectral index 2.4. The isotropic spectra were taken at specific positions in the `gll_iem_v02.fit` FITS cube[26], which contains the diffuse flux at 30 energies in the range 50 MeV to 100 GeV. Linear interpolation in log energy was used, which is responsible for the steps seen in the spectral index on the right. Linear interpolation was chosen for this plot because second or third order spline interpolation results in an oscillation in spectral index at 10 GeV. The Galactic diffuse emission at very high Galactic latitudes has the same order of magnitude as the isotropic emission. In the Galactic anticenter or 10 degrees above the Galactic center it is about an order of magnitude higher, and in the Galactic plane at longitudes 0 or 30 it is two orders of magnitude higher. The spectral index of the background in the 10 to 100 GeV band ranges from 2 to 3, depending on the location in the sky. The spectrum is the sum of thre components: pion decay from hadronic interactions and inverse Compton and Bremsstrahlung from electrons (see e.g. Aharonian and Atoyan (2000) and Zhang et al. (2009))

does not match expectations obtained from GALPROP simulations of cosmic ray acceleration, propagation and interactions in the Milky Way.

Recently Su et al. (2010) discovered the "Fermi bubbles", gigantic lobes of gamma-ray emission, which are not included in `gll_iem_v02.fit` at all. These structures as well as other large-scale unmodelled components can be seen in Figure 4.18.

4.5.2. Isotropic

There is gamma-ray background from unresolved extragalactic sources (e.g. AGN) that is roughly isotropic. Furthermore for each any set of analysis cuts, there will be a residual level of cosmic rays in the data that can also be modelled as a roughly isotropic flux. For DATACLEAN cuts, the Fermi LAT collaboration has published the `isotropic_iem_p6v3dataclean_v02.txt` isotropic background spectrum[28].

As shown in The Fermi-LAT collaboration (2010), the isotropic gamma-ray background is a power law in the range 200 MeV to 100 GeV with spectral index 2.4 and intensity $I(E > 100MeV) = 1.0 \cdot 10^{-5} cm^{-2} s^{-1} sr^{-1}$. The residual cosmic ray intensity after DATACLEAN cuts corresponds to only 10% of the isotropic gamma-ray flux.

The isotropic background spectrum `isotropic_iem_p6v3dataclean_v02.txt`, including 10% contributions of residual cosmic rays, as appropriate for `P6_V3_DATACLEAN` analysis is shown in Figure 4.5.

The way to use `isotropic_iem_p6v3dataclean_v02.txt` in the Fermi science tools is as a `FileFunction`, which interpolates the given points to get a model at any given energy. Because `isotropic_iem_p6v3dataclean_v02.txt` has the last point at an energy of 124 GeV, but we wanted to analyze data up to 1000 GeV, the isotropic background model had to be extended at the high-energy end.

This was done using the following power law,

$$F(E) = 2.00 \cdot 10^{-12} cm^{-2} s^{-1} MeV^{-1} \left(\frac{E}{10.9 GeV} \right)^{-2.4} \tag{4.18}$$

obtained by taking the spectral index of 2.4 from The Fermi-LAT collaboration (2010) and normalizing it to go through the first flux point above 10 GeV. The normalization obtained corresponds to an integral flux above 100 MeV of $1.12 \cdot 10^{-5} cm^{-2} s^{-1}$, 10% above the flux published for the isotropic gamma-ray background (without residual cosmic rays) in The Fermi-LAT collaboration (2010), as expected.

[28] `http://fermi.gsfc.nasa.gov/ssc/data/access/lat/BackgroundModels.html`

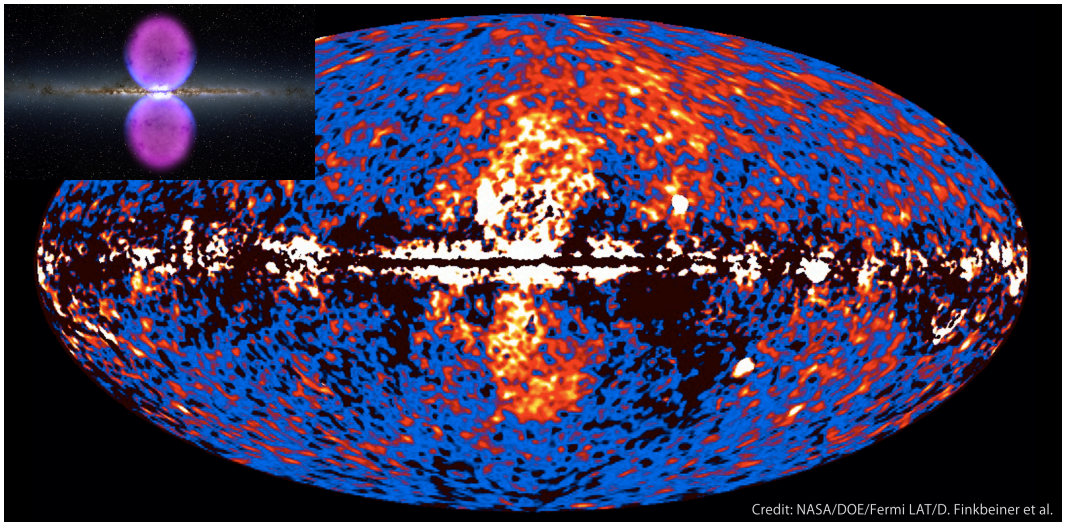

Figure 4.18.. Fermi all-sky residual map in the 1 to 10 GeV energy band, obtained by subtracting the contribution of point sources as well as the standard isotropic and Galactic diffuse emission models from the total count map and smoothing by ~ 1 deg (see Figures A.1 and 4.16). The most prominent feature are two large regions of positive excess extending to ± 50 deg above and below the Galactic center, known as the "Fermi bubbles" (shown as an artist's impression in the inset in the upper left corner). A positive excess is also visible from the Large Magellanic cloud (LMC) at $(l, b) = (-100, -33)$ deg as well as the Cygnus region at $(l, b) = (+80, +1)$, which in both cases might be due to a concentration of unresolved sources or truly diffuse emission. In general there is a negative excess along the Galactic plane, and a positive excess above and below the plane, indicating that the width in latitude in the Galactic diffuse model is too broad. Figure adapted from `http://www.nasa.gov/mission_pages/GLAST/news/new-structure.html`.

4.5.3. Background Parameters in Source Fitting

When analyzing sources in any given ROI, usually (i.e. for analyses including lower energies, typically the range 100 MeV to 100 GeV) the norm and sometimes also the spectral index of the diffuse Galactic background are left as free parameters both for the L_0 and L_1 fit.[29] The reason is that as explained in Section 4.5.1, the Galactic diffuse model is not perfect. If the norm is not adjusted for the ROI under investigation, the total N_{pred} will not match N_{obs} and the following errors will be made:

- If the background model is too high, the flux and significance of sources will be underestimated.
- If the background model is too low, the flux and significance of sources will be overestimated.

On the other hand, if the background norm is fitted in the ROI, the background level will generally be overestimated—and thus source fluxes and significances underestimated—because there are unmodelled sources in the ROI, the flux of which gets effectively attributed to the background in the likelihood fit.

After some experimentation for the results presented here I decided to fix both the isotropic and Galactic diffuse background components completely, for the following reasons:

1. The goal was to make survey significance maps, which meant that it is not possible to put other sources in the ROI in the background model, since then they would be background and not show up in the significance map. Anyways as shown in Section 4.7 the 2FGL does not represent the high-energy sources particularly well.
2. In the highest-energy band, above 100 GeV, there are too few photons per ROI at high latitudes to fit the background level reliably. For 10 counts, Poisson fluctuations of ± 3 are larger than the systematic error in the diffuse model normalizations.
3. For some ROIs very bright sources (such as Vela, Crab and the Cygnus region, see Figure 4.10) dominate over the diffuse background. As explained above, leaving the background level free, for test source positions beside the sources, the emission from the sources resulted in an overestimation of the background by a factor of up to ~ 2.
4. Last but not least, survey TS maps are very computationally intensive, and introducing an additional free fit parameter for the background means that a factor of a few more iterations are required for fit convergence.

[29] Technically this is done by using the `ConstantValue` and `PowerLaw` or `PowerLaw2` spectral models.

Luckily at high energies (above 10 GeV and even more so above 100 GeV) photons statistics is low, which means that statistical errors on derived source fluxes and spectral indices are very large and systematic errors due to incorrect background models don't dominate, as they would for Fermi analyses above 100 MeV.

4.6. Maps

Most of the Fermi maps have already been described in previous sections, this section will only summarize and make a few more remarks.

- Maps were produced for two regions, defined in Table 4.3. The higher resolution of the GPS maps allows a slightly better deblending and localization (see Section 4.7).
- Maps were produced in three small energy bands 10 – 30 – 100 – 1000 GeV, defined in Table 4.2 as well as for the full energy band 10 – 1000 GeV.
- Using the binned analysis as described in Section 4.4.2, count cubes were produced, some planes of which are shown in Figures A.1 and A.3 as well as exposure cubes with one plane shown in Figure 4.12. Using these uncorrelated cubes, it is possible to do aperture photometry for arbitrary regions (e.g. defined by Fermi, HESS, radio or X-ray sources) and to extract a spectrum by summing the counts and averaging the exposure in each energy band of the cubes.
- Using the unbinned analysis as described in Section 4.4.3, point source significance, flux and number of predicted counts maps were made. Note that these maps are effectively PSF-correlated, i.e. in contrast to the binned maps one simply reads off map values instead of summing over regions. The interpretation of the map values is simply the significance or flux if a point source were at that position. For the small energy bands the spectral model was a power-law source with spectral index of 2, for the full band the spectral index was a free fit parameter.
- The unbinned all-sky maps do contain one major artifact in the ROIs that contain the $RA = 0$ line (which is illustrated in Figure 4.12). At the moment it is not quite clear what happened, e.g. as Figure 4.10 shows it seems that N_{obs} was mirrored in DEC, which could be the result of a bug in the `survey_ts.py` script. Anyways the result is that these ROIs have significance zero as can be seen in Figure A.2, and potential sources in these ROIs are missing from the all-sky catalog presented in Section 4.7.
- Figure 4.20 illustrates another minor artifact of the unbinned maps. For the two-parameter fit (norm and spectral index) for the 10 – 1000 GeV

maps, the minimization or error computation (done with MINUIT James and Roos (1975)) failed. The flux and flux error maps from the small energy bands, where the spectral index was fixed to 2, do not show this problem. Because so few pixels are affected, probably none of the values reported in the catalog (see Section 4.7) are incorrect.

- Figure 4.19 shows the $\sqrt{TS}$ distribution of the maps for the two regions and four maps, which clearly does not follow the naive expectation of $\chi^2/2$ distributions. Without simulations it is impossible to say to what extent the following factors lead to a deviation from the naive expectation:

  1. The sky (and especially the Galactic plane) contains many (resolved and unresolved) sources.
  2. The diffuse Galactic model e.g. does not contain the Fermi bubbles, which as a result are huge regions of overestimated significance, visible in Figure A.2. Also the model is not perfect in the Galactic plane, as illustrated in Figure 4.18.
  3. The conditions in the derivation of the χ^2 distribution (large counts, no hard limit on fit parameter) are not satisfied for the Fermi high-energy significance maps[30] (Mattox et al., 1996).

  In this thesis—as is quite common—the term "significance" is used for the number $S = \sqrt{TS}$, even though this is somewhat incorrect. S is a measure for the probability that there is a source in the sense that the higher S the more likely it is that there is a source, but because the distribution of S for background only is unknown, it is not possible to make a quantitative statement.

4.7. Catalogs

In this section two catalogs are presented, one based on Fermi data above 10 and the other above 100 GeV. They are listed in Appendix B and the position of the sources is indicated in Figures A.4 and A.2.

Note that the catalogs are based on the point-source maps from the unbinned likelihood analysis presented in Section 4.4.3 and illustrated in Figure 4.15. This means that for extended sources, the significances and fluxes quoted will be too low, because the point-source analysis only attributes part of the extended emission to the assumed point source.

We will now describe the three steps that were performed to construct the catalogs: detection, measurement and association.

[30] http://silicondetector.org/download/attachments/28521/likelihood.pdf

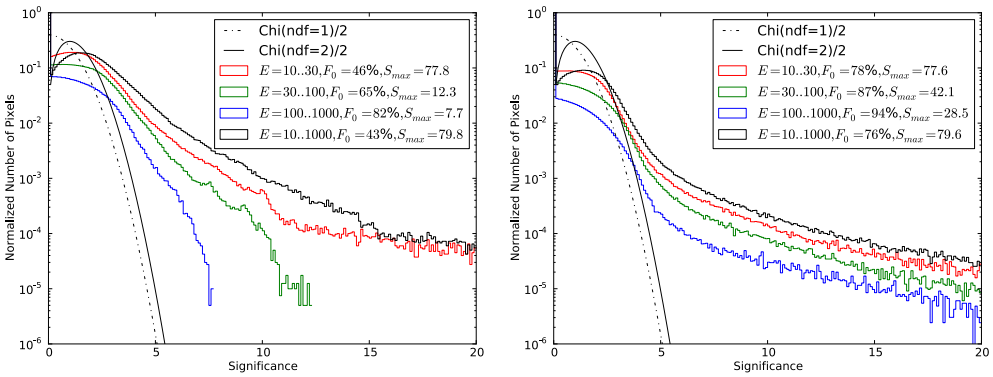

Figure 4.19.. Fermi significance (defined as $\sqrt{TS}$) distributions for the GPS region (left) and the whole sky (right). For the small energy bands (shown in RGB) only the norm of the test source was free in the fit of the alternate hypothesis, so the naive expectation is that the significance for background only should be chi-distributed with one parameter. For the full energy band (10–1000 GeV) both the norm and spectral index of the test source were fit, and the naive expectation is that the significance for background only follows a chi distribution with two parameters. In both cases a significance of zero is expected half of the time, i.e. for 50% of the pixels. The observed distributions only very roughly follow this naive expectation, mainly because they contain sources (high-significance tails), the statistics is low ($\sim 90\%$ of the positions in the sky are more than a few PSF widths away from the next photon above 100 GeV) and the background model is not perfect. The highest-significance source in the red and full energy band is Vela. In the green and blue band the highest-significance source is Mkn 421 outside the GPS region. Inside the GPS region the greenest source is the off-plane ($l = 332, b = 2.6$) AGN PMN J1603-4904 seen by Fermi, 2FGL J1603.8-4904, with no hint for emission by HESS. The bluest source in the GPS region is the UNID 2FGL J1836.8-0623c, HESS J1837-069, possibly the PWN of PSR J1838-0655.

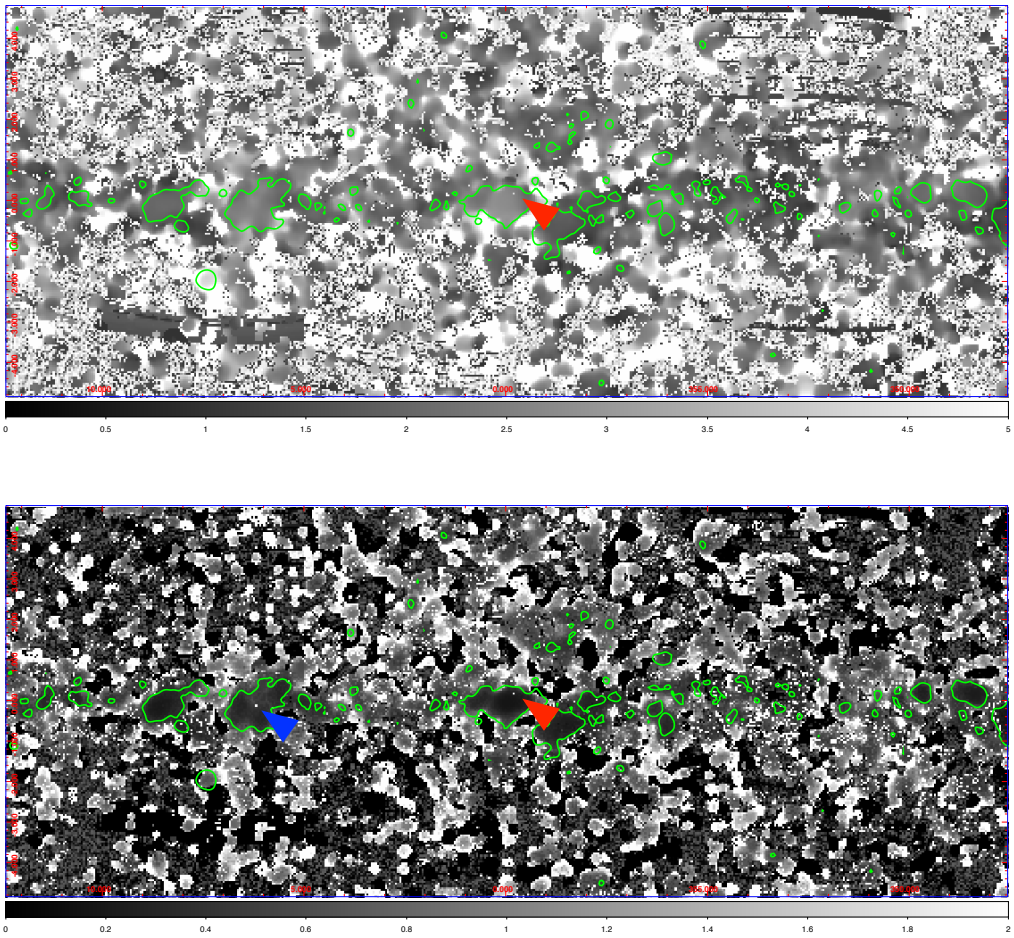

Figure 4.20.. Fermi spectral index (top) and spectral index error (bottom) map (25×10 deg FOV around the Galactic center) from the unbinned likelihood fit of a test power-law spectrum point source at each position in the 10 to 1000 GeV energy band. The green contours correspond to 5 sigma ($TS = 25$). In regions with no photon the map values are arbitrary, but also irrelevant. Only values inside the 5-sigma contours were used for the catalog, and there only very rarely did the fit not converge and the map contains incorrect numbers. The red arrows show such an example (a single white pixel) where both the minimization (MIGRAD) and the error matrix computation (HESSE) failed. The blue arrow shows an example (block of four white pixels) where the spectral index is correct (MIGRAD succeeded), but the error is incorrect (HESSE failed).

E_{min}	S_{min}	S_{seg}	C	Region	$N_{sources}$
10	7	5	0.01	GPS	67
				All-sky	347
100	5	3	1	GPS	38
				All-sky	87

Table 4.4.. Fermi source catalog summary. The detection parameters are the detection threshold S_{min} as well as two parameters controlling the deblending of nearby sources, the segmentation threshold S_{seg} and C =DEBLEND_MINCONT minimum contrast parameter from SExtractor. Also shown is the number of all-sky detections (including the ones from the GPS regions) as well as the number of sources in the GPS regions alone.
Note that 50% of the sources above 100 GeV are in the GPS region, but only 20% of the sources above 10 GeV and only 13% (239 out of 1873) for the 2FGL. This could in part be due to AGN having on average softer spectra than Galactic sources, but could just as well be the result of many false detections in the Galactic plane, e.g. due to an incorrect diffuse emission model or the detection of up fluctuations in the wings of bright extended sources, which happens more frequently with lower statistics, i.e. at higher energies. Or the other way around, the larger Fermi PSF at low energies can blend sources that are separated in the high energy catalogs, resulting in a low fraction of in-plane versus off-plane sources.

Detection

Source detection was performed using the significance maps as illustrated in Figure 4.21 using SExtractor[31] (Bertin and Arnouts, 1996) and the parameters listed in Table 4.4.

Any detection method uses a threshold, and here we chose 5 / 7 for the 100 / 10 GeV band. The choice of these thresholds is of course somewhat arbitrary, higher values would result in fewer false detections, but also more missed detections.

The reason I chose the very low threshold of 5 for the 100 GeV band is that a higher threshold of e.g. 7 would have resulted in only two detections in the GPS region (see Figure 4.19).

The background level is so low that a single photon results in a significance of 3 and three photons within a PSF radius of ~ 0.2 deg (or even two very close, very high energy photons) result in a significance > 5. In this low-count regime, the trial factor estimate $N_{trials} = A_{survey}/A_{PSF}$ no longer holds, because most of the sky is empty. There are $A_{sky} \sim 40,000$ deg^2 in the sky and $N_{photon} = 3500$ photons above 100 GeV, where the Fermi PSF has an area of $A_{PSF} \sim$

[31] http://www.astromatic.net/software/sextractor

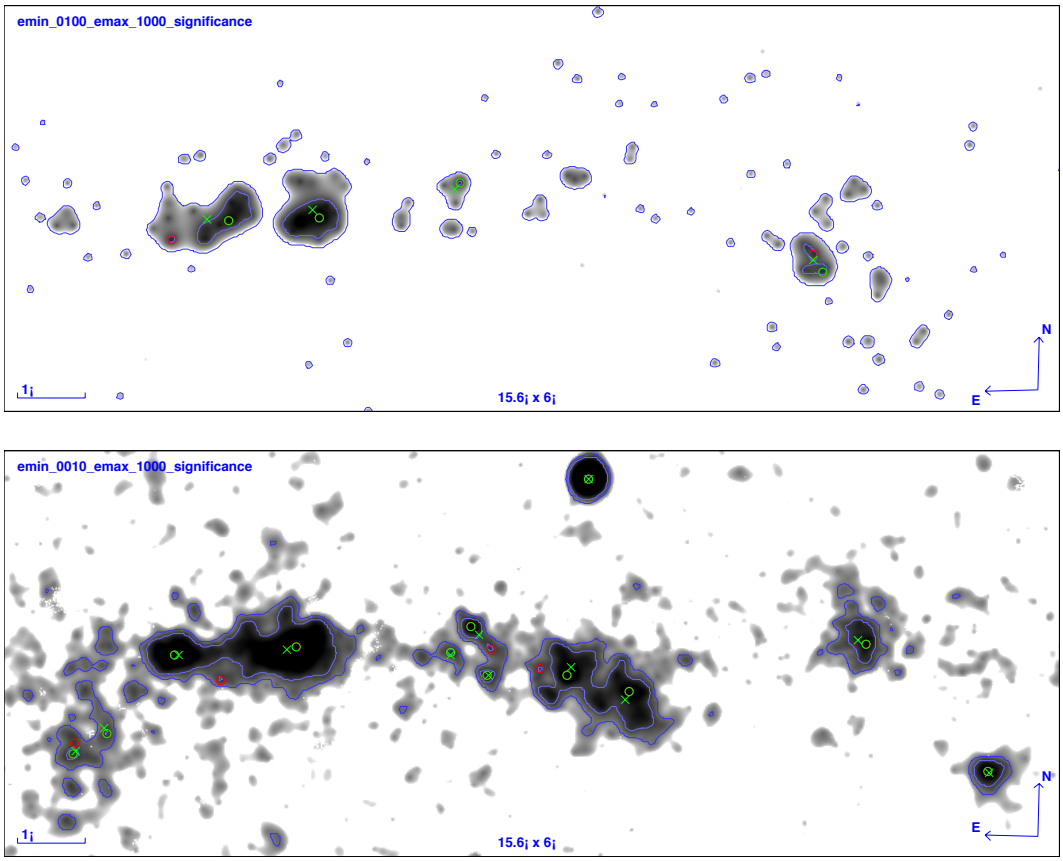

Figure 4.21.. Illustration of the Fermi detection method. The top image is centered on $(l, b) = (333, 0)$ and shows significance above 100 GeV on a linear greyscale in the range 3 to 7, with contours at 3 and 5. The bottom image is centered on $(l, b) = (22, 0)$ and shows significance above 10 GeV on a linear greyscale in the range 3 to 10, with contours at 5 and 7. The red circles show all peaks above the detection threshold (5 for 100 GeV, 7 for 10 GeV), the green circles only the ones included in the catalog (see main text and Table 4.4 for a definition of the detection method). Under every green circle there is a red circle. In addition for the catalog sources the barycenters (defined in the main text) are shown as green crosses.

n	Probability	Significance	$\langle N_{bins} \rangle$
1	2.66e-03	2.8	3.50e+03
2	3.55e-06	4.5	4.66e+00
3	3.15e-09	5.8	4.14e-03
4	2.10e-12	6.9	2.76e-06
5	1.12e-15	7.9	1.47e-09

Table 4.5.. Rough estimate of the probability of n-photon clusters in Fermi 100 GeV all-sky map. The assumption was made that the sky has $A_{sky}/A_{PSF} = N_{bins} = 1.3 \cdot 10^6$ independent bins and the $N_{photons} = 3500$ photons are isotropically distributed, i.e. the mean number of photons per bin is $\mu = N_{photons}/N_{bins} = 2.67 \cdot 10^{-3}$. The table shows the probability $P = poisson.sf(n, \mu)$ and equivalend significance $S = norm.isf(P)$ to find n or more photons in a given bin, as well as the expected number of bins $\langle N_{bins} \rangle$ containing n or more photons in an all-sky survey. See main text for further explanations.

$\pi(0.1deg)^2 = 0.031$ deg^2. This means that there will be one photon per 10 deg^2 or $\mu = 2.67 \cdot 10^{-3}$ per A_{PSF}. Table 4.5 shows the probability, significance and expected number of times per survey a cluster of n photons occurs. Note how rapidly the probability of n-photon cluster decreases with n, basically

$$P(\geq n) = \mu^n. \tag{4.19}$$

Of course this estimate was very simplistic, in reality the likelihood TS map takes the real shape of the PSF into account, the spectrum of the signal and background and most importantly the fact that the background level varies by a factor of 100 over the sky (see Figures 4.16 and 4.17).

The 100 GeV catalog (Appendix B) contains the significance S, number of predicted counts N_{pred} and number of counts $N_{0.3\ deg}$ within a radius of 0.3 deg around the peak position, so that the reader can easily apply her own detection criteria.

The motivation for the threshold of 7 in the 10 GeV band is that a lower threshold would have resulted in many false detections, as can be seen from the contours in Figure 4.21 and from the indication of a break in the TS distribution in Figure 4.19 (right) around significance 6.

However, the detection method applied here was not a simple thresholding. As illustrated in Figure 4.21, simply thresholding would lead to false detections in the wings of extended sources (the red circles). Imagine a perfectly smooth, but very extended source, e.g. of Gaussian or shell-type shape. The significance contours will follow this shape, but at any given level fluctuate by $\sim \pm 1\sigma$ because of the finite photon statistics. Thus thresholding at any given level will create segments and peaks corresponding to background fluctuations, not real sources.

One possible method to remove these wing-fluctuations is to introduce a second lower threshold. As can be seen from the contours in Figure 4.21, the segments defined by this lower threshold will typically include the wing-fluctuations and one can simply make a catalog with one source per segment, located at the highest peak within the segment. This method was applied with second threshold 3 / 5 for the 100 / 10 GeV map.

In the case of the 10 GeV map, this one source per segment approach is however not satisfactory, because the source density and average source extension is so high that clearly separated peaks get merged into one source (see the example in the middle and on the left of Figure 4.21, bottom). `SExtractor` provides a method to deblend such overlapping sources (or peaks in the intensity distribution of one source) into separate components using a multi-level thresholding algorithm, described in detail in the `SExtractor` manual. For each segment (above the lower threshold 5 for the 10 GeV map) 32 significance levels are chosen, linearly spaced between the lower threshold and the maximum significance in the segment. Then the algorithm goes downwards and constructs a tree representing source components. New segments appearing become new leaves in the tree and whenever segments touch, a decision is made to merge them or keep them as separate components based on the `DEBLEND_MINCONT` minimum contrast parameter. Setting `DEBLEND_MINCONT` to 0 means that every local peak will become a separate object, a contrast (sum of pixel values in sub-segment over sum of pixel values in total segment) of 1 can only be reached by the whole segment, so in that case no deblending will occur.

Again, as with the primary threshold, the choice of secondary thresholds and minimum contrast are somewhat arbitrary. However it turns out that the resulting catalog does not depend strongly on the exact values of these parameters, e.g. changing the lower threshold by ± 1 or `DEBLEND_MINCONT` by a factor of 10 only affects a handful of detections in the Galactic plane.

Measurement

The resolution of the maps is high enough that it is possible to simply read off the significance, flux, etc. for any given point source at the peak-significance position (see Figure 4.22). These values correspond to the ones one would get by running findsrc to determine the source position and then gtlike to measure its spectrum.

Of course we have made the assumption that each source is well isolated and point-like, the properties of big sources like e.g. Vela Jnr cannot be determined from these correlated maps (see Figure 4.23). Because the Vela Jnr SNR is so large (1 deg radius), it is detected as two sources in the 10 and 10 GeV catalog. In the 2FGL catalog its emission is represented by four sources. Even though the TS maps described in this thesis were made for point sources, they are still very useful to study the morphology (visually, not quantitatively) of extended sources.

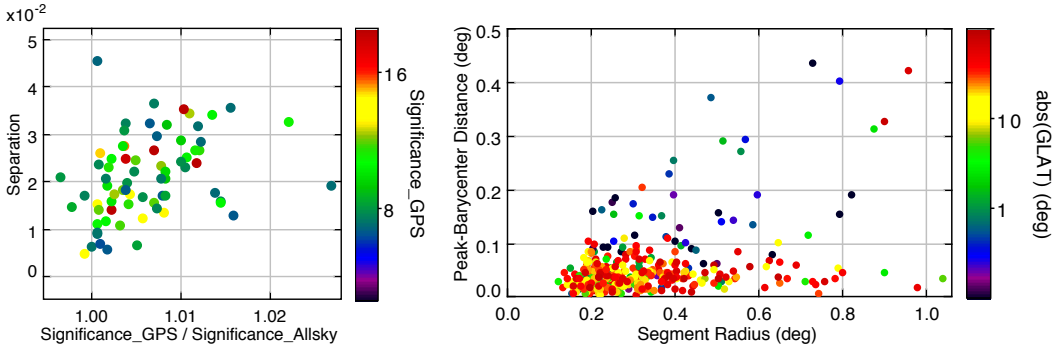

Figure 4.22.. Fermi 10 GeV catalog position accuracy. *Left:* Significance ratio versus separation for all 74 sources in the GPS region, as measured on the high-resolution (0.02 deg) GPS map and on the low-resolution (0.05 deg) all-sky map (pairs determined via a closest neighbor match). Binning errors cause localization errors in the all-sky map of typically 0.02 deg, up to 0.05 deg and relative significance errors of less than 2%. Similar scatter is found in the measured fluxes and spectral indices, indicating that the 0.05 deg resolution of the all-sky map is sufficient for measurements. *Right:* Peak-barycenter distance versus segment size. The segment size was computed as $\sqrt{ISOAREA\_WORLD/\pi}$, where `ISOAREA_WORLD` is measured by `SExtractor` as the area of the segment the source is in after thresholding the significance map at 5 sigma. Note that most of the large segment sources are high significance point sources like Crab, Vela and Mkn 421, not sources that are really extended. Also note that most sources with peak-barycenter separation > 0.1 deg lie in the Galactic plane, as a result of non-pointlike Galactic sources and source confusion.

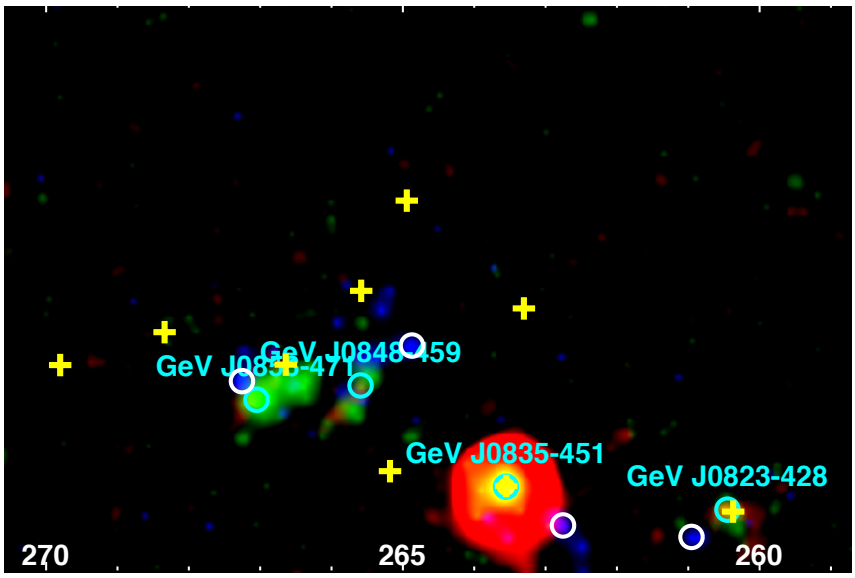

Figure 4.23.. Fermi high-energy view of the Vela region (R:10-30, R:30-100, B:100-1000 GeV).

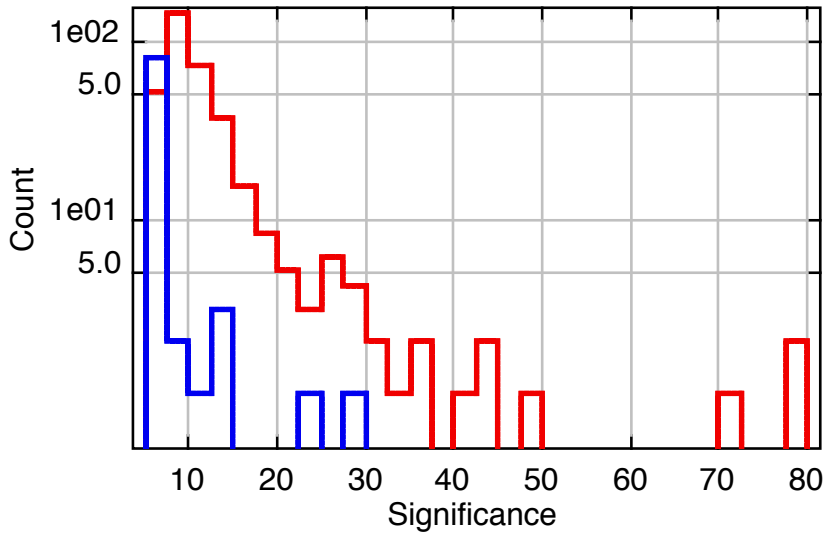

Figure 4.24.. Fermi catalog significance distribution, with the 10 GeV catalog in red and the 100 GeV catalog in blue. For the 10 GeV histogram the first bin is low because it extends from 5 to 7.5, but the detection threshold was at 7. A finer binning shows that the largest number of sources dN/dS has significances S right above the threshold S_{min}, as expected.

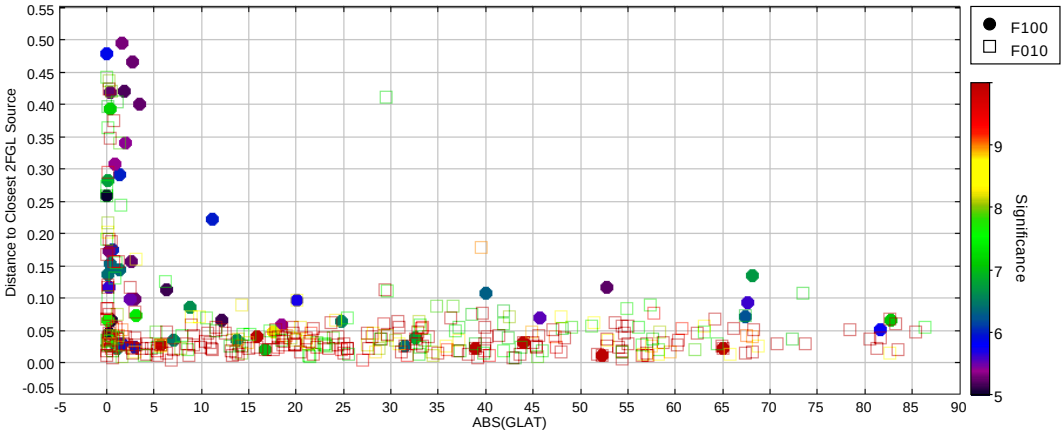

Figure 4.25.. Each Fermi 10 GeV catalog source (F010, open squares) and 100 GeV catalog source (F100, filled circles) was matched to the closest 2FGL source. For off-plane sources almost all sources are within 0.15 deg of a 2FGL source. At low latitudes (GLON < 2), about half of the sources are more than 0.15 deg away from a 2FGL source, i.e. are new detections (24 out of 62 = 40% for F010; 10 out of 18 = 55% for F100). Because of the high density of 2FGL sources in the plane, no offsets larger than 0.5 deg occur.

Associations

The tables in Appendix B list for each source the closest 2FGL and HESS source, if there is one within 0.3 deg.

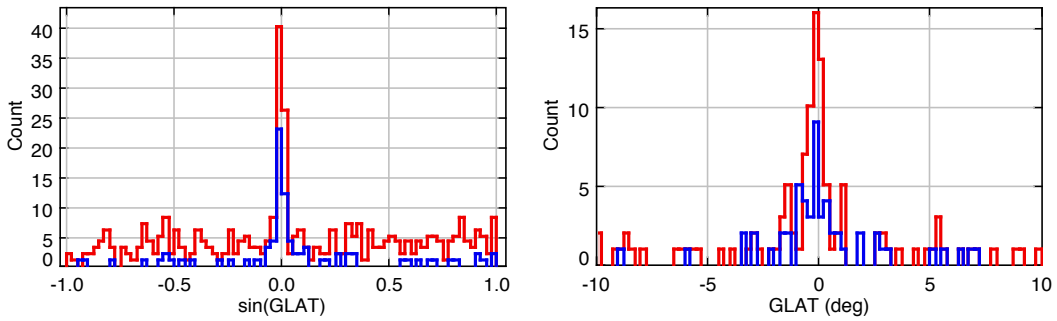

Figure 4.26.. Fermi catalog latitude distribution with the 10 GeV catalog in red and the 100 GeV catalog in blue. Binning in sin(GLAT) makes an isotropic distribution on the sky flat, whereas binning in GLAT would show, for an isotropic distribution, fewer sources in high-latitude bins, because such a bin corresponds to a smaller solid angle on the sky. However this effect is negligible for the $b = \pm 10$ deg range shown on the right, where it is convenient to see the familiar units of degrees. The extragalactic AGN population is clearly visible as a flat component and the population of Galactic sources as a peak at latitude zero.

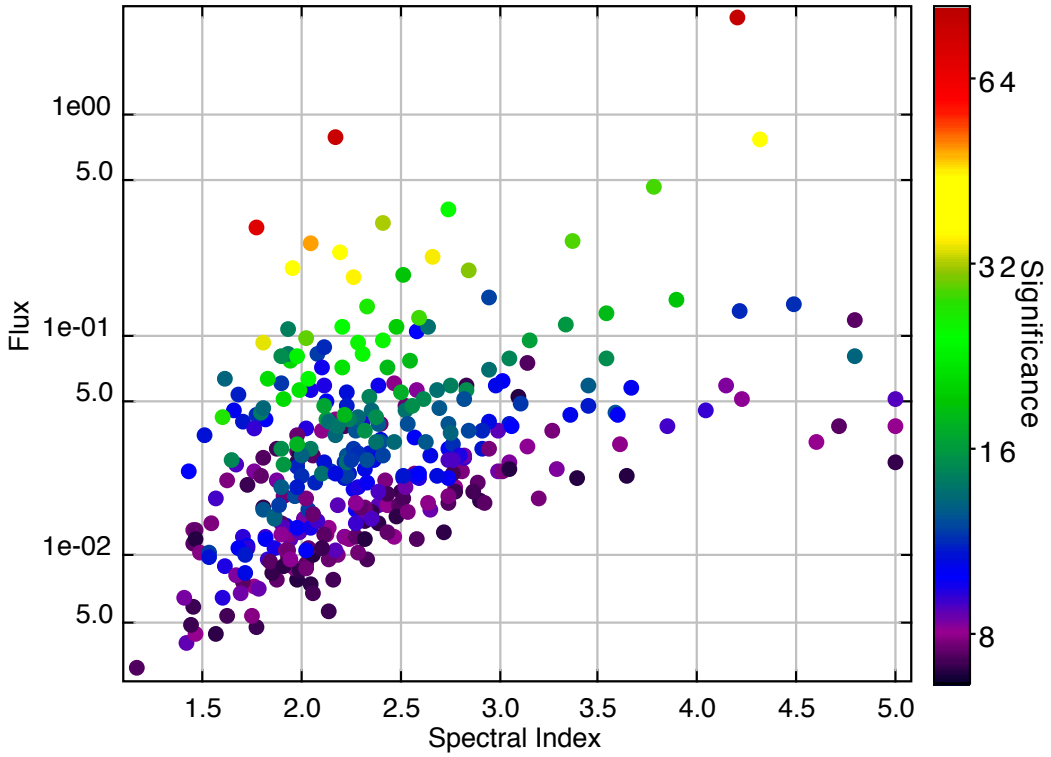

Figure 4.27.. Fermi catalog flux (differential flux at 10 GeV in $10^{-12}cm^{-2}s^{-1}MeV^{-1}$) versus spectral index, illustrating that the detection threshold varies by about an order of magnitude from the hardest to the softest sources. This plot corresponds to Figure 20 in the Fermi catalog paper Abdo et al. (2010a), which includes a theoretical expectation for the threshold.

5. Summary and Outlook

The main results of this work are the HESS Galactic plane survey (HGPS) maps and catalog described in Chapter 3 and shown in Appendix A and B. The HGPS was already the topic of previous theses (Funk, 2005; Hoppe, 2008) and publications Aharonian et al. (2005e, 2006a) based on 1/10th of the dataset avaibable now. Since then there have been dozens of HESS papers on individual sources, but no catalog or systematic study.

The ultimate goal of the HESS and Fermi survey work is to identify and characterize the Galactic gamma-ray source populations and answer questions like: What number of gamma-ray pulsars, pulsar wind nebulae, supernova remnants, etc. are present in the Milky Way? How do their sizes, fluxes and spectra evolve with time and what are the physical expansion / radiation mechanisms? It is unclear at the moment how much can actually be learned, but at least now with the HESS and Fermi surveys of the Galaxy we have a chance to tackle these questions. The maps and catalogs derived in this thesis represent the groundwork on which to base such studies in the future.

Let me briefly summarize the technical developments and progress made in this thesis for the HESS survey analysis (see Chapter 3):

- Detection and morphology measurements are based on maps. The survey maps presented in this thesis are much improved compared to previous versions (no holes and bands of overestimated background above and below the plane anymore), in large part due to improved exclusion regions and carefully chosen background estimation parameters. The available significance, flux and upper limit maps are good enough to allow population studies e.g. of high-energy pulsars simply by reading off the values in the HESS survey maps at their positions.

- Morphology likelihood fits were implemented and performed for all sources, finding many sources to be more extended than previously thought, possibly because previous analyses chose too small regions for the fit and attributed part of the outer emission of the sources to the background.

- It was recognized that the apertures chosen for spectral measurements in many previous analyses only contained a fraction of the actual source flux. The 90% containment radius was proposed as a default aperture, although as described in Section 3.3 this doesn't work in many cases.

- Model and residual significance maps were derived for the whole survey, making it more easy to identify new sources nearby other known sources.

- A spectral likelihood fit was implemented, which compared to the previously used chi^2 fit has the advantage that it is independent of the binning chosen to derive the flux points and that it can handle the low-statistics, high-energy end of the spectra correctly.

Now that we have a first version of the HESS GPS catalog, we can start to discuss the major choices that have to be made before publication:

- Is the goal simply to model all emission or is the goal to have one catalog source correspond to one cosmic accelerator?
- Should astrophysical knowledge (e.g. positions and morphology of radio / X-ray / GeV sources) be taken into account?
- Should decisions on the number of sources and morphologies modelled in a given region used in previous HESS publications be taken into account, or should a uniform set of criteria be applied even if that means that more or less sources are found for that region?
- Which morphological models are allowed?
- Do we allow for 'diffuse' components to model degree-scale emission without clear peaks or do we model this emission as a collection of multiple smaller overlapping 'sources'?
- What detection significance threshold do we choose, i.e. what is an acceptable probability to have one false detection in the whole survey? Should we include a second class of less-significant hotspots?
- What significance thresholds should we choose to prefer more complicated morphological and spectral models over simpler ones?
- What additional criteria (such as e.g. minimum separation or size difference or brightness contrast, ...) should be imposed to avoid bright sources from splitting up into multiple components?
- What cuts should we use for detection and morphological analysis. Traditionally detection and morphology measurement was done on hard cut maps without a safe energy cut, which leads to very different statistics wrt. the spectral analysis, where std cuts with a safe energy cut are used.
- To what extent do we allow per-target and per-ROI decisions? For example, how should the diffuse emission in the Galactic center ridge be modelled? And is it ok to cut out RX J1713.7-3946 in order to obtain better estimates for its surrounding sources? And should we choose spectral extraction regions based on the offsets of the wobble-observations of that source?

It is important to note that these decisions heavily influence the number of sources found, that number could easily reach 100 if the detection threshold is lowered a bit and big sources are modelled by several components. Also these decisions will heavily influence the usefulness of the catalog for population studies, e.g. the distribution of sources sizes and fluxes will be very different if the emission is modelled as a few big sources (possibly with a flag that their morphology is complex) or by many small sources.

In addition to these big-picture questions there are still a number of problems, remaining issues and tasks clearly identified:

- Sources previously found to be point-like, such as HESS J1745-290 and HESS J1302-638 appear extended in my Gaussian morphology fit. Clearly there is a problem either with the computed PSF or the convolution.

- In a few cases the spectral extraction radius was chosen slightly larger than the majority of wobble observation at 0.5 or 0.7 deg offset, so that a large fraction of the available livetime was lost because no reflected regions could be found.

- A few of the exponential cutoff fits don't converge and in general we find cutoffs in most sources. Although this has been observed before and is somewhat expected from astrophysics (cosmic accelerators run out of steam at some energy, leading to cosmic ray and radiation spectra that curve down at some point), further tests should be done to make sure this is not an artefact of the analysis.

- The systematic errors resulting from different choices of data quality, exclusion regions, background estimation parameters and spectral aperture have to be evaluated further. At the moment we almost always publish 20% flux and 0.2 index systematic errors, although for large sources it is probably worse.

- Consistent with HESS publication policy, all results (basically every number in the tables in Appendix B) have to be cross-checked by an independent analysis using the French calibration.

The second result of this work are the Fermi all-sky significance and flux maps above 10 and 100 GeV as well as corresponding catalogs of sources. Note that these quite easily can be improved significanctly simply by updating to the now available data set and recently published much improved P7 instrument response functions and much higher-resolution and accurate P7 diffuse model.[1]. Also it is possible to produce, similar as for HESS, significance, flux and upper limit maps for extended sources, assuming a morphological model such as a Gaussian or disk.

[1] `http://fermi.gsfc.nasa.gov/ssc/`

Next year, with the publication of the HESS survey paper and FITS survey maps, the systematic scan that has been going on for the past seven years will most likely be over. With HESS 2, with it's smaller FOV, it will not be possible to survey large regions of the Milky Way, instead the focus will be on individual objects that have been identified as the most interesting candidates using the HESS 1 and Fermi data. This mainly includes sources where a measurement of the spectrum or morphology in the current gap between Fermi and HESS around 100 GeV will help constrain e.g. the nature of the source or emission mechanism.

Concerning the question of how to combine the Fermi and HESS data, the most powerful (and simple for that matter) analysis method is a combined likelihood fit on energy cubes, although that would require significant extension of the existing analysis software on the HESS side. The current HESS technique of doing the morphology fit on maps, throwing away the energy information, and the spectrum using aperture photometry, throwing away spectral information is unsatisfactory and instead counts and exposure should be filled in energy cubes and used in a likelihood fit. The critical point will be to extend the ring and template background estimation methods to work well in small energy bands and the reflected background method to make maps. Because the HESS PSF only varies in width by a factor of two from the lowest to the highest energies and because most HESS sources don't show strong energy-dependent morphology, these energy cubes have not been implemented so far.

It should be pointed out that currently the CTA[2] project design phase is under way CTA Consortium (2010). CTA will be an order of magnitude more sensitive than HESS and provide a factor two or three better angular resolution. Obviously the lessons learned from the HESS (and Fermi) survey (basically spatial, extension and flux distribution of sources) are important for the design decisions. For example it is important to know how many sources can be resolved and in what detail their morphology and spectrum measured for a given FOV, effective area, background level and PSF size. But also the other way around, the software currently in development for CTA[3] is a viable option for the improved cube analysis of HESS data and combination with Fermi data described in the previous paragraph.

Another very exciting instrument is HAWC[4] On Behalf Of The Milagro et al. (2010), which is being constructed at the moment in Mexico and will perform an order of magnitude more sensitive survey of the TeV and multi-TeV sky than MILAGRO did (see Figure 1.3), although this time from the southern hemisphere, covering the whole HESS survey region.

Currently one of the main means of identification of sources discovered in the HESS survey is to perform hard X-ray observations with the Chandra, XMM-

[2] `http://www.cta-observatory.org/`

[3] `http://gammalib.sourceforge.net/` and `http://cta.irap.omp.eu/ctools/`

[4] `http://hawc.umd.edu/`

Newton or Suzaku satellites, which is time consuming and not always observation time is granted. The only existing X-ray survey that can be compared to HESS data is ROSAT Snowden et al. (1997), which has very poor sensitivity at high energies and low angular resolution. So another mission to look forward to is eROSITA[5], which will perform the first imaging all-sky survey in the medium X-ray range up to 10 keV and shed light on many of the HESS sources.

To conclude, although the HESS Galactic plane survey is coming to an end, the exploitation of its scientific potential by combining it with Fermi, X-ray, radio and other surveys (some of the most interesting ones only becoming available in the near future) as well as source population models is just starting.

[5] http://www.mpe.mpg.de/erosita/

A. Maps

This appendix contains the following maps:

A.1 Fermi all-sky map: counts

A.2 Fermi all-sky map: significance

A.3 Fermi GPS map: counts

A.4 Fermi GPS map: significance

A.5 HESS exclusion regions

A.9 HESS point-source sensitivity.

A.6, A.7, A.8 HESS significance for correlation radius 0.1, 0.22 and 0.4 deg

A.10, A.11 HESS PSF containment radius 68%, $95\%/68\%$

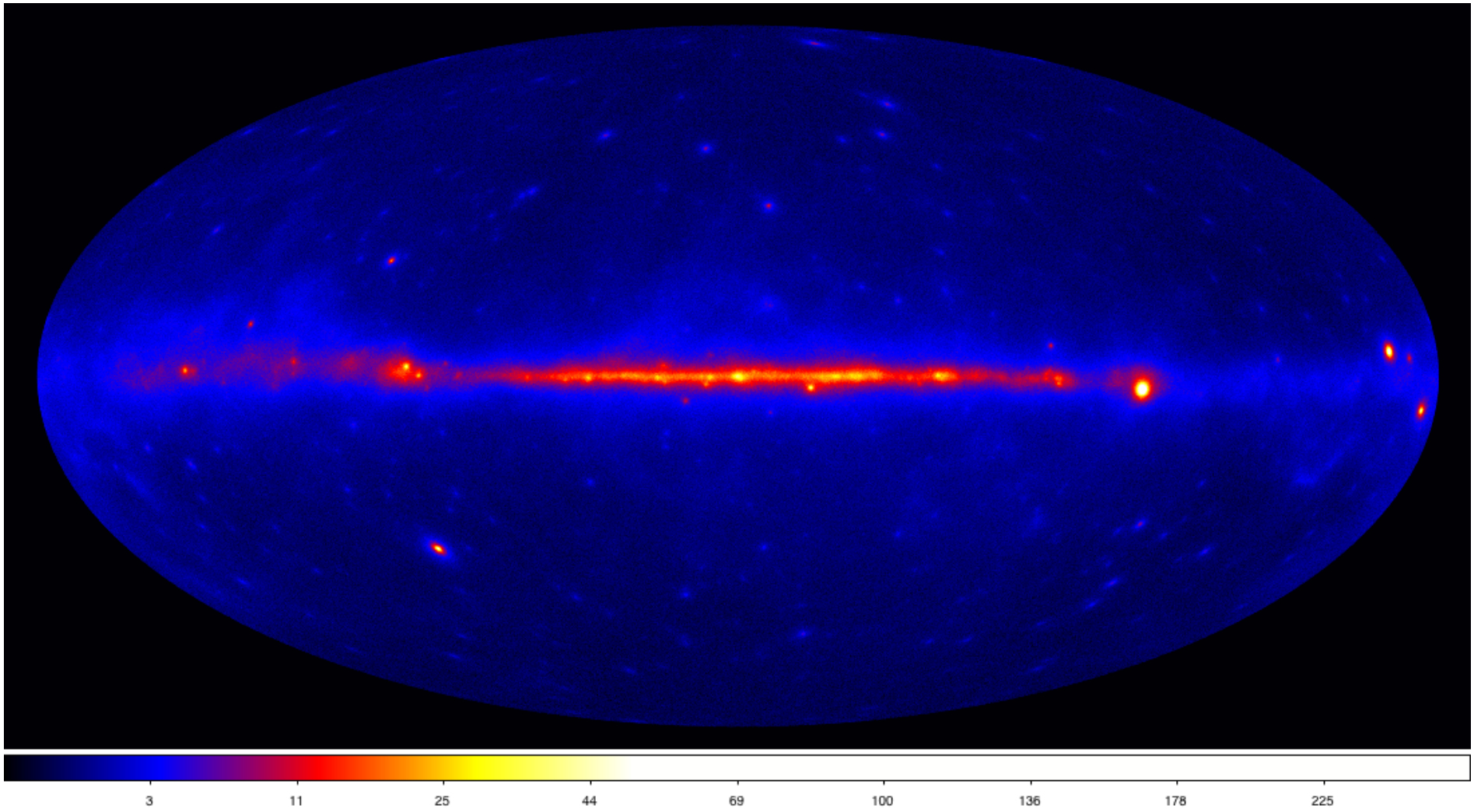
3
11
25
44
69
100
136
178
225

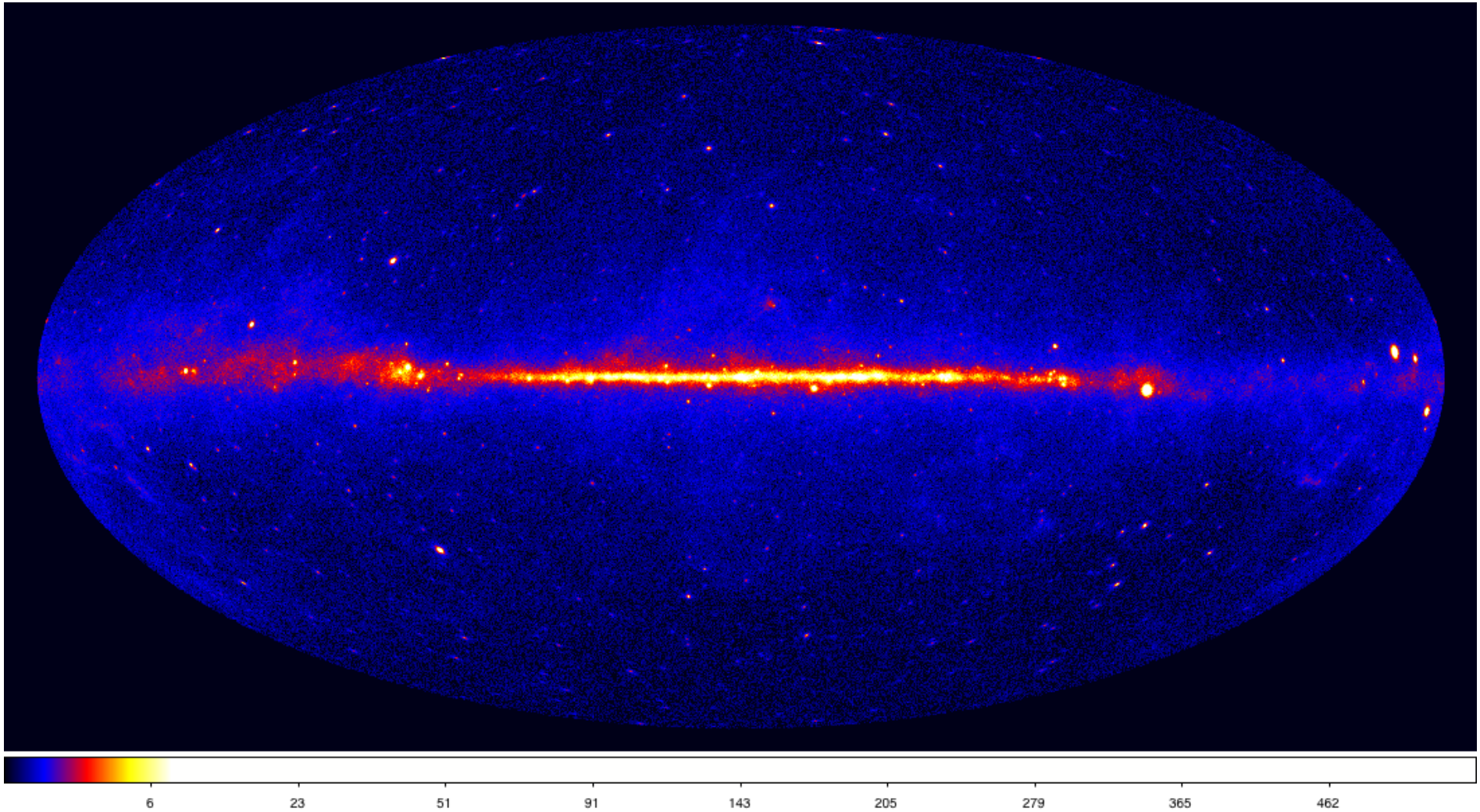

Figure A.1.. Fermi allsky count maps in the 100 MeV to 1 GeV (previous page) and 1 GeV to 10 GeV bands (this page). Note how in the higher energy map the angular resolution is improved by a factor ~ 7 (5 deg to 0.7 deg) but the statistics is reduced by a factor ~ 6 (20M to 3.5M events), see Table 4.2.

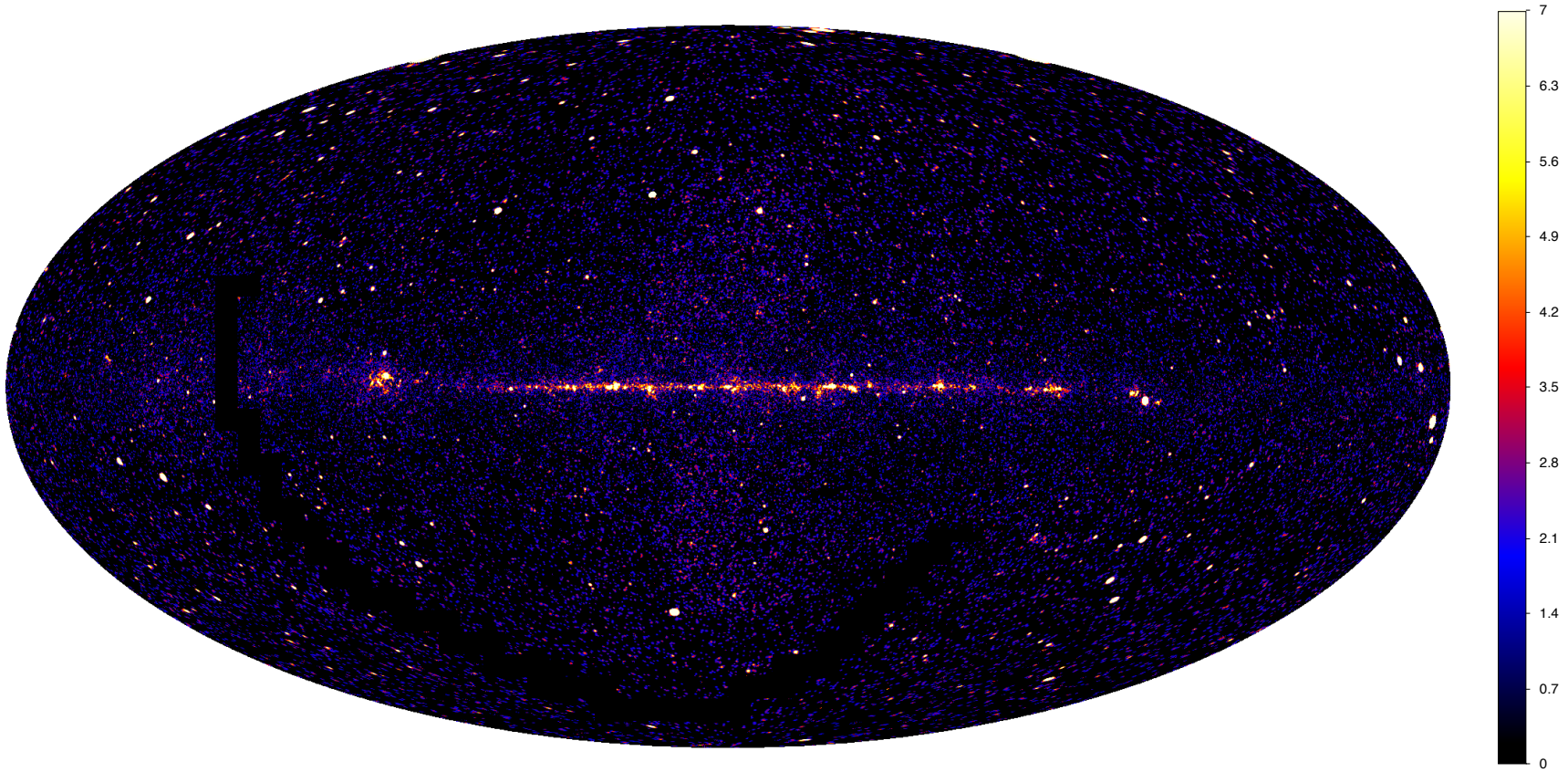
7
6.3
5.6
4.9
4.2
3.5
2.8
2.1
1.4
0.7
0

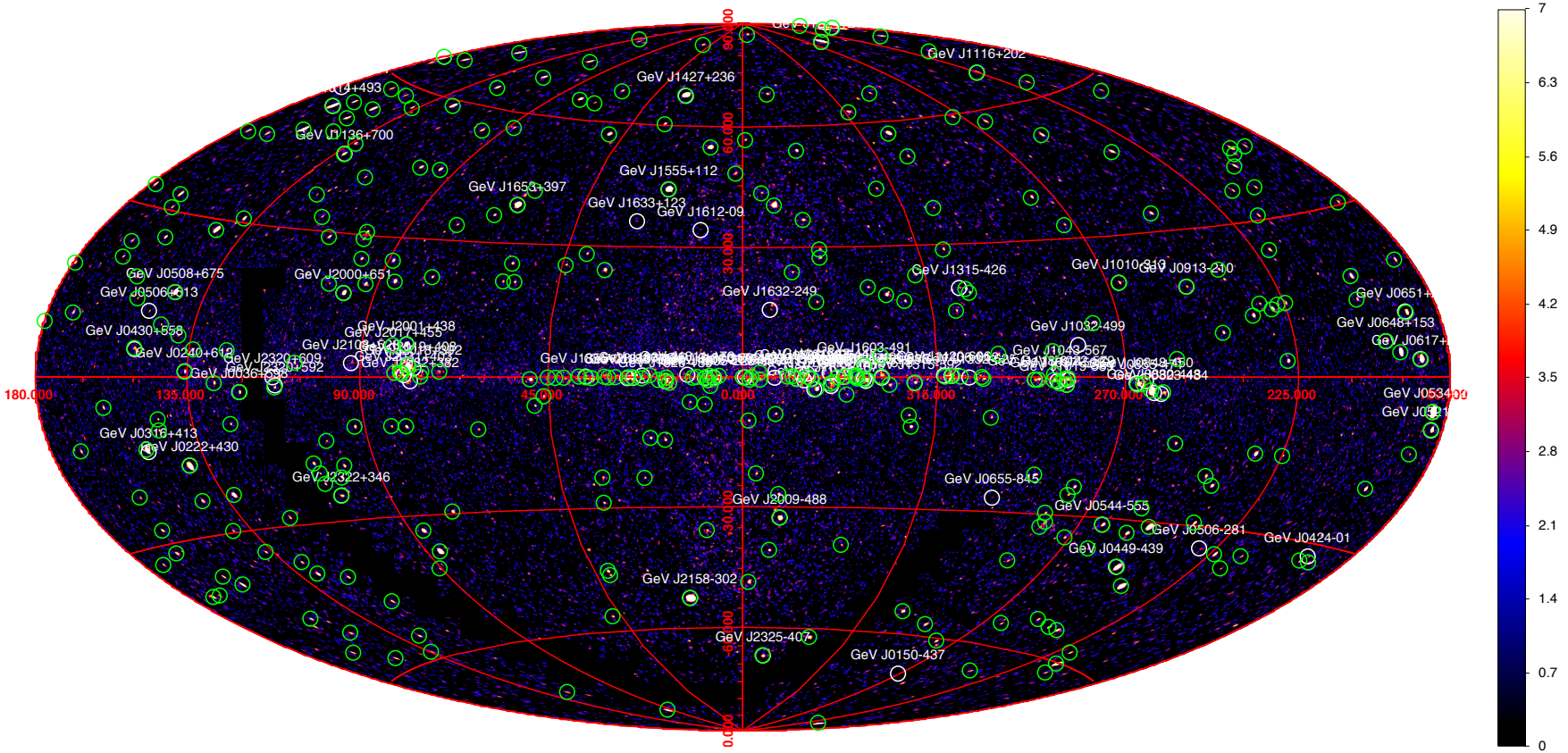

Figure A.2.. Fermi all-sky significance map (i.e. $\sqrt{TS}$) for the 10 – 1000 GeV energy band. The green circles show the catalog of 348 sources detected above 7 sigma. The Fermi bubbles are are clearly visible as regions with a positive bias of $\sim +1\sigma$, although that does not seem to have led to spurious detections, if anything the northern bubble shows a lack of sources. The previous page shows a non-annotated version.

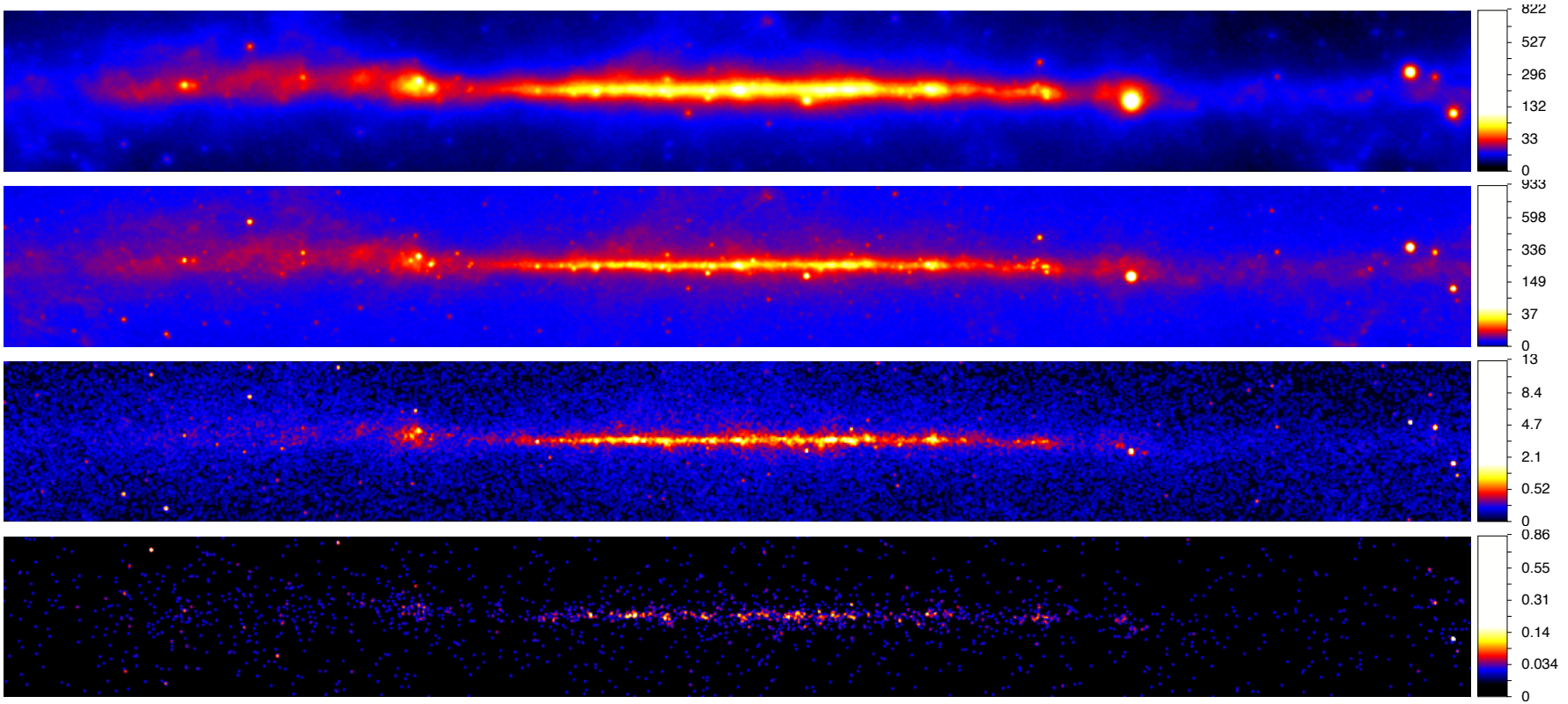

Figure A.3.. Fermi Galactic plane count maps (CAR projection, sqrt color scale, $b = \pm 10$ deg, 0.1 deg binning, smoothed with 0.5 deg Gauss for better visibility in the high energy bands). The energy bands are top to bottom: 0.1–1 GeV, 1–10 GeV, 10–100 GeV, 100–1000 GeV. Above 10 GeV single photons are visible. The 1–10 GeV band contains the most significant sources, because that is where Fermi has the best sensitivity.

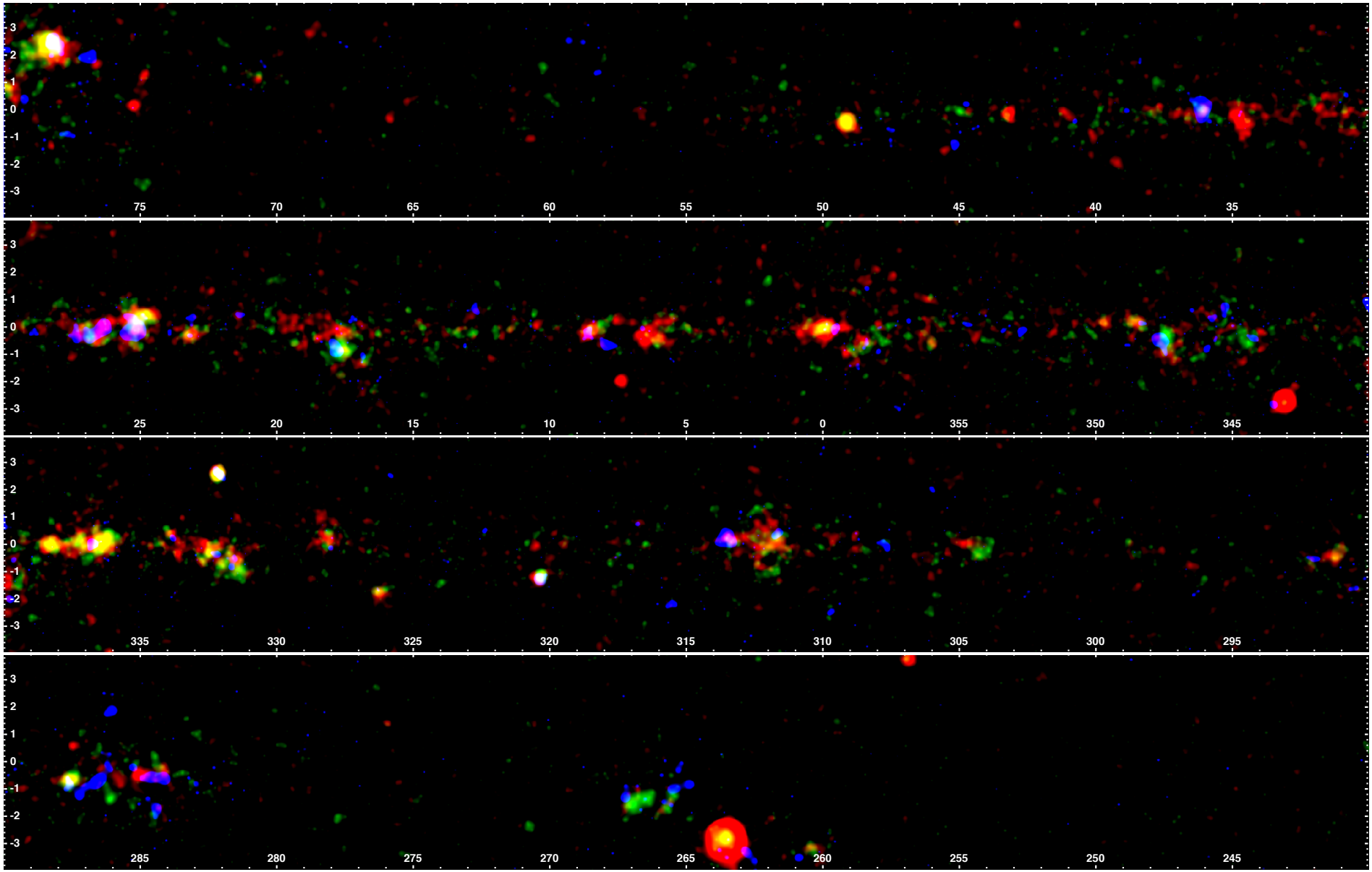
3
2
1
0
-1
-2
-3
75
70
65
60
55
50
45
40
35
25
20
15
10
5
0
355
350
345
335
330
325
320
315
310
305
300
295
285
280
275
270
265
260
255
250
245

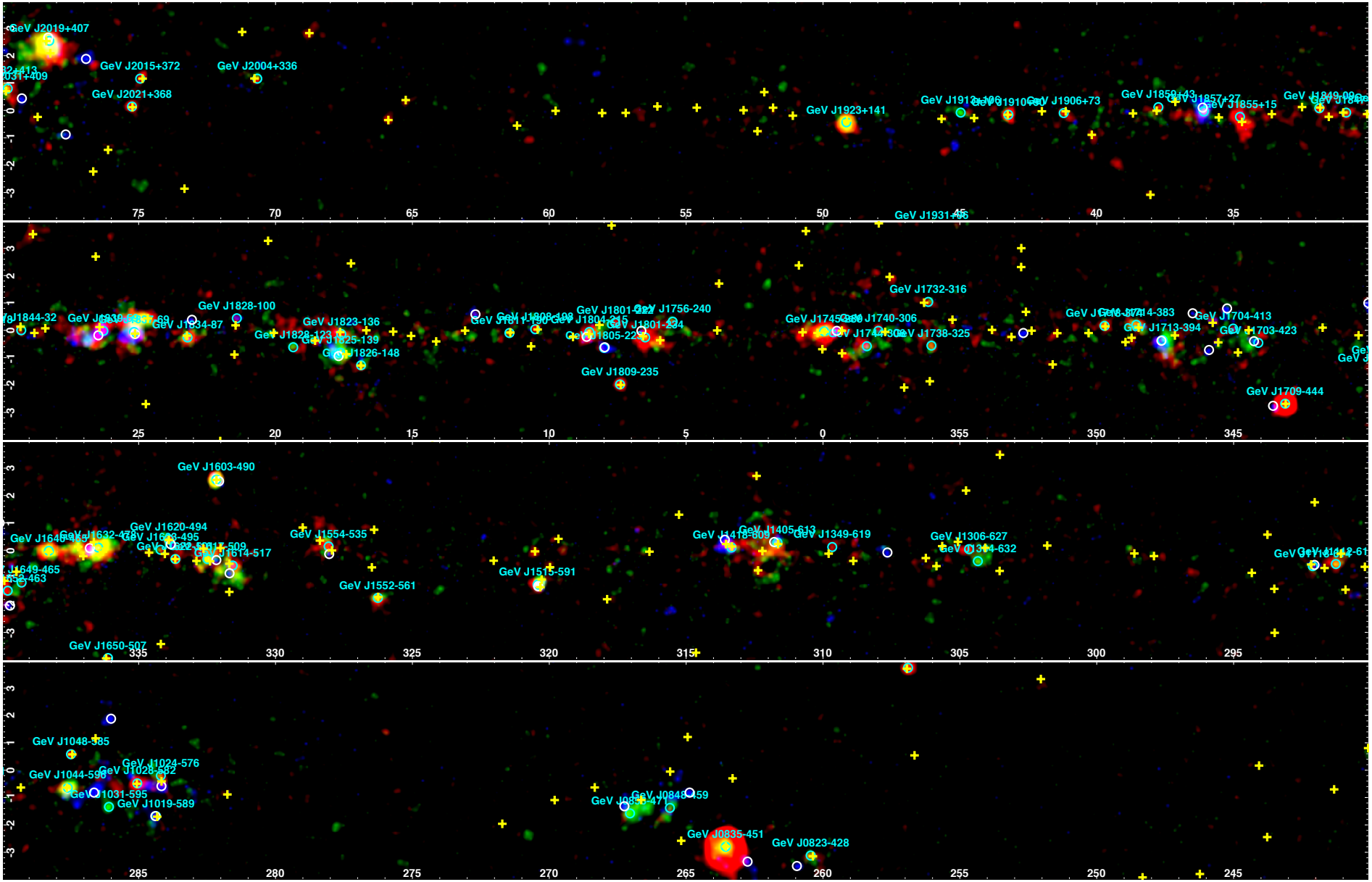

Figure A.4.. Fermi significance map (i.e. $\sqrt{TS}$) of the HESS GPS region in the 10 – 30 – 100 – 300 GeV bands as RGB color image. The color scale is linear in the range 3 to 7, except for th B band, where it is from 3 to 5. Sources above 100 GeV are shown as white circles, sources above 10 GeV as cyan circles and 2FGL sources as yellow unlabeled crosses. The previous page shows a non-annotated version.

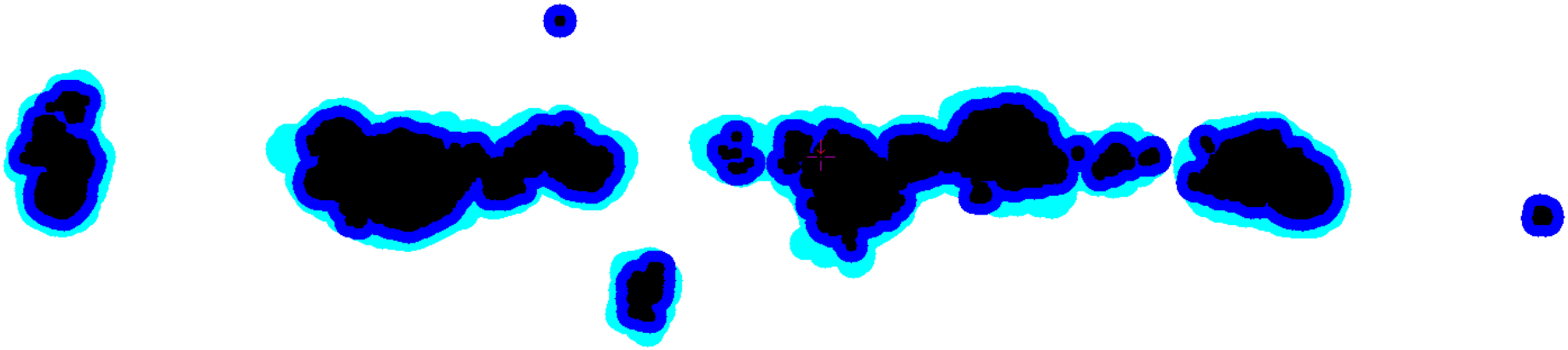

Figure A.5.. HESS GPS Map: Exclusion regions (small, standard, large) as defined in Table 3.1 and described in Section 3.2.

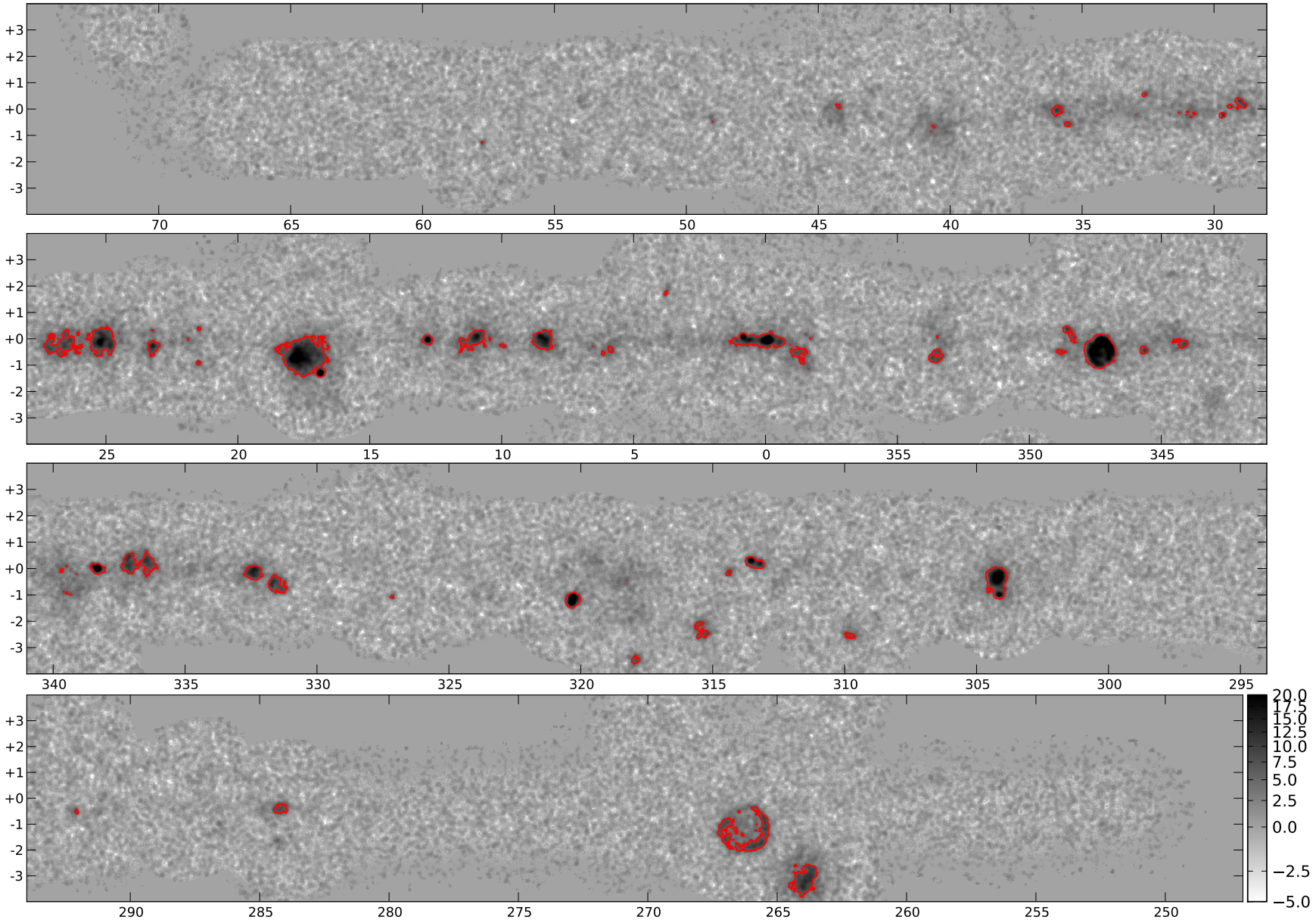

Figure A.6.. HESS GPS Map: significance for hard cuts and 0.1 deg correlation. The red contour is at the 6 sigma level.

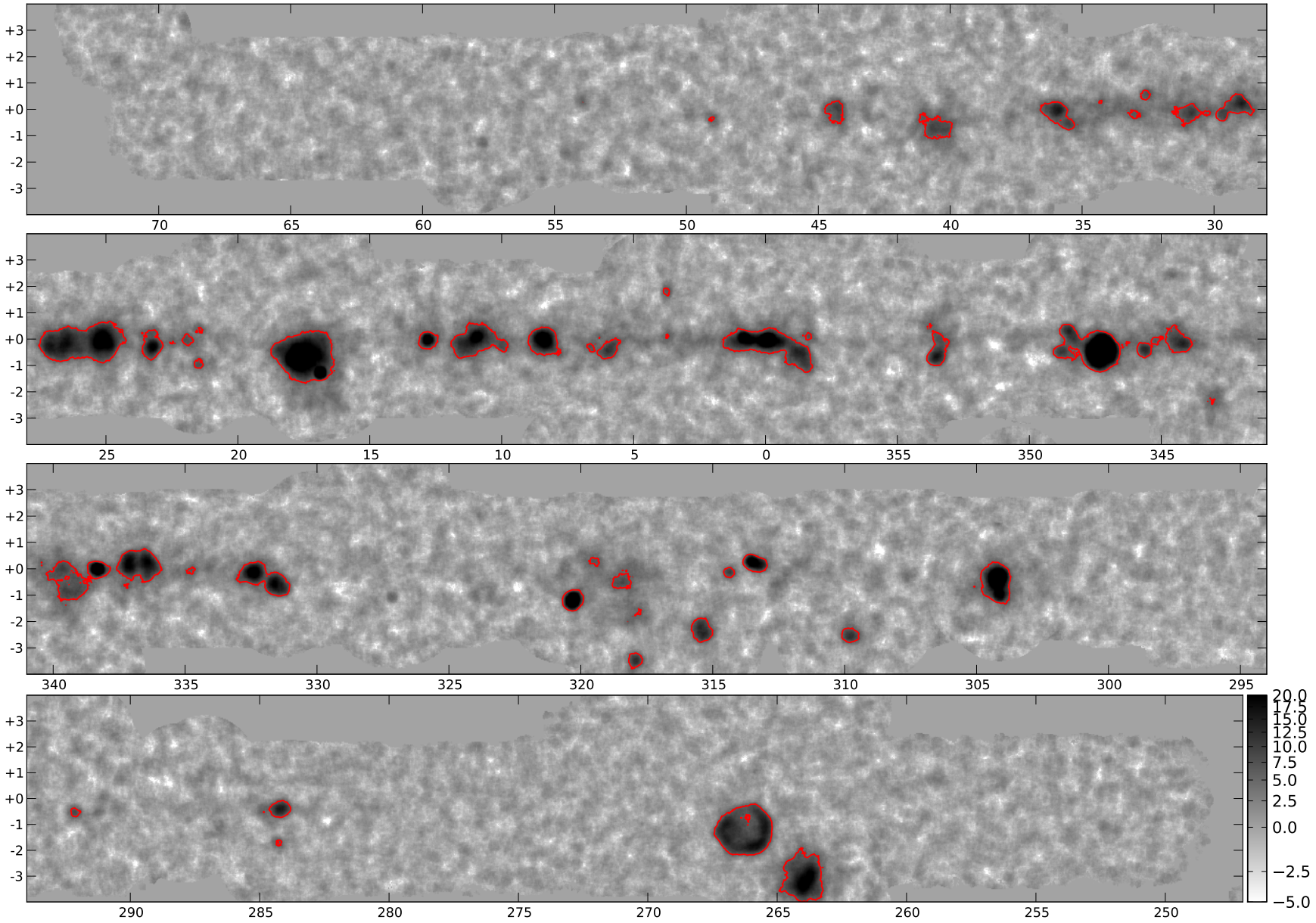

Figure A.7.. HESS GPS Map: significance for 0.22 deg correlation. The red contour is at the 6 sigma level.

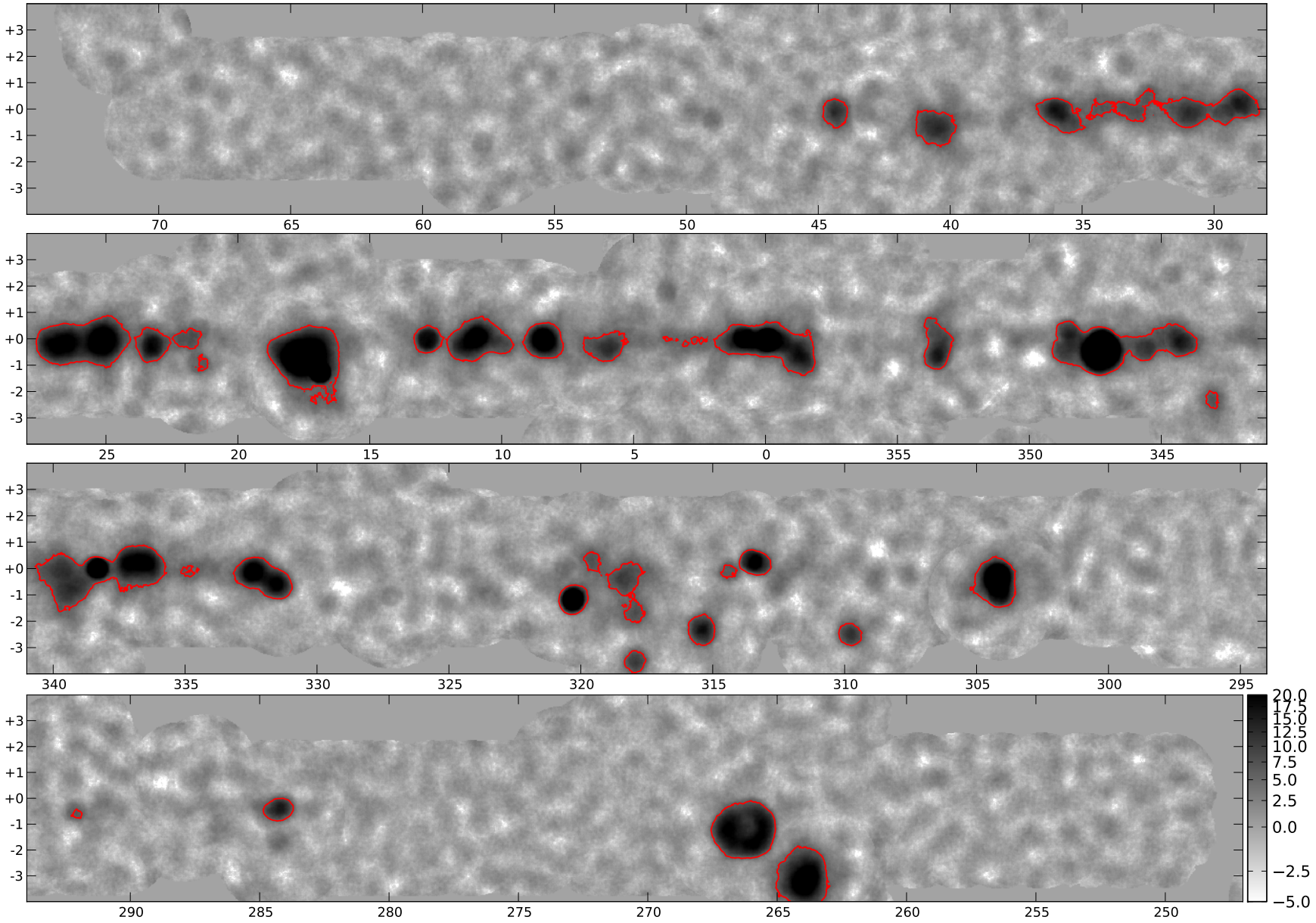

Figure A.8.. HESS GPS Map: significance for 0.4 deg correlation. The red contour is at the level of 6 sigma, corresponding to the detection threshold for the catalog.

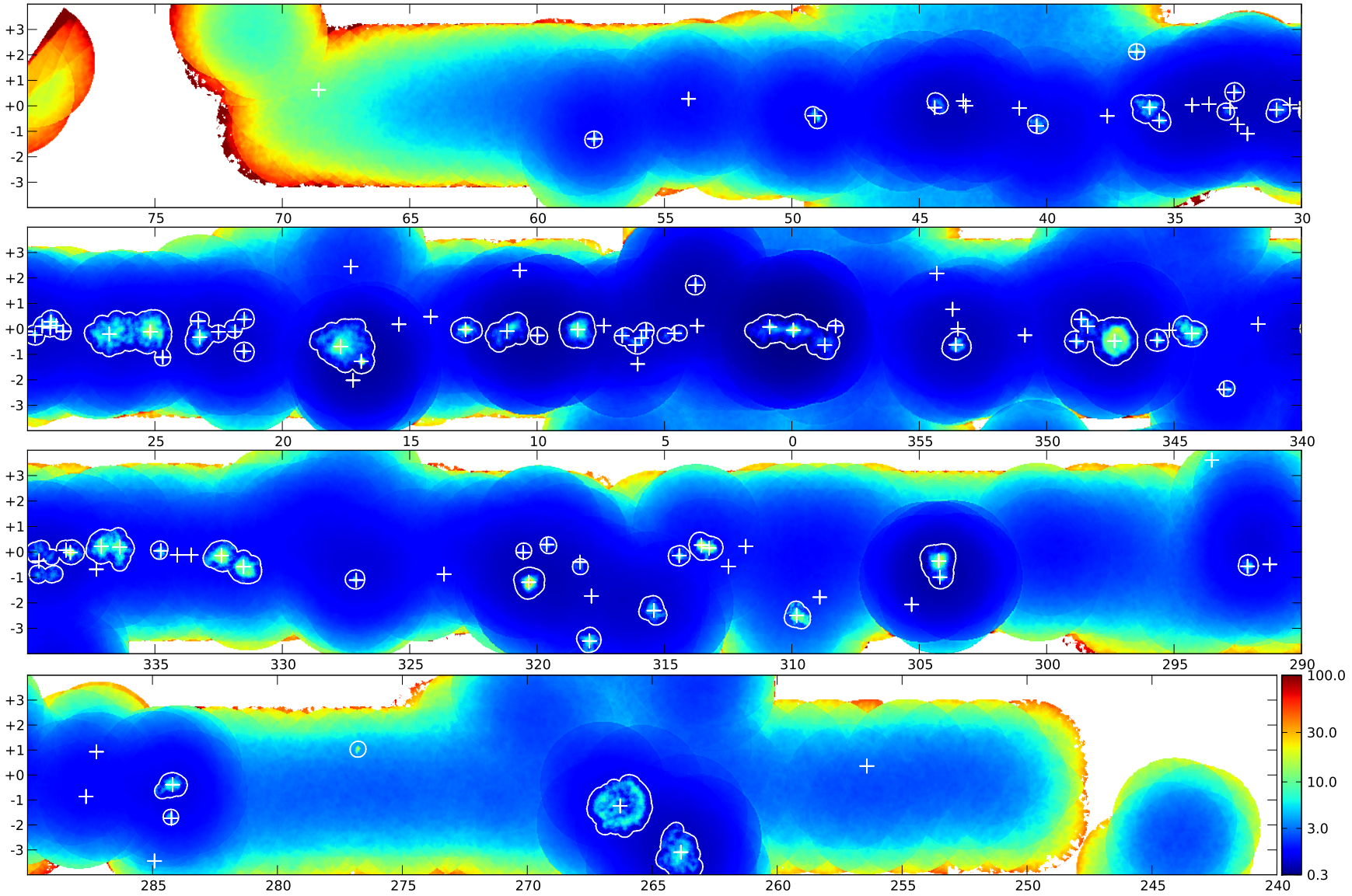

Figure A.9.. HESS GPS Map: sensitivity for 0.1 deg correlation. The sensitivity is given by the flux that is at least 5 sigma over the background level and a factor 3 above the flux of known sources. This second criterion accounts for the fact that existing sources effectively block the detection of other sources and has only been applied within the white contours, which were computed by thresholding the significance map at 5 and dilating by 0.3 deg. The sources from the HESS catalog are shown as white plusses.

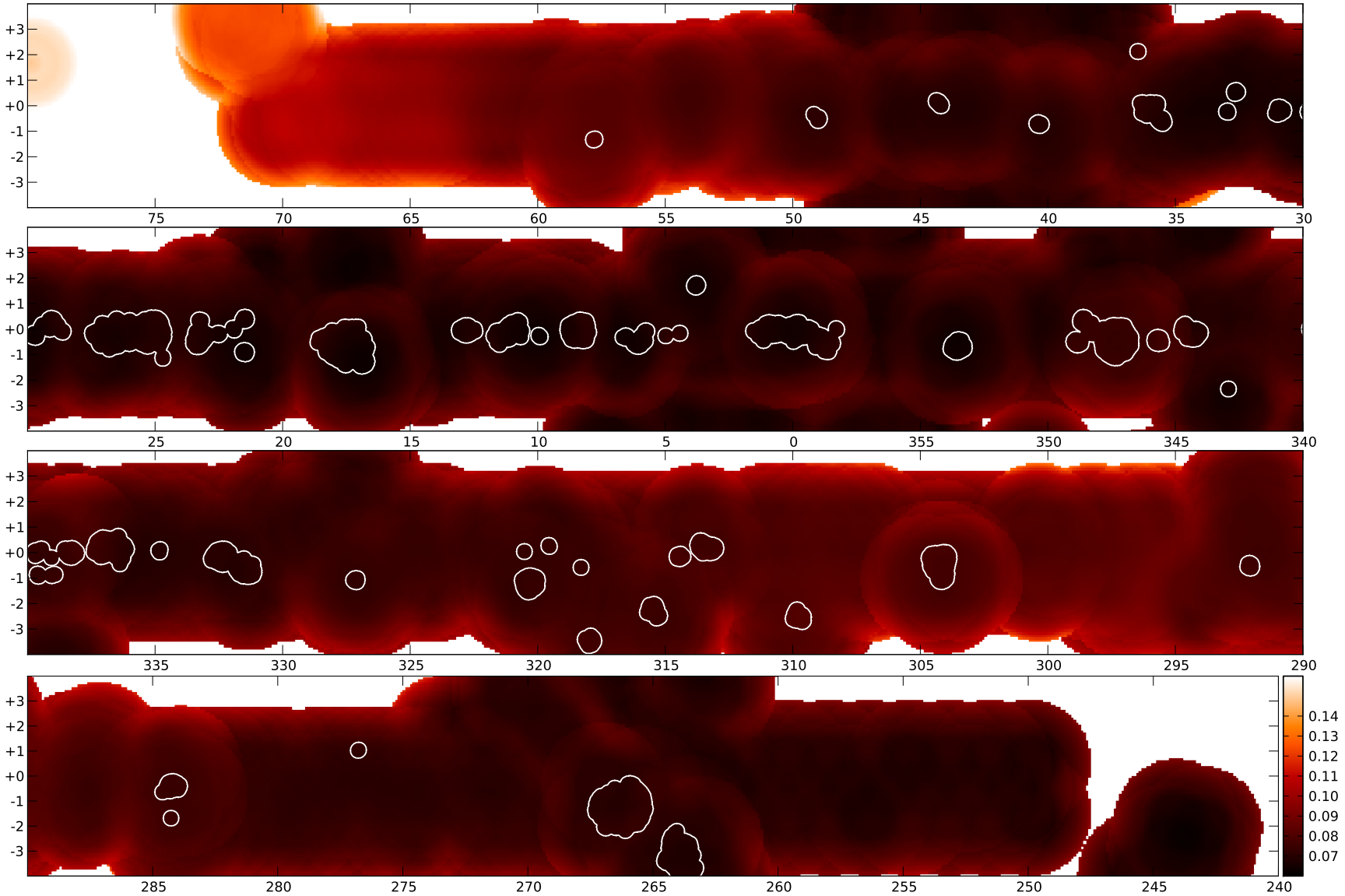

Figure A.10.. HESS GPS Map: PSF 68% containment for hard cuts for a source with a spectral index of 2 and a psi cut of 2.5 deg. The best PSF is $r_{68\%} = 0.063$ deg and increases by up to a factor of two at high offsets and zenith angles. The white contours are the same as in Figure A.9 and illustrate that while each source in the survey requires a custom PSF computation, the variation within any given source is only a few %.

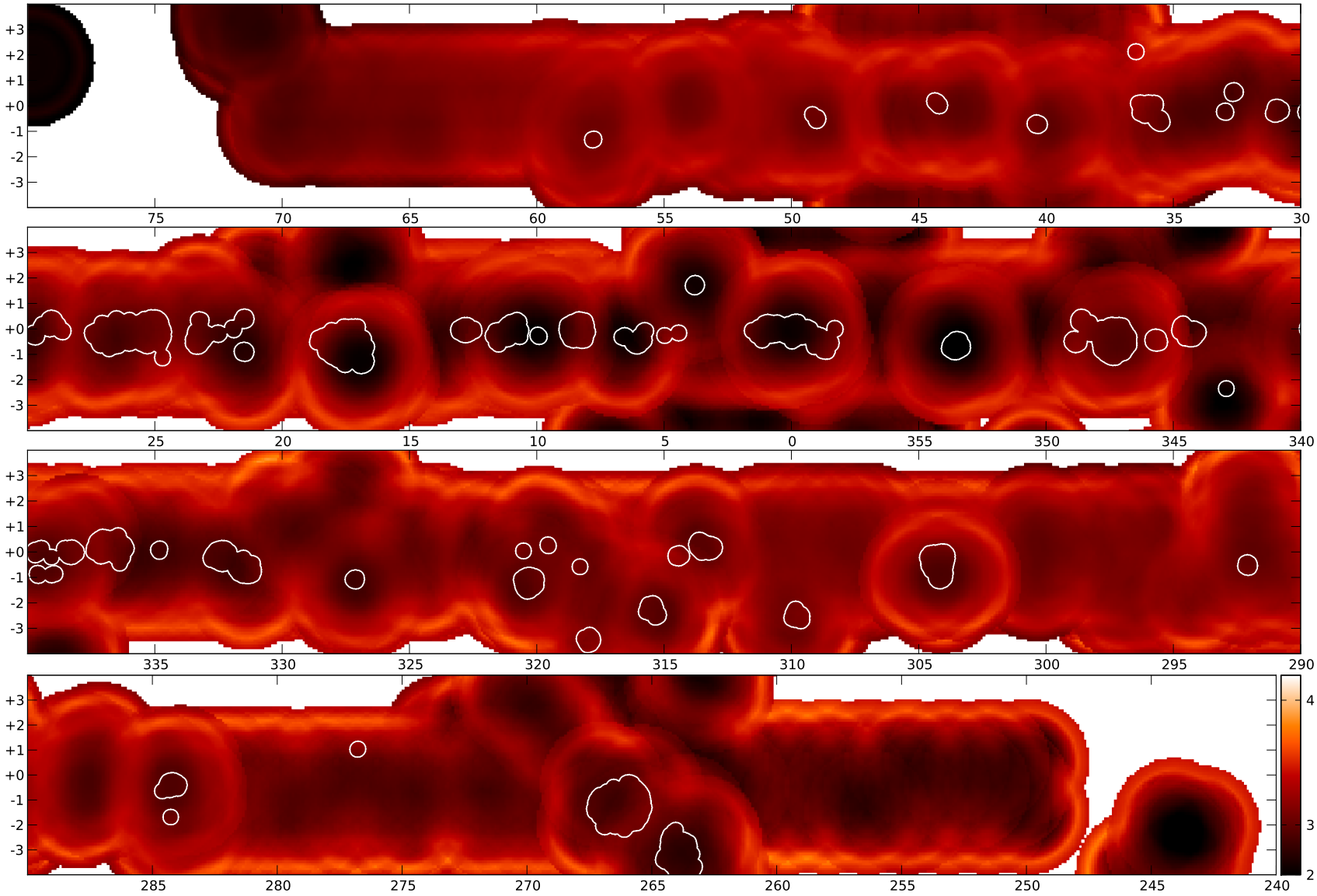

Figure A.11.. HESS GPS Map: PSF 95% to 68% containment ratio (see caption of Figure A.10 for details). For on-axis observations this ratio is ~ 2 and increases up to ~ 4 at the largest zenith angles. Within most sources the variation is $< 10\%$.

B. Catalogs

This appendix contains the following catalogs of high-energy Fermi sources, as described in Chapter 4:

F010 Fermi sources above 10 GeV (347 all-sky, 67 in GPS region)

- **B.1** Position and counterparts
- **B.2** Spectral parameters
- **B.3** HESS counterpart and measurement

F100 Fermi sources above 100 GeV (87 all-sky, 38 in GPS region)

- **B.4** Position and counterparts
- **B.5** Spectral parameters
- **B.6** HESS counterpart and measurement

Note that the identifiers 'F010' and 'F100' are inofficial and only used in this thesis to be able to clearly reference each catalog. To limit the page-count, for the F010 catalog only sources within the GPS region are listed here and only selected columns are shown. The full catalog is available in FITS format.

The following two HESS catalogs are given, as described in Chapter 3. Again only few selected columns are listed here and the full catalogs are available in FITS format.

HGPS The HESS Galactic plane survey catalog, the result of the semi-automatic pipeline described in Chapter 3.

- **B.7** Basic info and counterparts
- **B.8** Detection, morphology, aperture
- **B.9** Observation and statistics
- **B.10** Power-law spectral fit
- **B.11** Exponential cutoff spectral fit

Note that the identifier 'HGPS' is a working title used only in this thesis.

Table B.1.. F010: Fermi sources above 10 GeV — Position and counterparts. The source name was automatically generated from the peak significance RA, DEC position. $\theta_{p\to b}$ is the distance between peak and barycenter position on the significance map, $S = \sqrt{TS}$ is the significance, $E_{0.3}$ is the highest photon energy within 0.3 deg and $N_{0.3}$ is the number of photons above 100 GeV within 0.3 deg. The closest 2FGL source within 0.5 deg is listed (if any) and the offset is given in the θ_{2FGL} column. For convenience, the association and class for the listed 2FGL source is given. Only sources in the GPS region are listed.

#	Source Name	GLON	GLAT	$\theta_{p\to b}$	S	$E_{0.3}$	$N_{0.3}$	2FGL	θ_{2FGL}	2FGL ASSOC1	2FGL CLASS1
		deg	deg	deg		GeV			deg		
1	F010 J0823-428	260.45	-3.12	.15	8.4	115	0	2FGL J0823.0-4246	.16		spp
2	F010 J0835-451	263.55	-2.80	.04	79.8	215	1	2FGL J0835.3-4510	.01	PSR J0835-4510	PSR
3	F010 J0848-459	265.59	-1.38	.09	7.9	104	2	2FGL J0848.5-4535	.34		spp
4	F010 J0853-471	267.05	-1.58	.29	9.1	110	0	2FGL J0853.5-4711	.05		spp
5	F010 J1019-589	284.37	-1.68	.15	8.0	225	2	2FGL J1019.0-5856	.01	1FGL J1018.6-5856	HMB
6	F010 J1024-576	284.19	-.20	.19	8.4	165	0	2FGL J1022.7-5741	.20	PSR J1023-5746	PSR
7	F010 J1028-582	285.05	-.48	.01	11.6	1039	2	2FGL J1028.5-5819	.04	PSR J1028-5819	PSR
8	F010 J1031-595	286.09	-1.34	.05	7.2	125	0				
9	F010 J1044-596	287.59	-.64	.09	14.3	1221	3	2FGL J1045.0-5941	.01	Eta Carinae	
10	F010 J1048-585	287.47	.58	.00	7.8	239	0	2FGL J1048.2-5831	.04	PSR J1048-5832	PSR
11	F010 J1112-611	291.27	-.50	.11	9.5	187	0	2FGL J1112.5-6105	.02	PSR J1112-6103	psr
12	F010 J1118-614	292.11	-.58	.06	7.2	204	3	2FGL J1118.8-6128	.02	PSR J1119-6127	PSR
13	F010 J1304-632	304.35	-.40	.15	7.9	408	1	2FGL J1303.7-6316c	.04		
14	F010 J1306-627	304.67	.04	.11	7.7	230	0	2FGL J1309.6-6230c	.44		
15	F010 J1349-619	309.67	.12	.09	7.0	103	2	2FGL J1349.9-6222	.40		
16	F010 J1405-613	311.66	.28	.40	10.1	232	4	2FGL J1405.5-6121	.04		
17	F010 J1418-609	313.34	.10	.10	11.4	125	4	2FGL J1418.7-6058	.03	LAT PSR J1418-6058	PSR
18	F010 J1515-591	320.42	-1.26	.07	13.3	160	4	2FGL J1514.0-5915e	.15	MSH 15-52 PWN	PWN
19	F010 J1552-561	326.26	-1.74	.03	11.1	113	2	2FGL J1552.8-5609	.03		spp
20	F010 J1554-535	328.06	.14	.13	9.6	105	3	2FGL J1554.4-5317c	.29		
21	F010 J1603-490	332.16	2.58	.01	20.6	100	4	2FGL J1603.8-4904	.02	PMN J1603-4904	bzb
22	F010 J1614-517	331.56	-.56	.13	11.0	116	4	2FGL J1615.2-5138	.19		
23	F010 J1617-509	332.48	-.32	.14	11.8	250	1	2FGL J1615.0-5051	.42		spp
24	F010 J1620-494	333.90	.40	.17	10.7	240	3	2FGL J1620.8-4928	.03		
25	F010 J1622-501	333.66	-.32	.03	8.3	102	0	2FGL J1622.8-5006	.03		
26	F010 J1623-495	334.20	.02	.05	7.7	176	1	2FGL J1624.0-4941c	.19		
27	F010 J1632-478	336.48	.10	.15	14.6	173	3	2FGL J1632.4-4753c	.11		
28	F010 J1640-465	338.28	-.02	.06	14.4	153	1	2FGL J1640.5-4633	.01		spp
29	F010 J1649-465	339.28	-1.18	.09	7.2	116	1	2FGL J1648.4-4612	.40	PSR J1648-4611	PSR
30	F010 J1652-463	339.78	-1.48	.06	7.5	134	1	2FGL J1653.9-4627c	.24		

31	F010 J1703-423	344.10	-.46	.23	7.6	223	3				
32	F010 J1704-413	345.02	.06	.09	7.9	105	3				
33	F010 J1709-444	343.12	-2.68	.02	28.9	176	0	2FGL J1709.7-4429	.02	PSR J1709-4429	PSR
34	F010 J1713-394	347.60	-.36	.29	10.0	968	6	2FGL J1712.4-3941	.35		spp
35	F010 J1714-383	348.56	.20	.04	9.7	100	2	2FGL J1714.5-3829	.12		spp
36	F010 J1718-374	349.72	.16	.03	10.2	508	1	2FGL J1718.1-3725	.04		spp
37	F010 J1732-316	356.16	1.04	.04	7.7	156	2	2FGL J1732.5-3131	.15	LAT PSR J1732-3131	PSR
38	F010 J1738-325	356.04	-.56	.03	8.0	105	0	2FGL J1737.2-3213	.42		spp
39	F010 J1740-306	357.98	-.02	.05	7.3	123	2	2FGL J1740.4-3054c	.26		spp
40	F010 J1744-306	358.40	-.58	.37	9.2	259	3	2FGL J1743.9-3039c	.05		
41	F010 J1745-289	359.96	-.04	.08	25.0	129	2	2FGL J1745.6-2858	.02		spp
42	F010 J1756-240	5.50	.32	.10	8.0	129	2	2FGL J1758.8-2402c	.44		
43	F010 J1801-222	7.60	.28	.04	7.5	129	1				
44	F010 J1801-234	6.50	-.26	.19	10.1	129	4	2FGL J1801.3-2326e	.03	SNR G006.4-00.1	SNR
45	F010 J1804-215	8.54	-.06	.09	11.9	110	4	2FGL J1805.6-2136e	.17	SNR G008.7-00.1	SNR
46	F010 J1805-223	8.00	-.64	.02	7.0	125	6				
47	F010 J1808-198	10.51	.04	.02	7.7	139	3	2FGL J1808.6-1950c	.03	2MS-GC01	glc
48	F010 J1809-235	7.42	-1.98	.02	11.4	154	0	2FGL J1809.8-2332	.04	LAT PSR J1809-2332	PSR
49	F010 J1811-190	11.45	-.10	.16	7.5	235	1	2FGL J1811.1-1905c	.03		spp
50	F010 J1823-136	17.59	-.14	.06	9.7	114	3	2FGL J1823.1-1338c	.08		
51	F010 J1825-139	17.63	-.82	.03	11.2	303	3	2FGL J1824.5-1351e	.37	HESS J1825-137	PWN
52	F010 J1826-148	16.87	-1.28	.06	9.0	150	3	2FGL J1826.3-1450	.04	LS 5039	HMB
53	F010 J1828-100	21.41	.44	.02	7.2	283	3				
54	F010 J1828-123	19.35	-.62	.16	7.1	112	0				
55	F010 J1834-087	23.21	-.26	.10	11.4	373	2	2FGL J1834.3-0848	.07		spp
56	F010 J1837-069	25.17	-.06	.19	13.2	127	7	2FGL J1837.3-0700c	.08		
57	F010 J1839-059	26.29	-.02	.43	10.4	138	7	2FGL J1839.3-0558c	.07		
58	F010 J1844-032	29.29	-.00	.01	7.5	218	1	2FGL J1843.7-0312c	.27		
59	F010 J1847-018	30.89	-.08	.05	8.0	254	0	2FGL J1848.2-0139c	.21		
60	F010 J1849-009	31.87	.08	.08	7.4	107	0	2FGL J1849.3-0055	.03		spp
61	F010 J1855+015	34.77	-.24	.14	12.0	131	2	2FGL J1855.9+0121e	.19	SNR G034.7-00.4	SNR
62	F010 J1857+027	36.09	-.04	.15	10.8	141	6				
63	F010 J1859+043	37.75	.12	.18	7.5	142	1	2FGL J1901.1+0427	.36		
64	F010 J1906+073	41.21	-.10	.18	7.3	156	0	2FGL J1906.5+0720	.10		
65	F010 J1910+090	43.23	-.16	.01	13.8	151	1	2FGL J1911.0+0905	.03	SNR G043.3-00.2	snr
66	F010 J1913+106	44.97	-.08	.09	7.5	317	0				
67	F010 J1923+141	49.15	-.44	.05	19.1	779	0	2FGL J1923.2+1408e	.04	W51C	SNR

Table B.2.. F010: Fermi sources above 10 GeV — Spectral parameters. F is the differential flux at 10 GeV in units 10^{-14} cm^{-2} s^{-1} MeV^{-1}. For the full energy band the flux was derived by fitting the spectral index, for the small energy bands a fixed spectral index of 2 was assumed. Only sources in the GPS region are listed.

		10 to 1000 GeV						10 to 30 GeV			30 to 100 GeV			100 to 1000 GeV				
#	Source Name	F	ΔF	Γ	$\Delta\Gamma$	N	S	F	ΔF	S	F	ΔF	S	F	ΔF	N	S	
1	F010 J0823-428	216.4	86.5	1.9	.3	18.6	8.4	220.5	77.9	6.6	309.0	142.7	5.2	230.6	287.1	1.4	1.1	1.4
2	F010 J0835-451	26640.5	1569.8	4.2	.1	632.6	79.8	11959.0	493.4	77.6	764.5	218.6	10.7	381.9	308.6	2.4	3.1	2.4
3	F010 J0848-459	129.4	56.5	1.4	.2	19.4	7.9	146.5	66.1	4.8	416.6	184.2	5.3	717.9	416.2	4.6	3.3	4.6
4	F010 J0853-471	179.5	66.6	1.6	.2	22.6	9.1	139.8	67.6	4.1	613.5	207.6	8.0	519.0	362.5	3.3	2.3	3.3
5	F010 J1019-589	102.2	57.1	1.5	.3	15.8	8.0	134.0	58.9	4.7	172.8	121.8	2.6	679.7	389.0	4.7	5.9	4.7
6	F010 J1024-576	234.8	88.9	1.8	.3	25.4	8.4	281.7	88.4	6.2	302.1	149.6	5.1	473.6	364.0	3.3	2.0	3.3
7	F010 J1028-582	1358.8	380.1	4.5	.8	32.2	11.6	563.3	114.9	11.0	.0	.0	.0	709.3	419.9	4.9	3.3	4.9
8	F010 J1031-595	57.8	42.2	1.4	.4	9.5	7.2	.0	.0	.0	368.5	154.2	7.7	.0	.3	.0	.0	.0
9	F010 J1044-596	438.2	113.8	1.8	.2	45.9	14.3	438.7	102.7	9.9	795.2	214.8	9.5	613.3	367.0	4.2	3.8	4.2
10	F010 J1048-585	356.9	134.0	3.3	.7	12.9	7.8	217.3	69.2	7.7	48.0	79.1	.8	.0	.0	.0	.0	.0
11	F010 J1112-611	399.2	133.2	2.3	.3	26.1	9.5	349.2	94.4	7.4	271.4	132.7	5.9	.0	.1	.0	.0	.0
12	F010 J1118-614	163.2	69.0	1.8	.3	16.9	7.2	154.6	66.4	4.5	224.9	127.9	3.5	432.2	267.6	3.0	4.2	3.0
13	F010 J1304-632	138.4	65.2	1.5	.3	20.1	7.9	137.5	63.9	4.7	501.1	180.5	6.3	171.4	212.3	1.2	1.1	1.2
14	F010 J1306-627	389.2	140.5	2.4	.4	23.4	7.7	313.5	92.0	6.9	304.4	160.5	3.6	.0	.1	.0	.0	.0
15	F010 J1349-619	514.7	199.4	3.1	.7	20.5	7.0	318.0	94.4	5.8	119.1	101.6	3.5	192.1	233.6	1.3	1.1	1.3
16	F010 J1405-613	405.6	138.1	1.8	.2	40.7	10.1	414.1	117.5	6.4	603.3	210.7	6.5	746.6	383.8	5.1	4.3	5.1
17	F010 J1418-609	427.8	134.8	1.8	.2	45.6	11.4	525.1	121.9	8.4	423.1	172.8	5.3	1197.1	486.3	8.2	5.5	8.2
18	F010 J1515-591	451.3	118.8	1.8	.2	46.2	13.3	480.8	109.9	8.6	670.3	197.1	8.2	793.6	367.3	5.4	6.0	5.4
19	F010 J1552-561	465.5	133.4	2.2	.3	31.5	11.1	376.5	96.5	8.5	421.1	159.0	6.1	275.6	214.5	1.9	3.1	1.9
20	F010 J1554-535	580.2	177.9	2.1	.3	41.8	9.6	558.4	127.8	8.3	430.3	200.5	4.0	499.5	347.8	3.3	2.5	3.3
21	F010 J1603-490	756.7	154.3	1.9	.2	62.7	20.6	768.2	129.9	15.6	905.1	220.7	11.8	741.2	355.3	4.8	4.9	4.8
22	F010 J1614-517	394.1	121.2	1.7	.2	44.1	11.0	491.4	118.2	9.1	581.3	241.4	4.3	822.3	433.7	5.5	4.1	5.5
23	F010 J1617-509	589.5	148.4	1.9	.2	53.0	11.8	582.4	134.4	8.4	869.8	256.1	7.5	594.4	398.3	3.9	3.2	3.9
24	F010 J1620-494	540.6	153.3	2.2	.3	34.9	10.7	455.5	111.3	8.6	444.4	183.4	5.5	345.2	285.6	2.2	2.1	2.2
25	F010 J1622-501	555.4	204.2	2.6	.4	28.5	8.3	446.5	113.2	7.8	231.2	137.8	3.1	.0	.0	.0	.0	.0
26	F010 J1623-495	289.7	117.0	2.0	.3	23.3	7.7	277.8	93.5	5.6	414.6	184.9	5.2	116.9	208.8	.8	.7	.8
27	F010 J1632-478	1048.4	218.6	1.9	.2	86.3	14.6	1036.8	186.3	10.4	1477.9	338.2	9.8	697.2	449.7	4.4	3.5	4.4
28	F010 J1640-465	799.2	180.2	1.9	.2	67.4	14.4	835.3	161.8	10.1	1142.1	283.5	10.0	246.6	243.6	1.6	2.1	1.6
29	F010 J1649-465	203.4	79.3	1.7	.2	21.2	7.2	212.5	84.6	4.3	399.6	181.4	5.0	337.3	296.0	2.2	2.7	2.2
30	F010 J1652-463	377.3	129.2	2.2	.3	24.6	7.5	371.1	106.1	7.0	209.9	142.1	2.4	118.4	247.4	.8	.6	.8
31	F010 J1703-423	128.9	75.3	1.5	.3	18.7	7.6	174.7	77.7	4.4	308.3	187.3	3.6	650.7	382.6	4.1	4.6	4.1
32	F010 J1704-413	213.3	82.7	1.6	.2	24.0	7.9	284.1	96.5	5.4	271.7	182.0	3.7	733.6	469.5	4.5	4.1	4.5

33	F010 J1709-444	4608.3	639.5	3.8	.3	125.6	28.9	2366.1	226.7	28.2	160.6	97.2	3.8	.0	.0	.0	.0	.0
34	F010 J1713-394	235.6	93.8	1.4	.2	35.3	10.0	238.2	94.1	4.3	770.6	262.2	5.6	1504.2	574.4	9.3	7.2	9.3
35	F010 J1714-383	548.5	179.0	2.0	.3	39.2	9.7	531.1	130.1	7.8	588.9	220.9	5.4	321.8	296.4	2.0	1.6	2.0
36	F010 J1718-374	485.4	162.9	2.1	.3	32.4	10.2	479.7	118.6	8.3	410.1	176.2	5.0	190.6	190.7	1.2	3.0	1.2
37	F010 J1732-316	463.0	186.8	2.5	.5	22.1	7.7	339.2	102.3	6.6	262.7	143.8	3.6	128.6	247.1	.8	.6	.8
38	F010 J1738-325	403.9	150.4	2.2	.3	25.3	8.0	351.1	103.5	6.7	457.5	188.3	4.7	.0	.0	.0	.0	.0
39	F010 J1740-306	299.2	117.1	1.9	.3	24.7	7.3	294.5	102.0	4.7	440.0	215.6	4.2	424.7	302.5	2.5	3.7	2.5
40	F010 J1744-306	366.7	120.5	1.8	.2	34.3	9.2	419.6	121.3	6.4	531.1	217.9	5.1	736.2	440.8	4.4	4.0	4.4
41	F010 J1745-289	3648.8	489.4	2.7	.2	153.4	25.0	2672.1	265.2	22.9	1046.6	277.1	8.4	612.3	407.5	3.7	3.4	3.7
42	F010 J1756-240	360.2	132.1	2.1	.3	23.3	8.0	322.5	106.2	5.8	339.2	173.3	4.1	344.5	289.5	2.0	3.8	2.0
43	F010 J1801-222	1133.7	4502.9	4.8	12.8	20.6	7.5	399.2	113.2	7.1	134.4	138.5	1.3	19.8	204.8	.1	.1	.1
44	F010 J1801-234	1009.8	287.2	2.6	.3	45.5	10.1	803.5	171.8	8.2	279.3	153.7	5.4	500.5	361.8	2.9	2.1	2.9
45	F010 J1804-215	800.1	193.0	2.1	.2	52.7	11.9	797.6	162.8	9.4	554.3	214.4	5.5	914.6	485.2	5.3	4.7	5.3
46	F010 J1805-223	117.0	54.7	1.5	.2	15.9	7.0	198.0	91.2	3.4	31.4	67.6	.6	1269.4	537.2	7.4	6.8	7.4
47	F010 J1808-198	340.5	141.0	2.0	.3	24.3	7.7	376.7	113.6	6.9	224.7	160.5	2.4	459.0	337.2	2.6	2.3	2.6
48	F010 J1809-235	1259.3	343.1	4.2	.6	27.4	11.4	558.3	119.4	10.6	57.9	58.2	2.8	.0	.1	.0	.0	.0
49	F010 J1811-190	288.6	120.5	2.0	.3	19.8	7.5	284.0	97.3	5.9	316.4	163.0	4.0	181.5	219.6	1.0	1.3	1.0
50	F010 J1823-136	700.0	191.3	2.1	.2	44.4	9.7	680.0	155.3	8.6	481.8	240.7	3.5	800.2	507.4	4.5	3.0	4.5
51	F010 J1825-139	520.6	238.1	1.7	.3	51.1	11.2	485.9	128.9	7.1	1322.4	343.0	7.5	1259.8	592.4	7.1	4.7	7.1
52	F010 J1826-148	250.4	113.1	1.7	.3	24.9	9.0	312.8	104.2	5.3	408.4	191.0	5.5	596.3	421.3	3.4	4.2	3.4
53	F010 J1828-100	262.2	116.5	2.0	.3	18.3	7.2	301.0	100.9	5.1	78.6	77.7	3.0	680.9	401.1	3.8	4.6	3.8
54	F010 J1828-123	283.2	124.2	2.0	.3	20.0	7.1	260.4	102.2	4.5	428.3	180.1	5.8	.0	.0	.0	.0	.0
55	F010 J1834-087	856.2	229.8	2.1	.2	53.3	11.4	822.2	166.8	8.8	690.5	253.5	5.8	655.5	416.3	3.7	4.2	3.7
56	F010 J1837-069	625.5	150.6	1.6	.1	66.5	13.2	782.7	165.5	9.3	977.9	322.2	5.9	2340.0	762.6	13.0	7.2	13.0
57	F010 J1839-059	449.7	142.9	1.7	.2	44.6	10.4	629.6	156.5	8.1	293.9	190.6	3.3	1810.1	680.8	10.0	6.0	10.0
58	F010 J1844-032	271.7	121.6	1.8	.3	22.6	7.5	314.7	108.5	5.5	349.4	183.6	4.3	407.7	365.7	2.3	2.3	2.3
59	F010 J1847-018	588.2	202.0	2.5	.4	27.7	8.0	456.8	129.9	6.2	359.7	181.2	5.0	.0	.0	.0	.0	.0
60	F010 J1849-009	733.8	285.4	3.1	.7	23.6	7.4	455.5	123.3	7.1	207.3	172.8	1.6	.0	.1	.0	.0	.0
61	F010 J1855+015	1441.2	443.4	2.9	.5	50.9	12.0	1013.1	184.8	11.3	27.1	124.0	.2	476.9	336.1	2.6	4.2	2.6
62	F010 J1857+027	344.2	100.3	1.5	.2	42.1	10.8	456.9	122.2	6.9	592.4	222.6	5.8	1890.4	660.9	10.5	6.0	10.5
63	F010 J1859+043	280.1	140.0	2.0	.4	18.6	7.5	298.9	99.4	6.3	201.8	144.3	3.6	209.4	218.8	1.2	2.0	1.2
64	F010 J1906+073	578.0	237.3	2.8	.6	22.2	7.3	405.4	116.2	6.6	174.6	126.7	2.6	.0	.0	.0	.0	.0
65	F010 J1910+090	1062.0	268.7	2.6	.3	45.8	13.8	814.4	148.5	13.0	331.0	171.4	4.4	177.5	235.1	1.0	1.1	1.0
66	F010 J1913+106	112.0	82.4	1.4	.4	15.2	7.5	98.9	63.0	3.0	462.6	187.2	6.9	280.9	378.9	1.6	.9	1.6
67	F010 J1923+141	1842.9	332.3	2.5	.2	87.6	19.1	1405.2	193.0	16.3	1127.1	278.2	10.0	.0	.1	.0	.0	.0

Table B.3.. F010: Fermi sources above 10 GeV — HESS counterpart and measurement. The closest Galactic HESS source within the 90% containment radius $+0.1$ deg is listed (if any) and the offset is given in the θ_{HGPS} column. Also the point-source flux F, sensitivity F_S, upper limit F_{UL} (all integral above 1 TeV in X assuming a spectral index of 2.5) and significance S at the Fermi source position is given, as well as the significance $S_{0.22}$ for an 0.22 deg and $S_{0.4}$ for an 0.4 deg correlation radius. Because there might be small offsets between the Fermi and HESS source, additionally the maximum point-source significance $S_{0.1}^{max}$ within a search radius of 0.1 deg of the Fermi source position is given. Only sources in the GPS region are considered.

				std point							std			hard
#	Source Name	HGPS	θ_{HGPS}	F	F_S	F_{UL}	$S_{0.1}$	$S_{0.1}^{max}$	$S_{0.22}$	$S_{0.4}$	$S_{0.1}$	$S_{0.1}^{max}$	$S_{0.22}$	$S_{0.4}$
1	F010 J0823-428			13.6	164.0	80.3	.5	2.6	.1	.1	.0	2.0	1.3	1.0
2	F010 J0835-451	HGPS J0834-457	1.1	14.8	13.5	20.4	5.4	7.9	11.8	15.1	8.4	10.4	15.7	20.9
3	F010 J0848-459	HGPS J0851-464	1.4	25.3	17.8	32.9	7.0	7.2	12.8	17.7	5.8	8.2	15.0	20.7
4	F010 J0853-471	HGPS J0851-464	1.6	33.5	19.3	42.5	8.5	8.6	13.7	17.8	9.4	10.0	13.4	17.0
5	F010 J1019-589	HGPS J1018-589	.2	25.7	25.9	36.8	5.0	5.8	4.8	3.6	5.0	6.1	5.6	4.4
6	F010 J1024-576	HGPS J1023-578	.4	31.6	23.1	41.8	6.8	9.9	12.0	13.8	5.0	8.0	9.3	14.0
7	F010 J1028-582			8.6	25.7	18.7	1.7	2.1	.4	2.0	2.7	3.3	4.1	4.1
8	F010 J1031-595			8.3	32.3	21.2	1.3	2.3	.2	1.4	-.0	1.6	1.1	1.7
9	F010 J1044-596			2.3	26.8	12.7	.4	2.5	-.2	1.3	1.2	2.0	1.1	1.1
10	F010 J1048-585			-3.0	27.5	7.6	-.6	2.7	2.5	3.1	2.1	3.0	2.3	2.8
11	F010 J1112-611			9.2	25.9	19.6	1.8	3.5	3.6	1.6	2.7	4.0	5.0	2.3
12	F010 J1118-614	HGPS J1119-614	.1	25.2	25.1	36.1	5.1	6.5	8.1	5.8	5.6	7.8	8.4	7.3
13	F010 J1304-632	HGPS J1303-632	.2	65.7	.0	71.6	24.9	31.0	50.3	56.2	24.8	32.6	51.0	55.5
14	F010 J1306-627			7.9	13.6	13.3	2.9	7.2	10.0	16.8	2.4	3.9	6.5	13.4
15	F010 J1349-619			-4.7	33.5	8.0	-.7	1.8	1.2	.7	.3	1.9	1.1	1.8
16	F010 J1405-613			23.4	35.1	38.0	3.4	3.8	5.6	6.1	1.7	3.5	3.6	4.1
17	F010 J1418-609	HGPS J1417-609	.2	70.0	29.8	84.5	11.2	14.9	20.1	21.8	9.8	14.6	19.8	23.2
18	F010 J1515-591	HGPS J1514-591	.2	102.8	18.5	112.7	25.4	36.9	43.9	36.8	27.9	41.4	46.6	38.4
19	F010 J1552-561			13.8	24.3	23.8	2.9	2.9	2.4	2.9	1.3	1.9	.8	.8
20	F010 J1554-535			1.3	21.7	9.8	.3	1.5	2.1	3.1	-.6	1.0	1.0	1.8
21	F010 J1603-490			-6.0	154.3	52.0	-.2	2.3	.0	.1	1.5	1.5	-.9	-.6
22	F010 J1614-517	HGPS J1614-518	.1	51.4	27.7	65.1	9.0	12.1	18.7	21.9	9.2	12.6	20.5	23.2
23	F010 J1617-509	HGPS J1616-508	.4	54.9	26.6	68.0	9.9	14.5	17.5	25.0	10.3	13.9	19.4	26.0
24	F010 J1620-494	HGPS J1626-491	1.9	-.4	27.5	10.2	-.1	1.3	-.4	.4	1.6	3.6	2.3	2.1
25	F010 J1622-501			3.2	26.1	13.5	.6	2.8	2.1	3.9	1.7	2.8	2.6	3.5
26	F010 J1623-495	HGPS J1626-491	1.1	13.0	26.2	23.6	2.5	4.4	4.3	4.5	2.8	4.0	4.7	4.8
27	F010 J1632-478	HGPS J1632-478	.1	31.8	22.4	42.0	7.0	11.5	19.4	24.6	8.1	10.8	17.3	23.2
28	F010 J1640-465	HGPS J1640-465	.1	135.3	14.9	144.3	39.1	39.2	39.5	29.5	42.3	43.3	39.2	28.9

29	F010 J1649-465	HGPS J1647-459	1.4	3.8	17.3	10.7	1.1	3.7	3.9	9.0	1.5	4.0	4.9	10.2
30	F010 J1652-463	HGPS J1647-459	2.0	6.7	20.6	15.2	1.7	2.8	3.9	7.7	.6	2.8	3.4	7.1
31	F010 J1703-423	HGPS J1702-419	.9	5.3	29.1	16.8	.9	3.8	5.7	10.4	.5	4.9	6.6	10.2
32	F010 J1704-413	HGPS J1702-419	1.4	6.1	22.2	15.1	1.4	3.2	5.9	9.0	1.0	3.4	5.8	8.3
33	F010 J1709-444	HGPS J1708-442	.7	7.7	25.3	17.8	1.5	3.1	4.0	5.1	-.4	3.3	4.1	5.2
34	F010 J1713-394	HGPS J1713-397	.6	59.9	12.7	65.9	22.2	26.0	43.5	53.5	25.7	29.0	47.3	58.2
35	F010 J1714-383	HGPS J1713-382	.3	20.6	15.0	26.9	6.8	10.1	15.7	17.2	5.4	9.2	13.8	14.9
36	F010 J1718-374			10.9	18.1	18.5	3.1	4.4	2.5	3.4	2.6	3.4	2.5	3.2
37	F010 J1732-316			-1.6	29.6	9.6	-.3	1.2	.2	.8	-1.3	.9	.8	.8
38	F010 J1738-325			-2.1	26.4	7.8	-.5	1.1	.7	.0	.1	2.1	-.4	.6
39	F010 J1740-306			5.4	13.1	10.7	2.1	2.5	2.2	3.5	.9	3.2	1.5	3.3
40	F010 J1744-306	HGPS J1744-303	.6	12.9	10.8	17.3	5.9	6.9	9.1	14.7	4.9	7.0	9.0	13.0
41	F010 J1745-289	HGPS J1745-290	.0	126.5	.0	130.7	77.0	77.1	73.2	54.6	82.0	82.0	74.0	56.2
42	F010 J1756-240	HGPS J1800-239	1.6	4.5	14.9	10.3	1.5	3.2	3.7	6.6	1.4	3.1	2.6	4.8
43	F010 J1801-222			-2.9	14.6	2.7	-1.0	2.2	2.3	6.0	.1	1.6	1.3	3.1
44	F010 J1801-234	HGPS J1800-239	1.0	15.3	14.7	21.5	5.2	7.3	9.6	12.5	4.4	6.3	5.7	8.9
45	F010 J1804-215	HGPS J1804-217	.3	45.1	12.5	51.4	17.0	20.0	34.5	38.2	14.2	18.1	30.5	34.0
46	F010 J1805-223			3.9	14.5	9.5	1.3	3.6	4.0	7.9	2.3	3.8	3.7	7.8
47	F010 J1808-198	HGPS J1810-193	1.2	7.6	9.9	11.6	3.8	6.0	8.8	15.0	5.3	6.3	11.0	17.6
48	F010 J1809-235			8.4	32.0	21.8	1.4	2.5	2.0	-.6	-.7	1.4	.8	-.4
49	F010 J1811-190	HGPS J1810-193	.7	15.6	11.8	20.7	6.6	7.5	11.0	18.3	7.8	8.6	13.8	19.6
50	F010 J1823-136	HGPS J1825-138	.9	19.6	10.6	24.3	9.1	12.7	19.7	26.7	10.2	11.8	18.4	24.6
51	F010 J1825-139	HGPS J1825-138	.4	42.2	8.9	46.4	22.2	27.0	42.5	52.3	19.0	25.2	42.8	54.3
52	F010 J1826-148	HGPS J1826-148	.0	86.7	8.0	91.2	47.5	47.7	36.3	29.5	53.4	53.4	38.0	29.0
53	F010 J1828-100	HGPS J1831-098	1.3	12.9	18.4	20.6	3.6	5.2	4.3	4.5	5.4	7.0	5.9	4.4
54	F010 J1828-123			-3.9	23.5	5.2	-.8	.3	-1.5	-.0	.2	.7	-1.6	-.4
55	F010 J1834-087	HGPS J1834-087	.1	53.4	17.1	61.8	14.8	15.5	21.0	21.9	15.9	16.4	19.8	19.1
56	F010 J1837-069	HGPS J1837-069	.1	74.9	18.4	84.5	18.8	20.0	32.7	38.3	21.0	24.1	33.2	37.0
57	F010 J1839-059	HGPS J1840-056	.9	24.4	17.0	31.9	7.1	8.1	13.7	21.3	8.7	10.8	14.4	22.3
58	F010 J1844-032	HGPS J1843-033	.6	10.4	16.3	17.0	3.2	6.1	8.4	11.5	3.8	7.6	8.8	12.8
59	F010 J1847-018	HGPS J1848-017	.3	17.9	14.1	24.1	6.3	7.0	11.0	13.7	4.9	6.7	10.3	12.7
60	F010 J1849-009	HGPS J1848-017	1.8	12.5	13.5	18.2	4.6	5.0	5.3	7.3	3.4	4.3	4.2	7.0
61	F010 J1855+015			8.2	14.5	14.2	2.9	3.3	3.1	5.8	2.0	2.8	2.0	6.0
62	F010 J1857+027	HGPS J1857+027	.1	44.7	20.1	54.2	10.7	12.9	16.2	19.2	8.7	11.9	14.6	17.9
63	F010 J1859+043			-9.8	36.5	3.7	-1.4	1.4	.3	1.9	-.8	2.0	1.0	1.9
64	F010 J1906+073	HGPS J1907+064	1.8	8.6	19.6	16.6	2.3	3.5	3.4	5.2	2.0	3.5	4.6	6.2
65	F010 J1910+090			15.2	14.6	21.3	5.2	6.1	6.3	3.3	3.0	3.8	3.6	3.3

66	F010 J1913+106	HGPS J1913+101	1.2	2.5	16.8	8.9	.7	2.7	2.4	4.3	-.3	2.3	1.5	3.2
67	F010 J1923+141	HGPS J1922+141	.2	20.0	26.1	31.3	3.9	5.7	6.0	4.8	1.5	5.3	5.8	4.2

Table B.4.. F100: Fermi sources above 100 GeV — Position and counterparts. See Table B.1 for explanations. All sources are listed.

#	Source Name	GLON	GLAT	$\theta_{p\to b}$	S	$E_{0.3}$	$N_{0.3}$	2FGL	θ_{2FGL}	2FGL ASSOC1	2FGL CLASS1
		deg	deg	deg		GeV			deg		
1	F100 J0036+598	121.00	-2.96	.06	6.0	149	3	2FGL J0035.8+5951	.02	1ES 0033+595	bzb
2	F100 J0150-437	270.87	-69.54	.08	5.7	128	2				
3	F100 J0222+430	140.14	-16.75	.13	7.0	123	3	2FGL J0222.6+4302	.02	3C 66A	BZB
4	F100 J0240+612	135.68	1.10	.12	6.6	199	3	2FGL J0240.5+6113	.02	LS I+61 303	HMB
5	F100 J0316+413	150.17	-13.71	.03	6.6	111	3	2FGL J0316.6+4119	.03	IC 310	rdg
6	F100 J0424-001	194.28	-32.20	.13	5.3	166	2				
7	F100 J0430+558	150.38	5.10	.24	5.6	293	2				
8	F100 J0449-439	248.92	-39.97	.12	6.3	115	3	2FGL J0449.4-4350	.11	PKS 0447-439	bzb
9	F100 J0506+613	149.07	12.18	.22	5.2	140	2	2FGL J0505.9+6116	.06	NVSS J050558+611336	agu
10	F100 J0506-281	229.97	-34.22	.16	5.1	102	1				
11	F100 J0508+675	143.84	15.90	.02	13.5	149	12	2FGL J0508.0+6737	.04	1ES 0502+675	bzb
12	F100 J0521+212	183.57	-8.77	.02	6.6	233	3	2FGL J0521.7+2113	.08	VER J0521+211	bzb
13	F100 J0534+220	184.55	-5.76	.08	23.9	111	31	2FGL J0534.5+2201	.02	PSR J0534+2200	PSR
14	F100 J0544-555	263.54	-31.47	.05	6.4	124	3	2FGL J0543.9-5532	.02	1RXS J054357.3-553206	bzb
15	F100 J0617+225	189.11	3.07	.19	7.4	124	5	2FGL J0617.2+2234e	.07	SNR G189.1-03.0	SNR
16	F100 J0648+153	198.91	6.29	.05	5.2	503	2	2FGL J0648.9+1516	.11	VER J0648+152	agu
17	F100 J0651+249	190.42	11.16	.14	6.0	247	3	2FGL J0650.7+2505	.22	1ES 0647+250	bzb
18	F100 J0655-845	296.82	-26.89	.12	5.1	181	2				
19	F100 J0823-434	260.95	-3.50	.07	5.3	188	2	2FGL J0823.4-4305	.40		spp
20	F100 J0830-448	262.75	-3.34	.16	5.4	134	2				
21	F100 J0848-450	264.87	-.82	.55	5.3	384	2				
22	F100 J0855-471	267.25	-1.32	.22	6.0	108	2	2FGL J0853.5-4711	.29		spp
23	F100 J0913-210	249.62	18.51	.07	5.4	142	2	2FGL J0912.9-2102	.06	MRC 0910-208	bzb
24	F100 J1010-313	266.88	20.02	.04	5.7	178	2	2FGL J1009.7-3123	.09	1RXS J101015.9-311909	bzb
25	F100 J1014+493	165.72	52.72	.07	5.2	155	2	2FGL J1015.1+4925	.12	1H 1013+498	bzb
26	F100 J1016+411	178.95	55.34	.05	5.8	157	2				
27	F100 J1019-589	284.39	-1.68	.17	6.0	121	2	2FGL J1019.0-5856	.03	1FGL J1018.6-5856	HMB
28	F100 J1022-579	284.17	-.58	.42	6.0	961	3	2FGL J1023.5-5749c	.17		
29	F100 J1032-499	281.19	6.95	.09	5.1	349	2				
30	F100 J1037-593	286.63	-.82	.25	6.4	168	4				
31	F100 J1043-567	286.01	1.88	.08	6.0	118	3				
32	F100 J1104+382	179.84	65.02	.59	28.5	118	36	2FGL J1104.4+3812	.02	Mkn 421	bzb
33	F100 J1116+202	225.48	67.36	.03	6.2	114	2	2FGL J1117.2+2013	.07	RBS 0958	bzb
34	F100 J1118-614	292.05	-.54	.02	5.0	204	3	2FGL J1118.8-6128	.06	PSR J1119-6127	PSR

35	F100 J1136+700	131.90	45.71	.07	5.6	180	2	2FGL J1136.7+7009	.07	Mkn 180	bzb
36	F100 J1221+302	185.87	82.76	.24	7.1	357	3	2FGL J1221.3+3010	.06	PG 1218+304	bzb
37	F100 J1224+213	254.97	81.61	.00	5.8	148	2	2FGL J1224.9+2122	.05	4C +21.35	BZQ
38	F100 J1315-426	307.54	20.01	.03	5.5	103	2				
39	F100 J1332-625	307.65	-.08	.13	5.3	119	3				
40	F100 J1406-612	311.78	.30	.14	5.7	101	4	2FGL J1405.5-6121	.11		
41	F100 J1420-606	313.58	.38	.20	6.4	371	4	2FGL J1420.1-6047	.15	PSR J1420-6048	PSR
42	F100 J1427+236	29.16	68.14	.04	6.7	137	3	2FGL J1427.0+2347	.13	PKS 1424+240	bzb
43	F100 J1515-592	320.40	-1.32	.08	6.4	112	4	2FGL J1514.0-5915e	.14	MSH 15-52 PWN	PWN
44	F100 J1555+112	21.92	43.98	.05	11.7	156	7	2FGL J1555.7+1111	.03	PG 1553+113	bzb
45	F100 J1555-538	328.04	-.14	.02	5.0	152	2				
46	F100 J1603-491	332.06	2.52	.07	5.5	202	4	2FGL J1603.8-4904	.10	PMN J1603-4904	bzb
47	F100 J1612-009	11.13	34.19	.16	5.1	117	1				
48	F100 J1616-512	332.16	-.36	.08	5.3	135	3	2FGL J1615.0-5051	.42		spp
49	F100 J1616-518	331.68	-.84	.17	5.4	318	2	2FGL J1615.2-5138	.30		
50	F100 J1621-496	333.82	.22	.03	5.3	109	3	2FGL J1620.8-4928	.17		
51	F100 J1632-249	353.60	15.47	.15	5.7	127	2				
52	F100 J1633+123	28.60	36.07	.12	5.0	605	2				
53	F100 J1634-476	336.78	.08	.08	6.4	130	5	2FGL J1634.4-4743c	.13		
54	F100 J1642-445	340.08	1.00	.19	5.7	123	4				
55	F100 J1653+397	63.58	38.85	.08	14.4	155	10	2FGL J1653.9+3945	.02	Mkn 501	BZB
56	F100 J1654-467	339.70	-2.02	.07	5.4	111	3	2FGL J1653.9-4627c	.34		
57	F100 J1701-406	345.24	.80	.39	5.3	293	3				
58	F100 J1703-421	344.26	-.40	.02	5.6	122	4				
59	F100 J1706-397	346.50	.62	.00	5.2	162	2				
60	F100 J1710-410	345.90	-.72	.07	5.1	107	3				
61	F100 J1711-441	343.56	-2.76	.08	5.3	301	3	2FGL J1709.7-4429	.46	PSR J1709-4429	PSR
62	F100 J1714-394	347.64	-.38	.15	7.2	252	8	2FGL J1712.4-3941	.39		spp
63	F100 J1727-351	352.68	-.10	.07	5.5	144	4				
64	F100 J1744-293	359.50	-.02	.16	5.9	170	4	2FGL J1745.6-2858	.48		spp
65	F100 J1800-232	6.64	-.02	.09	5.0	127	2	2FGL J1801.3-2326e	.26	SNR G006.4-00.1	SNR
66	F100 J1805-215	8.64	-.24	.11	5.0	202	5	2FGL J1805.6-2136e	.04	SNR G008.7-00.1	SNR
67	F100 J1805-223	7.98	-.62	.07	6.8	125	6				
68	F100 J1811-176	12.69	.58	.11	5.1	167	3				
69	F100 J1826-139	17.69	-.94	.24	5.7	211	4				
70	F100 J1831-086	23.05	.38	.13	5.7	202	3				
71	F100 J1837-070	25.13	-.14	.16	7.7	137	8	2FGL J1837.3-0700c	.06		

72	F100 J1840-058	26.47	-.18	.32	6.8	156	5	2FGL J1839.3-0558c	.28			
73	F100 J1856+028	36.13	.10	.06	6.8	308	7					
74	F100 J2000+651	98.06	17.65	.06	8.3	166	5	2FGL J2000.0+6509	.04	1ES 1959+650	bzb	
75	F100 J2001+438	79.05	7.09	.03	6.5	150	3	2FGL J2001.1+4352	.03	MAGIC J2001+435	bzb	
76	F100 J2009-488	350.34	-32.59	.03	6.8	180	3	2FGL J2009.5-4850	.04	PKS 2005-489	BZB	
77	F100 J2017+455	82.07	5.60	.02	5.8	460	2					
78	F100 J2018+392	76.92	1.88	.04	5.2	145	3	2FGL J2018.2+3850c	.42	TXS 2016+386	agu	
79	F100 J2019+408	78.30	2.66	.35	5.2	102	2	2FGL J2019.1+4040	.15		spp	
80	F100 J2031+403	79.26	.44	.16	5.5	509	2					
81	F100 J2032+382	77.66	-.88	.03	5.0	104	3					
82	F100 J2108+520	92.30	2.97	.13	5.3	171	2	2FGL J2107.9+5207c	.10			
83	F100 J2158-302	17.74	-52.25	.04	13.7	212	10	2FGL J2158.8-3013	.01	PKS 2155-304	bzb	
84	F100 J2320+592	111.57	-1.66	.23	5.3	251	2	2FGL J2323.4+5849	.49	SNR G111.7-02.1	snr	
85	F100 J2320+609	112.15	-.02	.02	5.4	271	2					
86	F100 J2322+346	102.85	-24.77	.15	6.5	117	2	2FGL J2322.6+3435	.06	TXS 2320+343	bzb	
87	F100 J2325-407	349.91	-67.59	.03	5.6	103	2	2FGL J2324.7-4042	.09	1ES 2322-409	bzb	

Table B.5.. F100: Fermi sources above 100 GeV — Spectral parameters. See Table B.2 for explanations. All sources are listed.

		10 to 1000 GeV						10 to 30 GeV			30 to 100 GeV			100 to 1000 GeV				
#	Source Name	F	ΔF	Γ	$\Delta\Gamma$	N	S	F	ΔF	S	F	ΔF	S	F	ΔF	N	S	
1	F100 J0036+598	295.6	83.0	1.9	.2	32.3	6.0	283.8	69.4	10.3	432.2	138.8	9.9	396.8	230.0	3.2	6.0	3.2
2	F100 J0150-437	11.9	10.9	1.1	.4	3.0	5.7	19.6	20.2	2.1	.0	.1	.0	319.8	226.5	2.0	5.7	2.0
3	F100 J0222+430	2303.1	275.4	2.2	.1	158.2	7.0	2064.6	198.5	36.3	2086.0	324.9	22.7	613.6	313.1	4.1	7.0	4.1
4	F100 J0240+612	493.6	124.9	2.3	.2	37.9	6.6	442.6	87.4	12.4	185.6	96.6	4.3	466.0	260.0	3.8	6.6	3.8
5	F100 J0316+413	353.7	129.4	1.9	.2	33.1	6.6	294.1	106.0	5.7	648.3	211.5	6.8	505.0	286.4	3.4	6.6	3.4
6	F100 J0424-001	22.5	183.8	1.3	3.8	4.0	5.3	46.4	35.8	3.8	.0	.2	.0	384.5	273.2	2.1	5.3	2.1
7	F100 J0430+558	19.5	12.7	1.0	.2	7.8	5.6	.0	.1	.0	127.3	91.8	2.2	514.6	280.6	4.1	5.6	4.1
8	F100 J0449-439	943.0	170.5	2.0	.1	70.2	6.3	936.5	138.1	21.8	1028.6	233.8	16.0	475.4	275.5	3.0	6.3	3.0
9	F100 J0506+613	29.2	25.4	1.4	.4	6.2	5.2	7.0	17.1	.5	120.6	72.0	4.1	333.0	215.0	2.7	5.2	2.7
10	F100 J0506-281	6.6	4.8	1.0	.0	2.1	5.1	.0	.0	.0	.0	.0	.0	350.9	252.1	2.1	5.1	2.1
11	F100 J0508+675	431.2	87.8	1.6	.1	68.2	13.5	495.1	88.5	16.2	898.1	190.3	17.2	1438.7	415.5	12.0	13.5	12.0
12	F100 J0521+212	771.5	156.8	2.0	.2	58.2	6.6	688.1	122.5	15.3	1133.6	256.8	14.0	566.3	326.3	3.4	6.6	3.4
13	F100 J0534+220	7621.6	522.6	2.2	.1	481.5	23.9	7057.7	383.7	63.8	5344.9	546.1	37.7	5973.3	1020.7	35.7	23.9	35.7
14	F100 J0544-555	199.9	74.6	1.9	.3	18.4	6.4	224.5	66.8	9.5	148.4	86.2	6.2	438.6	254.9	3.0	6.4	3.0
15	F100 J0617+225	3120.4	370.7	2.4	.1	169.5	7.4	2663.5	244.3	26.7	1505.5	306.3	12.5	1374.2	508.6	8.3	7.4	8.3
16	F100 J0648+153	97.7	43.5	1.5	.2	11.8	5.2	141.1	58.0	6.0	176.9	102.3	5.6	347.8	246.4	2.0	5.2	2.0

17	F100 J0651+249	203.8	71.9	1.6	.2	25.2	6.0	253.9	78.6	6.6	441.1	158.6	6.9	667.8	345.3	4.1	6.0	4.1
18	F100 J0655-845	5.6	3.5	1.0	.0	2.0	5.1	.0	.0	.0	.0	.2	.0	293.9	209.8	2.0	5.1	2.0
19	F100 J0823-434	.0	.0	4.4	.2	.0	5.3	.0	.0	.0	58.7	99.3	.7	365.2	258.7	2.3	4.7	2.3
20	F100 J0830-448	211.3	126.1	2.0	.4	16.6	5.4	237.2	103.9	4.7	60.6	75.8	1.2	632.9	370.7	4.0	5.3	4.0
21	F100 J0848-450	10.1	6.9	1.0	.0	3.4	5.3	.0	.1	.0	.0	.0	.0	606.8	386.6	3.9	5.2	3.9
22	F100 J0855-471	121.2	54.4	1.5	.2	16.8	6.0	116.9	62.5	3.2	379.0	182.0	4.0	584.1	352.9	3.7	6.0	3.7
23	F100 J0913-210	47.8	34.1	1.4	.4	6.4	5.4	66.1	39.1	4.6	59.9	65.8	1.7	391.4	273.8	2.2	5.4	2.2
24	F100 J1010-313	63.2	33.1	1.4	.3	9.4	5.7	112.6	51.2	5.5	101.3	79.0	2.7	377.9	264.5	2.2	5.7	2.2
25	F100 J1014+493	916.7	197.1	2.4	.2	56.8	5.2	777.5	119.2	20.7	454.1	147.0	10.0	285.3	202.1	2.0	5.2	2.0
26	F100 J1016+411	6.0	3.9	1.0	.0	2.1	5.8	.0	.0	.0	.0	.0	.0	320.1	225.7	2.1	5.8	2.1
27	F100 J1019-589	102.2	57.1	1.5	.3	15.8	6.0	134.0	58.9	4.7	172.8	121.8	2.6	679.7	389.0	4.7	5.9	4.7
28	F100 J1022-579	122.6	70.9	1.5	.3	19.2	6.0	208.9	82.1	4.3	97.9	137.3	.8	716.7	386.1	5.0	6.0	5.0
29	F100 J1032-499	5.9	4.2	1.0	.0	2.0	5.1	.0	.0	.0	.0	.0	.0	316.9	225.8	2.1	5.1	2.1
30	F100 J1037-593	56.2	33.6	1.2	.2	14.0	6.4	78.7	50.6	2.6	126.8	129.3	1.4	917.3	429.3	6.3	6.3	6.3
31	F100 J1043-567	10.4	6.2	1.0	.0	3.8	6.0	.0	.1	.0	.0	.0	.0	543.7	315.3	3.7	6.0	3.7
32	F100 J1104+382	3004.0	265.4	1.8	.1	308.9	28.5	3150.4	243.3	48.8	4942.8	496.0	41.9	5697.1	925.4	38.1	28.5	38.1
33	F100 J1116+202	156.4	66.4	1.8	.3	13.4	6.2	155.3	59.2	7.5	230.7	115.5	6.8	352.2	249.0	2.0	6.2	2.0
34	F100 J1118-614	147.7	68.2	1.8	.3	15.6	5.0	142.5	68.1	3.8	187.0	127.5	2.4	431.7	267.1	3.0	4.9	3.0
35	F100 J1136+700	148.3	56.1	1.9	.3	17.4	5.6	155.0	49.5	8.8	188.5	88.3	6.5	239.4	169.4	2.0	5.6	2.0
36	F100 J1221+302	551.3	130.9	1.8	.2	51.2	7.1	528.6	116.2	13.0	1050.9	256.6	14.1	728.2	355.4	4.5	7.1	4.5
37	F100 J1224+213	906.8	188.8	2.3	.2	52.4	5.8	781.5	128.4	21.1	651.6	194.0	12.5	371.2	260.2	2.2	5.8	2.2
38	F100 J1315-426	18.8	22.2	1.1	.5	4.7	5.5	22.9	25.4	2.3	85.3	76.8	3.2	332.4	235.1	2.1	5.5	2.1
39	F100 J1332-625	19.1	12.9	1.0	.0	7.1	5.3	3.3	25.7	.1	157.8	117.2	2.2	512.7	303.8	3.6	4.9	3.6
40	F100 J1406-612	362.1	138.1	1.8	.2	38.0	5.7	360.4	119.8	4.6	609.1	212.6	6.1	728.8	385.0	5.0	5.4	5.0
41	F100 J1420-606	200.6	78.3	1.5	.2	28.2	6.4	325.1	99.3	5.4	160.0	117.1	2.1	1150.4	468.6	7.9	6.1	7.9
42	F100 J1427+236	1781.1	260.2	2.3	.1	105.1	6.7	1555.5	180.9	26.7	1405.3	280.4	16.9	531.6	306.4	3.2	6.7	3.2
43	F100 J1515-592	435.5	117.0	1.8	.2	44.4	6.4	463.7	108.0	8.5	630.2	195.2	7.7	793.6	368.0	5.4	6.2	5.4
44	F100 J1555+112	1981.9	250.3	2.0	.1	145.0	11.7	2007.2	208.3	34.0	2369.4	369.6	26.3	1614.8	540.6	9.1	11.7	9.1
45	F100 J1555-538	233.2	103.1	1.8	.3	23.6	5.0	240.5	97.2	4.1	332.7	164.4	3.8	476.3	302.4	3.2	5.0	3.2
46	F100 J1603-491	705.2	148.5	1.9	.2	59.8	5.5	718.4	127.9	13.2	888.8	221.4	10.4	736.6	354.4	4.8	5.4	4.8
47	F100 J1612-009	6.0	4.4	1.0	.0	1.8	5.1	.0	.1	.0	.0	.0	.0	357.7	260.5	2.0	5.1	2.0
48	F100 J1616-512	240.0	115.9	1.6	.2	31.2	5.3	267.0	118.8	3.3	600.6	251.8	4.4	731.2	399.3	4.9	5.2	4.9
49	F100 J1616-518	213.9	90.0	1.5	.2	30.6	5.4	225.9	98.6	3.4	678.0	255.8	4.3	685.8	402.5	4.6	5.2	4.6
50	F100 J1621-496	365.7	142.1	2.0	.3	27.7	5.3	338.4	123.3	3.9	275.3	167.2	2.8	560.8	321.1	3.6	5.3	3.6
51	F100 J1632-249	26.9	54.5	1.3	.9	4.7	5.7	48.4	41.2	2.1	.0	.0	.0	488.1	319.6	2.8	5.7	2.8
52	F100 J1633+123	8.3	5.3	1.0	.0	2.5	5.0	14.8	24.2	.8	.0	.0	.0	347.2	249.0	2.0	5.0	2.0
53	F100 J1634-476	932.7	196.3	1.9	.2	76.8	6.4	986.7	181.6	9.5	1017.3	344.3	4.3	1042.5	467.5	6.6	6.4	6.6

54	F100 J1642-445	35.1	50.9	1.3	.6	6.9	5.7	37.3	61.0	.7	.0	.0	.0	697.7	375.2	4.3	5.4	4.3
55	F100 J1653+397	906.6	151.5	1.8	.1	89.2	14.4	957.0	136.7	23.8	1318.3	257.0	20.1	1652.5	503.5	11.0	14.4	11.0
56	F100 J1654-467	122.4	102.8	1.8	.5	11.6	5.4	143.7	70.3	3.5	.0	.2	.0	517.6	304.1	3.3	5.3	3.3
57	F100 J1701-406	128.3	75.4	1.5	.3	17.2	5.3	137.6	79.5	2.4	317.3	171.3	3.5	755.8	421.2	4.6	4.9	4.6
58	F100 J1703-421	142.6	82.3	1.4	.3	21.8	5.6	135.1	77.3	2.6	548.7	226.7	3.9	748.4	397.8	4.7	5.3	4.7
59	F100 J1706-397	120.5	91.2	1.8	.5	10.7	5.2	139.7	73.9	2.7	27.5	95.6	.3	401.5	283.1	2.5	5.1	2.5
60	F100 J1710-410	63.6	52.1	1.4	.4	10.6	5.1	79.5	63.5	1.6	86.5	130.7	.8	759.2	419.7	4.7	5.0	4.7
61	F100 J1711-441	807.1	290.5	2.7	.4	35.8	5.3	633.5	168.9	5.4	.0	.0	.0	556.0	320.7	3.5	5.2	3.5
62	F100 J1714-394	235.6	93.8	1.4	.2	35.3	7.2	238.2	94.1	4.3	770.6	262.2	5.6	1504.2	574.4	9.3	7.2	9.3
63	F100 J1727-351	40.2	20.6	1.2	.2	8.8	5.5	53.2	58.0	1.1	.0	.1	.0	792.9	411.4	4.8	5.3	4.8
64	F100 J1744-293	695.0	241.9	2.1	.3	44.6	5.9	717.4	173.9	7.3	274.0	155.3	3.7	943.5	470.2	5.7	5.5	5.7
65	F100 J1800-232	548.7	193.9	2.3	.3	29.9	5.0	461.7	140.9	5.6	219.7	156.5	2.4	527.5	339.2	3.1	5.0	3.1
66	F100 J1805-215	744.6	185.7	2.0	.2	50.8	5.0	775.2	161.0	9.5	478.2	204.8	4.2	977.8	477.6	5.7	4.9	5.7
67	F100 J1805-223	117.0	54.7	1.5	.2	15.9	6.8	198.0	91.2	3.4	31.4	67.6	.6	1269.4	537.2	7.4	6.8	7.4
68	F100 J1811-176	195.5	88.3	1.8	.3	17.5	5.1	232.6	95.2	4.1	115.7	131.2	1.1	727.8	400.2	4.1	5.1	4.1
69	F100 J1826-139	402.1	132.1	1.6	.2	43.6	5.7	383.8	120.7	5.9	1167.6	327.6	7.0	1233.9	572.9	7.0	5.6	7.0
70	F100 J1831-086	123.6	77.2	1.6	.3	12.8	5.7	163.6	80.5	3.6	24.1	113.4	.2	730.7	417.0	4.1	5.7	4.1
71	F100 J1837-070	611.5	142.6	1.6	.1	64.3	7.7	770.8	164.4	8.8	895.5	314.8	5.8	2241.4	742.3	12.4	7.5	12.4
72	F100 J1840-058	390.1	127.9	1.6	.2	44.6	6.8	589.7	150.4	7.1	302.1	230.8	1.9	1915.6	713.4	10.6	6.8	10.6
73	F100 J1856+028	261.9	91.4	1.5	.2	34.9	6.8	343.9	116.8	5.2	496.9	217.2	5.1	1820.8	642.8	10.2	6.7	10.2
74	F100 J2000+651	615.2	123.8	2.0	.2	61.0	8.3	610.8	98.1	17.7	573.5	151.9	12.3	593.2	266.7	5.0	8.3	5.0
75	F100 J2001+438	1065.4	188.6	2.2	.2	74.9	6.5	931.9	134.8	19.2	935.8	217.8	14.2	452.0	261.0	3.1	6.5	3.1
76	F100 J2009-488	497.2	119.3	1.9	.2	42.1	6.8	480.0	99.3	14.9	721.7	198.0	13.0	504.7	289.3	3.2	6.8	3.2
77	F100 J2017+455	7.9	5.4	1.0	.0	3.0	5.8	.0	.2	.0	.0	.1	.0	306.7	216.0	2.2	5.8	2.2
78	F100 J2018+392	33.9	23.3	1.1	.3	10.0	5.2	45.8	44.2	1.8	99.2	89.1	2.8	727.3	378.4	4.9	5.1	4.9
79	F100 J2019+408	615.2	153.1	1.8	.2	59.5	5.2	610.9	132.0	9.4	1007.6	259.2	9.3	741.5	405.0	5.0	5.2	5.0
80	F100 J2031+403	52.6	128.9	1.3	1.0	10.8	5.5	91.5	61.0	2.3	166.2	120.1	3.0	420.4	284.5	2.9	5.2	2.9
81	F100 J2032+382	58.3	47.2	1.4	.4	9.8	5.0	31.8	42.9	.9	207.6	136.3	3.8	564.0	343.0	3.7	5.0	3.7
82	F100 J2108+520	15.1	14.2	1.2	.4	4.2	5.3	10.2	41.2	.3	.0	.0	.0	402.6	263.3	2.9	5.3	2.9
83	F100 J2158-302	2532.9	289.7	2.0	.1	175.3	13.7	2465.4	229.5	39.3	2491.1	376.2	26.8	1921.7	578.2	11.4	13.7	11.4
84	F100 J2320+592	10.0	8.4	1.0	.0	4.2	5.3	6.1	22.0	.3	25.8	54.7	.6	389.2	250.5	3.1	5.3	3.1
85	F100 J2320+609	8.8	8.8	1.0	.0	3.7	5.4	1.1	8.0	.1	21.0	89.5	.2	284.9	200.7	2.3	5.4	2.3
86	F100 J2322+346	107.1	55.0	1.7	.3	11.3	6.5	108.9	50.2	5.5	142.3	88.2	4.0	419.3	265.7	2.7	6.5	2.7
87	F100 J2325-407	119.3	57.6	1.8	.3	10.9	5.6	110.7	49.6	5.6	179.2	112.9	3.6	334.7	236.5	2.1	5.6	2.1

Table B.6.. F100: Fermi sources above 100 GeV — HESS counterpart and measurement. See Table B.3 for explanations. Only sources in the GPS region are considered.

				std point			std				hard			
#	Source Name	HGPS	θ_{HGPS}	F	F_S	F_{UL}	$S_{0.1}$	$S_{0.1}^{max}$	$S_{0.22}$	$S_{0.4}$	$S_{0.1}$	$S_{0.1}^{max}$	$S_{0.22}$	$S_{0.4}$
19	F100 J0823-434			-11.8	74.7	11.8	-1.1	.6	-.2	-.1	1.3	1.5	.5	1.4
20	F100 J0830-448			.3	15.6	6.3	.1	1.5	-1.2	.9	-.1	3.3	2.1	3.6
21	F100 J0848-450			5.2	22.1	14.0	1.2	1.9	1.2	2.7	1.7	2.1	.4	1.6
22	F100 J0855-471	HGPS J0851-464	2.0	30.3	19.3	39.0	7.7	7.8	11.0	14.6	7.1	8.4	12.1	16.0
27	F100 J1019-589	HGPS J1018-589	.2	20.7	26.0	31.4	4.0	5.8	4.3	3.3	4.5	6.1	5.6	4.5
28	F100 J1022-579	HGPS J1023-578	.3	21.0	22.4	30.7	4.7	8.7	10.6	13.9	5.9	8.9	11.3	14.3
30	F100 J1037-593			11.8	27.7	23.0	2.2	4.6	2.9	4.1	.5	2.0	1.5	2.4
31	F100 J1043-567			6.6	80.6	37.5	.4	2.0	.2	.1	-.1	2.0	1.4	1.3
34	F100 J1118-614	HGPS J1119-614	.2	28.6	24.7	39.4	5.8	6.5	7.0	5.7	7.6	7.8	7.6	6.8
39	F100 J1332-625			3.7	35.6	17.7	.5	2.6	2.8	1.9	-.8	2.0	2.0	3.2
40	F100 J1406-612	HGPS J1411-616	1.5	21.0	35.2	35.7	3.0	5.0	5.1	6.0	2.1	3.3	3.3	3.7
41	F100 J1420-606	HGPS J1420-607	.2	67.1	30.2	81.9	10.6	18.1	18.1	17.6	12.3	22.1	20.8	18.7
43	F100 J1515-592	HGPS J1514-591	.3	105.1	18.6	114.8	25.8	35.8	39.4	36.1	28.2	40.2	43.0	37.9
45	F100 J1555-538			2.3	21.4	11.1	.6	2.3	2.0	1.8	-.8	1.3	1.1	.7
46	F100 J1603-491			54.1	134.9	116.3	2.2	2.4	1.0	-.2	.0	1.9	-.7	.1
48	F100 J1616-512	HGPS J1616-508	.6	25.5	27.2	37.3	4.7	9.9	12.9	19.2	6.3	9.8	12.9	21.2
49	F100 J1616-518	HGPS J1614-518	.5	35.0	28.4	48.2	6.1	7.7	10.9	16.6	6.8	9.2	11.8	17.4
50	F100 J1621-496	HGPS J1626-491	2.0	-2.4	26.5	7.5	-.5	1.6	.9	2.3	1.2	3.2	2.4	3.4
53	F100 J1634-476	HGPS J1632-478	.7	24.0	21.4	33.3	5.6	8.3	14.5	24.3	6.9	7.9	12.4	23.0
54	F100 J1642-445			5.0	22.5	13.7	1.1	1.2	-.4	.1	-.3	1.1	.9	1.6
56	F100 J1654-467			3.0	26.8	13.6	.6	2.3	2.0	4.5	-.3	1.8	-.3	1.6
57	F100 J1701-406			9.3	28.5	20.5	1.6	2.0	1.8	1.7	.5	1.9	.6	1.4
58	F100 J1703-421	HGPS J1702-419	.6	29.1	28.4	41.8	5.1	7.5	8.8	12.4	5.1	7.9	8.9	13.2
59	F100 J1706-397	DIFF J1708-407	2.1	3.1	17.2	9.9	.9	2.1	.8	1.7	1.7	3.0	1.4	2.1
60	F100 J1710-410			7.1	16.5	13.9	2.2	3.9	4.1	6.3	.3	2.2	2.0	6.8
61	F100 J1711-441	HGPS J1708-442	1.3	-2.4	26.6	7.7	-.5	1.1	-.4	.9	-.0	1.2	-.5	2.7
62	F100 J1714-394	HGPS J1713-397	.6	55.2	12.7	61.2	20.7	25.4	42.0	50.4	22.8	27.7	46.3	55.0
63	F100 J1727-351			1.7	13.4	7.0	.6	2.6	3.1	3.3	1.5	2.4	2.2	2.5
64	F100 J1744-293	DIFF J1745-291	.7	12.3	.0	15.4	8.5	10.9	17.3	26.6	9.4	12.4	17.8	26.1
65	F100 J1800-232	HGPS J1800-239	1.4	11.9	14.4	17.9	4.2	5.2	7.8	10.1	.5	3.1	3.8	6.7
66	F100 J1805-215	HGPS J1804-217	.6	22.3	11.8	27.5	9.3	14.3	21.9	30.9	7.7	10.8	17.2	27.7
67	F100 J1805-223			3.9	14.5	9.7	1.4	3.4	4.8	8.7	2.2	3.8	4.5	8.4

68	F100 J1811-176			4.5	20.4	12.5	1.1	1.7	2.9	5.3	.6	1.9	3.6	4.7
69	F100 J1826-139	HGPS J1825-138	.7	29.4	8.9	33.4	15.9	21.4	36.7	48.4	17.1	22.5	36.6	51.1
70	F100 J1831-086			5.6	17.4	12.6	1.6	3.8	6.5	7.6	2.0	3.8	5.0	5.4
71	F100 J1837-070	HGPS J1837-069	.1	61.4	18.4	70.7	15.7	20.0	31.9	38.3	18.3	24.1	32.6	36.7
72	F100 J1840-058	HGPS J1840-056	.4	32.6	16.8	40.1	9.5	10.0	16.8	23.3	8.8	10.6	19.1	23.8
73	F100 J1856+028	HGPS J1857+027	.4	17.8	20.5	26.4	4.3	9.3	13.2	17.5	3.3	7.0	11.5	15.5

Table B.7.. HGPS: HESS Galactic plane survey catalog — Basic info and counterparts.
Columns: l and b are the position in Galactic J2000 coordinates. r_{95} is the 90% probability position error circle radius. σ is the width of the fitted Gaussian. F the flux according to the power-law fit model above 1 TeV in % of the Crab flux. S is the $\sqrt{(TS)}$ significance of the source from the fit. The HESS Name is the that of the nearest previously reported source or hotspot

			Characteristics					
#	Source Name	HESS Name	l	b	r_{95}	σ	F	S
1	HGPS J0834-457	HESS J0835-455	263.96	-3.19	-1.00	.55	52.2	-1.0
2	HGPS J0851-464	HESS J0852-463	266.27	-1.32	-1.00	.71	106.3	-1.0
3	HGPS J1018-589	HESS J1018-589	284.28	-1.71	-1.00	.13	1.8	-1.0
4	HGPS J1023-578	HESS J1023-575	284.21	-.42	-1.00	.21	10.5	-1.0
5	HGPS J1119-614	HESS J1119-614	292.13	-.54	-1.00	.12	4.1	-1.0
6	HGPS J1302-638	HESS J1302-638	304.18	-1.01	-1.00	.06	2.4	-1.0
7	HGPS J1303-632	HESS J1303-631	304.24	-.36	-1.00	.22	24.5	-1.0
8	HGPS J1355-645	HESS J1356-645	309.80	-2.52	-1.00	.21	15.5	-1.0
9	HGPS J1411-616	HESS J1414-619	312.33	-.24	-1.00	.48	16.7	-1.0
10	HGPS J1417-609	HESS J1418-609	313.23	.14	-1.00	.10	10.1	-1.0
11	HGPS J1420-607	HESS J1420-607	313.57	.26	-1.00	.08	10.5	-1.0
12	HGPS J1427-608	HESS J1427-608	314.39	-.17	-1.00	.10	1.7	-1.0
13	HGPS J1442-624	HESS J1442-624	315.42	-2.32	-1.00	.27	9.3	-1.0
14	HGPS J1456-594	HESS J1457-593	318.20	-.33	-1.00	.48	35.0	-1.0
15	HGPS J1500-608	HESS J1459-608	317.97	-1.76	-1.00	.37	7.9	-1.0
16	HGPS J1502-582	HESS J1503-582	319.52	.32	-1.00	.23	10.9	-1.0
17	HGPS J1506-623	HESS J1507-622	317.94	-3.47	-1.00	.16	10.2	-1.0
18	HGPS J1514-591	HESS J1514-591	320.32	-1.20	-1.00	.11	19.6	-1.0
19	HGPS J1554-550	HESS J1554-550	327.16	-1.09	-1.00	.03	1.3	-1.0
20	HGPS J1614-518	HESS J1614-518	331.53	-.62	-1.00	.24	30.9	-1.0
21	HGPS J1616-508	HESS J1616-508	332.41	-.16	-1.00	.21	32.9	-1.0
22	HGPS J1626-491	HESS J1626-490	334.77	-.02	-1.00	.59	25.2	-1.0
23	HGPS J1632-478	HESS J1632-478	336.45	.13	-1.00	.36	27.4	-1.0
24	HGPS J1635-472	HESS J1634-472	337.17	.17	-1.00	.22	13.5	-1.0
25	HGPS J1640-465	HESS J1640-465	338.32	-.03	-1.00	.06	9.2	-1.0
26	HGPS J1647-459	HESS J1646-458	339.55	-.52	-1.00	.81	38.5	-1.0
27	HGPS J1702-419	HESS J1702-420	344.35	-.09	-1.00	.36	46.3	-1.0
28	HGPS J1708-410	HESS J1708-410	345.66	-.44	-1.00	.08	3.4	-1.0
29	HGPS J1708-442	HESS J1708-443	343.10	-2.33	-1.00	.30	16.5	-1.0
30	HGPS J1713-382	HESS J1713-381	348.60	.35	-1.00	.07	1.9	-1.0
31	HGPS J1713-397	HESS J1713-397	347.32	-.42	-1.00	.36	76.0	-1.0

32	HGPS J1714-385	HESS J1714-385	348.38	.07	-1.00	.10	2.5	-1.0
33	HGPS J1718-385	HESS J1718-385	348.84	-.50	-1.00	.13	2.9	-1.0
34	HGPS J1728-343	WARMS 16	353.45	.15	-1.00	.46	9.0	-1.0
35	HGPS J1732-347	HESS J1731-347	353.54	-.70	-1.00	.18	10.2	-1.0
36	HGPS J1744-303	HESS J1745-303	358.71	-.61	-1.00	.43	11.8	-1.0
37	HGPS J1745-290	HESS J1745-290	359.94	-.05	-1.00	.04	8.7	-1.0
38	HGPS J1747-248	HESS J1747-248	3.78	1.73	-1.00	.08	1.3	-1.0
39	HGPS J1747-281	HESS J1747-281	.87	.06	-1.00	.02	2.6	-1.0
40	HGPS J1800-239	HESS J1800-240	5.99	-.28	-1.00	.60	15.1	-1.0
41	HGPS J1804-217	HESS J1804-216	8.41	-.06	-1.00	.25	20.8	-1.0
42	HGPS J1808-204	HESS J1808-204	9.90	-.21	-1.00	.26	.1	-1.0
43	HGPS J1810-193	HESS J1809-193	11.09	-.03	-1.00	.43	29.9	-1.0
44	HGPS J1813-178	HESS J1813-178	12.81	-.05	-1.00	.08	10.4	-1.0
45	HGPS J1825-138	HESS J1825-137	17.62	-.60	-1.00	.49	61.1	-1.0
46	HGPS J1826-148	HESS J1826-148	16.88	-1.29	-1.00	.02	4.9	-1.0
47	HGPS J1831-098	HESS J1831-098	21.84	-.03	-1.00	.58	17.7	-1.0
48	HGPS J1833-105	HESS J1833-105	21.49	-.92	-1.00	.04	1.3	-1.0
49	HGPS J1834-087	HESS J1834-087	23.25	-.32	-1.00	.22	13.3	-1.0
50	HGPS J1837-069	HESS J1837-069	25.12	-.09	-1.00	.37	64.4	-1.0
51	HGPS J1840-056	HESS J1841-055	26.69	-.21	-1.00	.46	30.2	-1.0
52	HGPS J1843-033	HESS J1843-033	29.04	.16	-1.00	.37	20.8	-1.0
53	HGPS J1846-029	HESS J1846-029	29.71	-.24	-1.00	.03	2.1	-1.0
54	HGPS J1848-017	HESS J1848-018	31.02	-.15	-1.00	.55	27.9	-1.0
55	HGPS J1849+000	HESS J1849-000	32.64	.53	-1.00	.05	2.2	-1.0
56	HGPS J1857+027	HESS J1857+026	36.04	-.08	-1.00	.27	15.2	-1.0
57	HGPS J1858+020	HESS J1858+020	35.54	-.59	-1.00	.09	2.8	-1.0
58	HGPS J1907+064	HESS J1908+063	40.54	-.70	-1.00	.55	25.0	-1.0
59	HGPS J1913+101	HESS J1912+101	44.38	-.14	-1.00	.33	11.0	-1.0
60	HGPS J1922+141	HESS J1923+141	49.04	-.39	-1.00	.12	2.7	-1.0
61	HGPS J1930+187	HESS J1930+186	53.99	.29	-1.00	.13	3.6	-1.0
62	HGPS J1943+212	HESS J1943+213	57.75	-1.28	-1.00	.05	2.2	-1.0

Table B.8.. HGPS: HESS Galactic plane survey catalog — Detection, morphology, aperture.
Columns: l and b are the fitted Galactic longitude GLON and latitude GLAT (J2000 epoch), r_{68} and r_{95} are the 68% and 95% position uncertainty derived assuming a symmetric Gaussian error of magnitude $r_{1\sigma} = \sqrt{(}\Delta l \times \Delta b)$. N and σ the norm and extension of the fitted symmetric Gaussian model. Note that N has arbitrary units and is highly correlated with σ. R_{90} is the 90% containment radius of the source emission after PSF convolution, θ is the aperture used for spectral analysisAll positions and extensions are in deg.

		Position						Morphology					
#	Source Name	l	Δl	b	Δb	r_{68}	r_{95}	N	ΔN	σ	$\Delta\sigma$	R_{90}	θ
1	DIFF J1509-589	319.873	.177	-.719	.155	-1.000	-1.000	8.620	1.152	.860	.108	1.849	1.000
2	DIFF J1708-407	345.882	.147	-.252	.070	-1.000	-1.000	14.477	1.979	.639	.059	1.378	1.000
3	DIFF J1715-390	348.124	.136	-.397	.057	-1.000	-1.000	19.554	2.398	.529	.045	1.143	1.000
4	DIFF J1745-291	359.833	.021	-.071	.012	-1.000	-1.000	33.581	1.840	.335	.012	.727	.727
5	DIFF J1747-282	.849	.025	-.061	.013	-1.000	-1.000	29.111	1.819	.318	.015	.691	.691
6	DIFF J1853+007	33.902	.179	-.212	.093	-1.000	-1.000	8.583	.875	1.025	.100	2.203	1.000
7	HGPS J0834-457	263.956	.015	-3.191	.017	-1.000	-1.000	54.136	1.616	.552	.013	1.190	1.000
8	HGPS J0851-464	266.271	.021	-1.321	.020	-1.000	-1.000	53.424	1.496	.709	.013	1.527	1.000
9	HGPS J1018-589	284.282	.029	-1.712	.032	-1.000	-1.000	66.775	15.681	.133	.022	.313	.313
10	HGPS J1023-578	284.208	.017	-.421	.014	-1.000	-1.000	96.774	8.533	.207	.012	.462	.462
11	HGPS J1119-614	292.126	.021	-.544	.020	-1.000	-1.000	90.478	20.215	.121	.019	.291	.291
12	HGPS J1302-638	304.181	.006	-1.013	.005	-1.000	-1.000	282.847	57.296	.065	.009	.192	.192
13	HGPS J1303-632	304.245	.005	-.364	.005	-1.000	-1.000	188.724	5.370	.219	.004	.487	.407
14	HGPS J1355-645	309.798	.021	-2.517	.021	-1.000	-1.000	139.258	16.770	.210	.017	.471	.471
15	HGPS J1411-616	312.334	.153	-.238	.152	-1.000	-1.000	18.671	5.145	.483	.118	1.045	.700
16	HGPS J1417-609	313.235	.012	.143	.009	-1.000	-1.000	299.805	43.773	.100	.011	.251	.207
17	HGPS J1420-607	313.569	.007	.260	.006	-1.000	-1.000	568.188	62.374	.083	.006	.220	.181
18	HGPS J1427-608	314.393	.015	-.167	.016	-1.000	-1.000	149.906	29.494	.098	.013	.246	.246
19	HGPS J1442-624	315.419	.017	-2.323	.019	-1.000	-1.000	55.464	3.908	.271	.013	.596	.596
20	HGPS J1456-594	318.201	.056	-.332	.047	-1.000	-1.000	25.514	2.658	.481	.040	1.040	.869
21	HGPS J1500-608	317.973	.057	-1.764	.053	-1.000	-1.000	21.197	3.083	.367	.040	.797	.797
22	HGPS J1502-582	319.519	.050	.319	.049	-1.000	-1.000	24.895	5.413	.235	.044	.519	.519
23	HGPS J1506-623	317.943	.016	-3.470	.018	-1.000	-1.000	127.830	16.529	.163	.014	.374	.374
24	HGPS J1514-591	320.324	.003	-1.204	.003	-1.000	-1.000	538.626	22.269	.108	.003	.263	.263
25	HGPS J1554-550	327.156	.010	-1.087	.010	-1.000	-1.000	444.709	303.995	.030	.012	.143	.150
26	HGPS J1614-518	331.531	.013	-.616	.013	-1.000	-1.000	148.942	9.273	.241	.009	.531	.531
27	HGPS J1616-508	332.412	.010	-.159	.010	-1.000	-1.000	208.601	12.711	.212	.008	.471	.471
28	HGPS J1626-491	334.769	.113	-.018	.071	-1.000	-1.000	17.745	3.116	.588	.087	1.268	.892
29	HGPS J1632-478	336.449	.037	.128	.020	-1.000	-1.000	83.960	7.163	.359	.034	.781	.500
30	HGPS J1635-472	337.173	.019	.172	.017	-1.000	-1.000	90.213	7.652	.221	.018	.491	.345

31	HGPS J1640-465	338.316	.003	-.028	.003	-1.000	-1.000	884.766	70.110	.058	.003	.175	.175
32	HGPS J1647-459	339.548	.042	-.522	.039	-1.000	-1.000	25.457	1.228	.813	.032	1.749	1.000
33	HGPS J1702-419	344.353	.032	-.092	.024	-1.000	-1.000	71.296	5.817	.363	.024	.789	.789
34	HGPS J1708-410	345.663	.011	-.442	.012	-1.000	-1.000	147.313	26.903	.079	.010	.211	.211
35	HGPS J1708-442	343.096	.042	-2.334	.054	-1.000	-1.000	30.599	5.159	.304	.037	.662	.662
36	HGPS J1713-382	348.600	.011	.354	.011	-1.000	-1.000	141.005	29.080	.075	.011	.204	.167
37	HGPS J1713-397	347.318	.005	-.422	.005	-1.000	-1.000	180.141	2.814	.362	.003	.787	.787
38	HGPS J1714-385	348.384	.020	.074	.027	-1.000	-1.000	54.905	16.373	.100	.027	.250	.207
39	HGPS J1718-385	348.844	.025	-.501	.020	-1.000	-1.000	50.028	9.035	.131	.019	.308	.308
40	HGPS J1728-343	353.451	.047	.147	.062	-1.000	-1.000	16.899	1.820	.459	.039	.992	.500
41	HGPS J1732-347	353.541	.015	-.703	.015	-1.000	-1.000	58.296	5.133	.175	.010	.391	.391
42	HGPS J1744-303	358.709	.023	-.605	.025	-1.000	-1.000	25.837	1.538	.425	.020	.920	.600
43	HGPS J1745-290	359.943	.001	-.047	.001	-1.000	-1.000	1413.745	96.707	.036	.001	.137	.150
44	HGPS J1747-248	3.776	.015	1.733	.023	-1.000	-1.000	61.364	19.886	.077	.017	.200	.200
45	HGPS J1747-281	.866	.003	.064	.003	-1.000	-1.000	1338.675	519.942	.017	.004	.121	.150
46	HGPS J1800-239	5.988	.050	-.283	.040	-1.000	-1.000	19.682	1.981	.600	.052	1.293	1.000
47	HGPS J1804-217	8.409	.009	-.063	.009	-1.000	-1.000	106.975	4.530	.255	.007	.559	.559
48	HGPS J1808-204	9.896	.041	-.212	.041	-1.000	-1.000	15.332	2.638	.260	.037	.569	.476
49	HGPS J1810-193	11.094	.018	-.035	.016	-1.000	-1.000	42.783	1.833	.430	.015	.928	.776
50	HGPS J1813-178	12.808	.005	-.048	.005	-1.000	-1.000	428.696	48.853	.080	.006	.206	.206
51	HGPS J1825-138	17.623	.008	-.605	.007	-1.000	-1.000	87.343	1.550	.491	.006	1.059	.800
52	HGPS J1826-148	16.876	.001	-1.289	.001	-1.000	-1.000	2999.778	473.448	.020	.002	.125	.150
53	HGPS J1831-098	21.839	.082	-.028	.071	-1.000	-1.000	15.427	3.264	.582	.126	1.255	.800
54	HGPS J1833-105	21.488	.010	-.919	.012	-1.000	-1.000	243.486	104.690	.043	.012	.152	.152
55	HGPS J1834-087	23.254	.013	-.315	.016	-1.000	-1.000	89.130	9.935	.220	.023	.487	.487
56	HGPS J1837-069	25.119	.010	-.091	.010	-1.000	-1.000	128.457	4.184	.371	.009	.805	.805
57	HGPS J1840-056	26.693	.019	-.210	.015	-1.000	-1.000	68.011	2.531	.462	.012	.999	.835
58	HGPS J1843-033	29.041	.028	.161	.024	-1.000	-1.000	42.330	3.641	.370	.025	.803	.671
59	HGPS J1846-029	29.707	.006	-.242	.005	-1.000	-1.000	730.986	327.429	.025	.006	.131	.150
60	HGPS J1848-017	31.017	.043	-.145	.036	-1.000	-1.000	22.705	1.750	.552	.033	1.191	1.000
61	HGPS J1849+000	32.642	.015	.534	.012	-1.000	-1.000	127.497	58.676	.053	.016	.167	.167
62	HGPS J1857+027	36.042	.021	-.080	.018	-1.000	-1.000	69.737	5.995	.270	.018	.593	.495
63	HGPS J1858+020	35.537	.018	-.587	.014	-1.000	-1.000	95.634	21.976	.088	.014	.225	.225
64	HGPS J1907+064	40.541	.036	-.700	.035	-1.000	-1.000	33.901	2.348	.547	.028	1.180	1.000
65	HGPS J1913+101	44.379	.028	-.138	.031	-1.000	-1.000	30.738	2.759	.332	.020	.722	.722
66	HGPS J1922+141	49.043	.024	-.394	.029	-1.000	-1.000	74.732	19.836	.115	.020	.276	.276
67	HGPS J1930+187	53.987	.035	.289	.040	-1.000	-1.000	65.358	19.978	.130	.026	.308	.308

68	HGPS J1943+212	57.745	.017	-1.284	.014	-1.000	-1.000	367.057	202.913	.046	.015	.174	.174

Table B.9.. HGPS: HESS Galactic plane survey catalog — Observation and statistics.
Columns: T_{FoV} is the available livetime the source center was within a 2 deg FOV, T_{Spec} is the livetime that was available for spectral analysis, % is their ratio. Zen and Off are the mean zenith and offset. θ is the aperture radius used for the spectral analysis. A is the area factor, i.e. the mean number of off regions. N_{on} and N_{off} are the total number of on and off counts. Next we give the excess, background and significance before and after applying the safe energy cut, as well as their ratio in %. The events used for spectral analysis are the ones after safe energy cut.

		Observation									Excess			Background			Significance		
#	Source Name	T_{FoV}	T_{Spec}	%	Zen	Off	θ	A	N_{on}	N_{off}	all	safe	%	all	safe	%	all	safe	%
1	HGPS J0834-457	76.6	12.1	15	23	1.4	1.00	1.3	5219	5375	1844	1000	54	9715	4218	43	13.4	10.9	81
2	HGPS J0851-464	39.8	.4	1	34	1.7	1.00	1.0	395	324	827	71	8	4455	324	7	9.7	2.6	27
3	HGPS J1018-589	42.1	40.3	95	40	1.3	.31	5.9	2965	15869	266	262	98	4964	2702	54	3.5	4.6	132
4	HGPS J1023-578	46.7	39.2	84	39	1.0	.46	2.0	7799	13384	1952	1258	64	11793	6540	55	14.2	12.3	86
5	HGPS J1119-614	45.7	44.3	97	40	1.1	.29	7.2	3592	21646	432	585	135	5200	3006	57	5.5	9.7	174
6	HGPS J1302-638	132.9	98.3	73	44	.7	.19	3.0	5903	14280	1796	1205	67	7803	4697	60	16.9	14.5	85
7	HGPS J1303-632	133.7	88.9	66	43	1.0	.41	3.2	23471	57412	10239	5730	55	27889	17740	63	50.0	35.4	70
8	HGPS J1355-645	19.9	19.9	99	43	1.2	.47	4.2	4103	13771	811	820	101	5954	3282	55	9.2	12.3	133
9	HGPS J1411-616	29.5	17.7	60	42	1.5	.70	1.7	7883	11799	1499	896	59	17028	6986	41	9.4	8.3	88
10	HGPS J1417-609	23.7	23.7	100	41	1.0	.21	8.2	1851	8650	986	798	80	1858	1052	56	19.8	20.7	104
11	HGPS J1420-607	22.9	22.9	100	41	.9	.18	9.0	1644	7532	914	806	88	1423	837	58	20.8	23.0	110
12	HGPS J1427-608	33.7	33.2	98	41	1.4	.25	10.3	2001	17921	532	270	50	2869	1730	60	9.2	6.0	65
13	HGPS J1442-624	79.5	30.6	38	41	1.1	.60	1.2	12373	13224	1788	1116	62	20661	11256	54	9.2	7.6	82
14	HGPS J1456-594	53.3	6.2	11	37	1.6	.87	1.4	3520	4312	728	478	65	16531	3041	18	4.2	6.4	153
15	HGPS J1500-608	52.0	7.4	14	38	1.7	.80	1.2	3304	3803	363	115	31	8536	3188	37	3.0	1.5	49
16	HGPS J1502-582	57.7	45.1	78	36	1.4	.52	2.9	12027	30510	2400	1561	65	18675	10465	56	14.8	12.8	86
17	HGPS J1506-623	24.0	24.0	99	40	1.2	.37	3.2	3503	8899	755	694	91	4644	2808	60	9.3	10.9	116
18	HGPS J1514-591	46.1	29.7	64	37	1.0	.26	4.0	5128	10927	3124	2420	77	4763	2707	56	36.3	36.1	99
19	HGPS J1554-550	39.3	39.3	99	34	.9	.15	13.0	773	8217	161	141	87	980	631	64	4.8	5.2	108
20	HGPS J1614-518	16.2	12.5	76	30	1.3	.53	3.7	4022	9987	1395	1298	93	4807	2723	56	16.9	20.3	119
21	HGPS J1616-508	18.4	12.7	68	30	1.5	.47	4.7	3452	9894	1681	1322	78	3645	2129	58	23.4	23.4	100
22	HGPS J1626-491	19.8	5.6	28	27	1.6	.89	1.5	3725	4666	654	549	83	9660	3175	32	5.2	7.2	139
23	HGPS J1632-478	39.1	34.8	88	32	1.6	.50	3.5	7727	18181	2972	2473	83	9471	5253	55	25.4	27.6	108
24	HGPS J1635-472	57.5	55.1	95	33	1.4	.34	4.5	6423	18661	2618	2313	88	7603	4109	54	25.6	29.7	115
25	HGPS J1640-465	80.7	62.0	76	33	1.1	.17	7.5	3383	11858	2220	1800	81	2605	1582	60	36.0	36.2	100
26	HGPS J1647-459	79.2	2.2	2	32	1.8	1.00	1.0	1926	1623	2520	303	12	21381	1623	7	12.1	5.1	42
27	HGPS J1702-419	12.4	3.0	24	25	1.6	.79	1.1	2023	1753	1020	439	43	4753	1583	33	10.6	7.5	70
28	HGPS J1708-410	62.5	61.6	98	35	1.3	.21	7.0	3967	22388	1020	797	78	5753	3169	55	12.2	12.7	104
29	HGPS J1708-442	17.2	9.7	56	24	1.1	.66	1.9	4754	8332	418	354	84	7585	4399	57	3.8	4.2	110

30	HGPS J1713-382	94.5	79.9	84	32	1.5	.17	14.7	2305	26546	712	503	70	3093	1801	58	11.9	11.0	91
31	HGPS J1713-397	103.2	6.2	6	25	1.6	.79	2.5	3456	5531	1490	1208	81	6457	2247	34	14.9	19.5	130
32	HGPS J1714-385	120.2	101.2	84	33	1.5	.21	11.0	4512	42355	1064	668	62	6651	3843	57	12.2	10.0	82
33	HGPS J1718-385	73.6	69.9	94	32	1.3	.31	4.5	7348	30480	990	574	58	12002	6773	56	8.0	6.2	77
34	HGPS J1728-343	55.6	38.0	68	16	1.2	.50	3.8	8241	27276	1060	1004	94	12501	7236	57	8.3	10.2	123
35	HGPS J1732-347	55.2	41.2	74	17	.8	.39	3.0	7705	17865	1606	1711	106	10067	5993	59	13.4	18.1	134
36	HGPS J1744-303	124.1	79.5	64	21	1.6	.60	2.7	22654	54784	2635	2612	99	40407	20042	49	11.1	15.4	138
37	HGPS J1745-290	177.5	128.8	72	21	.9	.15	5.8	9167	22815	6263	5235	83	6710	3932	58	61.3	63.9	104
38	HGPS J1747-248	68.4	68.4	100	20	.8	.20	6.9	2853	18082	382	240	62	4223	2612	61	5.4	4.3	79
39	HGPS J1747-281	175.8	135.6	77	20	1.2	.15	10.0	4918	35558	1716	1349	78	5839	3568	61	20.4	20.2	99
40	HGPS J1800-239	38.7	1.3	3	16	1.8	1.00	1.0	753	713	387	40	10	6584	713	10	3.4	1.0	30
41	HGPS J1804-217	60.0	47.3	78	16	1.5	.56	2.0	15080	20710	5947	4611	77	20191	10468	51	32.7	33.7	103
42	HGPS J1808-204	89.4	67.6	75	16	1.0	.48	1.8	16605	26555	1166	1664	142	25020	14940	59	5.9	10.6	181
43	HGPS J1810-193	88.3	15.9	18	14	1.7	.78	1.9	6246	9791	3429	1151	33	20097	5094	25	19.4	12.5	64
44	HGPS J1813-178	29.3	26.3	89	18	1.4	.21	7.3	2186	9207	1172	926	79	1987	1259	63	22.5	21.9	97
45	HGPS J1825-138	117.6	44.5	37	20	1.5	.80	1.3	25607	22203	12945	8181	63	42262	17425	41	45.5	42.0	92
46	HGPS J1826-148	116.3	67.7	58	21	.8	.15	4.3	3668	9059	1917	1564	81	3262	2103	64	27.4	27.2	99
47	HGPS J1831-098	43.3	15.6	35	25	1.5	.80	2.1	7133	12724	1367	1167	85	16406	5965	36	8.6	12.0	138
48	HGPS J1833-105	38.5	38.5	99	22	1.1	.15	9.3	1270	9482	315	257	81	1531	1012	66	7.4	7.4	99
49	HGPS J1834-087	43.5	34.8	79	26	1.4	.49	2.6	8348	17322	2802	1807	64	11664	6540	56	21.1	18.0	85
50	HGPS J1837-069	37.4	13.1	34	30	1.5	.81	1.1	8086	6190	4696	2291	48	14431	5794	40	26.4	19.8	75
51	HGPS J1840-056	40.0	9.2	22	31	1.6	.83	1.1	7106	6667	2812	1305	46	14622	5800	39	16.7	11.9	71
52	HGPS J1843-033	40.0	28.1	70	26	1.5	.67	2.2	11278	20875	2190	1712	78	18298	9565	52	13.1	14.0	106
53	HGPS J1846-029	40.9	40.1	97	28	1.0	.15	8.1	1534	9576	464	358	77	1803	1175	65	9.9	9.4	95
54	HGPS J1848-017	57.6	11.2	19	28	1.7	1.00	1.0	6525	5775	3489	750	21	33101	5775	17	14.4	6.8	46
55	HGPS J1849+000	52.7	48.0	91	28	1.2	.17	10.8	1460	12733	277	278	100	1773	1181	66	6.1	7.5	121
56	HGPS J1857+027	36.5	27.2	74	33	1.5	.50	4.2	6276	19952	1879	1482	78	8779	4793	54	17.3	18.2	104
57	HGPS J1858+020	45.6	35.1	76	32	1.4	.23	10.0	1835	15054	423	334	79	2432	1500	61	7.9	7.9	99
58	HGPS J1907+064	47.2	4.8	10	42	1.8	1.00	1.6	3195	4583	1427	409	28	16378	2785	17	9.2	5.9	64
59	HGPS J1913+101	79.0	52.0	65	39	1.5	.72	2.8	20654	55755	2008	1015	50	38850	19638	50	8.7	6.2	70
60	HGPS J1922+141	29.9	29.9	100	40	1.0	.28	7.6	2352	15532	449	301	67	3431	2050	59	7.0	6.1	86
61	HGPS J1930+187	26.4	26.4	99	47	.9	.31	6.4	2523	13909	358	347	96	4101	2175	53	5.1	6.7	131
62	HGPS J1943+212	32.9	32.9	100	48	1.0	.17	13.7	1016	11944	234	140	59	1512	875	57	5.7	4.4	78

Table B.10.. HGPS: HESS Galactic plane survey catalog — Power-law spectral fit.
Columns: E_{min} and E_{max} are the minimum and maximum event energy used in the spectral fit. Typically the first significant spectral point can be obtained at an energy a bit higher than E_{min} and the last spectral point at half of E_{max}, although this can vary depending on the energy distribution of the excess and background. E_0 is the pivot energy. F the differential flux at E_0 in units 10^{-12} cm^{-2} s^{-1} TeV^{-1}. Γ is the spectral index. $\log(L)$ is the best-fit log likelihood statistic. Then three common alternative ways to quote the flux are listed, computed using the best-fit model with errors propagated from the fit parameters F and Γ. $F_{@1}$ is the differential flux at 1 TeV in units 10^{-12} cm^{-2} s^{-1} TeV^{-1}, $F_{>Emin}$ and $F_{>1}$ are the integral fluxes above the energy threshold and 1 TeV in units 10^{-12} cm^{-2} s^{-1}.

#	Source Name	E_{min}	E_{max}	E_0	F	ΔF	Γ	$\Delta\Gamma$	$\log(L)$	$F_{@1}$	$\Delta F_{@1}$	$F_{>Emin}$	$\Delta F_{>Emin}$	$F_{>1}$	$\Delta F_{>1}$
1	HGPS J0834-457	.46	61.90	3.02	1.20	.10	2.04	.06	-43.4	11.40	1.17	24.20	2.35	10.80	.88
2	HGPS J0851-464	.75	46.42	3.32	2.01	.61	2.05	.24	-20.5	23.50	9.79	29.90	9.96	22.00	6.85
3	HGPS J1018-589	.46	74.99	.95	.97	.24	3.22	.48	-19.2	.83	.21	2.05	.59	.37	.12
4	HGPS J1023-578	.46	68.13	1.40	1.46	.12	2.60	.11	-30.6	3.50	.32	7.47	.74	2.18	.20
5	HGPS J1119-614	.42	61.90	1.27	.74	.09	2.67	.14	-16.6	1.42	.17	3.60	.49	.85	.11
6	HGPS J1302-638	.38	90.85	1.16	.58	.05	2.75	.14	-39.4	.87	.08	2.67	.30	.50	.05
7	HGPS J1303-632	.42	90.85	2.06	1.26	.03	2.35	.02	-53.0	6.85	.19	16.30	.48	5.07	.12
8	HGPS J1355-645	.51	90.85	2.26	.64	.06	2.34	.09	-17.4	4.31	.50	7.91	.89	3.21	.30
9	HGPS J1411-616	.46	90.85	3.65	.25	.03	2.16	.10	-23.3	4.02	.74	8.44	1.50	3.46	.46
10	HGPS J1417-609	.42	68.13	1.70	.81	.04	2.32	.05	-26.1	2.77	.16	6.56	.41	2.09	.11
11	HGPS J1420-607	.42	51.09	1.87	.67	.03	2.23	.05	-35.5	2.68	.16	6.29	.37	2.17	.11
12	HGPS J1427-608	.42	68.13	.87	1.22	.25	3.15	.47	-22.3	.77	.16	2.30	.57	.36	.12
13	HGPS J1442-624	.38	61.90	1.54	1.00	.14	2.54	.12	-26.9	2.99	.44	8.51	1.40	1.93	.26
14	HGPS J1456-594	.46	51.09	1.27	6.44	.82	2.68	.18	-23.4	12.20	1.66	26.50	3.94	7.26	1.02
15	HGPS J1500-608	.51	61.90	10.51	.02	.01	1.88	.40	-30.5	1.48	1.53	2.99	2.65	1.63	1.08
16	HGPS J1502-582	.38	90.85	1.05	3.43	.26	2.73	.11	-32.1	3.91	.30	11.90	1.08	2.26	.21
17	HGPS J1506-623	.51	90.85	2.26	.42	.04	2.30	.08	-31.4	2.77	.30	5.10	.54	2.12	.19
18	HGPS J1514-591	.38	61.90	1.40	2.49	.08	2.34	.03	-31.0	5.46	.19	14.70	.55	4.07	.15
19	HGPS J1554-550	.38	61.90	2.49	.04	.01	2.17	.17	-26.5	.32	.08	.84	.22	.27	.05
20	HGPS J1614-518	.32	61.90	1.16	6.61	.36	2.48	.06	-26.8	9.49	.52	35.20	2.26	6.41	.40
21	HGPS J1616-508	.29	61.90	1.16	6.78	.36	2.41	.05	-29.8	9.66	.52	39.80	2.62	6.82	.41
22	HGPS J1626-491	.29	68.13	1.40	3.33	.53	2.47	.17	-38.4	7.67	1.30	32.60	7.26	5.22	.88
23	HGPS J1632-478	.29	90.85	1.16	5.97	.25	2.51	.05	-24.7	8.59	.36	37.30	1.99	5.69	.27
24	HGPS J1635-472	.26	90.85	1.27	2.26	.10	2.45	.05	-38.1	4.08	.19	19.70	1.23	2.81	.14
25	HGPS J1640-465	.26	82.54	1.05	2.50	.08	2.48	.03	-45.5	2.83	.09	14.00	.59	1.91	.07
26	HGPS J1647-459	.29	46.42	1.05	10.66	2.09	2.51	.22	-29.9	12.10	2.37	52.90	12.50	7.98	1.90
27	HGPS J1702-419	.29	34.81	1.70	3.63	.46	2.20	.12	-32.4	11.60	1.63	43.10	7.23	9.58	1.27
28	HGPS J1708-410	.22	82.54	.95	1.29	.11	2.59	.08	-38.5	1.14	.09	8.19	.90	.71	.07
29	HGPS J1708-442	.24	61.90	3.32	.32	.04	1.96	.09	-39.5	3.35	.59	13.90	2.76	3.42	.48

30	HGPS J1713-382	.22	90.85	.79	1.32	.13	2.73	.12	-24.6	.68	.07	5.63	.73	.39	.05
31	HGPS J1713-397	.32	61.90	1.54	7.50	.43	2.27	.05	-36.6	20.10	1.23	68.10	4.79	15.80	.93
32	HGPS J1714-385	.22	90.85	1.54	.25	.03	2.29	.09	-30.3	.68	.08	3.84	.57	.53	.06
33	HGPS J1718-385	.22	68.13	6.50	.02	.00	1.76	.08	-49.6	.47	.09	1.96	.42	.60	.09
34	HGPS J1728-343	.22	61.90	1.40	1.12	.10	2.30	.07	-26.9	2.43	.22	13.80	1.62	1.86	.17
35	HGPS J1732-347	.24	61.90	1.27	1.62	.09	2.33	.05	-29.3	2.83	.16	14.40	1.04	2.12	.13
36	HGPS J1744-303	.22	90.85	.96	4.10	.26	2.50	.06	-27.9	3.66	.23	24.30	1.95	2.44	.19
37	HGPS J1745-290	.20	61.90	.96	2.67	.05	2.33	.02	-54.0	2.40	.05	15.80	.40	1.80	.04
38	HGPS J1747-248	.20	68.13	1.40	.16	.03	2.34	.15	-35.8	.35	.06	2.30	.57	.26	.04
39	HGPS J1747-281	.20	68.13	1.05	.67	.03	2.38	.05	-40.3	.76	.04	5.17	.35	.55	.03
40	HGPS J1800-239	.38	38.31	1.87	.92	.90	2.01	.45	-25.4	3.24	3.29	8.38	8.51	3.13	3.08
41	HGPS J1804-217	.22	56.23	.72	18.22	.65	2.71	.04	-35.6	7.40	.29	59.90	2.67	4.32	.23
42	HGPS J1808-204	.20	61.90	22.63	.00	.00	5.06	.04	-38.6	.10	.02	18.40	4.53	.02	.00
43	HGPS J1810-193	.26	90.85	1.87	1.91	.15	2.23	.07	-37.7	7.69	.70	32.60	3.71	6.21	.50
44	HGPS J1813-178	.20	61.90	1.27	1.55	.08	2.21	.05	-32.3	2.63	.14	15.60	1.16	2.16	.13
45	HGPS J1825-138	.24	68.13	1.15	12.81	.33	2.43	.02	-64.1	18.20	.47	99.70	3.26	12.70	.37
46	HGPS J1826-148	.22	31.62	1.05	1.19	.05	2.30	.04	-45.5	1.33	.05	7.55	.39	1.01	.05
47	HGPS J1831-098	.26	61.90	1.70	1.41	.18	2.28	.13	-30.0	4.70	.68	20.40	3.85	3.66	.49
48	HGPS J1833-105	.20	68.13	1.05	.33	.06	2.39	.18	-39.3	.37	.07	2.58	.65	.26	.06
49	HGPS J1834-087	.22	90.85	.86	7.06	.43	2.73	.08	-33.1	4.76	.30	39.00	3.44	2.75	.24
50	HGPS J1837-069	.29	68.13	1.15	13.99	.71	2.49	.05	-36.6	20.00	1.04	86.30	5.66	13.40	.76
51	HGPS J1840-056	.26	61.90	.95	11.42	1.25	2.60	.12	-42.7	10.10	1.10	53.90	7.38	6.27	.83
52	HGPS J1843-033	.26	61.90	1.87	1.31	.10	2.20	.06	-30.9	5.20	.43	21.60	2.14	4.31	.32
53	HGPS J1846-029	.22	68.13	1.27	.33	.04	2.32	.10	-34.1	.58	.07	3.32	.50	.44	.05
54	HGPS J1848-017	.29	61.90	1.54	2.89	.41	2.41	.12	-24.8	8.19	1.26	33.70	6.36	5.78	.85
55	HGPS J1849+000	.26	61.90	2.74	.06	.01	1.94	.09	-35.3	.44	.07	1.65	.28	.46	.06
56	HGPS J1857+027	.26	90.85	.95	6.02	.38	2.68	.07	-28.1	5.32	.33	30.30	2.42	3.15	.25
57	HGPS J1858+020	.26	90.85	1.16	.59	.08	2.44	.15	-32.0	.84	.12	4.06	.74	.58	.09
58	HGPS J1907+064	.38	61.90	1.54	2.57	.61	2.38	.20	-25.6	7.20	1.84	19.60	5.42	5.19	1.26
59	HGPS J1913+101	.29	90.85	1.40	1.46	.15	2.46	.08	-56.2	3.34	.35	14.10	1.73	2.29	.24
60	HGPS J1922+141	.42	68.13	1.40	.37	.07	2.60	.20	-22.0	.89	.18	2.22	.51	.55	.11
61	HGPS J1930+187	.51	68.13	1.40	.51	.10	2.70	.27	-24.8	1.28	.26	2.36	.51	.76	.15
62	HGPS J1943+212	.56	82.54	1.87	.15	.03	2.57	.19	-26.0	.73	.15	1.14	.23	.46	.08

Table B.11.. HGPS: HESS Galactic plane survey catalog — Exponential cutoff spectral fit.
The following sources are missing from this table because the fit did not converge: HGPS J1018-589, HGPS J1456-594, HGPS J1808-204, HGPS J1907+064, HGPS J1913+101.
Columns: The three fit parameters F, Γ and λ as well as the pivot energy are those from the exponential cutoff power-law model: $F(E) = F(E/E_0)^{-\Gamma} \exp(-\lambda E)$. $E_{cut} = 1/\lambda$. $\log(L)$ is the best-fit log likelihood fit statistic and $S = \sqrt{(TS)}$ is the significance wrt. the one of the power-law model. For units of fluxes and the additional flux columns see the description in Table B.10.

		ECPL														
#	Source Name	E_0	F	ΔF	Γ	$\Delta\Gamma$	λ	$\Delta\lambda$	E_{cut}	$\log(L)$	S	$F_{@1}$	$\Delta F_{@1}$	$F_{>Emin}$	$\Delta F_{>Emin}$	$F_{>1}$	$\Delta F_{>1}$
1	HGPS J0834-457	1.56	5.67	.67	1.05	.20	.17	.04	6.0	-18.6	7.1	7.64	1.30	18.10	2.20	11.80	.95
2	HGPS J0851-464	1.71	12.98	7.00	.21	1.56	.38	.24	2.6	-17.7	2.4	9.95	9.79	23.90	9.97	21.20	7.33
4	HGPS J1023-578	.96	3.89	.38	2.59	.17	.00	.03	243.9	-30.6	.1	3.50	.33	7.44	.79	2.19	.21
5	HGPS J1119-614	.66	4.36	.85	1.99	.51	.26	.23	3.8	-15.2	1.7	1.44	.20	3.13	.56	.95	.12
6	HGPS J1302-638	.96	.95	.09	2.82	.17	-.02	.02	-60.6	-39.1	.6	.87	.08	2.74	.33	.49	.05
7	HGPS J1303-632	.96	7.54	.23	2.08	.05	.06	.01	17.4	-28.5	7.0	6.61	.20	15.00	.48	5.33	.12
8	HGPS J1355-645	1.41	2.04	.23	2.08	.18	.04	.03	22.8	-15.6	1.9	4.01	.55	7.34	.94	3.32	.32
9	HGPS J1411-616	1.56	1.52	.23	2.29	.19	-.02	.02	-64.1	-23.0	.8	4.24	.76	8.95	1.62	3.42	.45
10	HGPS J1417-609	1.06	2.54	.17	2.10	.10	.05	.02	19.8	-22.4	2.7	2.73	.21	6.22	.54	2.20	.21
11	HGPS J1420-607	.96	3.08	.22	1.77	.14	.12	.04	8.5	-25.5	4.5	2.56	.17	5.63	.39	2.35	.12
12	HGPS J1427-608	.66	2.90	.71	3.13	.65	.01	.18	101.0	-22.3	.1	.77	.18	2.29	.54	.36	.14
13	HGPS J1442-624	.80	5.16	1.06	1.60	.33	.25	.11	4.0	-21.4	3.3	2.80	.49	6.39	1.27	2.38	.30
15	HGPS J1500-608	2.51	.24	.12	2.30	.45	-.03	.03	-28.7	-30.0	1.0	2.09	1.40	3.97	2.50	1.76	.85
16	HGPS J1502-582	.72	9.63	.90	2.66	.18	.03	.06	39.2	-32.0	.5	3.94	.47	11.70	1.43	2.30	.39
17	HGPS J1506-623	.96	3.07	.43	1.69	.29	.15	.08	6.7	-27.1	2.9	2.48	.36	4.51	.59	2.30	.21
18	HGPS J1514-591	.87	7.75	.31	2.12	.06	.06	.02	18.1	-21.6	4.3	5.49	.20	14.00	.58	4.32	.16
19	HGPS J1554-550	1.56	.13	.03	1.82	.39	.06	.07	17.2	-25.9	1.1	.28	.09	.71	.24	.28	.06
20	HGPS J1614-518	.79	17.62	1.17	2.22	.12	.08	.04	13.1	-23.1	2.7	9.77	.55	32.50	2.43	6.96	.45
21	HGPS J1616-508	.80	17.31	1.08	2.22	.10	.05	.03	18.5	-26.8	2.5	9.89	.54	37.10	2.78	7.28	.46
22	HGPS J1626-491	.80	14.27	2.99	2.14	.41	.11	.12	9.0	-38.1	.8	7.84	1.41	28.50	8.19	5.61	1.00
23	HGPS J1632-478	.72	19.58	.97	2.45	.09	.02	.03	55.2	-24.3	.9	8.67	.38	36.50	2.21	5.80	.30
24	HGPS J1635-472	.87	5.81	.30	2.34	.08	.03	.02	38.0	-36.3	1.9	4.12	.20	18.70	1.28	2.92	.15
25	HGPS J1640-465	.60	10.46	.48	2.11	.08	.15	.04	6.6	-26.1	6.2	3.04	.11	12.30	.61	2.11	.08
26	HGPS J1647-459	.88	18.73	4.53	1.96	.50	.14	.13	6.9	-29.0	1.4	12.50	3.58	41.90	8.76	9.66	6.88
27	HGPS J1702-419	.96	12.41	1.84	2.27	.21	-.02	.04	-58.1	-32.3	.4	11.60	1.64	44.60	8.27	9.34	1.36
28	HGPS J1708-410	.45	9.18	1.21	1.94	.31	.36	.20	2.8	-33.6	3.1	1.33	.13	6.47	1.00	.82	.08
29	HGPS J1708-442	1.42	2.16	.48	.87	.39	.21	.08	4.8	-30.5	4.2	2.38	.73	7.40	2.18	3.98	.56
30	HGPS J1713-382	.45	6.36	.91	2.37	.30	.22	.21	4.5	-23.0	1.8	.76	.09	4.96	.80	.42	.06
31	HGPS J1713-397	.87	29.02	2.22	1.81	.13	.12	.04	8.4	-24.7	4.9	20.20	1.34	58.50	4.89	17.90	1.07

32	HGPS J1714-385	.88	.96	.12	2.03	.18	.06	.05	16.6	-28.7	1.8	.69	.08	3.26	.59	.58	.06
33	HGPS J1718-385	1.71	.26	.06	.37	.39	.22	.07	4.6	-31.9	6.0	.26	.09	.99	.23	.72	.10
34	HGPS J1728-343	.66	6.66	.84	1.75	.25	.19	.11	5.3	-21.2	3.4	2.65	.43	10.70	2.13	2.21	.49
35	HGPS J1732-347	.72	6.25	.42	2.13	.10	.06	.03	17.7	-25.6	2.7	2.93	.17	13.30	1.09	2.28	.14
36	HGPS J1744-303	.54	17.75	1.58	2.16	.18	.17	.10	5.9	-25.6	2.1	3.99	.28	21.30	2.33	2.64	.21
37	HGPS J1745-290	.66	6.69	.15	2.17	.03	.06	.01	16.2	-33.8	6.4	2.53	.05	14.70	.40	1.91	.05
38	HGPS J1747-248	.88	.51	.11	1.88	.37	.12	.10	8.2	-34.7	1.5	.35	.07	1.68	.60	.30	.05
39	HGPS J1747-281	.60	2.75	.18	1.90	.13	.20	.06	5.1	-24.3	5.7	.85	.05	4.18	.37	.64	.04
40	HGPS J1800-239	1.71	5.90	5.13	.00	1.93	.53	.18	1.9	-23.4	2.0	3.46	3.58	9.03	11.30	6.50	8.81
41	HGPS J1804-217	.34	141.97	8.44	2.23	.13	.37	.11	2.7	-27.2	4.1	8.52	.40	53.40	2.96	4.52	.26
43	HGPS J1810-193	1.17	5.56	.50	2.15	.12	.01	.02	78.1	-37.3	.8	7.63	.71	31.00	4.07	6.39	.55
44	HGPS J1813-178	.79	4.66	.30	1.96	.09	.07	.02	13.6	-25.7	3.6	2.76	.16	13.80	1.16	2.37	.15
45	HGPS J1825-138	.60	64.32	2.21	2.09	.06	.12	.03	8.4	-34.7	7.7	19.50	.53	86.90	3.57	14.30	.43
46	HGPS J1826-148	.66	3.68	.19	2.05	.08	.10	.03	10.2	-38.1	3.9	1.42	.09	6.81	.48	1.10	.10
47	HGPS J1831-098	1.06	4.05	.58	2.36	.20	-.02	.02	-64.1	-29.9	.4	4.71	.68	21.50	4.52	3.56	.53
48	HGPS J1833-105	.72	.87	.19	2.05	.38	.11	.13	9.2	-38.6	1.2	.40	.11	2.15	.78	.30	.11
49	HGPS J1834-087	.66	15.25	1.04	2.68	.12	.02	.03	52.1	-32.9	.6	4.82	.32	38.10	3.76	2.81	.26
50	HGPS J1837-069	.54	92.47	6.82	2.20	.17	.12	.08	8.1	-34.0	2.3	21.10	1.19	79.10	6.27	14.30	.91
51	HGPS J1840-056	.60	41.55	6.24	2.05	.29	.23	.14	4.3	-39.6	2.5	11.40	1.27	45.60	7.63	7.46	1.02
52	HGPS J1843-033	.88	7.06	.66	2.02	.13	.04	.03	28.3	-28.7	2.1	5.22	.45	19.90	2.29	4.61	.36
53	HGPS J1846-029	.72	1.26	.17	2.11	.21	.06	.06	17.2	-33.5	1.1	.60	.10	3.00	.55	.47	.11
54	HGPS J1848-017	1.06	7.90	1.34	1.91	.28	.10	.06	9.7	-22.6	2.1	7.97	1.57	26.20	6.51	6.73	1.65
55	HGPS J1849+000	1.41	.25	.04	1.43	.26	.09	.04	11.3	-32.1	2.5	.38	.08	1.22	.30	.50	.12
56	HGPS J1857+027	.45	43.59	4.32	2.25	.19	.20	.11	5.1	-23.1	3.2	5.83	.40	26.20	2.63	3.55	.29
57	HGPS J1858+020	.88	1.20	.19	2.26	.25	.04	.05	23.9	-31.6	1.0	.86	.12	3.71	.81	.62	.10
60	HGPS J1922+141	.72	2.07	.60	1.97	.65	.20	.26	4.9	-20.9	1.5	.89	.20	1.93	.52	.64	.13
61	HGPS J1930+187	1.06	1.08	.23	2.75	.37	-.01	.06	-78.1	-24.8	.2	1.29	.27	2.38	.55	.75	.15
62	HGPS J1943+212	.87	1.01	.27	2.29	.59	.07	.18	14.0	-25.7	.8	.70	.17	1.08	.26	.48	.09

C. Capability of Cherenkov Telescopes to Observe Ultra-fast Optical Flares

During the first year (2008) of this three-year thesis, in parallel to mainly working on the HESS 2 drive system, I completed the analysis of the data taken in May 2007 for my diploma thesis Deil et al. (2008b). The project was a pioneering study to determine the capability of Cherenkov telescopes to observe ultra-fast optical flares. 40 hours of microsecond-time resolution optical photometry measurements using photomultipliers was conducted on X-ray binary systems. No flares of astrophysical origin were detected. The detector, analysis methods and observations are described in Deil (2007) and Deil et al. (2009). In this appendix, the content of the publication Deil et al. (2009) is reproduced on the following seven pages.

Astroparticle Physics 31 (2009) 156–162

Contents lists available at ScienceDirect

Astroparticle Physics

journal homepage: www.elsevier.com/locate/astropart

Capability of Cherenkov telescopes to observe ultra-fast optical flares

C. Deil *, W. Domainko, G. Hermann, A.C. Clapson, A. Förster, C. van Eldik, W. Hofmann

Max-Planck-Institute for Nuclear Physics, P.O. Box 103980, 69029 Heidelberg, Germany

ARTICLE INFO

Article history:
Received 18 November 2008
Received in revised form 19 December 2008
Accepted 19 December 2008
Available online 31 December 2008

PACS:
95.55.Ka
95.55.Qf
95.75.Wx
97.80.Jp

Keywords:
Ultra-fast optical photometry
Cherenkov telescope

ABSTRACT

The large optical reflector (~100 m^2) of a H.E.S.S. Cherenkov telescope was used to search for very fast optical transients of astrophysical origin. Forty-three hours of observations targeting stellar-mass black holes and neutron stars were obtained using a dedicated photometer with microsecond time-resolution. The photometer consists of seven photomultiplier tube pixels: a central one to monitor the target and a surrounding ring of six pixels to veto background events. The light curves of all pixels were recorded continuously and were searched offline with a matched-filtering technique for flares with a duration of 2 μs–100 ms. As expected, many unresolved (<3 μs) and many long (>500 μs) background events originating in the earth's atmosphere were detected. In the time range 3–500 μs the measurement is essentially background-free, with only eight events detected in 43 h; five from lightning and three presumably from a piece of space debris. The detection of flashes of brightness ~0.1 Jy and only 20 μs duration from the space debris shows the potential of this setup to find rare optical flares on timescales of tens of microseconds. This timescale corresponds to the light crossing time of stellar-mass black holes and neutron stars.

1. Introduction

At optical wavelengths, the sky has been surveyed in deep exposures typically lasting minutes to hours. Much faster optical flares may have escaped detection, since the dynamic sky at sub-second timescales has rarely been explored in the past [1]. The availability of high quantum-efficiency, fast photodetectors (photomultiplier tubes (PMTs), avalanche photodiodes or charge-coupled devices (CCDs)) has lead a few groups to construct high-time-resolution photometers, imagers or spectrographs and operate them on medium to large optical telescopes [2–6].

The very large light collecting areas (>100 m^2) of reflectors of imaging Cherenkov telescopes such as H.E.S.S. [7], MAGIC [8] and VERITAS [9] provide an interesting alternative to normal optical telescopes [1]. Up to now, the only optical observations performed using the reflector of a Cherenkov telescope concerned the measurement of the optical pulsed emission from the Crab pulsar [10,11].

Compact objects like neutron stars and stellar-mass black holes are prime candidates as sources of fast optical flares. The fastest expected time variability of the emission from these systems is given by the light travel time through the immediate vicinity of the compact object, 10–100 μs for a typical size of tens of kilometers [1]. Such short flares can be produced by the accretion of lumps of matter, for instance in X-ray binary systems from the stellar companion [12]. Relativistic outflows can further shorten the observed timescales by Doppler boosting (for exceptional examples in the case of super-massive black holes see [13–15]). Optical variability in the millisecond range has been observed for pulsars [16] and X-ray binaries [17–19] and has been searched for in objects known to exhibit flares in other wavelength regions, for instance at radio frequencies from rotating radio transients (RRATs) [20,21]. No optical variability on timescales shorter than 100 μs has been detected from any astronomical target so far.

When trying to detect astronomical flares, natural and artificial flaring events occurring in the earth's atmosphere or orbit have to be considered. Known producers of such terrestial optical flares on sub-second timescales are airplanes, satellites, lightning and shooting stars [22]. Additionally, cosmic-ray induced air showers produce light flashes lasting a few nanoseconds [23].

This paper reports on 43 h of high-time-resolution optical photometry of X-ray binaries and one RRAT using the reflector of a H.E.S.S. Cherenkov telescope during moonshine. A comparison of the performance of H.E.S.S. with regular optical telescopes for such fast photometry observations is presented in Section 2. The custom-built detector that was used to record continuous light curves at microsecond time resolution is described in Section 3. An overview of the observations and a description of the flare-finding algorithm that was used to search for flares on timescales of 2 μs–100 ms is given in Section 4. The events that were detected are presented in Section 5, and Section 6 gives an outlook on how this new technique might be improved in the future.

* Corresponding author.
E-mail address: Christoph.Deil@mpi-hd.mpg.de (C. Deil).

0927-6505/$ - see front matter © 2008 Elsevier B.V. All rights reserved.
doi:10.1016/j.astropartphys.2008.12.008

2. Comparison with regular optical telescopes

The main difference in optical performance between Cherenkov and regular optical telescopes is that Cherenkov telescopes have huge reflectors but poor angular resolution, whereas optical telescopes have smaller reflectors and good angular resolution (see also [24]). Thus we assume here that the sensitivity of a Cherenkov telescope is limited by the shot noise from night-sky background (NSB) photons, whereas the optical telescope is considered completely background-free and photon-limited.

Consider a flare of known duration τ occuring at a known point in time. This scenario might happen when a flare is detected in X-ray or radio observations and searched for in the optical band. For an optical telescope of diameter D_O, the minimum detectable flux ϕ_O (ph m^{-2} s^{-1}) is given by the requirement that it has to collect at least one photon,

$$\phi_O \sim \frac{4}{\pi}\frac{1}{D_O^2\tau}. \quad (1)$$

The detection limit for a Cherenkov telescope is given by the condition that the number of photons detected from the source $S = \phi_C \frac{\pi}{4} D_C^2 \tau$ must be at least as large as the fluctuations in the number of photons from the NSB during the flare. The photodetector aperture σ_C (rad) must be chosen to be approximately equal to the width of the point spread function (PSF) of the telescope. For an isotropic night-sky surface brightness ψ_{NSB} (ph m^{-2} s^{-1} sr^{-1}), telescope diameter D_C and flare duration τ, the average number of NSB photons during the flare will be $B = \psi_{NSB}\left(\frac{\pi}{4}\right)^2 D_C^2 \sigma_C^2 \tau$ and the Poisson noise $N = \sqrt{B}$.

Solving the equation $S/N \sim 1$ for ϕ_C gives the minimum detectable flux

$$\phi_C \sim \frac{\sigma_C}{D_C}\frac{\sqrt{\psi_{NSB}}}{\sqrt{\tau}}, \quad (2)$$

and hence

$$\frac{\phi_C}{\phi_O} \sim \frac{\pi}{4}\frac{\sigma_C}{D_C} D_O^2 \sqrt{\psi_{NSB}\tau}. \quad (3)$$

The main result from Eq. (3) is that the relative sensitivity ϕ_C/ϕ_O scales with $\sqrt{\tau}$, i.e. that Cherenkov telescopes perform better relative to optical telescopes for the detection of shorter flares. Inserting the values for H.E.S.S. into Eq. (3), an absolute comparison with regular optical telescopes can be made. Fig. 1 shows that even under moderate moonshine conditions Cherenkov telescopes are competitive with meter-class optical telescopes in the sub-millisecond time domain, whereas for the search of longer flares optical telescopes perform better.

For observations of high-mass X-ray binary systems with a bright companion optical telescopes will be background-limited as well. Then, the relative sensitivity of Cherenkov and optical telescopes no longer depends on the flare duration, but is given by

$$\frac{\phi_C}{\phi_O} \sim \frac{D_O}{D_C}\sqrt{\frac{R_{C,Background}}{R_{O,Background}}}, \quad (4)$$

where $R_{Background}$ are photon detection background rates. These rates are the sum of the rates caused by light from a companion star, light from the night sky, or potentially a dark rate in the detector.

3. The camera system

For the optical high-time-resolution observations, a 7-pixel camera was custom-built and mounted on the lid of the Cherenkov camera of a H.E.S.S. telescope using a plane secondary mirror to put it into focus (see Fig. 2). The central pixel was used to continuously record the light curve of the astronomical target, while a ring of six 'outer' pixels was used both to monitor the NSB level and as a veto system to reject terrestial background events occurring in the atmosphere (see Fig. 3).

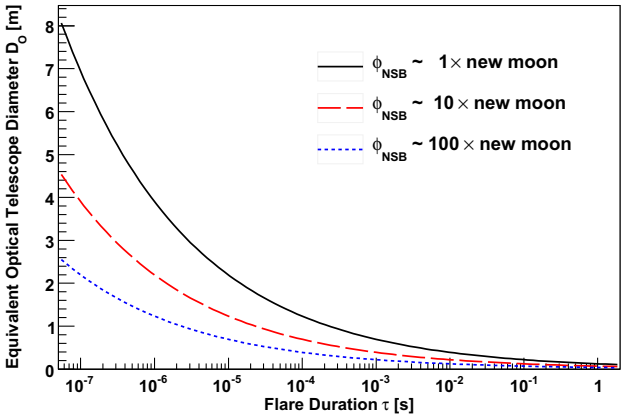

Fig. 1. Comparison of a H.E.S.S. Cherenkov telescope (100 m^2) with a normal optical telescope for high-time-resolution photometry. For a given flare duration τ, the diameter of a background-free optical telescope was calculated to achieve the same sensitivity as H.E.S.S. using Eq. (3) and the condition $\frac{\phi_C}{\phi_O} = 1$ with the following parameters: H.E.S.S. telescope diameter $D_C \sim 11$ m, PSF width $\sigma_C \sim 2.5$ arcmin and typical NSB brightness without moon at the H.E.S.S. site $\psi_{NSB} \sim 2 \times 10^{12}$ phm^{-2} s^{-1} sr^{-1} in the wavelength range 300–650 nm [25]. For typical NSB levels during moonshine see Fig. 4.

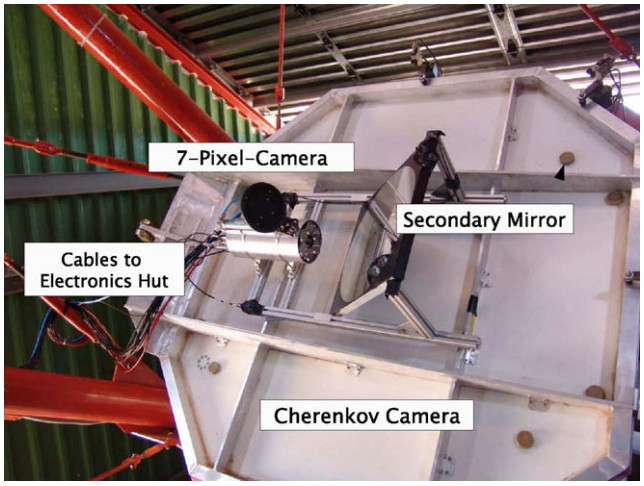

Fig. 2. The 7-pixel camera mounted on the lid of the H.E.S.S. Cherenkov camera.

For all seven pixels, Photonis PMTs of type XP2960 were used as light detectors. For this setup, the total system response mainly is in the wavelength range 350–550 nm, roughly matching the canonical astronomical B band (effective wavelength 445 nm, effective width 94 nm). In this range the average transmissivity of the atmosphere is known to be ~70% at 15° zenith angle [26]. The primary and secondary mirror reflectivities (both on average ~80%) and PMT quantum-efficiency (on average ~20%) have been measured in the lab as a function of wavelength. Assuming a flat spectrum in this range, an observed photoelectron rate can be converted into an actual flux density in Jansky.

The PMTs were equipped with hexagonal light funnels of 10 arcmin width [27], and the central pixel had a circular aperture of 5 arcmin (see Fig. 3). This diameter was chosen such that it contains more than 90% of the light from the target, but blocks ~3/4) of the NSB compared to the outer pixels. Note that the H.E.S.S.

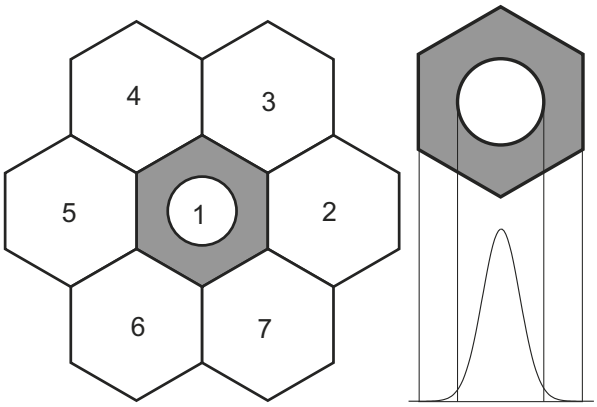

Fig. 3. *Left*: Front view of the 7-pixel camera. *Right*: Comparison of the dimensions of the H.E.S.S. optical PSF full width at half maximum (FWHM = 2.5 arcmin), central pixel aperture diameter (5.0 arcmin) and hexagonal outer pixel flat-to-flat width (10 arcmin). The telescope focal length is 15 m resulting in a plate scale of 4.4 mm/arcmin.

optical PSF has a full width at half maximum (FWHM) of 2.5 arcmin. The advantage of this pixel layout is that there are no gaps in the veto ring and that no part of the signal from the astronomical target will enter one of the veto pixels. However, the NSB level in the outer pixels is a factor ∼4 higher compared to the central pixel, making them 2 times less sensitive to detect similar flares.

Pointing corrections for atmospheric refraction, for bending of the masts holding the Cherenkov camera, and for the offset of the central pixel relative to the optical axis of the telescope were applied. The pointing accuracy was checked frequently by observing a bright star near the target. This was done by closing the pneumatic lid of the 7-pixel camera and taking a picture of the image of the star on that lid with a CCD located between mirror segments in the center of the H.E.S.S. reflector. The remaining mispointing was below 0.5 arcmin, compared to 5 arcmin diameter of the central pixel, resulting only in a negligible signal loss.

The analog signals from the PMTs were transmitted via 50 m coaxial cables to an electronics container. There, they were amplified and passed through an analog low-pass filter with a cutoff near 0.5 μs. Then, the signals were continuously digitized with a sampling period of 10 ns, and 256 consecutive samples were averaged to reduce the data rate to 6 megabyte/s, resulting in a 2.56 μs sampling. The absolute time of each sample is known with a precision of ∼1 μs from a GPS clock. An additional coaxial cable was connected to a termination resistor in the 7-pixel camera and its signal was used to monitor possible electronic interference (for details see [28]).

4. Observations and data analysis

In May 2007 high-time-resolution observations of several X-ray binaries containing a black hole or a neutron star (Sco X-1, GX 339-4, MXB 1735-44, V4641 Sgr and SS 433) and of the isolated neutron star RRAT J1317-5759 were performed during moonshine. After removing runs where clouds entered the field of view, 43 h (∼1 terabyte) of good quality data remain. The level of the NSB depends mainly on the brightness of the moon, the altitude of the target and the moon-target angular separation. Our observations range from new moon to more than 3/4 moon, altitudes of 30°–90° and moon-target separations of 30°–120°. The measured NSB level increases up to a factor of ∼20 relative to no moon (see Fig. 4). Note that the shot noise from the NSB, which determines the sensitivity for detecting flares, varies by a factor of $\sim\sqrt{20}$ for these conditions.

Non-astronomical events are expected to occur, producing a background of events that has to be rejected to find flares from the astronomical target. Airplanes, satellites and shooting stars [10] passing through the field of view of the whole camera and also the central pixel are expected to produce time-shifted flares with the following pattern: first in one or two of the outer pixels, then in the central pixel and then in one or two of the outer pixels on the opposite side (see Fig. 5 top). Lightning at the horizon being scattered in the atmosphere will illuminate all pixels in the same way, making it easy to veto (see Fig. 5 bottom). Cosmic-ray induced air showers typically show an elliptical light distribution on the sky with diameters of ∼30 arcmin and last for a few nanoseconds. Such flashes will register as temporally unresolved events in our detector. Given the ∼30 arcmin field of view of the 7-pixel camera, cosmic rays seen in the central pixel should be seen simultaneously by at least one veto pixel.

The data from all seven pixels and the electronics interference monitoring channel were searched for events that stand out above the noise. The challenge of finding weak signals in a noise-dominated time series is similar to the one faced by gravitational wave detectors, and a large set of literature exists on the topic (see [29] and references therein). The complexity of the methods and their performances depend to a large degree on the assumptions that can be made both on the noise in the series and the characteristics of the signal.

Of particular interest for its simplicity is the *matched filter*, where a particular waveform is assumed for the signal. A generic flare search algorithm called *Peak Correlator* (*PC*) was derived from this principle (presented in [30], implemented in [31]), using a bank of Gaussian templates $\exp(-t^2/2\tau^2)$ as assumed signal shapes. Gaussians roughly fit any structureless flare, and using several widths τ_i makes it possible to cover a range $(\tau_{\mathrm{Min}}, \tau_{\mathrm{Max}})$ of timescales. The template spacing is chosen such that the loss of detection significance for an actual Gaussian shaped flare does not decrease by more than some ϵ for any width τ in the specified range.

The PC algorithm calculates the statistical significance of flares, assuming a Gaussian waveform, by taking the noise in the series into account, estimated by the power spectral density (PSD) of the data. In practice, the time series is split into chunks of length T_{Chunk} and each chunk into a number of windows N_{Windows} such that the length of a window $T_{\mathrm{Window}} = T_{\mathrm{Chunk}}/N_{\mathrm{Window}}$ is large compared to τ_{Max}. The PSD of a chunk is the average of the PSDs of its win-

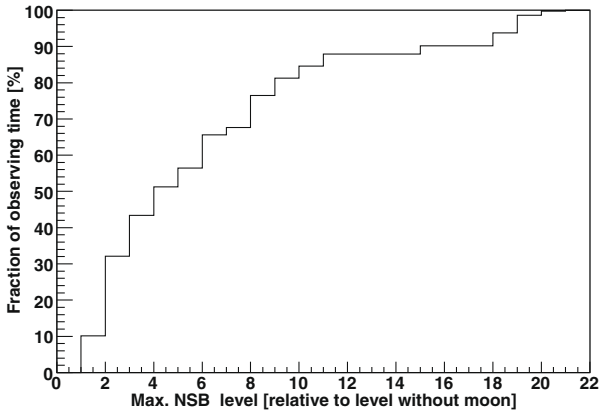

Fig. 4. NSB levels during the 43 h of good quality observations in May 2–29, 2007, roughly one moon period. This integral plot shows the fraction of the observing time the NSB was below a given level, relative to the NSB level without moon ($\psi_{\mathrm{NSB}} \sim 2 \times 10^{12}$ ph m^{-2} s^{-1} sr^{-1} in the wavelength range 300–650 nm [25]). Note that about 50% of the observations occured at NSB levels less than five times the level without moon.

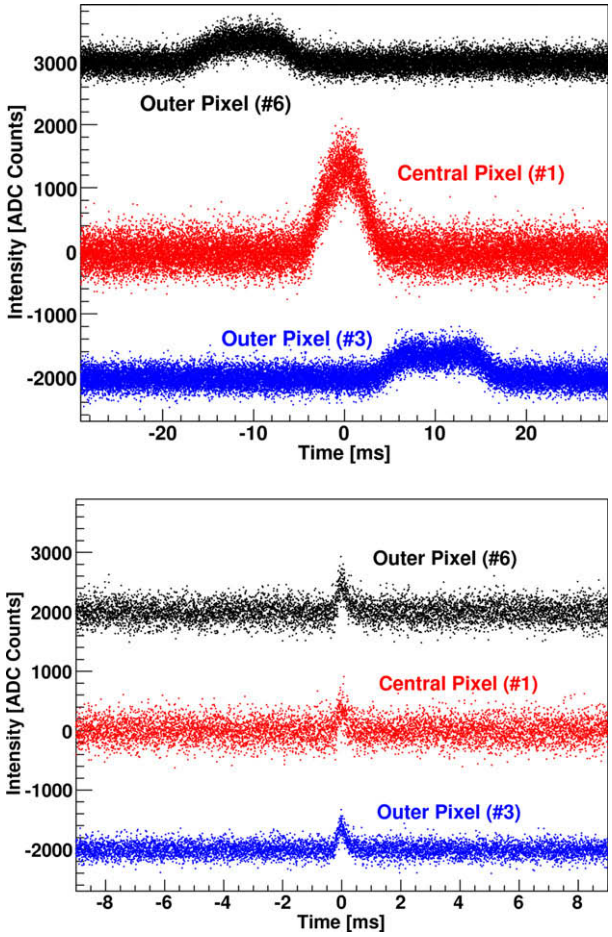

Fig. 5. Example background events very likely caused by a shooting star (*top*) and lightning (*bottom*). The intensities were arbitrarily offset such that the light curves from different channels do not overlap.

dows. The underlying assumption is that the noise level is stable on timescales longer than T_{Chunk}.

As can be seen in Fig. 6, above ~100 Hz (corresponding to timescales shorter than ~10 ms), the noise is approximately flat, which is characteristic of shot noise from random photon arrival times. This background is usually dominated by the NSB and sometimes by a bright star in the field of view. It changes slowly with zenith angle on timescales of many minutes while the telescope tracks the target. Additionally, due to field rotation (the H.E.S.S. telescope has an altitude-azimuth mount), a bright star sometimes rotates around the center and moves from one outer pixel to the next, changing their background levels on timescales of many minutes. Below 100 Hz (corresponding to timescales above 10 ms) the signal is dominated by electronic noise ($1/f$ noise). Its level changes mainly with temperature, again on timescales much longer than T_{Chunk}. The PSD contains strong lines at 50 Hz and multiples up to ~1 kHz, resulting from electrical interference from the power supply. The PC algorithm correctly takes these noise components into account and prevents false event detections on the corresponding timescales.

The output of the PC filter for a given template width τ_i is a time series of signal-to-noise ratio (SNR) values at the same sampling as the original light curve ($t_s = 2.56$ µs). For an input time series of Gaussian-distributed noise, the output is also Gaussian. Thus a simple amplitude threshold $A_{\text{Thr,Det}}$ on the SNR series can be used to trigger a detection in the central pixel, and $A_{\text{Thr,Veto}}$ to trigger a detection in one of the six outer pixels or in the electronics interference monitoring channel. For actual parameter values used in this analysis see Table 1.

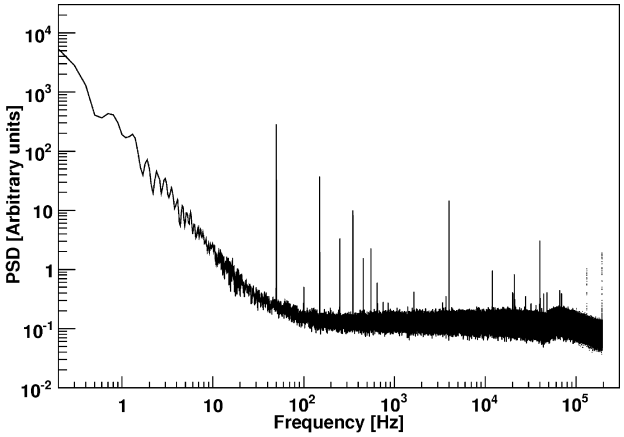

Fig. 6. A typical PSD calculated from one chunk of data containing no detected events (see text for explanations).

Table 1
Flare search parameters for the PC and veto algorithm (see text for explanations).

Parameter	Symbol	Value
Timescale range	$(\tau_{\text{Min}}, \tau_{\text{Max}})$	(2 µs, 100 ms)
Maximum significance loss	ϵ	1%
Chunk duration	T_{Chunk}	21 s
Windows per chunk	N_{Windows}	16
Detection SNR threshold	$A_{\text{Thr,Det}}$	8
Veto SNR threshold	$A_{\text{Thr,Veto}}$	7
Clustering factor	n	4
Veto window	ΔT_{Veto}	100 ms

When consecutive samples are above threshold, the first and last ones define the start t_{Start} and stop time t_{Stop} of a so called micro-event. The SNR of the micro-event is given by the maximum SNR value in this time range, and the micro-event time is determined by the time of this maximum SNR. A flare will trigger on several nearby timescales τ_i and might contain substructures, leading to several close-by micro-events. Micro-events are clustered if their clustering windows $(t_{\text{Start}} - n\tau_i, t_{\text{Stop}} + n\tau_i)$ overlap, where n is the clustering factor of Table 1. The time, timescale and SNR of the clustered event is defined by the micro-event with the highest SNR.

The following simple coincidence veto algorithm was applied to every event detected in the central pixel: if any of the six outer pixels had detected an event on any of the tested timescales within ΔT_{Veto} of the central pixel event time, the flare was vetoed. The longest observed time shifts are 50 ms for some shooting stars, thus a veto time window $\Delta T_{\text{Veto}} = 100$ ms was chosen conservatively. The veto threshold $A_{\text{Thr,Veto}} = 7$ was chosen such that even the shortest timescales do not trigger on statistical fluctuations due to the large number of trial factors (~10^{11}). Electrical interference will also influence the signal from the PMTs, although with a much lower significance, since their time series is dominated by photon shot noise, which is absent from the resistor channel. Whenever the electronics interference monitoring channel detected an interference signal within ΔT_{Veto} of the central pixel event time, this event was rejected. In Section 5 only events where no electronic interference occured are discussed. When applying this veto algorithm, a total of 4% of the observation time is vetoed.

5. Results

Applying this flare search and veto algorithm to the data, with the parameters shown in Table 1, we find the events shown in

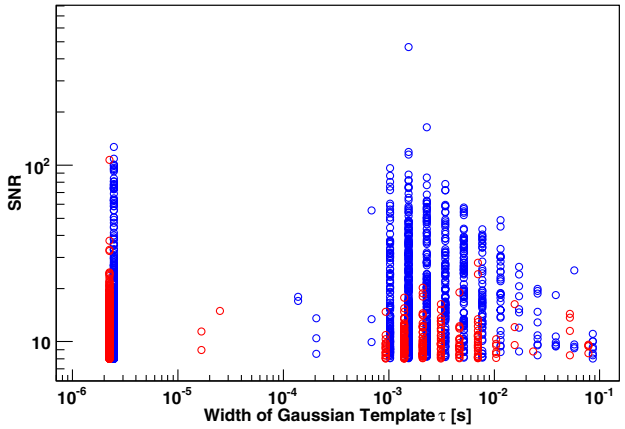

Fig. 7. SNR and timescale τ for all events in 43 h of observations. Every circle represents a flare detected in the central pixel. Red events were not vetoed, blue events were. Note that blue events were shifted to the right by multiplying their τ by a factor 1.1 such that they can be seen more clearly. Events vetoed by the electronics interference monitoring channel are not shown at all. (For interpretation of the references to colour in this figure legend, the reader is referred to the web version of this article.)

Fig. 7. On timescales above 500 μs, a large number of 1175 events was detected. Most of these events are probably background from shooting stars, since a visual inspection of their light curves shows that most have a temporal pattern similar to the pattern of the event shown in Fig. 5 top; 21% of these events are not vetoed, especially those of low SNR. This is understandable as some shooting stars might travel close to head-on towards the telescope. These events may remain in an outer pixel for some time and give a flat-topped flare that is not very Gaussian-like.

Events with $\tau < 3$ μs (1538 events, 51% not vetoed) must be considered as temporally unresolved, since they last only one or two samples, which would also be the case for much shorter flares because of the analog shaping of 0.5 μs. These events might be due to air showers of a few nanoseconds duration. In that case many low-SNR events might not be detected by the outer pixels because air showers exhibit large intensity variations within the shower on scales of few arcminutes.

In the time range 3–500 μs, where the fastest flares from stellar-mass black holes and neutron stars are expected to occur, there is considerably less backgound: only eight events were detected. The five vetoed events at $\tau \sim 120$ μs are isolated events that occured in the nights of May 11 and 12. They show the same structureless waveform in all pixels and are most likely caused by single lightning flashes (Fig. 5 bottom shows the one with the highest SNR as an example).

The three events at $\tau \sim 20$ μs (light curves shown in Fig. 8) were not vetoed by any of the outer pixels. They are separated by 68.608 (3) ms from each other and thus only form one exceptional event. Using the method explained in Section 3, the peak flux of the brightest flare (SNR = 15 at $\tau = 22$ μs) was determined as 0.2 Jy. The flares were recorded while observing the X-ray binary black hole candidate V4641 Sgr on May 14, 2007 at 3:47 UTC. Observing conditions were very good (altitude 63°, 2.6 days before new moon, moon-target separation 101°). A careful analysis of the data shows, however, that the flares were not caused by the astronomical target, but very likely by a piece of space debris crossing the field of view. A flare separation of 68.6 ms corresponds to a rotation frequency of 14.6 Hz. One shiny surface would produce a beam of reflected sunlight of diameter 0.5°, the diameter of the sun on the sky. A telescope placed in this rotating beam would see flares of approximately rectangular shape and 0.5°/360° × 68.6 ms = 95 μs duration. Given that the telescope might not be located in the center of the 0.5° circular beam but towards the edge, any flare duration shorter than but of the same order as 95 μs is possible, in rough agreement with the observed $\tau = 20$ μs (corresponding flare FWHM = $2.4\tau = 50$ μs). One consequence of this interpretation would be that at a separation of a few times 68.6 ms further flares should be present in one of the outer pixels

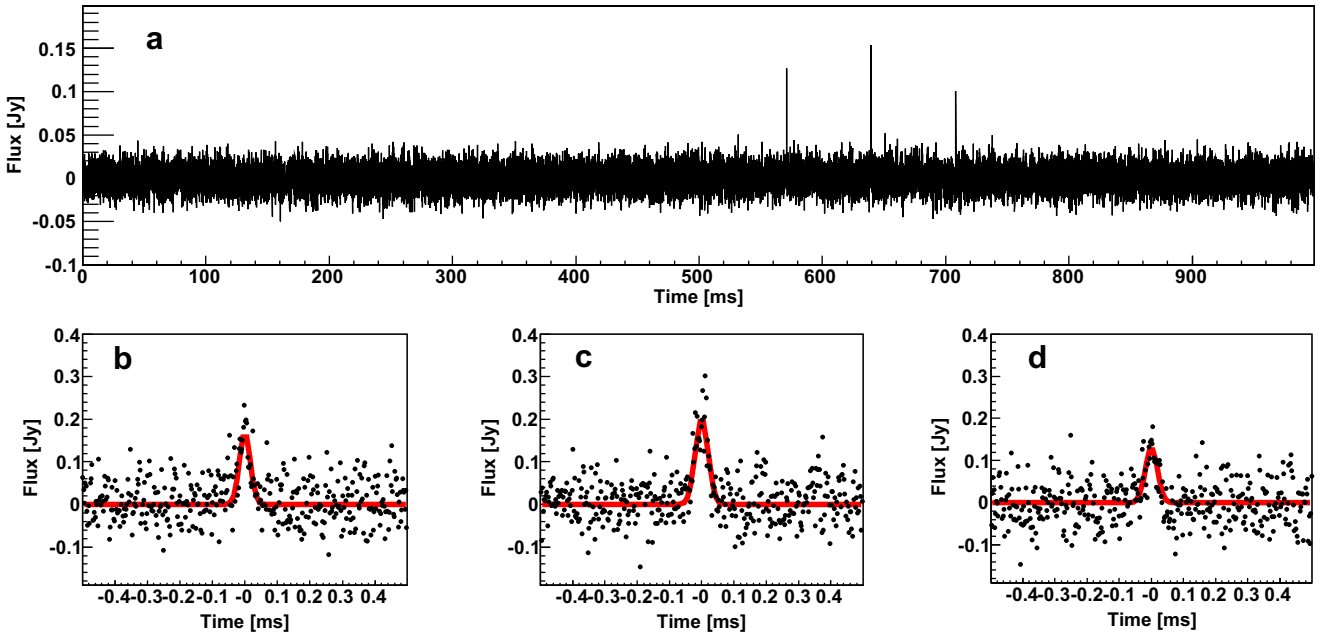

Fig. 8. Light curve of the three optical flares from the direction of V4641 Sgr on May 14, 2007. Panel (a) shows one second of the raw light curve with a binning of 38.4 μs (15 samples). The time is given relative to 3:47:28 UTC. (Due to technical problems with the time synchronization of the measurement computer, the absolute time of the event might be offset by at most 10 s. For the relative timing between samples, the GPS signal was used directly by the analog-to-digital converter and is thus correct.) Panels (b)–(d) each show a zoom-in of one millisecond of observations at the original binning of 2.56 μs, with the time axis centered on the flare peaks. The solid curve is a fit of a Gaussian (width and amplitude as free parameters).

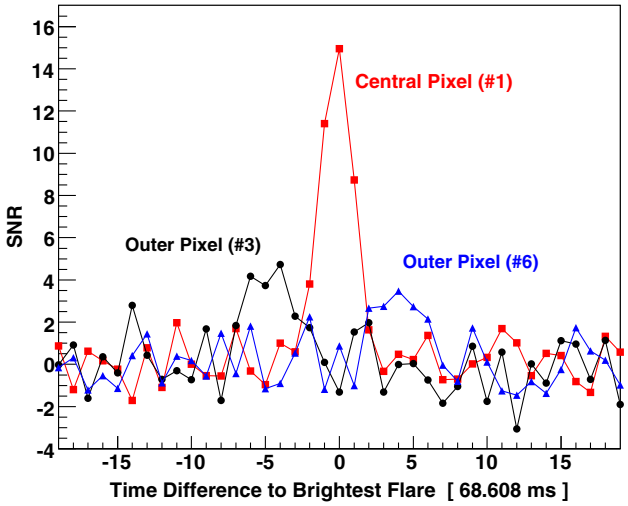

Fig. 9. Temporal signature of the space debris events. This plot shows the SNR (for $\tau = 22$ μs) at multiples of 68.608 ms before and after the SNR = 15 event in the central pixel.

when the debris passed through their field of view. As can be seen in Fig. 9, this is actually the case. Three events at SNR ~ 4 occurred in outer pixel #3 right before the events in the central pixel, and five events at SNR ~ 3 right after in the opposite outer pixel #6. This shows that indeed an object was crossing the field of view of the whole camera and that the flares cannot be of astrophysical origin. Assuming a height of $\sim$1000 km (the object had to be above 600 km to be outside the earth's shadow and almost all space debris is at a height of less that 2000 km), the angular speed of 0.6°/s corresponds to a speed of 10 km/s, a typical value for space debris orbits [32,33]. An airplane with strobe lights could in principle produce the observed signal, but neither the 15 Hz repetition rate, nor the 20 μs duration are used in airplane strobes, and the Namibian air control confirmed that there were no airplanes within 100 km of the H.E.S.S. site at the time the flares occurred. Satellites do not have strobe lights and do not rotate as fast as 15 Hz and can thus also be excluded as the origin of the flares.

6. Outlook

In this paper it is demonstrated that the huge optical reflector of Cherenkov telescopes can be used to observe faint optical flashes in the sub-millisecond time domain. Flares with a duration of $\sim$20 μs as faint as 0.1 Jy have been detected with high statistical significance using a H.E.S.S. telescope equipped with a dedicated detector during moderate moonshine.

Compact objects like neutron stars and black holes are known to produce bright and short optical flares (e.g. [34]), indicating a spatially small emission region. The small size of the emission region also constrains the nature of the radiation mechanism [35]: ultra-fast flashes are likely of non-thermal origin, e.g. cyclotron or synchrotron radiation [19,?,36]. If the emission is generated in a relativistic jet, the shortest observed variability timescale can place a lower limit on the Doppler factor of this outflow [1].

X-ray binaries have been pointed out as promising targets for sub-millisecond time-resolution. Several interesting aspects related to the compact objects in these systems could be investigated:

- The distinction whether the compact object has a solid surface or is a black hole: a blob of matter spiraling into the event horizon of a black hole would produce a series of progressively weaker flares, whereas accretion onto a neutron star would end in a final bright flash when the matter hits its surface [12,37].
- Measurement of the black hole spin: Fukumura and Kanzanas [38] propose that photons emitted inside the ergosphere can orbit a rapidly rotating black hole. After leaving the vicinity of the black hole, they may arrive at a distant observer as double or triple flares, separated by constant time lags, which is connected to the spin of the black hole.
- Study of the characteristics of super-Eddington flows: another exotic possibility to create fast flashes of radiation are bubbles filled with photons, which could be created during accretion onto a neutron star [39,40].

For the study of bright objects, the night-sky background faced by optical observations with a Cherenkov telescope is less critical and a large reflector is especially important. In this case Cherenkov telescopes could be used to monitor such systems, since, e.g. H.E.S.S. is not operated during moonshine. Significant observing time ($\sim$40 h/month) is available without interfering with normal gamma-ray observations, whereas time on large optical telescopes is expensive.

The observations presented here show that a considerable background of optical flashes with origin likely in the earth's atmosphere is present on timescales below 3 μs and above 0.5 ms. A ring of veto pixels has been shown to be effective, but not perfect to reject these events. A more efficient veto system could consist of a second telescope at a distance of several hundred kilometers observing the same target at the same time. Any flare from an astronomical target must occur coincident with the same waveform in both telescopes. Light sources at smaller distances will be seen by only one system if the parallax of the light emitting object is larger than the angular diameter of the central pixel. A separation of the two telescopes of 700 km with an angular diameter of the central pixel of 0.1° will place any coincident event at a distance of at least 400 000 km and thus outside the earth–moon system.

The H.E.S.S. array will be extended with a fifth, much larger telescope. This H.E.S.S. II telescope will feature a light collecting area of 600 m^2, allowing more sensitive searches for ultra-fast optical transients. Continuing high-time-resolution optical photometry observations with an improved setup (higher quantum-efficiency, smaller pixels, faster readout) in conjunction with a second telescope (optical or Cherenkov) at a large distance seems promising.

Acknowledgements

The authors would like to thank the H.E.S.S. collaboration for permission to use a H.E.S.S. telescope for these observations. We thank Thomas Kihm for help with the design and implementation of the data acquisition and Stefan Schmidt and Christian Neureuther for constructing the 7-pixel camera. Toni Hanke and Eben Tjingaete were very helpful with the installation and operation of the instrument in Namibia.

References

[1] D. Eichler, G. Beskin, PhRvL 85 (2000) 2669.
[2] V.F. Shvartsman, I.N. Bernstein, G.M. Beskin, et al., A&AT 13 (1997) 13.
[3] C. Straubmeier, G. Kanbach, F. Schrey, ExA 11 (2001) 157.
[4] O. Ryan, M. Redfern, A. Shearer, ExA 21 (2006) 23.
[5] V.S. Dhillon, T.R. Marsh, M.J. Stevenson, et al., MNRAS 378 (2007) 825.
[6] F. Hormuth et al., arXiv:0807.0497.
[7] J.A. Hinton, NewAR 48 (2004) 331.
[8] E. Lorenz, NewAR 48 (2004) 339.
[9] F. Krennrich, I.H. Bond, P.J. Boyle, et al., NewAR 48 (2004) 345.
[10] J. Hinton, G. Hermann, P. Krötz, S. Funk, APh 26 (2006) 22.
[11] F. Lucarelli, J.A. Barrio, P. Antoranz, et al., NIMPA 589 (2008) 415.

[12] J.E. Dolan, PASP 113 (2001) 974.
[13] J.A. Gaidos et al., Natur 383 (1996) 319.
[14] F. Aharonian et al., H.E.S.S. Collaboration, ApJ 664 (2007) 71.
[15] J. Albert et al., MAGIC Collaboration, ApJ 669 (2007) 862.
[16] A. Shearer, B. Stappers, P. O'Connor, et al., Science 301 (2003) 493.
[17] C. Bartolini, A. Guarnieri, A. Piccioni, G.M. Beskin, S.I. Neizvestny, ApJS 92 (1994) 455.
[18] G. Beskin, S. Neizvestny, V. Plokhotnichenko, et al., A&A 289 (1994) 141.
[19] G. Kanbach, C. Straubmeier, H.C. Spruit, T. Belloni, Natur 414 (2001) 180.
[20] M.A. McLaughlin, A.G. Lyne, D.R. Lorimer, et al., Natur 439 (2006) 817.
[21] V.S. Dhillon, T.R. Marsh, S.P. Littlefair, MNRAS 372 (2006) 209.
[22] B.E. Schaefer, H. Pedersen, C. Gouiffes, J.M. Poulsen, G. Pizzichini, A&A 174 (1987) 338.
[23] W. Galbraith, J.V. Jelley, Natur 171 (1953) 349.
[24] G.M. Beskin, V. Plokhotnichenko, C. Bartolini, et al., A&AS 138 (1999) 589.
[25] S. Preuss, G. Hermann, W. Hofmann, A. Kohnle, NIMPR A 481 (2002) 229.
[26] K. Bernlöhr, APh 12 (2000) 255.
[27] K. Bernlöhr, APh 20 (2003) 111.
[28] C. Deil, W. Domainko, G. Hermann, AIPC 984 (2008) 140. arXiv:0810.3155.
[29] I. Jaranowski, A. Krolak, Living Rev. Relativity 8 (2005) 3.
[30] N. Arnaud et al., Phys. Rev. D 59 (2002) 08.
[31] BuL—Virgo Burst Software Library, http://virgo.web.lal.in2p3.fr/BuL/home.html.
[32] Technical Report on Space Debris, United Nations, New York, 1999, A/AC.105/720, available at http://www.unoosa.org/.
[33] NASA Orbital Debris Quaterly News, Volume 12, Issue 2 (April 2008), available at http://orbitaldebris.jsc.nasa.gov/.
[34] Uemura et al., PASJ 56 (2004) 61.
[35] V.F. Shvartsman et al., SvAL 15 (1989) 252.
[36] A.C. Fabian et al., A&A 111 (1982) L9.
[37] W.R. Stoeger, MNRAS 190 (1980) 715.
[38] K. Fukumura, D. Kanzanas, ApJ 679 (2008) 1413.
[39] R. Klein et al., ApJ 457 (1996) L85.
[40] J.G. Jernigan et al., ApJ 530 (2000) 875.

D. HESS 2

About 14 months of this thesis (January 2008 to March 2009) were devoted to the pre-commissioning of the HESS 2 drive system at MPIK, Heidelberg. This work was supervised by German Hermann (MPIK Heidelberg) and done in close collaboration with the company MT Mechatronics[1] in Mainz, who designed the drive system as well as other parts of the HESS 2 telescope.

At the time when I joined that project it was foreseen that commissioning of the drive system in Namibia would take place in 2009. The initial idea for my PhD project was that I would help commissioning the drive system as a technical part and then use first light data of the HESS 2 telescope as the science part. Due to problems with the steel construction commissioning will only start in early 2012, so unfortunately the most interesting aspects—driving the 600 ton telescope for the first time and first light—are yet to come.

The pre-commissioning at MPIK consisted mainly of checking that the drive system electronics and software worked as expected and would be able to provide the needed functionality and safety. E.g. it was noticed that the park-in procedure that had been implemented was insufficient and those parts of the software were adjusted and re-tested.

There is no 'data' to show yet about the HESS 2 drive system, like e.g. the precision and speed it will achieve once in operation. The HESS 2 drive system and tests are described in internal reports and manuals, and there is no point in reproducing that information here, so in this appendix I will simply reproduce a proceeding I wrote Deil et al. (2008a) that gives a high-level overview of the HESS 2 telescope and drive system. The HESS 2 camera and preliminary performance analyses can be found in Vincent et al. (2005); Delagnes et al. (2006); Becherini et al. (2008b,b).

Figure D.1 shows an image of the HESS 2 construction as well as an artist's impression of what the HESS array will look like after the fifth telescope has been added.

[1] www.mt-mechatronics.de

Figure D.1.. *Top:* An artist view of HESS 2 located in the center of the existing HESS 1 telescopes (Horns and the HESS Collaboration, 2007). *Bottom:* A picture showing the HESS 2 construction status, taken by Julien Bolmont in January 2011.

H.E.S.S. II – Telescope Structure, Reflector and Drive System

C. Deil, C. van Eldik, A. Förster, G. Hermann, W. Hofmann and M. Panter for the H.E.S.S. Collaboration

Max-Planck-Institut für Kernphysik, P.O. Box 103980, D-69029 Heidelberg, Germany

Abstract. The currently operating phase I of the imaging atmospheric Cherenkov telescope array H.E.S.S. consists of four telescopes, each with a 107 m^2 reflector, which are arranged on the corners of a square of 120 m side length. At the moment, the collaboration is building a much larger 600 m^2 telescope in the center of the array. This will not only increase the sensitivity in the currently accessible energy regime, but will in addition lower the energy threshold of the system. The H.E.S.S. II telescope will have a parabolic reflector of 36 m focal length consisting of 850 individual mirrors, which can be automatically aligned, similar to the H.E.S.S. I telescopes. The drive system will have a repositioning speed of 100 deg/min in elevation and 200 deg/min in azimuth and achieve an online tracking accuracy of $\sim$ 1 arcmin and an offline absolute pointing accuracy of $\sim$ 10 arcsec. This proceeding contribution presents details on the technical implementation of the telescope mechanics, optics and drive system.

Keywords: H.E.S.S., Cherenkov Telescope

INTRODUCTION

The sensitivity of an array of Cherenkov telescopes increases with the number of telescopes and the size of each individual telescope. Since the end of 2003, the H.E.S.S. array in Namibia consists of four 107 m^2 telescopes and has observed many gamma-ray sources in the 300 GeV – 30 TeV energy range [1]. Currently a fifth much larger telescope called H.E.S.S. II (see Tab. 1 and Fig. 1) is under construction in the center of the array (see Fig. 3), with observations planned to start in 2009. This will significantly lower the energy threshold of the H.E.S.S. array and increase the sensitivity in the currently accessible energy range [2, 3].

Measurements below 100 GeV are important to address some of the most interesting questions in very-high energy (VHE) gamma-ray astronomy. Examples are the understanding of VHE pulsar emission [4] or the question which VHE gamma-ray emitters (e.g. supernova remnants) are of hadronic and which of leptonic origin. Also the universe is more transparent at these energies, making it possible to see active galactic nuclei at larger redshift.

H.E.S.S. II will be the largest Cherenkov telescope ever built with a reflector area of 600 m^2. Here some details about the technical implementation of the telescope mechanics, optics and drive system are presented.

TABLE 1. H.E.S.S. II telescope specifications

Parameter	Value
Reflector Area	600 m^2
Reflector Size	24 m × 30 m
Focal length	36 m
Camera field of view	3.2°
Weight	560 metric tons
Speed azimuth, elevation	200°/min, 100°/min

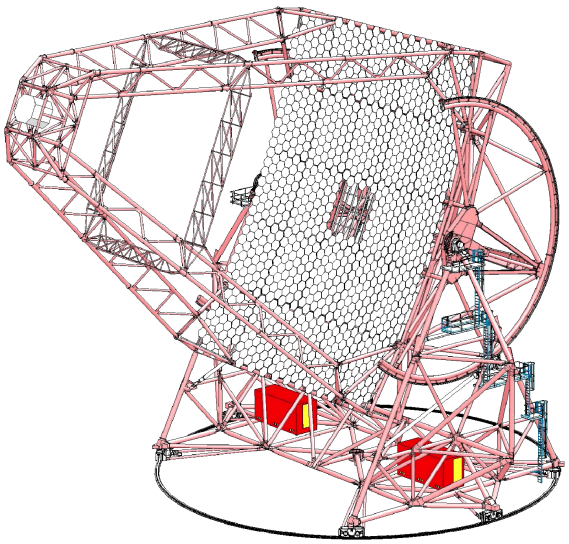

FIGURE 1. H.E.S.S. II telescope drawing

CP1085, *High Energy Gamma-Ray Astronomy, 4th International Meeting on High Energy Gamma-Ray Astronomy*, edited by F. A. Aharonian, W. Hofmann, and F. M. Rieger

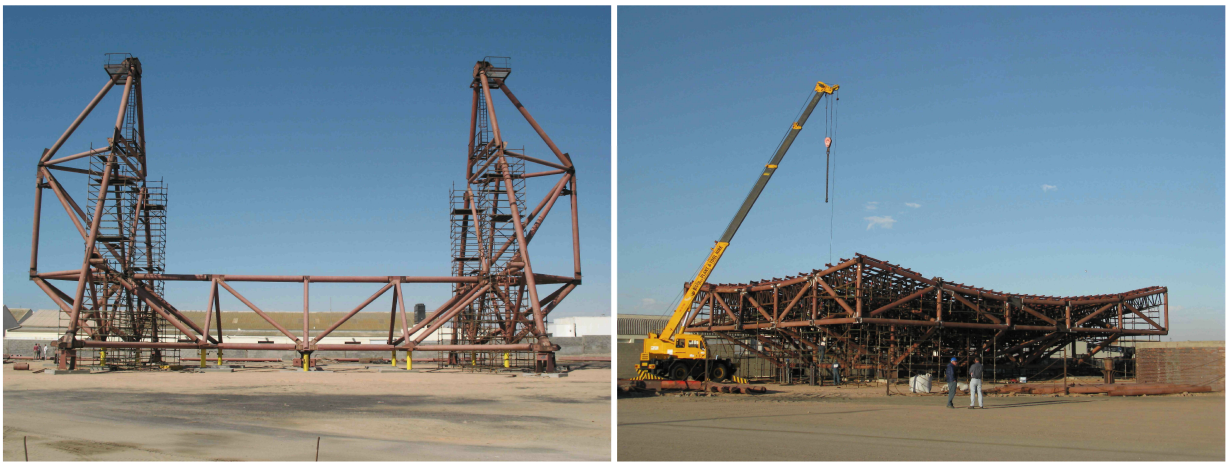

FIGURE 2. H.E.S.S. II trial assembly in Walvis Bay, Namibia. *Left:* Mount. *Right:* Dish and mirror support structure.

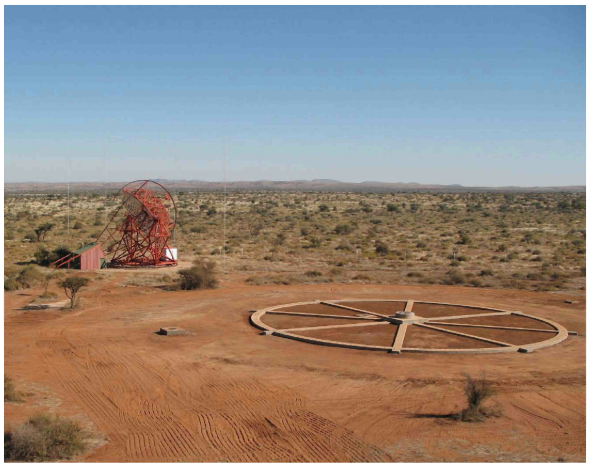

FIGURE 3. H.E.S.S. II foundation and H.E.S.S. I telescope.

TELESCOPE STRUCTURE

H.E.S.S. II is being built as a steel space-frame structure consisting of the following parts (see Fig. 1 and 2):

- A mount rotating in azimuth that supports the two elevation bearings on the top of two towers, 24 m above ground.
  The total weight of the telescope of $\sim$ 560 tonnes is supported by six bogies, each containing two wheels that run on a circular rail of 36 m diameter.
- A dish to support the mirror facets which is connected to the elevation bearings. Finite element model calculations show that the reflector will keep its nominal parabolic shape under gravitational and wind loads with an rms deviation of the mirror facets of < 150 μrad.
- A quadrupod to support the Cherenkov camera.

A trial assembly of parts of the steel structure was done at the construction site in Walvis Bay, Namibia (see Fig. 2), before transport to the H.E.S.S. site.

REFLECTOR

The H.E.S.S. II reflector (see Fig. 4) will consist of 850 hexagonal mirror facets of 90 cm flat-to-flat. The facets are made of glass (thickness 1.5 cm, weight 25 kg) with the front side ground and polished to a spherical shape of 36.4 m focal length. They are front-coated with a reflecting aluminum layer and on top with a quartz coating to protect the reflecting surface from the atmosphere. The overall reflector shape is parabolic with a focal length of 36 m and an approximately rectangular aperture of $\sim$ 24 m $\times$ 30 m. During an automatic alignment procedure the orientation of every facet will be adjusted to achieve the overall reflector shape with highest precision.

DRIVE SYSTEM

During normal operation, the H.E.S.S. II telescope will be driven by four 24 kW servo motors per telescope axis. The motors acting on the same axis work with a predefined torque bias against each other to avoid any kind of play in the components. Most drive-system related electronics (controlled by a PC running a real-time control system) is contained inside a container fixed to the mount (see Fig. 1). The azimuth axis will have a total motion range of 540° and a maximum rotation speed of 200°/min. The elevation axis will have a total motion range of $-32°$ (the park position) to 180° (although usu-

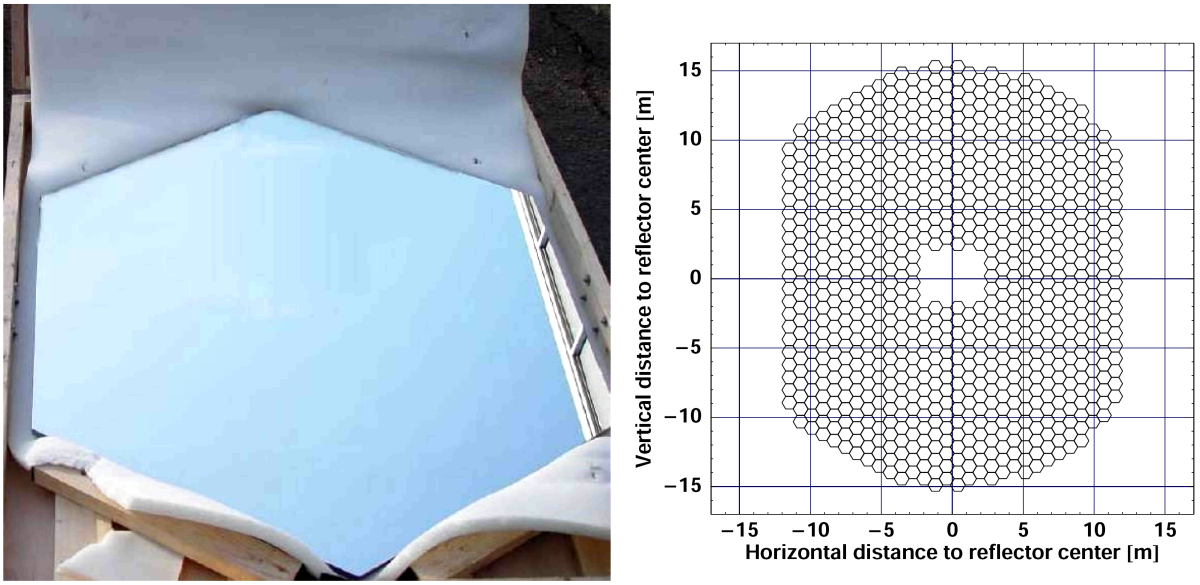

FIGURE 4. *Left:* H.E.S.S. II mirror facet. *Right:* Reflector layout consisting of 850 facets.

ally only the range up to 90° is used for observations) and a maximum speed of 100°/min. The position feedback is given by digital encoders with 10 arcsec resolution attached directly to each telescope axis inside the bearings.

In case parts of the servo drive system fail a subset of motors can be used to drive the telescope in a degraded mode at reduced speed. In case the whole servo drive system fails a completely independent emergency drive system—two 5 kW motors per axis—can be used to drive the telescope manually to the safe stowing position.

CONCLUSIONS

The construction of the H.E.S.S. II Cherenkov telescope is well advanced, according to the current schedule data taking could start in 2009. For the first time H.E.S.S. II will allow to explore the southern sky at energies significantly below 100 GeV, which is very important to address current questions in high-energy astrophysics. Furthermore the design, construction and operation of H.E.S.S. II will be a valuable experience for the construction of CTA [6], the next generation of imaging atmospheric Cherenkov telescopes.

ACKNOWLEDGMENTS

The support of the Namibian authorities and of the University of Namibia in facilitating the construction and operation of H.E.S.S. is gratefully acknowledged, as is the support by the German Ministry for Education and Research (BMBF), the Max Planck Society, the French Ministry for Research, the CNRS-IN2P3 and the Astroparticle Interdisciplinary Programme of the CNRS, the U.K. Science and Technology Facilities Council (STFC), the IPNP of the Charles University, the Polish Ministry of Science and Higher Education, the South African Department of Science and Technology and National Research Foundation, and by the University of Namibia. We appreciate the excellent work of the technical support staff in Berlin, Durham, Hamburg, Heidelberg, Palaiseau, Paris, Saclay, and in Namibia in the construction and operation of the equipment.

REFERENCES

1. The H.E.S.S. web site: `http://www.mpi-hd.mpg.de/hfm/HESS/`
2. Y Becherini et al., these proceedings
3. P. Vincent et al., 2005, Proc. of the 29th ICRC, Pune, 5, 163–166
4. The MAGIC Collaboration: E. Aliu et al., 2008, arXiv:0809.2998v1 [astro-ph]
5. R. Cornils et al., 2005, Proc. of the 29th ICRC, Pune, 00, 101–106
6. The CTA web site: `http://www.cta-observatory.org/`

Bibliography

T. C. Weekes, M. F. Cawley, D. J. Fegan, K. G. Gibbs, A. M. Hillas, P. W. Kowk, R. C. Lamb, D. A. Lewis, D. Macomb, N. A. Porter, et al., ApJ **342**, 379 (1989).

M. Punch, C. W. Akerlof, M. F. Cawley, M. Chantell, D. J. Fegan, S. Fennell, J. A. Gaidos, J. Hagan, A. M. Hillas, Y. Jiang, et al., Nature **358**, 477 (1992).

J. Quinn, C. W. Akerlof, S. Biller, J. Buckley, D. A. Carter-Lewis, M. F. Cawley, M. Catanese, V. Connaughton, D. J. Fegan, J. P. Finley, et al., ApJL **456**, L83+ (1996).

T. Kifune, T. Tanimori, S. Ogio, T. Tamura, H. Fujii, M. Fujimoto, T. Hara, N. Hayashida, S. Kabe, F. Kakimoto, et al., ApJL **438**, L91 (1995), arXiv:astro-ph/9412091.

T. Tanimori, Y. Hayami, S. Kamei, S. A. Dazeley, P. G. Edwards, S. Gunji, S. Hara, T. Hara, J. Holder, A. Kawachi, et al., ApJL **497**, L25+ (1998), arXiv:astro-ph/9801275.

F. Aharonian, A. G. Akhperjanian, K.-M. Aye, A. R. Bazer-Bachi, M. Beilicke, W. Benbow, D. Berge, P. Berghaus, K. Bernlöhr, C. Boisson, et al., A&A **437**, 135 (2005a), arXiv:astro-ph/0502239.

F. Aharonian, A. G. Akhperjanian, K.-M. Aye, A. R. Bazer-Bachi, M. Beilicke, W. Benbow, D. Berge, P. Berghaus, K. Bernlöhr, C. Boisson, et al., A&A **432**, L9 (2005b), arXiv:astro-ph/0501512.

T. Yoshikoshi, M. Mori, P. G. Edwards, S. Gunji, S. Hara, T. Hara, A. Kawachi, Y. Mizumoto, T. Naito, K. Nishijima, et al., ApJ **702**, 631 (2009), 0906.4924.

T. Yoshikoshi, T. Kifune, S. A. Dazeley, P. G. Edwards, T. Hara, Y. Hayami, F. Kakimoto, T. Konishi, A. Masaike, Y. Matsubara, et al., ApJL **487**, L65+ (1997), arXiv:astro-ph/9707203.

H. Muraishi, T. Tanimori, S. Yanagita, T. Yoshida, M. Moriya, T. Kifune, S. A. Dazeley, P. G. Edwards, S. Gunji, S. Hara, et al., A&A **354**, L57 (2000), arXiv:astro-ph/0001047.

F. Aharonian, A. Akhperjanian, J. Barrio, K. Bernlöhr, H. Börst, H. Bojahr, O. Bolz, J. Contreras, J. Cortina, S. Denninghoff, et al., A&A **370**, 112 (2001), arXiv:astro-ph/0102391.

F. Aharonian, A. Akhperjanian, M. Beilicke, K. Bernlöhr, H. Börst, H. Bojahr, O. Bolz, T. Coarasa, J. Contreras, J. Cortina, et al., A&A **393**, L37 (2002), arXiv:astro-ph/0207528.

K. Tsuchiya, R. Enomoto, L. T. Ksenofontov, M. Mori, T. Naito, A. Asahara, G. V. Bicknell, R. W. Clay, Y. Doi, P. G. Edwards, et al., ApJL **606**, L115 (2004), arXiv:astro-ph/0403592.

H. Katagiri, R. Enomoto, L. T. Ksenofontov, M. Mori, Y. Adachi, A. Asahara, G. V. Bicknell, R. W. Clay, Y. Doi, P. G. Edwards, et al., ApJL **619**, L163 (2005), arXiv:astro-ph/0412623.

F. Aharonian, A. G. Akhperjanian, A. R. Bazer-Bachi, M. Beilicke, W. Benbow, D. Berge, K. Bernlöhr, C. Boisson, O. Bolz, V. Borrel, et al., ApJ **636**, 777 (2006a), arXiv:astro-ph/0510397.

J. Hinton and W. Hofmann, Annual Review of Astronomy and Astrophysics **47**, 523 (2009), http://arjournals.annualreviews.org/doi/pdf/10.1146/annurev-astro-082708-101816, URL http://arjournals.annualreviews.org/doi/abs/10.1146/annurev-astro-082708-101816.

C. Deil, C. van Eldik, A. Förster, G. Hermann, W. Hofmann, and M. Panter, in *American Institute of Physics Conference Series*, edited by F. A. Aharonian, W. Hofmann, and F. Rieger (2008a), vol. 1085 of *American Institute of Physics Conference Series*, pp. 693–695.

Y. Becherini, A. Djannati-Atai, M. Punch, K. Bernlöhr, S. Ehlert, J. Masbou, E. Moulin, and M. P. Arribas, in *American Institute of Physics Conference Series*, edited by F. A. Aharonian, W. Hofmann, & F. Rieger (2008a), vol. 1085 of *American Institute of Physics Conference Series*, pp. 738–741.

T. CTA Consortium, ArXiv e-prints (2010), 1008.3703.

S. Funk, J. A. Hinton, G. Hermann, and S. Digel, in *American Institute of Physics Conference Series*, edited by F. A. Aharonian, W. Hofmann, and F. Rieger (2008), vol. 1085 of *American Institute of Physics Conference Series*, pp. 886–889.

R. Atkins, W. Benbow, D. Berley, E. Blaufuss, J. Bussons, D. G. Coyne, T. DeYoung, B. L. Dingus, D. E. Dorfan, R. W. Ellsworth, et al., ApJ **608**, 680 (2004).

A. A. Abdo, B. Allen, D. Berley, S. Casanova, C. Chen, D. G. Coyne, B. L. Dingus, R. W. Ellsworth, L. Fleysher, R. Fleysher, et al., ApJL **664**, L91 (2007), 0705.0707.

F. Aharonian, A. G. Akhperjanian, G. Anton, U. Barres de Almeida, A. R. Bazer-Bachi, Y. Becherini, B. Behera, W. Benbow, K. Bernlöhr, C. Boisson, et al., A&A **499**, 723 (2009a), 0904.3409.

A. A. Abdo, B. T. Allen, T. Aune, D. Berley, C. Chen, G. E. Christopher, T. DeYoung, B. L. Dingus, R. W. Ellsworth, M. M. Gonzalez, et al., ApJL **700**, L127 (2009a), 0904.1018.

A. A. Abdo, B. Allen, T. Aune, D. Berley, E. Blaufuss, S. Casanova, C. Chen, B. L. Dingus, R. W. Ellsworth, L. Fleysher, et al., ApJ **688**, 1078 (2008), 0805.0417.

A. Sandoval, R. Alfaro, E. Belmont, V. Grabski, A. Renteria, A. R. Vasques, O. Vazquez, M. Magdalena Gonzalez, A. Carramiñana, C. Alvarez, et al., ArXiv e-prints (2009), 0912.3329.

On Behalf Of The Milagro, Hawc Collaborations, G. Sinnis, and on behalf of the Milagro and HAWC Collaborations, Nuclear Instruments and Methods in Physics Research A **623**, 410 (2010).

F. Aharonian, J. Buckley, T. Kifune, and G. Sinnis, Reports on Progress in Physics **71**, 096901 (2008).

T. C. Weekes, in *American Institute of Physics Conference Series*, edited by F. A. Aharonian, W. Hofmann, & F. Rieger (2008), vol. 1085 of *American Institute of Physics Conference Series*, pp. 3–17, 0811.1197.

R. C. Hartman, D. L. Bertsch, S. D. Bloom, A. W. Chen, P. Deines-Jones, J. A. Esposito, C. E. Fichtel, D. P. Friedlander, S. D. Hunter, L. M. McDonald, et al., ApJS **123**, 79 (1999).

W. B. Atwood, A. A. Abdo, M. Ackermann, W. Althouse, B. Anderson, M. Axelsson, L. Baldini, J. Ballet, D. L. Band, G. Barbiellini, et al., ApJ **697**, 1071 (2009), 0902.1089.

R. Rando and for the Fermi LAT Collaboration, ArXiv e-prints (2009), 0907.0626.

A. A. Abdo, M. Ackermann, M. Ajello, W. B. Atwood, M. Axelsson, L. Baldini, J. Ballet, D. L. Band, G. Barbiellini, D. Bastieri, et al., ApJS **183**, 46 (2009b), 0902.1340.

A. A. Abdo and for the Fermi-LAT Collaboration, ArXiv e-prints (2010), 1002.0150.

E. Aliu, H. Anderhub, L. A. Antonelli, P. Antoranz, M. Backes, C. Baixeras, J. A. Barrio, H. Bartko, D. Bastieri, J. K. Becker, et al., Science **322**, 1221 (2008), 0809.2998.

A. A. Abdo, M. Ackermann, M. Ajello, A. Allafort, E. Antolini, W. B. Atwood, M. Axelsson, L. Baldini, J. Ballet, G. Barbiellini, et al., ApJS **188**, 405 (2010a), 1002.2280.

D. Majaess, Acta Astronomica **60**, 55 (2010), 1002.2743.

J. P. Vallée, AJ **135**, 1301 (2008).

X. H. Sun, W. Reich, A. Waelkens, and T. A. Enßlin, A&A **477**, 573 (2008), 0711.1572.

D. L. Kong and Z. Zhu, Acta Astronomica Sinica **49**, 224 (2008).

A. W. Strong, I. V. Moskalenko, and V. S. Ptuskin, Annual Review of Nuclear and Particle Science **57**, 285 (2007), http://arjournals.annualreviews.org/doi/pdf/10.1146/annurev.nucl.57.090506.123011, URL http://arjournals.annualreviews.org/doi/abs/10.1146/annurev.nucl.57.090506.123011.

S. Rosswog and M. Bruggen, *Introduction to High-Energy Astrophysics* (Cambridge University Press, 2007).

A. M. Hillas, Journal of Physics G Nuclear Physics **31**, 95 (2005).

B. M. Gaensler and P. O. Slane, ARA&A **44**, 17 (2006), arXiv:astro-ph/0601081.

J. Knödlseder and for the Fermi/LAT Collaboration, ArXiv e-prints (2010), 1006.2635.

A. A. Abdo, M. Ackermann, M. Ajello, L. Baldini, J. Ballet, G. Barbiellini, M. G. Baring, D. Bastieri, B. M. Baughman, K. Bechtol, et al., ApJL **706**, L1 (2009c).

A. Abdo and for the Fermi LAT Collaboration, ArXiv e-prints (2010), 1001.1419.

A. A. Abdo, ArXiv e-prints (2010), 1002.2198.

The Fermi-LAT Collaboration: A. A. Abdo, ArXiv e-prints (2010), 1005.4474.

The Fermi-LAT Collaboration, ArXiv e-prints (2010), 1008.4190.

A. A. Abdo and Fermi LAT Collaboration, ArXiv e-prints (2011), 1103.5727.

The Fermi LAT Collaboration and P. Timing Consortium, ArXiv e-prints (2010), 1011.2076.

P. Slane, D. Castro, S. Funk, Y. Uchiyama, A. Lemiere, J. D. Gelfand, and M. Lemoine-Goumard, ArXiv e-prints (2010), 1004.2936.

A. A. Abdo, M. Ackermann, M. Ajello, W. B. Atwood, M. Axelsson, L. Baldini, J. Ballet, G. Barbiellini, M. G. Baring, D. Bastieri, et al., ApJ **708**, 1254 (2010b), 0911.2412.

M. Meyer, D. Horns, and H. Zechlin, ArXiv e-prints (2010), 1008.4524.

F. Aharonian, A. G. Akhperjanian, U. B. de Almeida, A. R. Bazer-Bachi, B. Behera, M. Beilicke, W. Benbow, K. Bernlöhr, C. Boisson, A. Bochow, et al., ApJ **692**, 1500 (2009b), 0810.2689.

HESS Collaboration and A. Abramowski, ArXiv e-prints (2011), 1105.3206.

F. Aharonian, A. G. Akhperjanian, A. R. Bazer-Bachi, M. Beilicke, W. Benbow, D. Berge, K. Bernlöhr, C. Boisson, O. Bolz, V. Borrel, et al., A&A **448**, L43 (2006b), arXiv:astro-ph/0601575.

F. Aharonian, A. G. Akhperjanian, K.-M. Aye, A. R. Bazer-Bachi, M. Beilicke, W. Benbow, D. Berge, P. Berghaus, K. Bernlöhr, C. Boisson, et al., A&A **435**, L17 (2005c), arXiv:astro-ph/0504120.

F. Aharonian, A. G. Akhperjanian, A. R. Bazer-Bachi, M. Beilicke, W. Benbow, D. Berge, K. Bernlöhr, C. Boisson, O. Bolz, V. Borrel, et al., A&A **460**, 365 (2006c), arXiv:astro-ph/0607548.

F. Aharonian, A. G. Akhperjanian, K.-M. Aye, A. R. Bazer-Bachi, M. Beilicke, W. Benbow, D. Berge, P. Berghaus, K. Bernlöhr, C. Boisson, et al., A&A **439**, 1013 (2005d), arXiv:astro-ph/0505219.

M. de Naurois, ArXiv e-prints (2011), 1104.1680.

F. Aharonian, A. G. Akhperjanian, A. R. Bazer-Bachi, M. Beilicke, W. Benbow, D. Berge, K. Bernlöhr, C. Boisson, O. Bolz, V. Borrel, et al., A&A **456**, 245 (2006d), arXiv:astro-ph/0606311.

The H. E. S. S Collaboration: S. Funk, J. A. Hinton, and O. C. deJager, ArXiv e-prints (2007), 0709.3125.

J. Vandenbroucke and for the Fermi LAT collaboration, ArXiv e-prints (2010), 1012.0849.

S. P. Reynolds, ARA&A **46**, 89 (2008).

W. Baade and F. Zwicky, Proceedings of the National Academy of Science **20**, 259 (1934).

A. R. Bell, MNRAS **182**, 147 (1978).

R. Blandford and D. Eichler, Phys. Rep. **154**, 1 (1987).

G. F. Krymskii, Akademiia Nauk SSSR Doklady **234**, 1306 (1977).

F. Aharonian, A. G. Akhperjanian, A. R. Bazer-Bachi, M. Beilicke, W. Benbow, D. Berge, K. Bernlöhr, C. Boisson, O. Bolz, V. Borrel, et al., A&A **464**, 235 (2007), arXiv:astro-ph/0611813.

J. J. Hester, ARA&A **46**, 127 (2008).

M. S. Longair, *High energy astrophysics. Vol.2: Stars, the galaxy and the interstellar medium* (Cambridge University Press, 1994).

E. Fermi, Physical Review **75**, 1169 (1949).

D. C. Ellison, D. J. Patnaude, P. Slane, P. Blasi, and S. Gabici, ApJ **661**, 879 (2007), arXiv:astro-ph/0702674.

D. Castro, P. Slane, D. J. Patnaude, and D. C. Ellison, ArXiv e-prints (2011), 1104.1179.

E. G. Berezhko and D. C. Ellison, ApJ **526**, 385 (1999).

V. N. Zirakashvili and F. Aharonian, A&A **465**, 695 (2007), arXiv:astro-ph/0612717.

S. Hoppe, Ph.D. thesis, Universität Heidelberg, Max-Planck-Institut für Kernphysik (2008).

D. Nedbal, Master's thesis, Universität Heidelberg, Max-Planck-Institut für Kernphysik (2008).

G. R. Blumenthal and R. J. Gould, Reviews of Modern Physics **42**, 237 (1970).

R. Moderski, M. Sikora, P. S. Coppi, and F. Aharonian, MNRAS **363**, 954 (2005), arXiv:astro-ph/0504388.

S. R. Kelner, F. A. Aharonian, and V. V. Bugayov, Phys. Rev. D **74**, 034018 (2006), arXiv:astro-ph/0606058.

S. Ohm, Ph.D. thesis, Universität Heidelberg (2010).

O. Bolz, Ph.D. thesis, Universität Heidelberg, Max-Planck-Institut für Kernphysik (2004).

S. Gillessen, Ph.D. thesis, Universität Heidelberg, Max-Planck-Institut für Kernphysik (2004).

D. Berge, Ph.D. thesis, Universität Heidelberg, Max-Planck-Institut für Kernphysik (2006).

S. Funk, Ph.D. thesis, Universität Heidelberg, Max-Planck-Institut für Kernphysik (2005).

F. Aharonian, A. G. Akhperjanian, K.-M. Aye, A. R. Bazer-Bachi, M. Beilicke, W. Benbow, D. Berge, P. Berghaus, K. Bernlöhr, O. Bolz, et al., Astroparticle Physics **22**, 109 (2004), arXiv:astro-ph/0408145.

W. Hofmann, I. Jung, A. Konopelko, H. Krawczynski, H. Lampeitl, and G. Pühlhofer, Astroparticle Physics **12**, 135 (1999), arXiv:astro-ph/9904234.

K. Bernlöhr, Astroparticle Physics **30**, 149 (2008), 0808.2253.

D. Heck, J. Knapp, J. N. Capdevielle, G. Schatz, and T. Thouw, *CORSIKA: a Monte Carlo code to simulate extensive air showers*. (., 1998).

K. Bernlohr, Astroparticle Physics **12**, 255 (2000), arXiv:astro-ph/9908093.

M. Lemoine-Goumard, B. Degrange, and M. Tluczykont, Astroparticle Physics **25**, 195 (2006), arXiv:astro-ph/0601373.

M. Naumann-Godó, M. Lemoine-Goumard, and B. Degrange, Astroparticle Physics **31**, 421 (2009), 0905.0359.

M. de Naurois and L. Rolland, Astroparticle Physics **32**, 231 (2009), 0907.2610.

S. Ohm, C. van Eldik, and K. Egberts, Astroparticle Physics **31**, 383 (2009), 0904.1136.

F. Aharonian, A. G. Akhperjanian, A. R. Bazer-Bachi, M. Beilicke, W. Benbow, D. Berge, K. Bernlöhr, C. Boisson, O. Bolz, V. Borrel, et al., A&A **457**, 899 (2006e), arXiv:astro-ph/0607333.

T. Li and Y. Ma, ApJ **272**, 317 (1983).

W. A. Rolke, A. M. López, and J. Conrad, Nuclear Instruments and Methods in Physics Research A **551**, 493 (2005), arXiv:physics/0403059.

R. D. Cousins, American Journal of Physics **63**, 398 (1995).

I. Narsky, ArXiv High Energy Physics - Experiment e-prints (2000), arXiv:hep-ex/0005019.

U. Schwanke, *Calculation of Upper Limits and Measurement Errors for Small Signals*, HESS Internal Note (2004).

V. L. Kashyap, D. A. van Dyk, A. Connors, P. Freeman, A. Siemiginowska, J. Xu, and A. Zezas, ArXiv e-prints (2010), 1006.4334.

D. Berge, S. Funk, and J. Hinton, A&A **466**, 1219 (2007), arXiv:astro-ph/0610959.

B. Glück, Ph.D. thesis, Universität Erlangen-Nürnberg, Universitätsstraße. 4, 91054 Erlangen (2011).

B. L. Refsdal, S. M. Doe, D. T. Nguyen, A. L. Siemiginowska, N. R. Bonaventura, D. Burke, I. N. Evans, J. D. Evans, A. Fruscione, E. C. Galle, et al., in *Proceedings of the 8th Python in Science Conference* (Pasadena, CA USA, 2009), pp. 51 – 57.

R. Refsdal, S. Doe, D. Nguyen, A. Siemiginowska, D. Burke, J. Evans, and I. Evans, in *Astronomical Society of the Pacific Conference Series*, edited by I. N. Evans, A. Accomazzi, D. J. Mink, & A. H. Rots (2011), vol. 442 of *Astronomical Society of the Pacific Conference Series*, pp. 687–+.

F. James and M. Roos, Computer Physics Communications **10**, 343 (1975).

F. Aharonian, A. G. Akhperjanian, A. R. Bazer-Bachi, M. Beilicke, W. Benbow, D. Berge, K. Bernlöhr, C. Boisson, O. Bolz, V. Borrel, et al., Nature **439**, 695 (2006f), arXiv:astro-ph/0603021.

A. Weinstein and for the VERITAS Collaboration, ArXiv e-prints (2009), 0912.4492.

M. R. Calabretta and E. W. Greisen, A&A **395**, 1077 (2002), arXiv:astro-ph/0207413.

A. A. Abdo, M. Ackermann, M. Ajello, J. Ampe, B. Anderson, W. B. Atwood, M. Axelsson, R. Bagagli, L. Baldini, J. Ballet, et al., Astroparticle Physics **32**, 193 (2009d), 0904.2226.

The Fermi-LAT Collaboration, ArXiv e-prints (2011), 1108.1435.

A. Neronov, D. V. Semikoz, and I. Vovk, ArXiv e-prints (2010), 1004.3767.

A. Neronov and D. V. Semikoz, ArXiv e-prints (2010), 1011.0210.

G. Kanbach, D. L. Bertsch, C. E. Fichtel, R. C. Hartman, S. D. Hunter, D. A. Kniffen, B. W. Hughlock, A. Favale, R. Hofstadter, and E. B. Hughes, Space Science Reviews **49**, 69 (1988).

D. J. Thompson, D. L. Bertsch, C. E. Fichtel, R. C. Hartman, R. Hofstadter, E. B. Hughes, S. D. Hunter, B. W. Hughlock, G. Kanbach, D. A. Kniffen, et al., ApJS **86**, 629 (1993).

J. A. Esposito, D. L. Bertsch, A. W. Chen, B. L. Dingus, C. E. Fichtel, R. C. Hartman, S. D. Hunter, G. Kanbach, D. A. Kniffen, Y. C. Lin, et al., ApJS **123**, 203 (1999).

W. D. Pence, L. Chiappetti, C. G. Page, R. A. Shaw, and E. Stobie, A&A **524**, A42+ (2010).

The Fermi-LAT collaboration, ArXiv e-prints (2010), 1002.3603.

J. R. Mattox, D. L. Bertsch, J. Chiang, B. L. Dingus, S. W. Digel, J. A. Esposito, J. M. Fierro, R. C. Hartman, S. D. Hunter, G. Kanbach, et al., ApJ **461**, 396 (1996).

R. Protassov, D. A. van Dyk, A. Connors, V. L. Kashyap, and A. Siemiginowska, ApJ **571**, 545 (2002), arXiv:astro-ph/0201547.

N. Gehrels, ApJ **303**, 336 (1986).

R. P. Kraft, D. N. Burrows, and J. A. Nousek, ApJ **374**, 344 (1991).

F. A. Aharonian and A. M. Atoyan, A&A **362**, 937 (2000), arXiv:astro-ph/0009009.

J. Zhang, Q. Yuan, and X. Bi, ArXiv e-prints (2009), 0908.1236.

T. M. Dame, D. Hartmann, and P. Thaddeus, ApJ **547**, 792 (2001), arXiv:astro-ph/0009217.

M. Su, T. R. Slatyer, and D. P. Finkbeiner, ApJ **724**, 1044 (2010), 1005.5480.

E. Bertin and S. Arnouts, A&A Supplement **117**, 393 (1996).

F. Aharonian, A. G. Akhperjanian, K.-M. Aye, A. R. Bazer-Bachi, M. Beilicke, W. Benbow, D. Berge, P. Berghaus, K. Bernlöhr, C. Boisson, et al., Science **307**, 1938 (2005e), arXiv:astro-ph/0504380.

S. L. Snowden, R. Egger, M. J. Freyberg, D. McCammon, P. P. Plucinsky, W. T. Sanders, J. H. M. M. Schmitt, J. Truemper, and W. Voges, ApJ **485**, 125 (1997).

C. Deil, W. Domainko, and G. Hermann, in *High Time Resolution Astrophysics: The Universe at Sub-Second Timescales*, edited by D. Phelan, O. Ryan, and A. Shearer (2008b), vol. 984 of *American Institute of Physics Conference Series*, pp. 140–147.

C. Deil, Master's thesis, Universität Heidelberg, Max-Planck-Institut für Kernphysik (2007).

C. Deil, W. Domainko, G. Hermann, A. C. Clapson, A. Förster, C. van Eldik, and W. Hofmann, Astroparticle Physics **31**, 156 (2009), 0812.3966.

P. Vincent, A. R. Bazer-Bachi, L. Chounet, P. Corona, Y. Degerly, B. Degrange, E. Delagnes, F. Feinstein, G. Fontaine, P. Goret, et al., in *High Energy Gamma-Ray Astronomy*, edited by F. A. Aharonian, H. J. Völk, & D. Horns (2005), vol. 745 of *American Institute of Physics Conference Series*, pp. 791–796.

E. Delagnes, Y. Degerli, P. Goret, P. Nayman, F. Toussenel, and P. Vincent, Nuclear Instruments and Methods in Physics Research A **567**, 21 (2006).

Y. Becherini, A. Djannati-Atai, and M. Punch, in *SF2A-2008*, edited by C. Charbonnel, F. Combes, & R. Samadi (2008b), pp. 165–+.

D. Horns and the HESS Collaboration, Journal of Physics Conference Series **60**, 119 (2007).

Acknowledgements

First of all I would like to thank Werner Hofmann for giving me the opportunity to work on the HESS survey. I still don't know what we can learn about the gamma-ray source population (which was the initial idea for my thesis), but I have learned a lot about data analysis and what it means to make survey maps and catalogs, and hopefully the astrophysical insights are in the near future. Stefan Funk took me in his group for two months in the fall of 2009 and kindly agreed to referee this thesis. Stefan Wagner was the third person in my IMPRS thesis advisory committee, and I would like to thank him for his constructive feedback.

At the beginning of my thesis I finished my diploma thesis project on the 7-pixel camera with Wilfried Domainko. Willi, thanks for your enthusiasm and for showing up in my office every day and inquiring about the state of things ('Na, wie schau mer aus?'). The technical part of my thesis was the testing and pre-commissioning of the HESS 2 drive system, and I would like to thank German Hermann for teaching me about switches, failsafes and how to test hardware systematically. Due to delays this project was eventually continued by Petter Hofverberg, whom I would also like to thank for the time we spent together at the testbench.

I would also like to thank all of my office mates—Dominik, Robert, Axel and David—for the nice time and fun we had together. A nice thing about the Hofmann group and the HESS collaboration is that there are many people working on gamma-ray astronomy and HESS in particular, and I would like to thank all of you for the discussions and nice time we had together. A special thanks to Joshua Lande and his parents for inviting me to their home in Washington DC (a magical place at Halloween) for the Fermi symposium. Also I would like to explicitly thank Karl Kosack, Stefan Ohm, Henning Gast and others for implementing many aspects of the HESS software that made the survey analysis presented in this thesis possible in the first place. Doug Hague and I implemented the new flux module, thanks for the many discussions on how to (or not to) make HESS spectra.

I would like to thank my parents Rita and Uli for always supporting me and for pushing me to finish the thesis.

Sophia's parents, Katrin and Rudi, thanks for helping us all the time, e.g. taking our daughter Anna every Thursday evening.

Finally I would like to thank Sophia for marrying me despite the fact that I forgot to mention her in the acknowledgements of my diploma thesis :-) Thank you for staying home with Anna in her first year and for the encouragement, patience and help you gave me during my thesis. I love you! You make me happy!

Heidelberg, September 2011
Christoph Deil